[redacted]

UNCLASSIFIED

THIS REPORT HAS [illegible] FOR O[illegible] PUBLICATION.

WT-1109

OPERATION TEAPOT—PROJECT 1.10

Report to the Test Director

AIRBLAST OVERPRESSURE AND DYNAMIC PRESSURE OVER VARIOUS SURFACES

UNCLASSIFIED

D.C. Sachs
L.M. Swift
F.M. Sauer

Stanford Research Institute
Menlo Park, California

CLASSIFICATION CANCELLED
OR CHANGED TO UNCLASSIFIED
BY AUTHORITY OF TID-1323
BY JC DATE 12/1/62

Issuance Date: September 9, 1957

[illegible]

THIS REPORT HAS [illegible] FOR OPEN PUBLICATI[illegible]

UNCLASSIFIED

[redacted]

[redacted]

AD617182

WT-1109

This document consists of 194 pages

No. 197 of 250 copies, Series A

UNCLASSIFIED

Operation TEAPOT

NEVADA TEST SITE

February – May 1955

UNCLASSIFIED

Project 1.10

AIRBLAST OVERPRESSURE AND DYNAMIC PRESSURE OVER VARIOUS SURFACES

COPY 1 OF 1

HARD COPY $. 13.00

MICROFICHE $. 1.25

192p

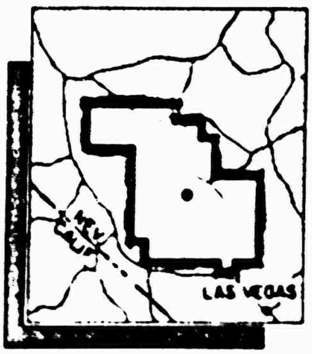

HEADQUARTERS FIELD COMMAND, ARMED FORCES SPECIAL WEAPONS PROJECT
SANDIA BASE, ALBUQUERQUE, NEW MEXICO

Chapter 1
INTRODUCTION

1.1 OBJECTIVE

The objective of Project 1.10 was to obtain data on the variation with ground range of static overpressure (side-on) and dynamic pressure from a nuclear explosion over a dust-free water surface, an asphalt surface, and a natural desert surface.

Particular attention was given to the relationship between overpressure and dynamic pressure in the regions of expected perturbed wave forms. These data were to be used for the modification and reinforcement of theory of blast effects and precursor formation. Accurate theory would permit establishment of damage criteria under a variety of burst conditions, when correlated with measurements of other blast phenomena. Specific data were also to be furnished to Programs 3 and 5 for use in analyzing structural effects.

1.2 BACKGROUND

Prior to 1952, the optimum height of burst for maximum area of desired ground level peak overpressure was obtained from Reference 1. This information was based on theoretical considerations and extrapolation from small-scale experiments, and on limited nuclear-explosion data from Bikini Able and a few tower shots. The Buster shots in 1951 indicated considerable disparity between predicted and observed pressures both in amplitude and wave form (Reference 2). The Tumbler shots in 1952 were planned to resolve some of these differences; the results confirmed that at certain relatively low-scale heights of burst these discrepancies were real (Reference 3). On Tumbler Shot 4 (particularly at pressure levels above approximately 8-psi peak) amplitudes were reduced, rise times were increased, and the velocity of propagation of the first effects was increased. These effects were shown to be associated with the thermal radiation acting jointly on the earth's surface and on surface-produced dust clouds to produce a thermal layer. Evidence indicated the existence of severe turbulence in these regions of interest, which complicated the problem of delineating the behavior of the blast wave by point measurements. At this time a rather satisfactory qualitative analysis of these phenomena was formulated. However, the quantitative data from Tumbler were insufficient to permit development of analytical techniques that would allow predictions of the magnitude of these disturbing effects under a given set of conditions other than for a desert-like surface.

The Upshot-Knothole shots in 1953, particularly Shots 1, 10, and 11, provided a great deal of quantitative data on these phenomena (References 4 and 5). Data from these and previous shots permitted the development of analytical techniques for prediction of overpressure to a satisfactory degree of accuracy, but it became increasingly obvious that the correlation between peak overpressure and damage effects was not satisfactory in these regions of distorted wave forms. This was particularly true on Upshot-Knothole Shot 10, where damage to several types of targets at some ground ranges was far greater than that expected on the basis of the peak overpressure observed. A number of measurements of dynamic pressure were planned and conducted, but the rather unexpected damage to the gage mountings themselves reduced the usefulness of the data (Reference 6).

Program 1 of Operation Teapot was therefore planned to give primary emphasis to measurement of dynamic pressures in those regions where the relationship between dynamic pressure and overpressure remained questionable. Analysis of earlier data had also indicated that the magnitude of these unpredicted effects probably depended on the nature of surfaces involved; Teapot, therefore, included an investigation of the effects of different types of surface upon blast phenomena.

Prior to Teapot, experimental data seemed to indicate that formation of the precursor was due to refraction of the incident shock wave by a layer of heated air near the ground surface. It was believed that if the temperature of the heated layer were sufficiently high with respect to the ambient air above it, the velocity of this refracted shock wave would be increased so that it would reach a ground radius station sooner than would the incident (undisturbed) shock wave. The refracted wave, as it was propagated through the heated air layer, also sent another shock wave into the ambient air above the thermal layer (Reference 7). Although few dynamic-pressure measurements had been obtained in the precursor region, the data available indicated that the dynamic pressures in the region of disturbed blast waves were equal to or greater than ideal and much greater than would be calculated from the measured overpressures using the classical Rankine-Hugoniot relationship applicable across a shock front.

These abnormally high dynamic-pressure measurements were at least partially explained when laboratory tests indicated that the pitot-static tube measurement is sensitive to dust or other particulate matter carried along by the shock wave. Differential pressures measured in the precursor region are therefore believed to represent the dynamic pressure of the air plus some portion of the dynamic pressure associated with dust.

Before Teapot, very little data was available for determining the effect of the physical properties of the ground surface upon precursor wave formation and development. A few measurements of distrubed blast waves over land and water and the results of the smoke experiments on Upshot-Knothole (Reference 7) indicated that conditions which altered the physical characteristics at or near a surface could have a profound effect upon measured pressures and wave forms. Furthermore, since it has become apparent that pressure measurements are influenced by such parameters as dust density, near-surface temperatures, and wind direction, the determination of these quantities assumes a greater importance than previously realized. For this reason, the Teapot program included extensive measurements of some of the more-fundamental blast parameters for which presumably dependable instrumentation had been developed previously, and included a limited number of exploratory measurements of the more-important physical parameters.

Finally, a limited program of drag-force measurement on simple shapes was included. These measurements, when coupled with the pressure measurements at the same locations, could permit later correlation with wind-tunnel and shock-tube experiments designed to investigate the drag forces developed by a precursor.

Chapter 2

PROCEDURE

2.1 DESCRIPTION OF TESTS

The two Operation Teapot Shots with which this report is concerned are Shots 6 and 12 (see Table 2.1).

Blast measurements on Shot 6, although limited in number, were included to explore the effects of different types of ground surface (desert and asphalt). In addition, it was thought that Teapot Shot 6 data could help clarify the results obtained on Upshot-Knothole Shot 10 (Reference 4), which was detonated at approximately the same burst height.

Shot 12 measurements, taken over three different surfaces (desert, asphalt, and water), were designed to obtain detailed information on the effects due to surface properties in the region of disturbed blast waves. Also, it was hoped that the measurements would yield definitive data on pitot-tube dynamic pressure, few of which were available from nuclear tests prior to Teapot.

2.2 GAGE LAYOUTS

2.2.1 Shot 6. The gage layout for Shot 6 (Figure 2.1) was designed to obtain maximum information practicable with the 24 available gage channels. Since ground zero was located near the northern edge of the paved area in Area T-7-1, blast lines were extended both north over the desert area and south over the paved area. The availability of these surfaces, similar to two of those used on Shot 12, was the basis of the decision to instrument this shot. However, the desert surface in this area was rough and boulder-strewn, in contrast with the smooth surface of the Frenchman Flat area of Shot 12. Also, the asphalt surface was broken and ridged in places, but still provided a definite contrast to the desert surface and was much greater in length and span than the Shot 12 asphalt line. On each line, gage stations were located to concentrate on the region of probable transition between precursor and normal wave forms. Ground ranges of 1,300, 1,650, and 2,000 feet in each direction were chosen as those most likely to produce the critical information, based on the pretest estimate of yield and on the results of Upshot-Knothole Shot 10.

It was decided that measurements of surface-level overpressure, and of overpressure and dynamic pressure (using a pitot-tube gage) at 10-foot elevation at each station would provide maximum useful information. To compute corrections to the measured dynamic pressure corresponding to variations in pitch angle of flow, pitch gages at 10 feet were included at each gage station. (The angle of pitch is defined as the flow angle measured in that vertical plane which is determined by the pitch gage and ground zero.)

2.2.2 Shot 12. The gage layout for Shot 12 (Figures 2.2 and 2.3) was a complex problem. The general concept of Program 1 for this shot was to instrument three different blast lines: one over a water surface, one over an asphalt surface, and the third over the natural desert. An effort was made to locate gages on each line to obtain the maximum information of interest and the maximum correlation between lines. A number of projects participated, and the resultant gage layout for Project 1.10 represented, in some instances, a compromise between interests for the best overall program results.

The general principle followed in instrument layout was as follows. Surface-level air pressures were measured at sufficient stations along each line to provide correlation with other shots and general information as to pressure level versus radius. Aboveground (10-foot) overpressure was measured at a few stations on each line for further correlation with other shots and for determination of any pressure gradients which might be detectable. Dynamic pressures with their associated overpressures were measured at 3- and 10-foot heights at intervals determined partly by practicability of towers and partly by the usefulness of this information to other projects and programs. At one station on each line, investigation was made of the variation of dynamic pressures with heights up to 40 feet. At two stations (1,500 and 2,500 feet) on the water line, the pitot-tube measurements were made at locations which were displaced from the main blast line (see Figure 2.4). It was hoped that these measurements would aid in determining the extent and time of feed-in of disturbances from the desert surface. Measurements on the water and asphalt lines were restricted in radius to that of the lines themselves. In general, for each gage measuring dynamic pressure, associated measurement of pitch was made by Project 1.11 (Sandia Corporation) for correction of measured pressures and for study of flow characteristics. Full detail of the gage layouts can be obtained from Figures 2.2 through 2.4. In conjunction with this project, seven instrument channels were supplied to Project 3.6 for their direct use, not connected with free-field phenomenology. Two channels were used for measurements of loading on beams under Project 3.2. These beam devices were located at 200- and 2,500-foot ground range on the desert line.

TABLE 2.1 DESCRIPTION OF TESTS

Shot	Code Name	Date	Location (Area)	Blast-Line Surface	Yield	Height	Atmos. Press. GZ	Atmos. Press. Burst Ht	Air Temp GZ	Air Temp Burst Ht
					kt	ft	mb	mb	°C	°C
6	Bee	Mar 22, 1955	T-7-1a (Yucca)	Desert Asphalt	7.76	500 Tower	876	871	1.0	5.0
12	Met	Apr 15, 1955	Frenchman Flat	Water Desert Asphalt	22.0	400 Tower	908	895	19.5	18.9

2.3 PREDICTIONS

In planning an experiment of this type, it is necessary to predict the values of the functions to be measured with an accuracy sufficient to allow the sensitivity of each channel to be set closely enough so that satisfactory deflections will be recorded. For best results, these should be within a factor of two from the true values.

Sufficient data were available (References 3, 4, and 5) from shots at similar heights of burst over desert soil to permit reasonably dependable predictions of peak overpressure versus radius for the desert lines of both shots. These same predictions were used for the asphalt lines, under the assumption that thermal effects would be similar to those on the desert lines. For prediction purposes, an ideal curve was constructed for the water-line of Shot 12, based on the free-air curve and assumed reflection factors.

Predictions of dynamic pressure on the desert lines were based largely on data from Upshot-Knothole Shots 1, 10, and 11 (References 4 and 6). While not as complete as overpressure data, they were sufficient to permit reasonably dependable predictions. For the water line, predictions were based on the theoretical relationships between overpressure and dynamic pressure, using the ideal curve of overpressure as a basis for calculation.

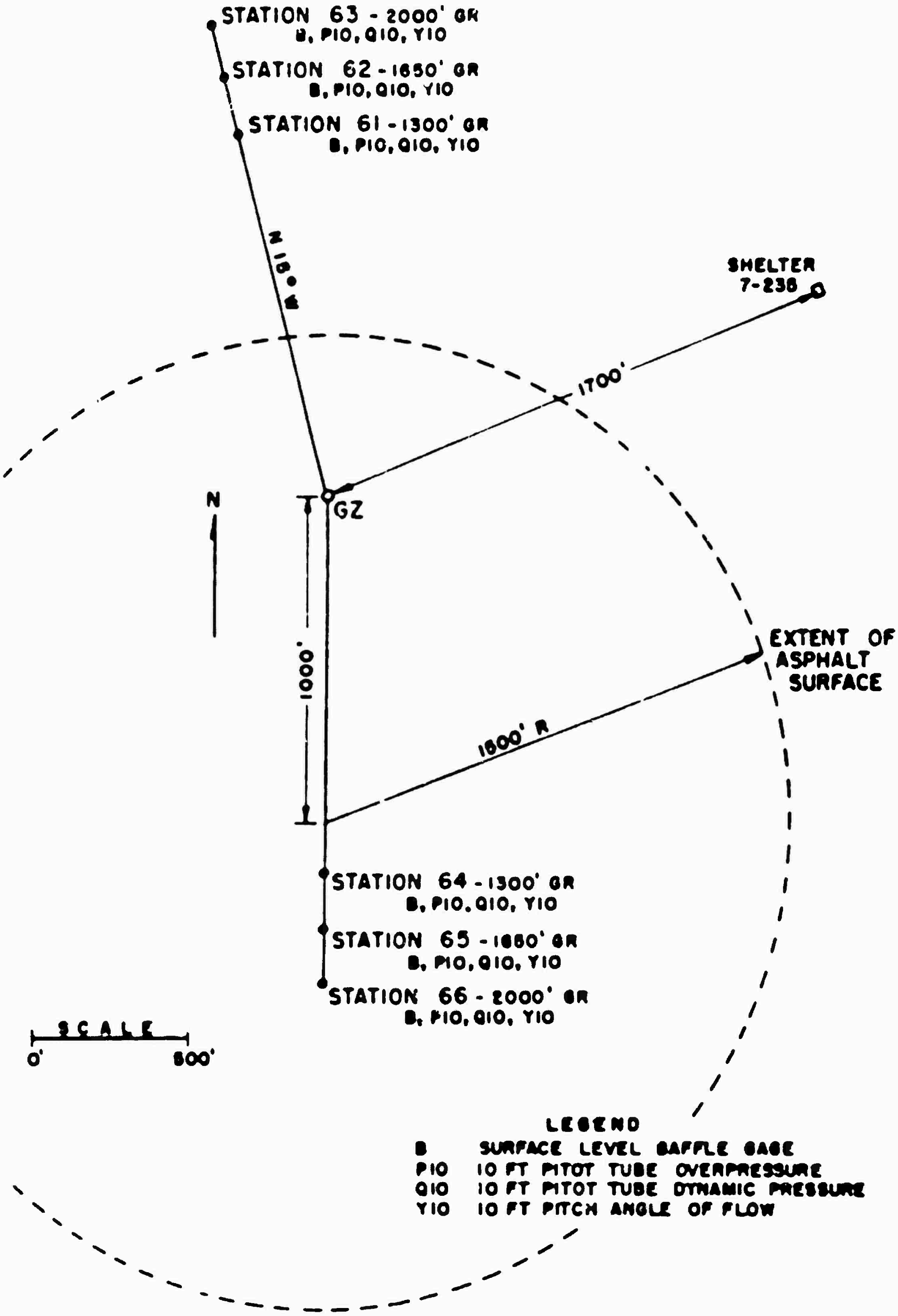

Figure 2.1 Gage layout, Shot 6.

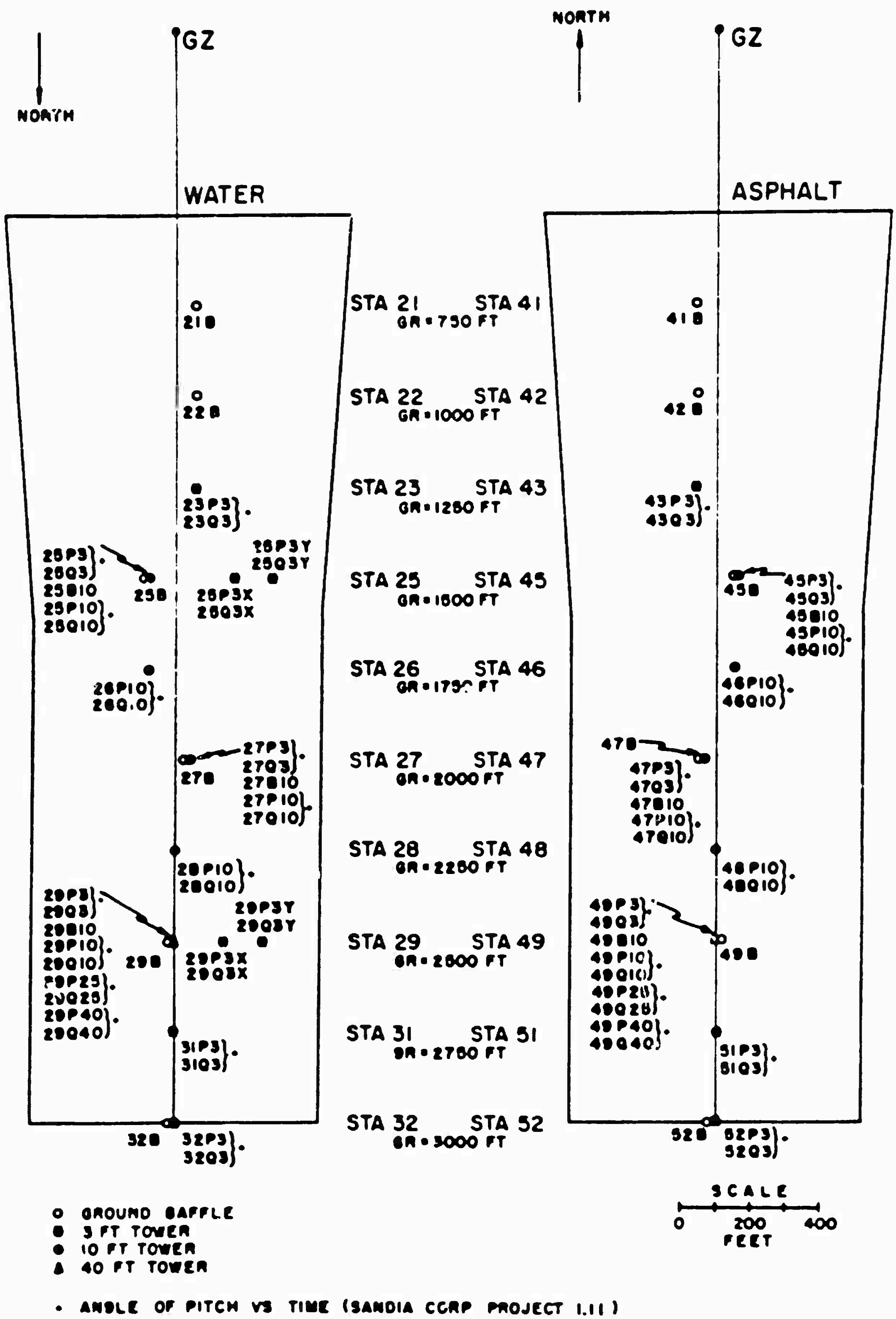

Figure 2.2 Gage layout, Shot 12, water and asphalt lines.

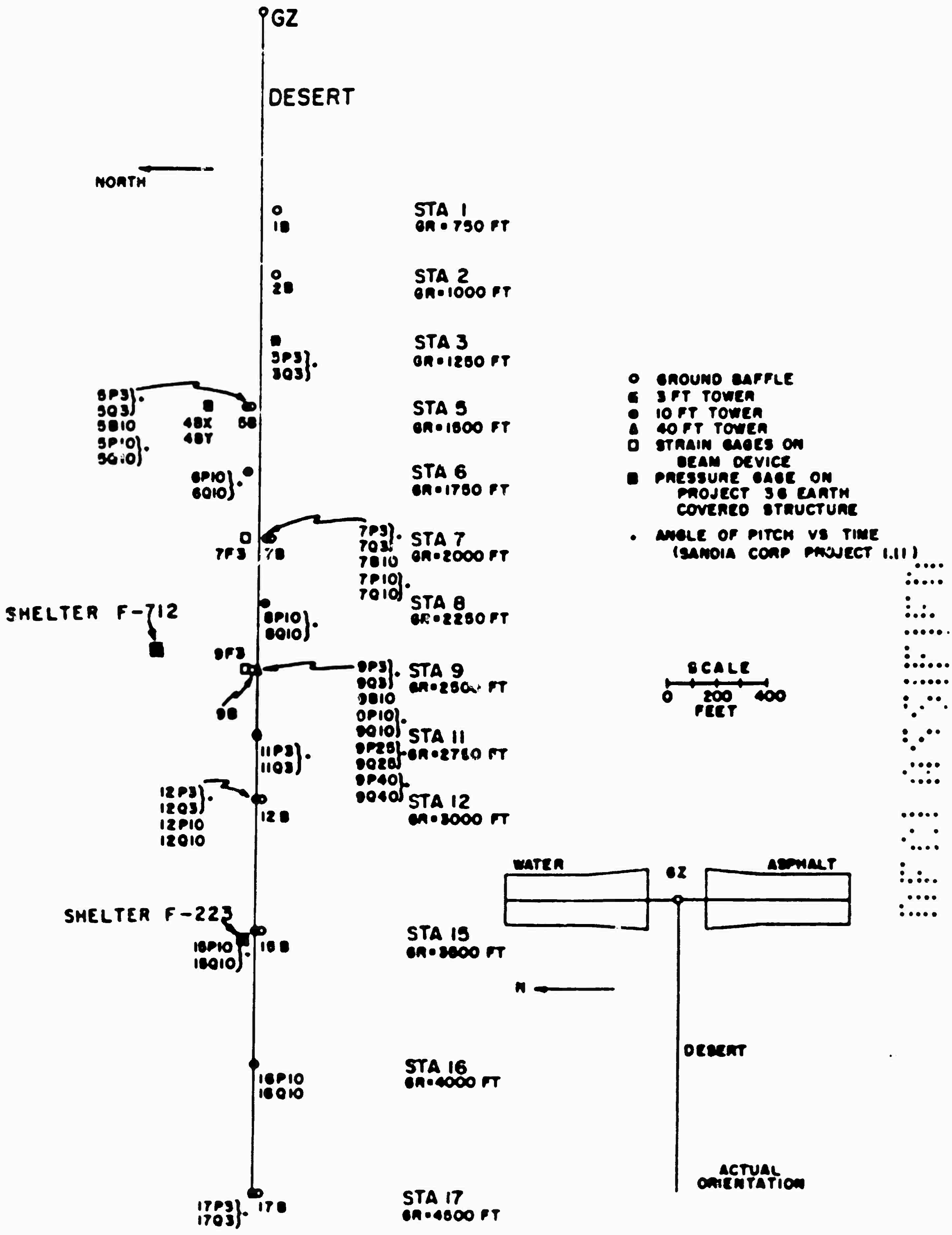

Figure 2.3 Gage layout, Shot 12, desert line and area layout.

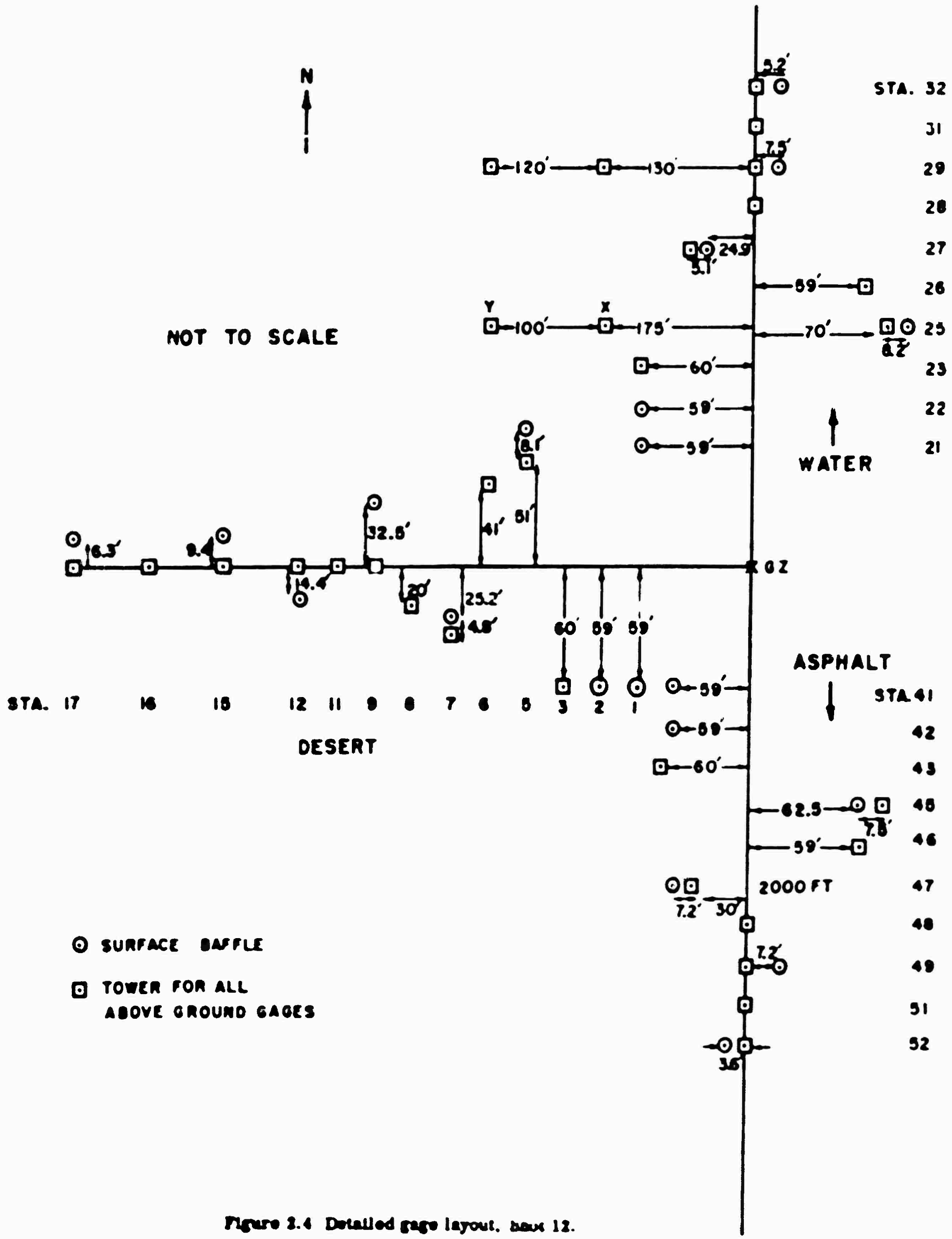

Figure 2.4 Detailed gage layout, Shot 12.

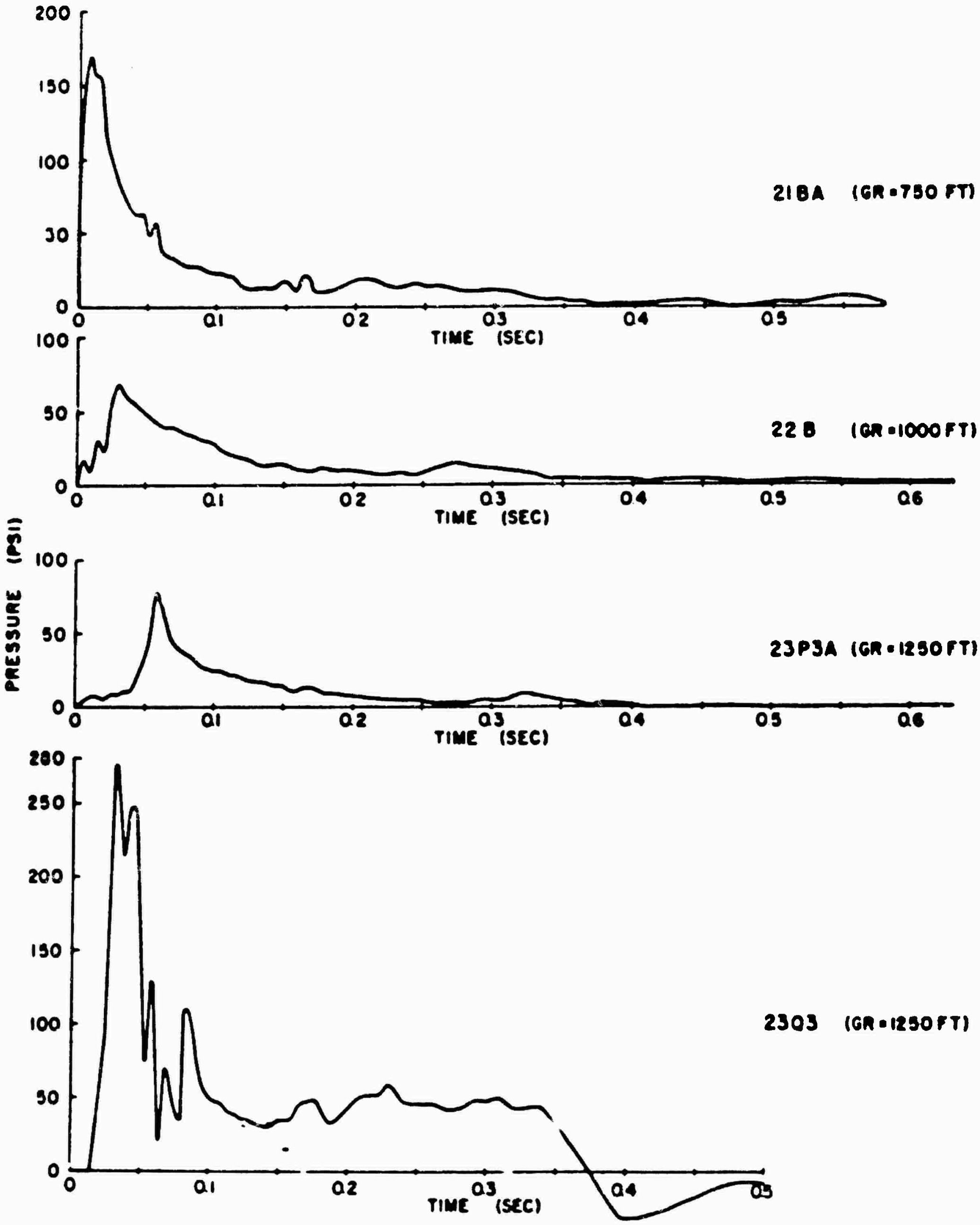

Figure 4.3 Pressure versus time, water line, Shot 12 (ground range = 750 feet – 1,250 feet).

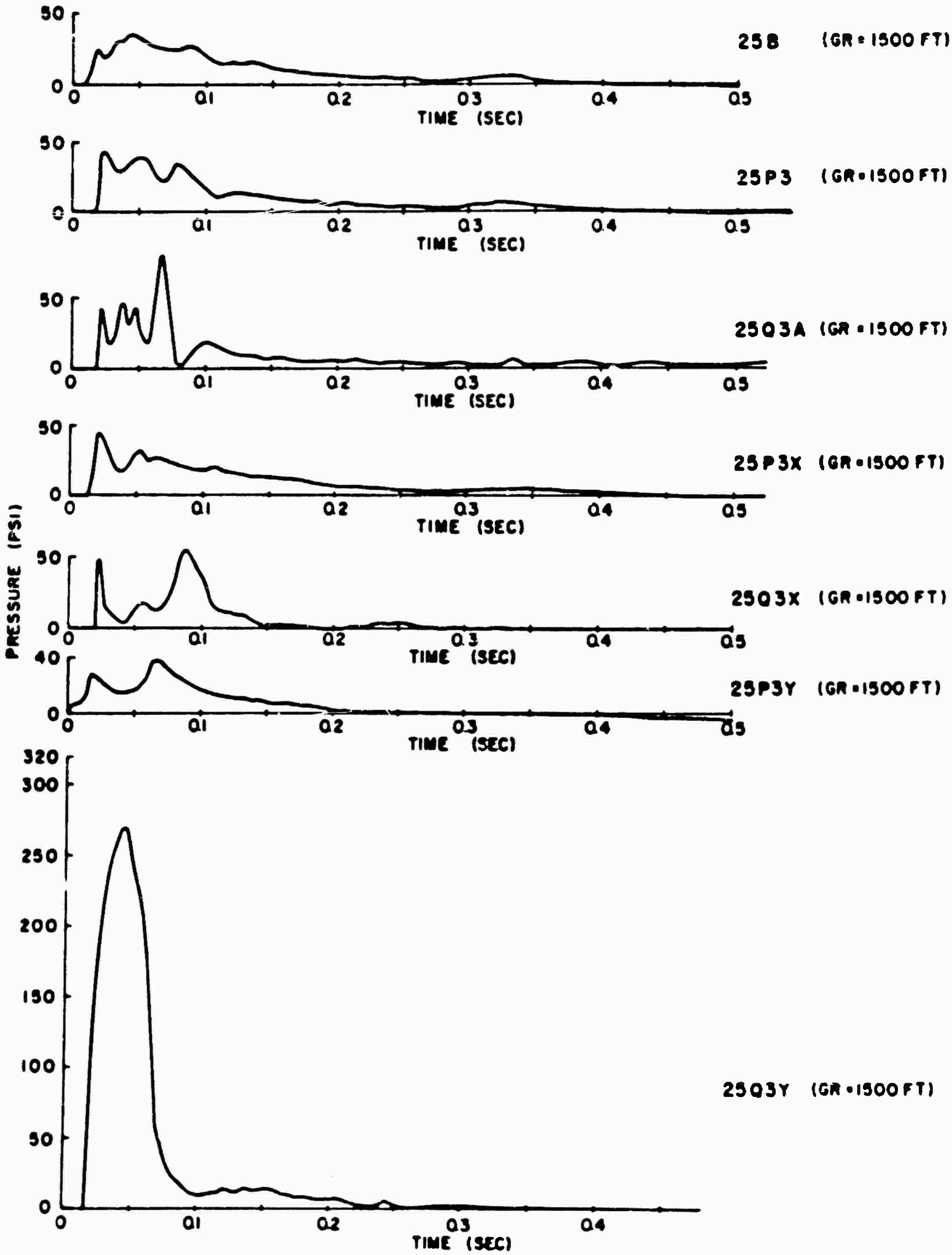

Figure 4.4 Pressure versus time, water line, Shot 12 (ground range = 1,500 feet).

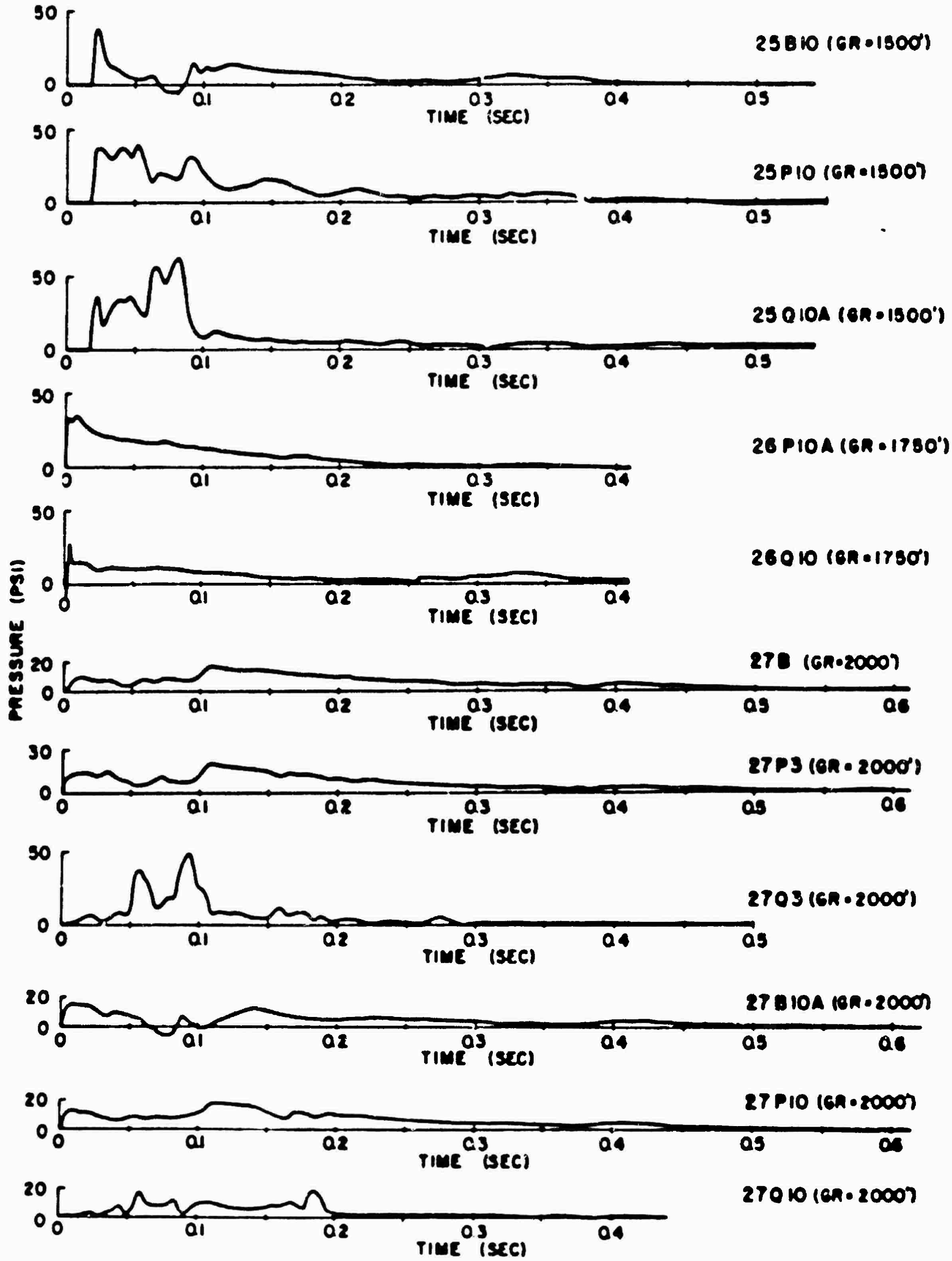

Figure 4.8 Pressure versus time, water line, Shot 12 (ground range = 1,500 feet–2,000 feet).

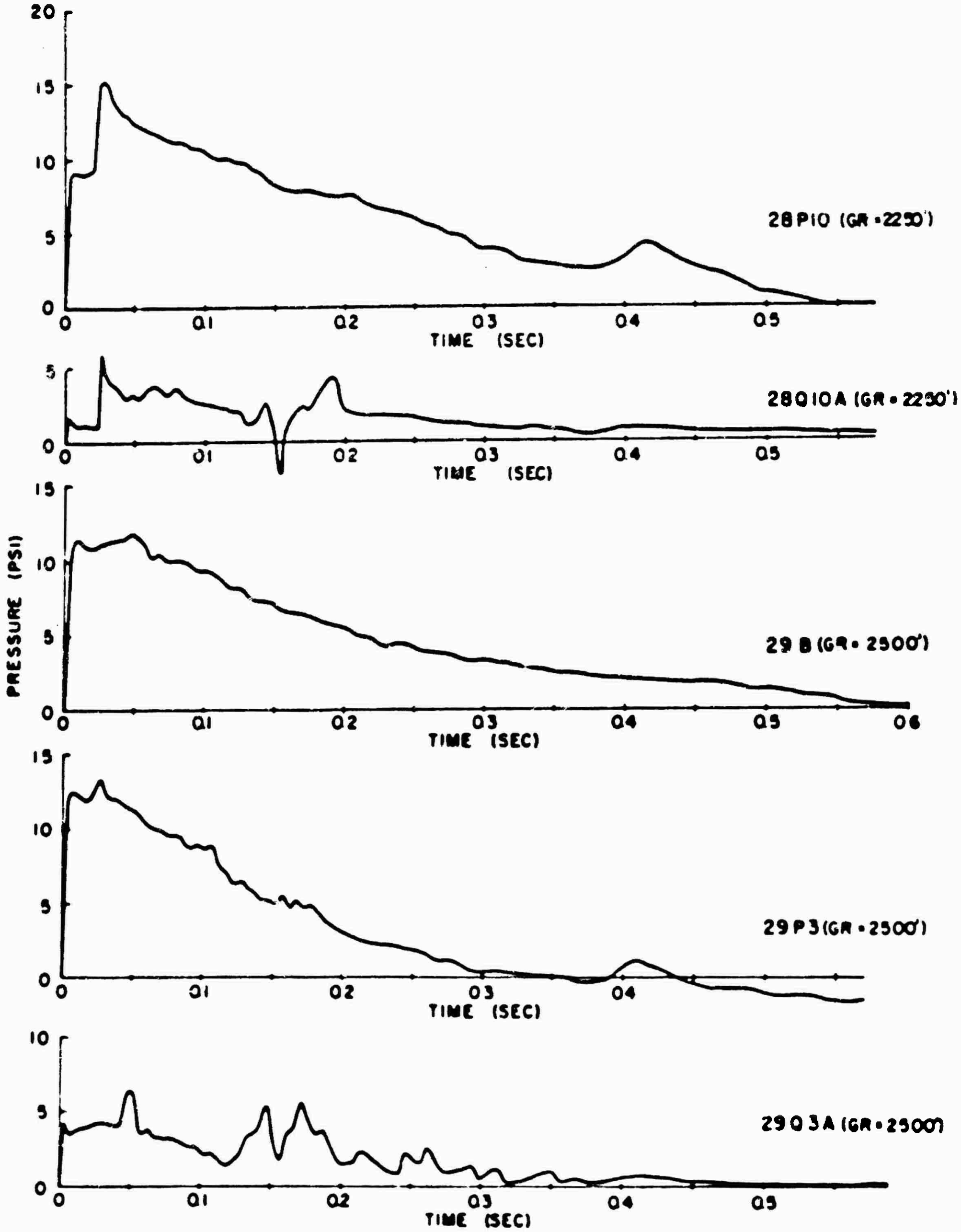

Figure 4.6 Pressure versus time, water line, Shot 12, (ground range = 2,250 feet–2,500 feet).

CONFIDENTIAL

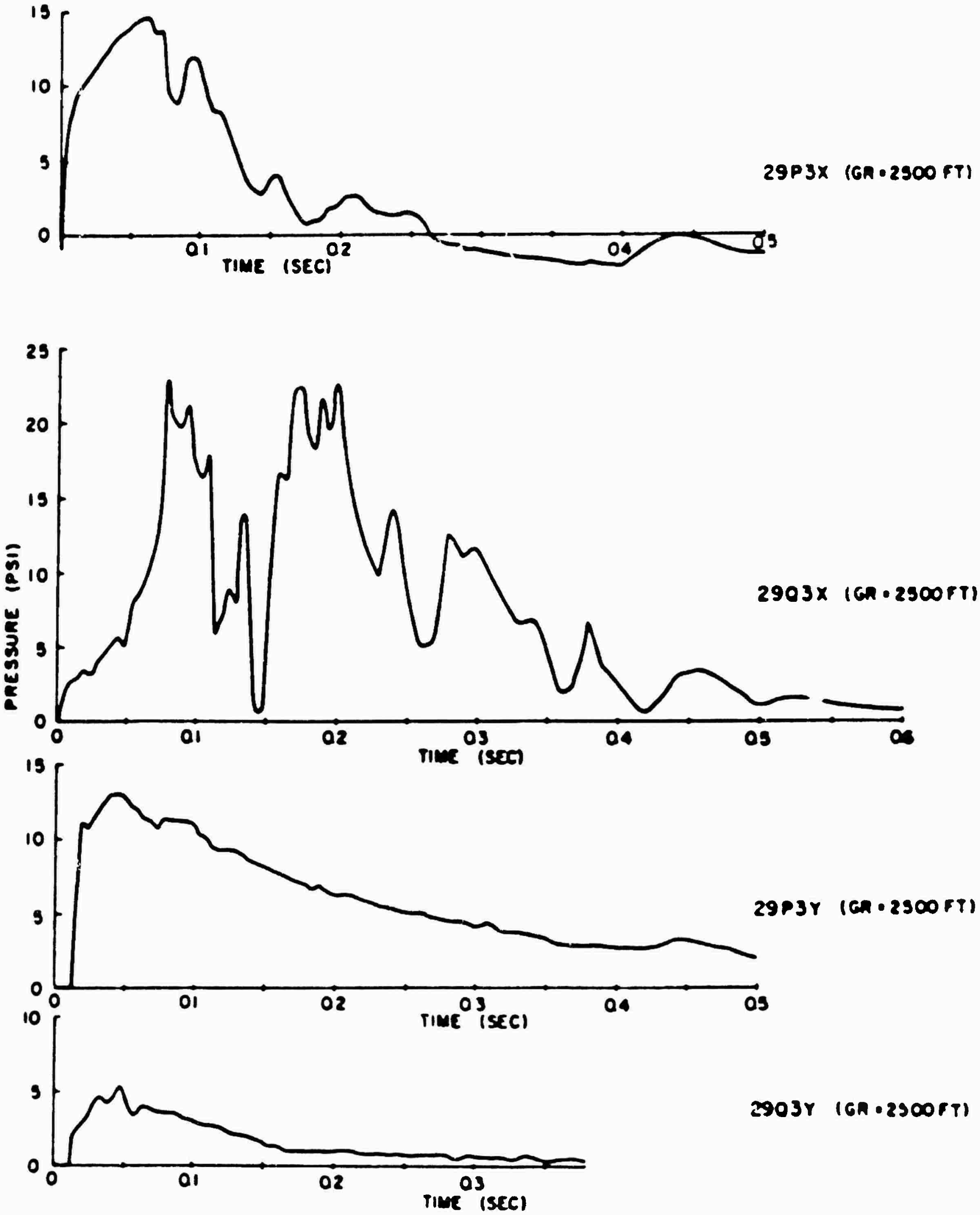

Figure 4.7 Pressure versus time, water line, Shot 12 (ground range = 2,500 feet).

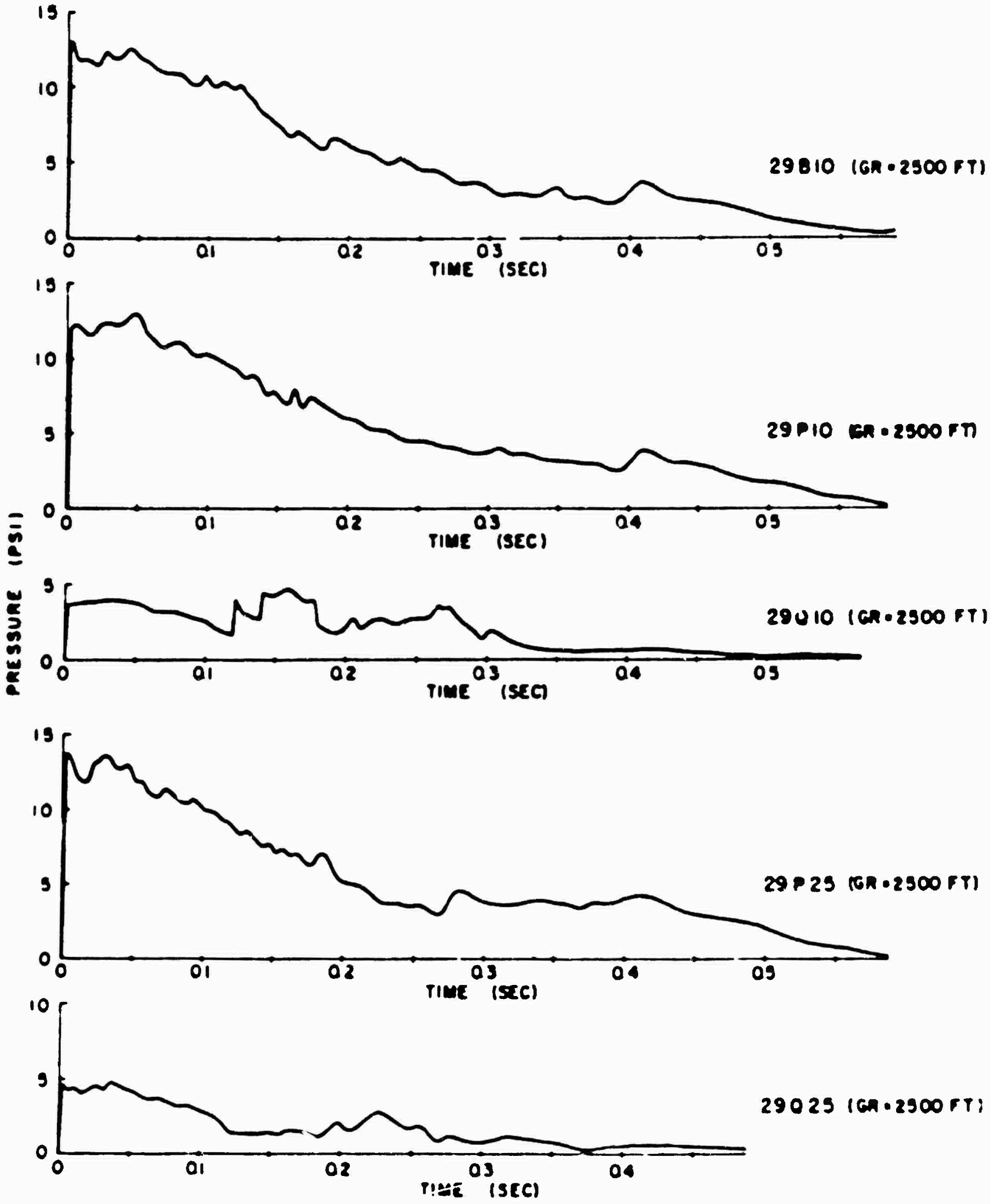

Figure 4.8 Pressure versus time, water line, Shot 12 (ground range = 2,500 feet).

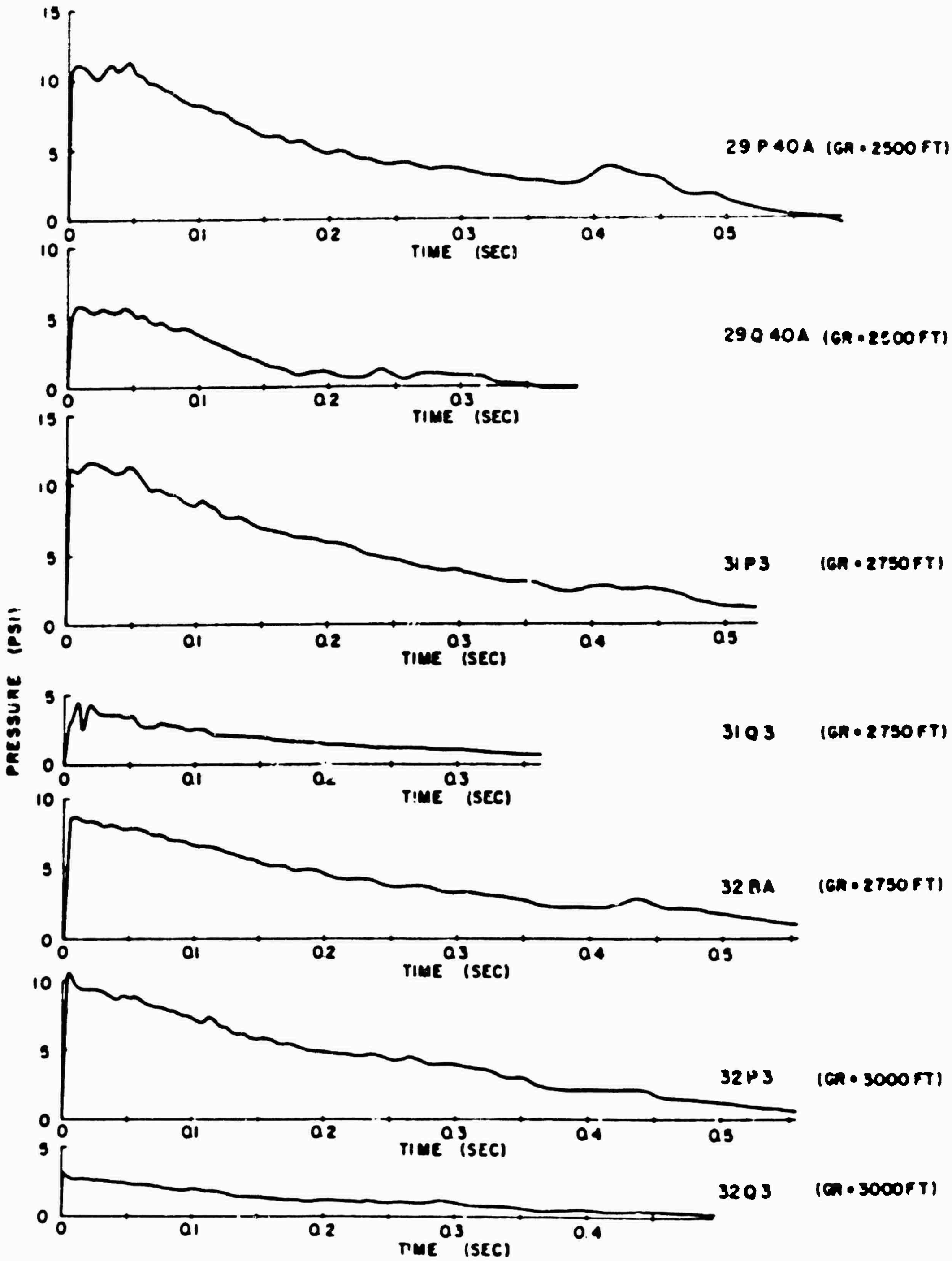

Figure 4.9 Pressure versus time, water line, Shot 12 (ground range = 2,500 feet–3,000 feet).

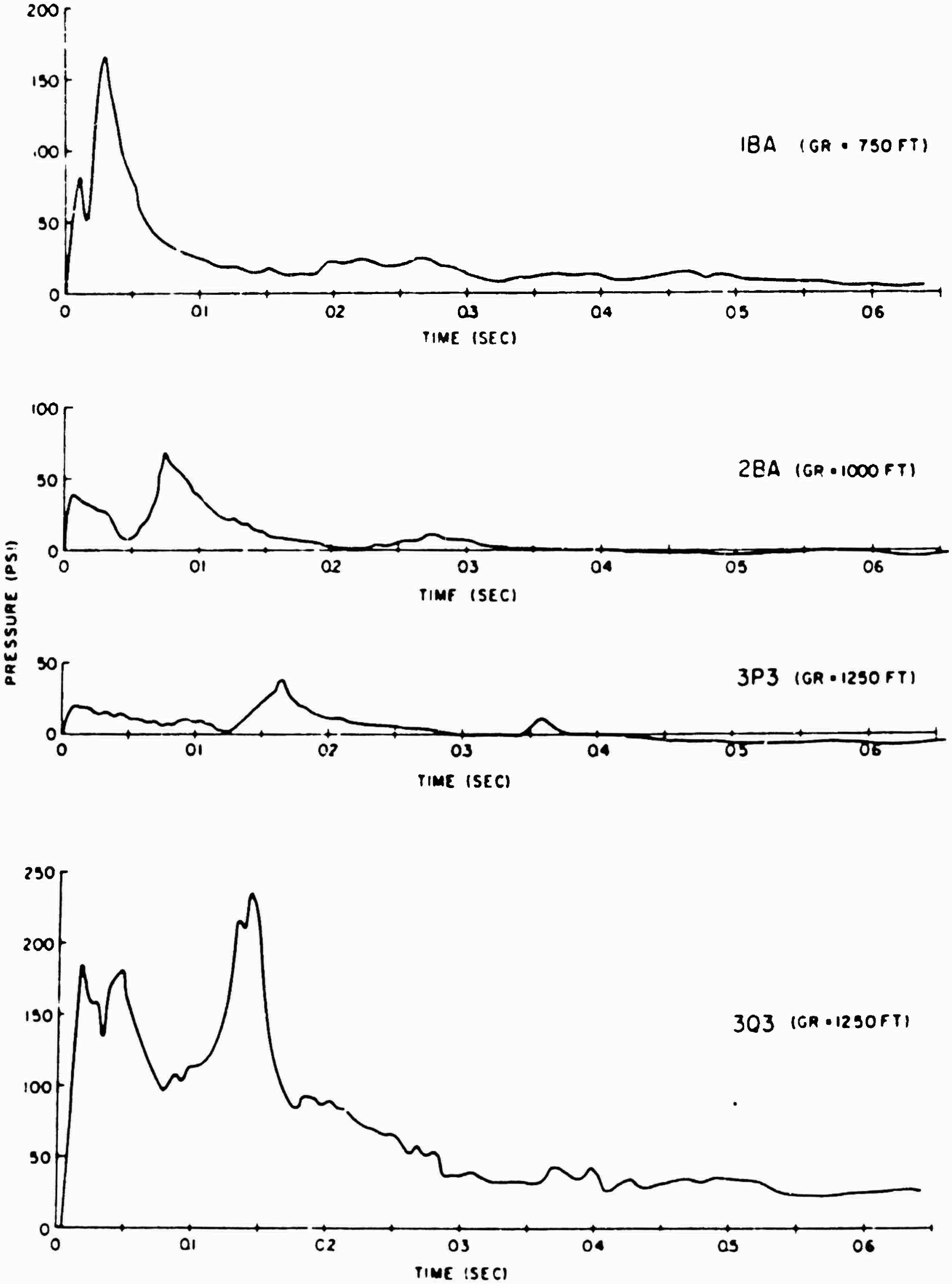

Figure 4.10 Pressure versus time, desert line, Shot 12 (ground range = 750 feet–1,250 feet).

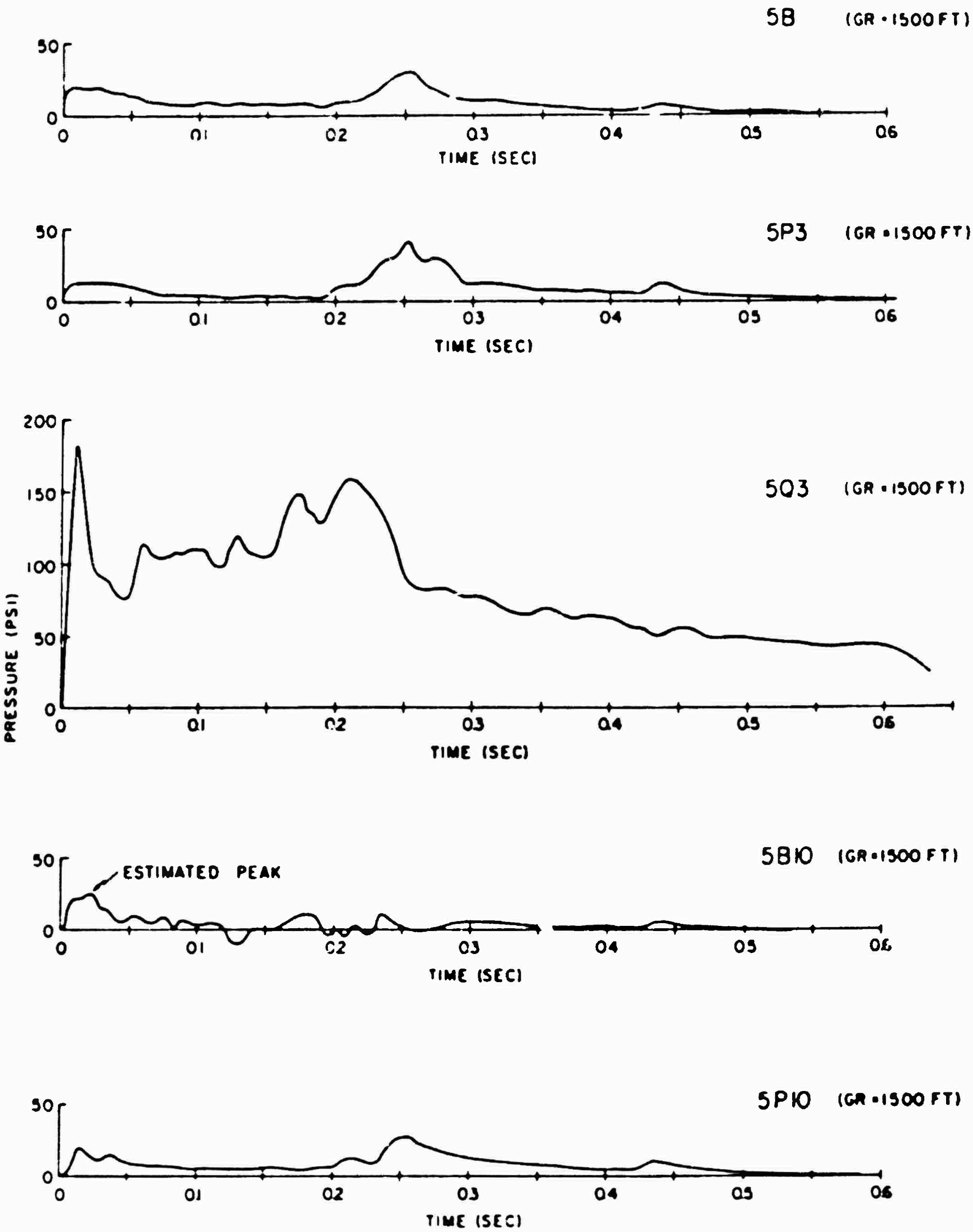

Figure 4.11 Pressure versus time, desert line, Shot 12 (ground range = 1 500 feet).

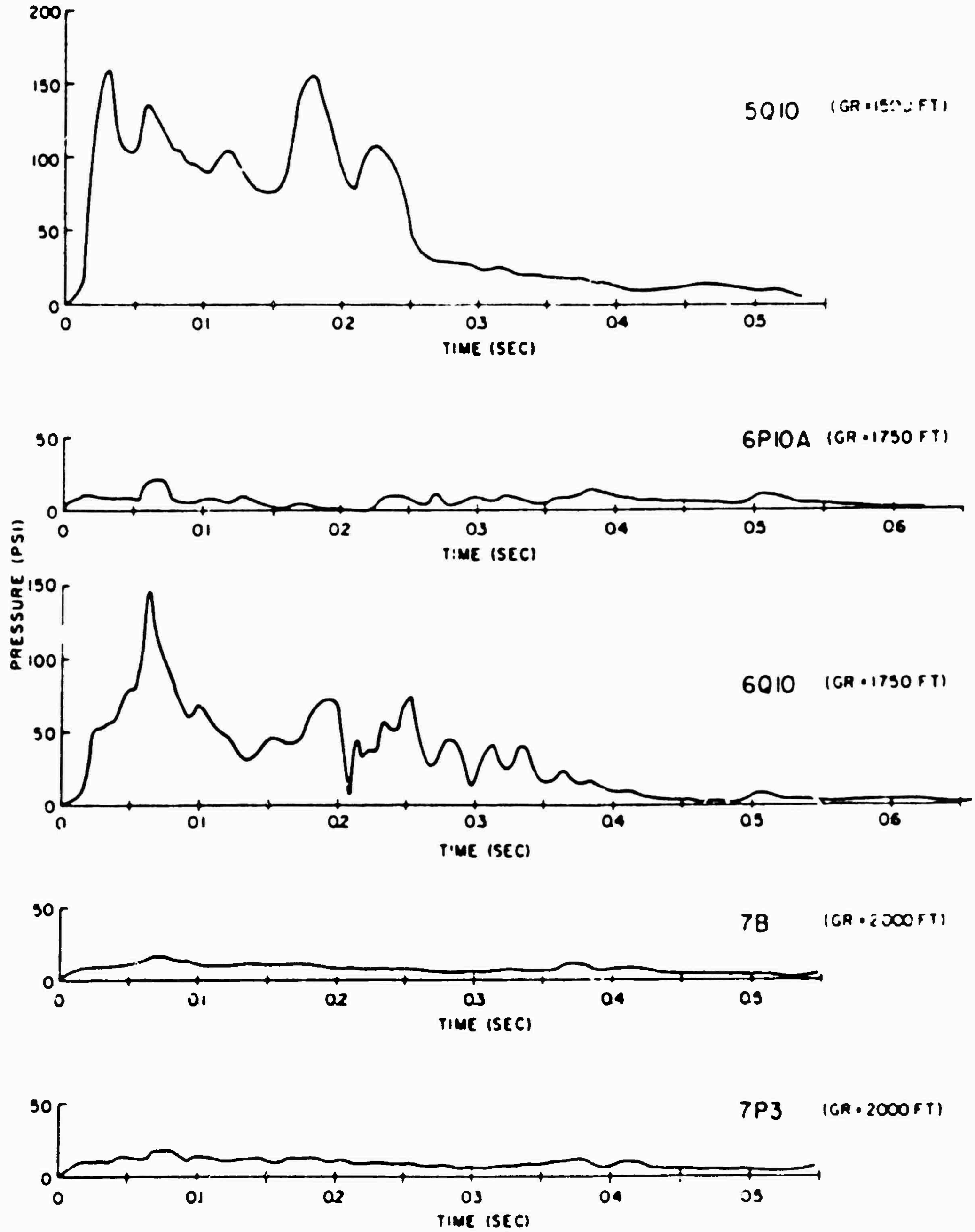

Figure 4.12 Pressure versus time, desert line, Shot 12 (ground range = 1,500 feet–2,000 feet).

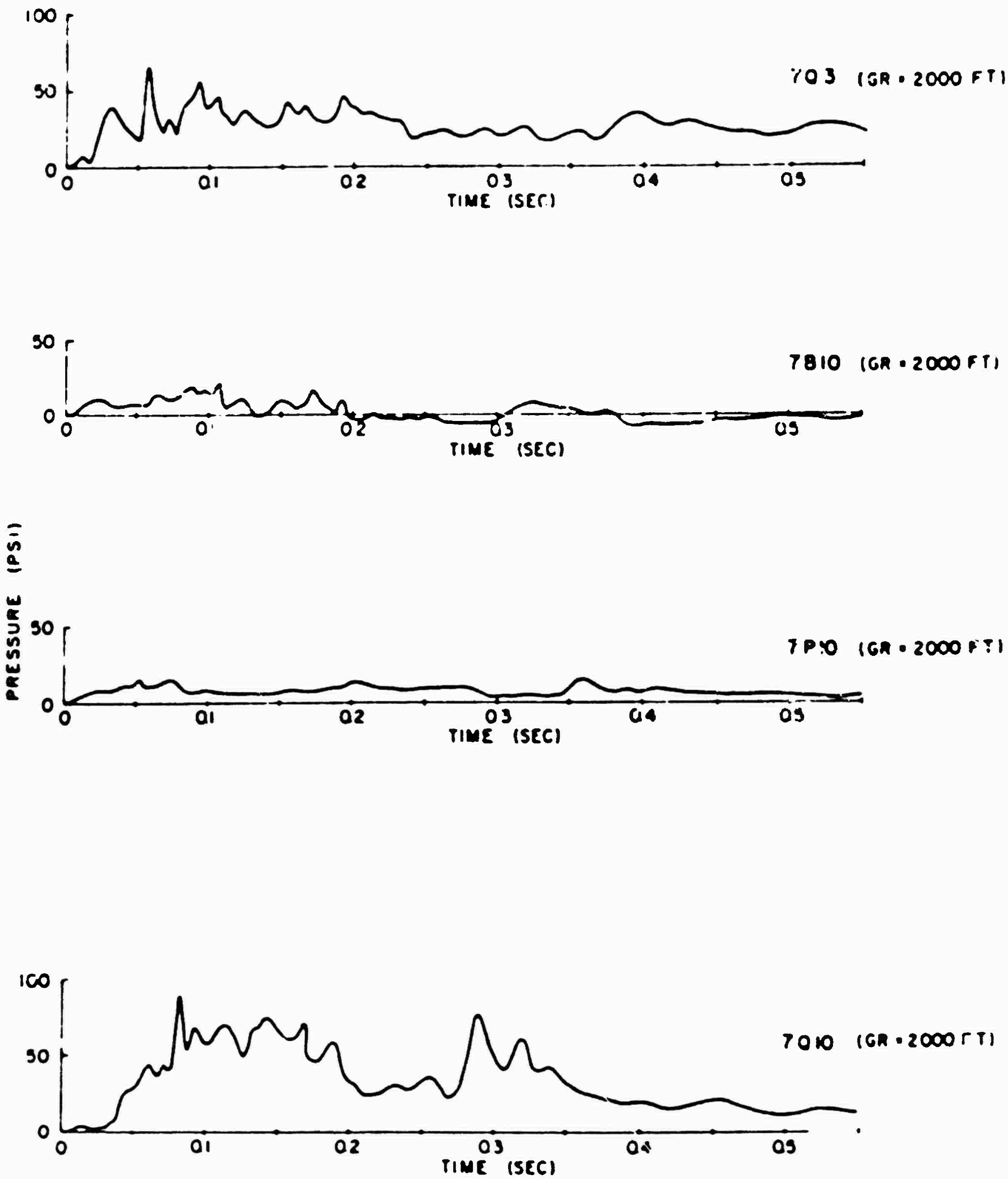

Figure 4.13 Pressure versus time, desert line, Shot 12 (ground range = 2,000 feet).

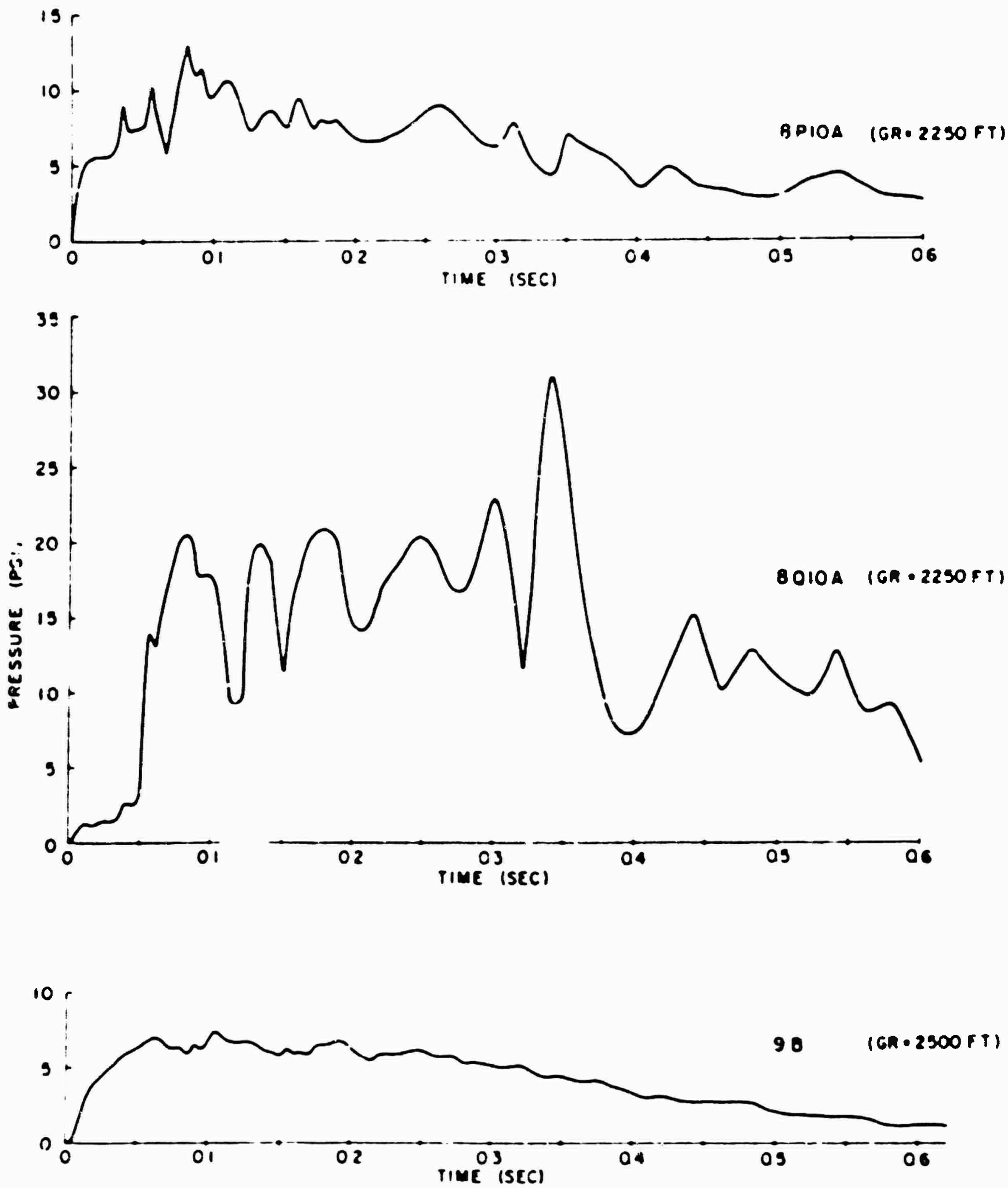

Figure 4.14 Pressure versus time, desert line, Shot 12 (ground range = 2,250 feet–2,500 feet).

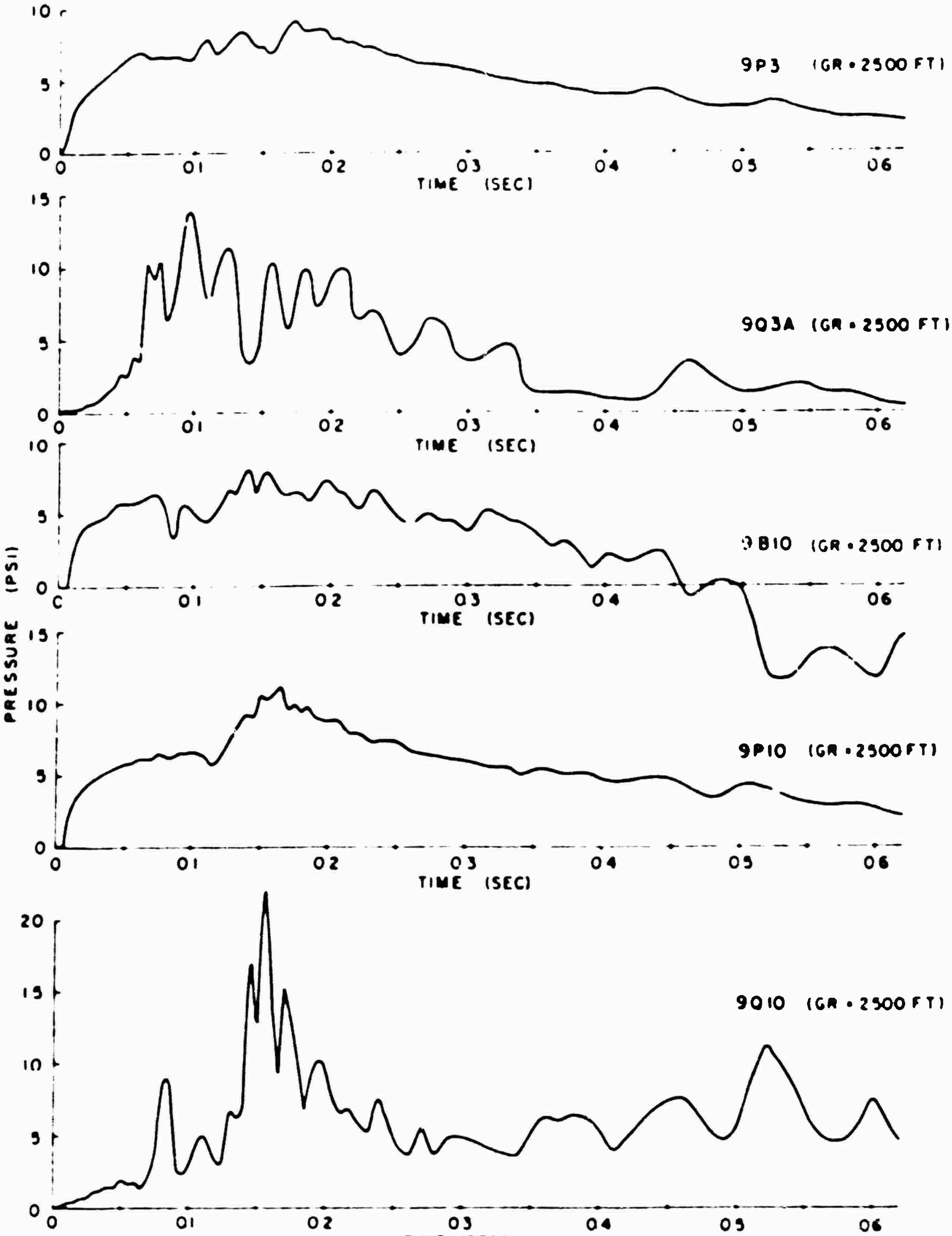

Figure 4.15 Pressure versus time, desert line, Shot 12 (ground range = 2,500 feet).

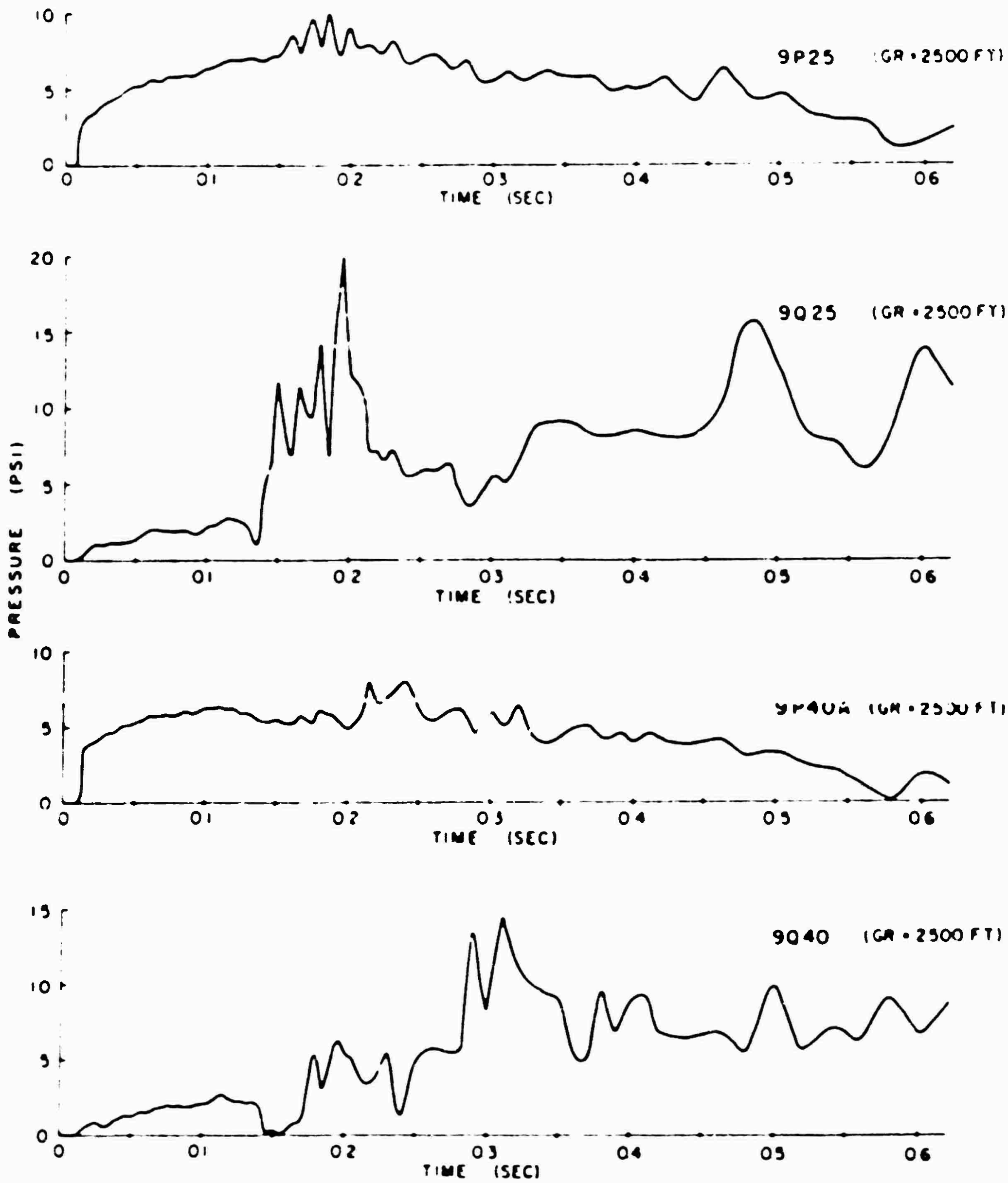

Figure 4.16 Pressure versus time, desert line, Shot 12 (ground range = 2,500 feet)

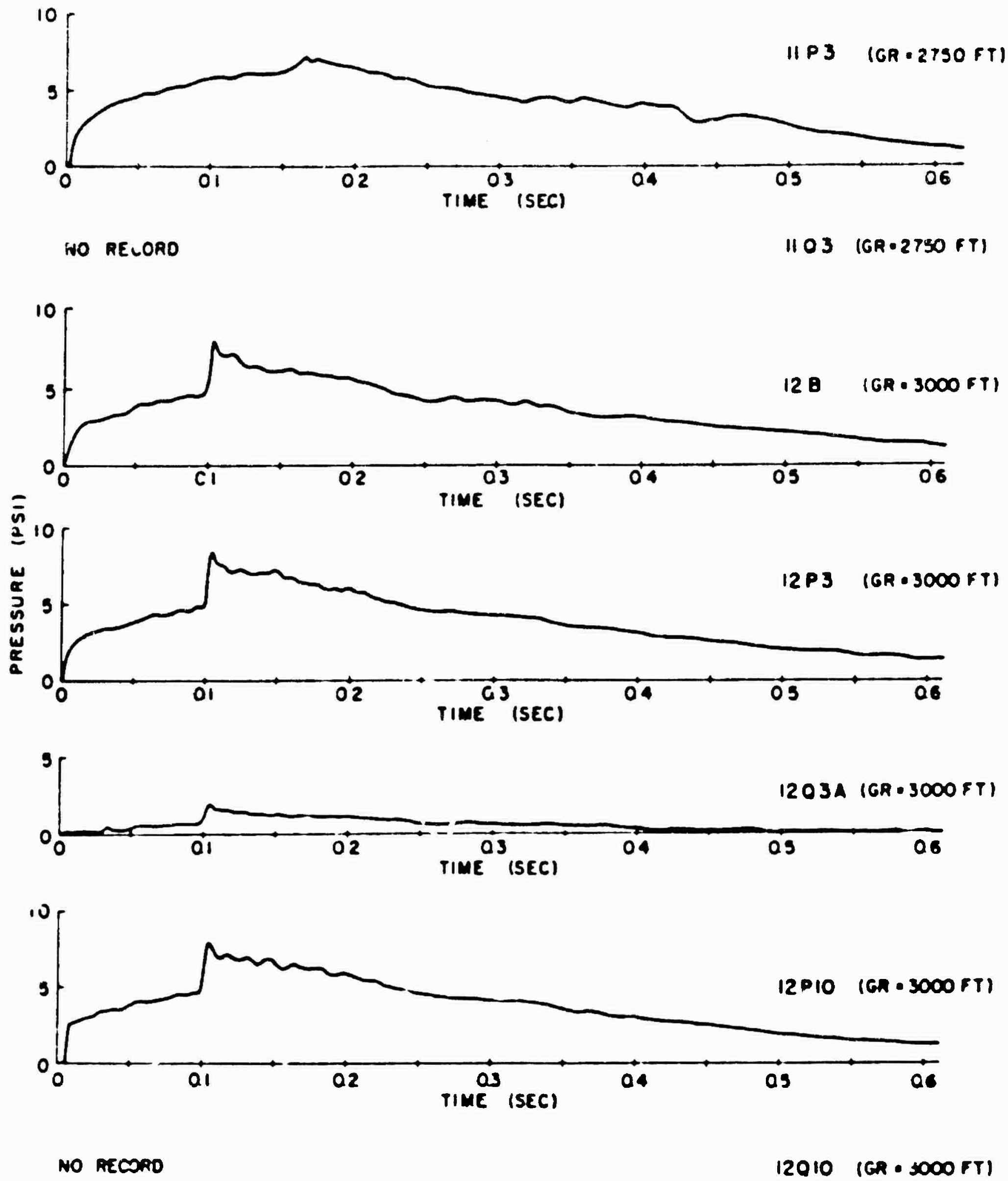

Figure 4.17 Pressure versus time, desert line, Shot 12 (ground range = 2,750 feet–3,000 feet).

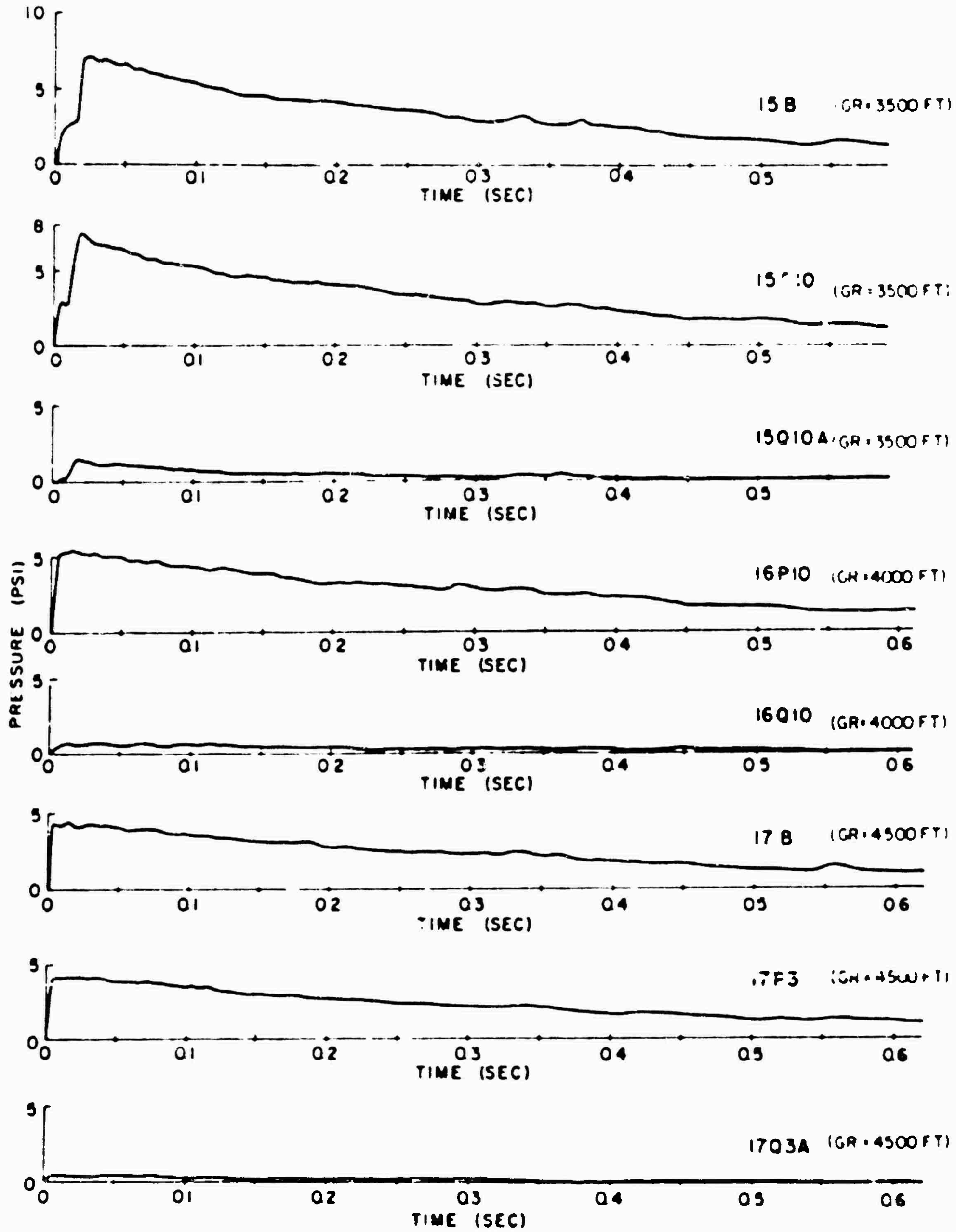

Figure 4.18 Pressure versus time, desert line, Shot 12 (ground range = 3,500 feet–4,000 feet).

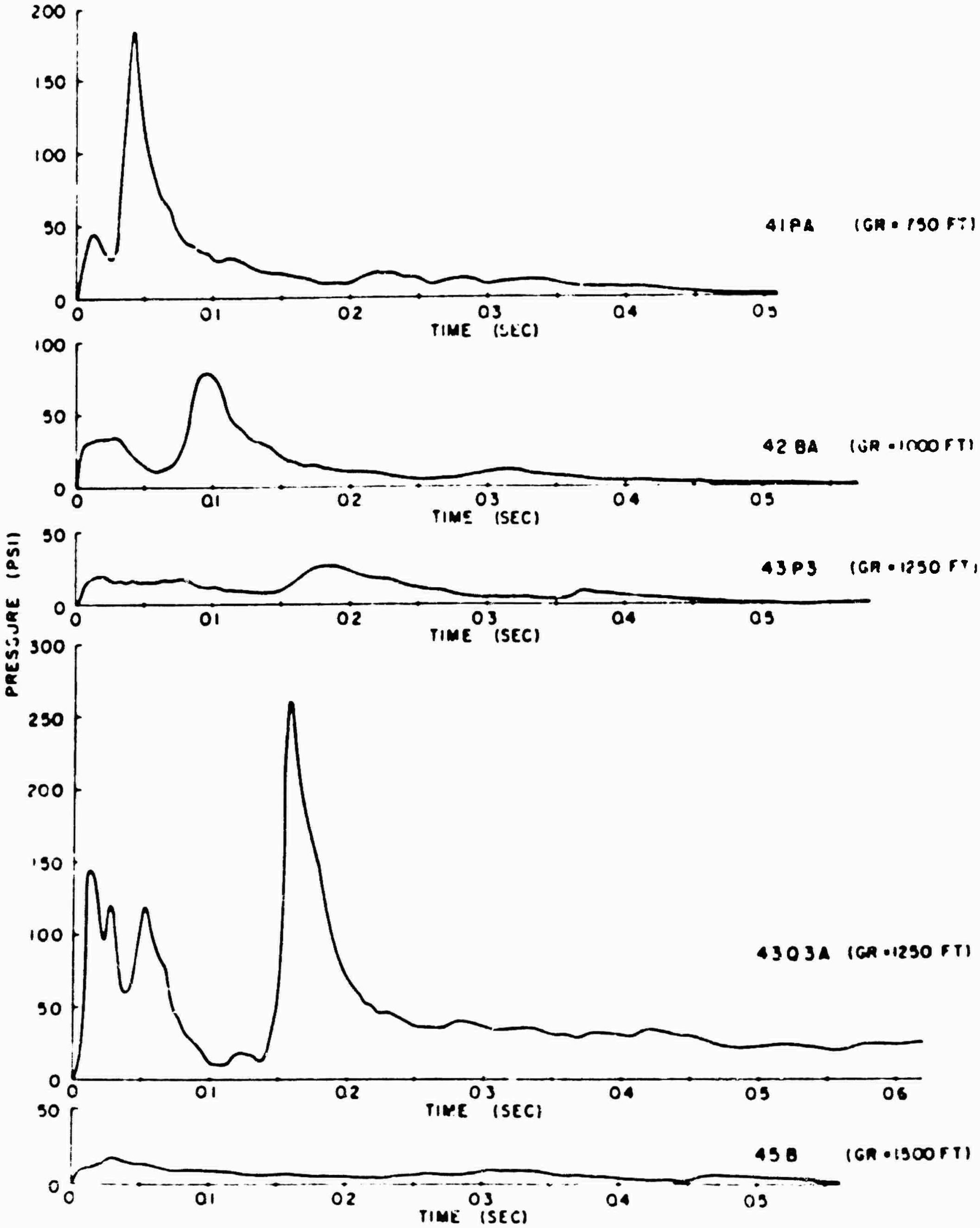

Figure 4.19 Pressure versus time, asphalt line, Shot 12 (ground range = 750 feet–1,500 feet).

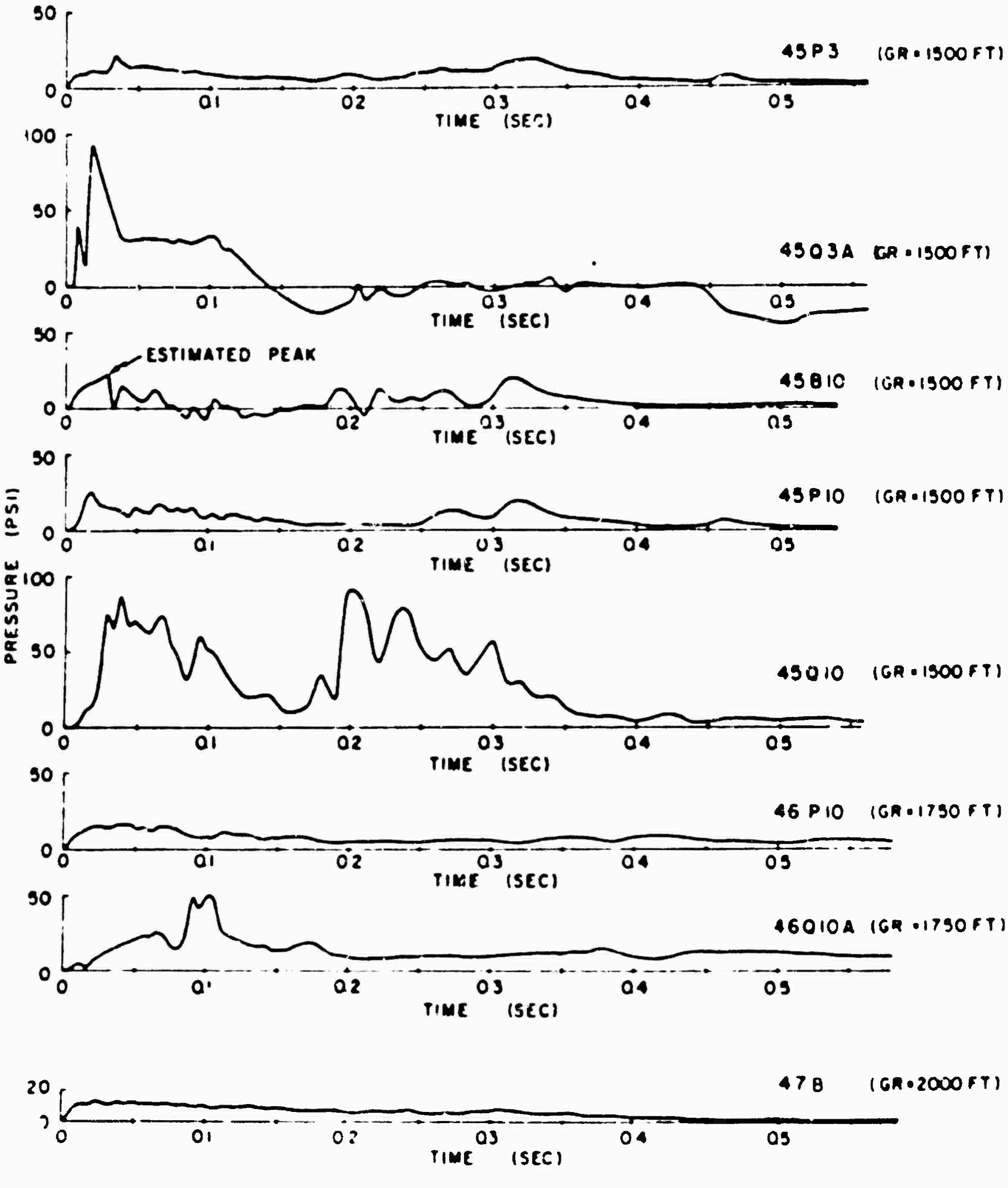

Figure 4.20 Pressure versus time, asphalt line, Shot 12 (ground range = 1,500 feet–2,000 feet).

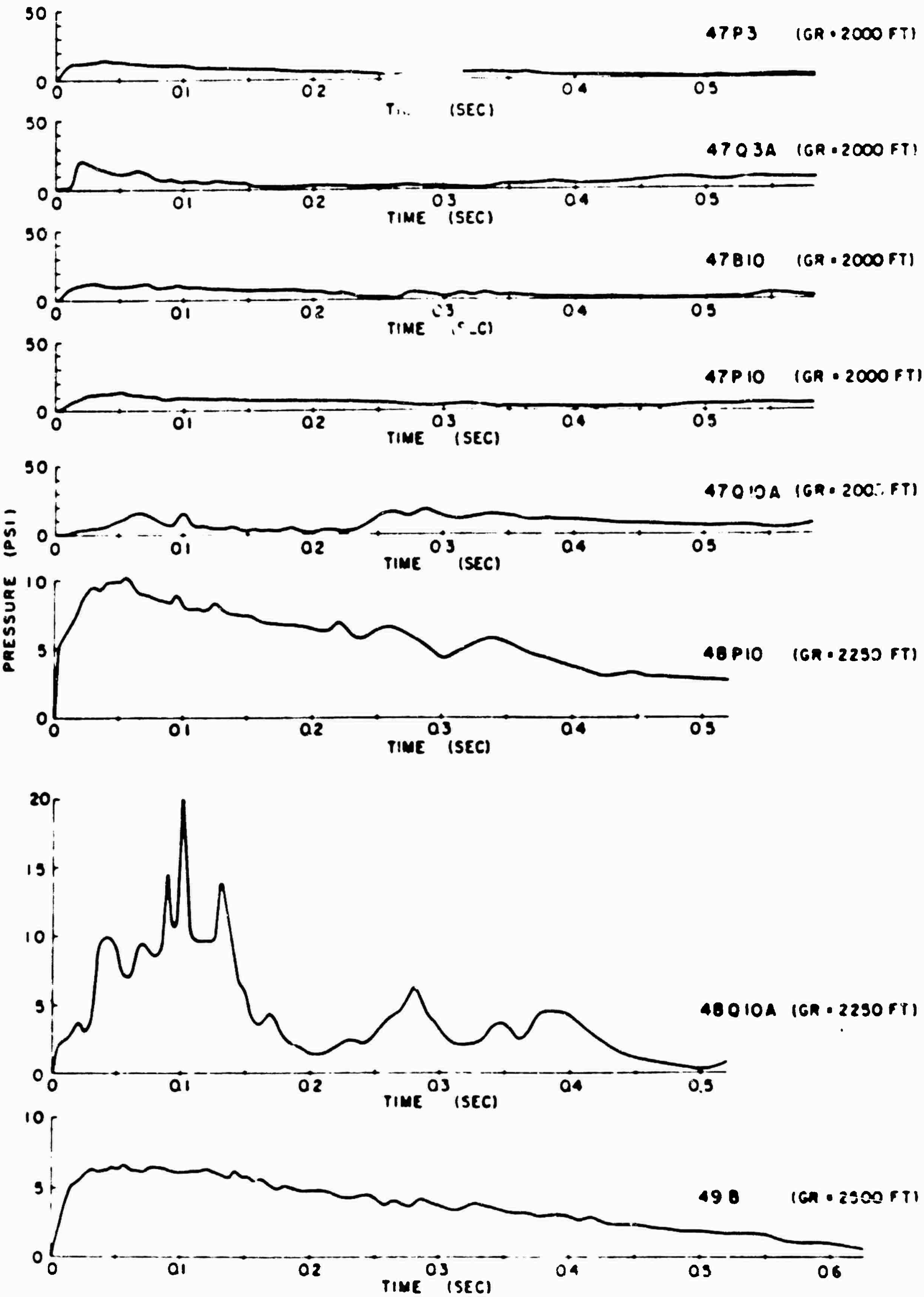

Figure 4.21 Pressure versus time, asphalt line, Shot 12 (ground range = 2,000 feet – 2,500 feet).

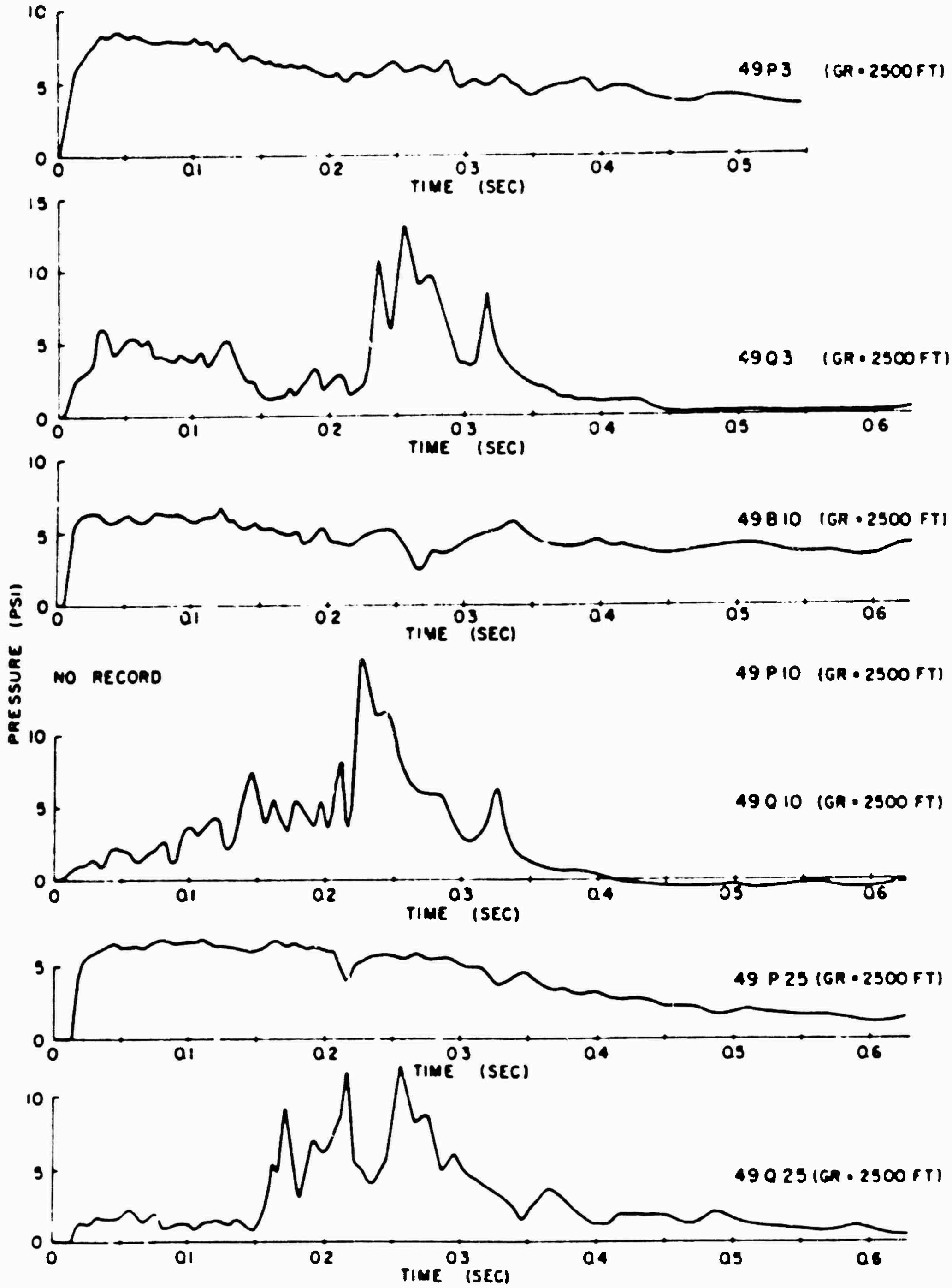

Figure 4.22 Pressure versus time, asphalt line, Shot 12 (ground range = 3,500 feet).

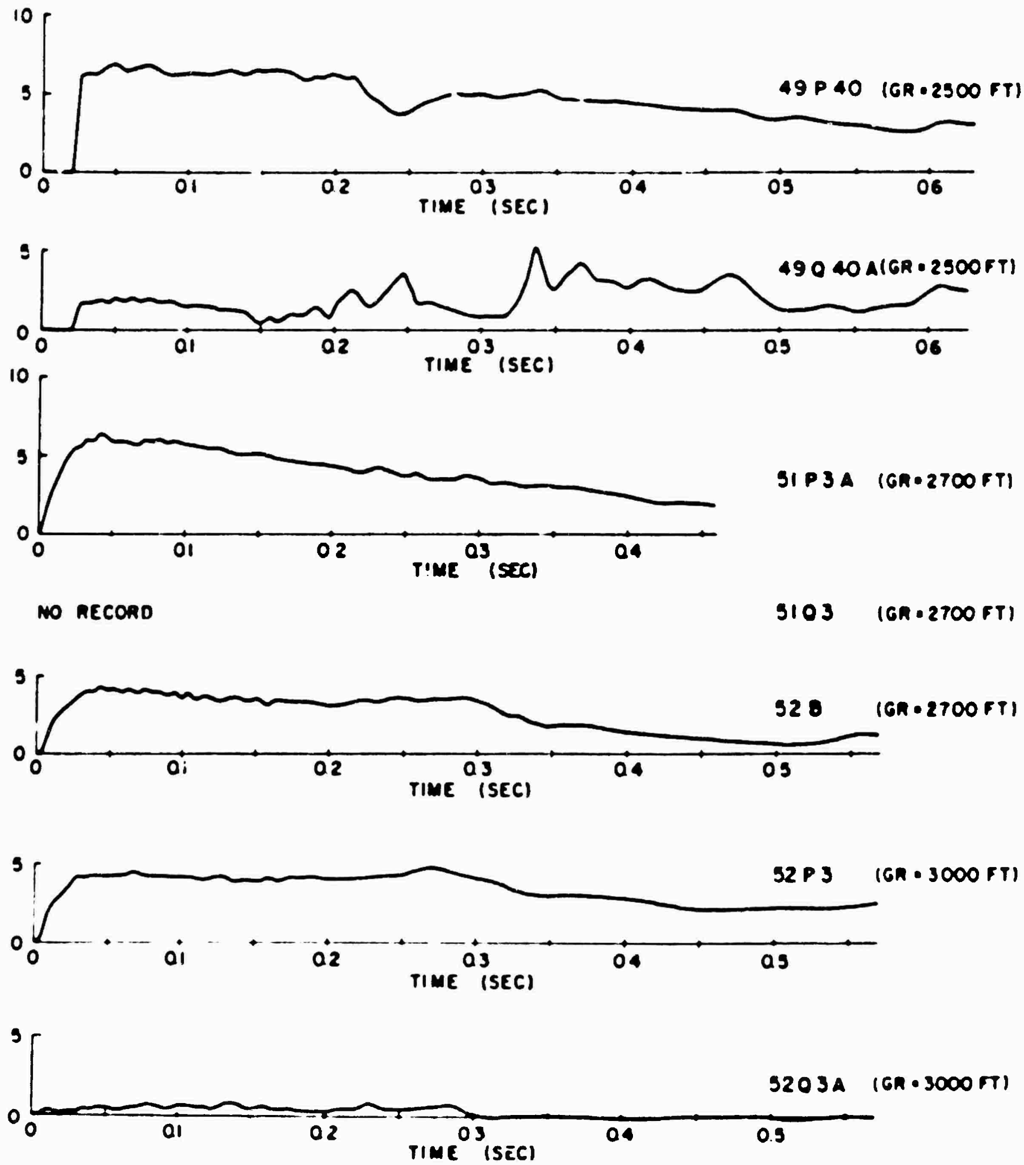

Figure 4.23 Pressure versus time, asphalt line, Shot 12 (ground range = 2,500 feet–3,000 feet).

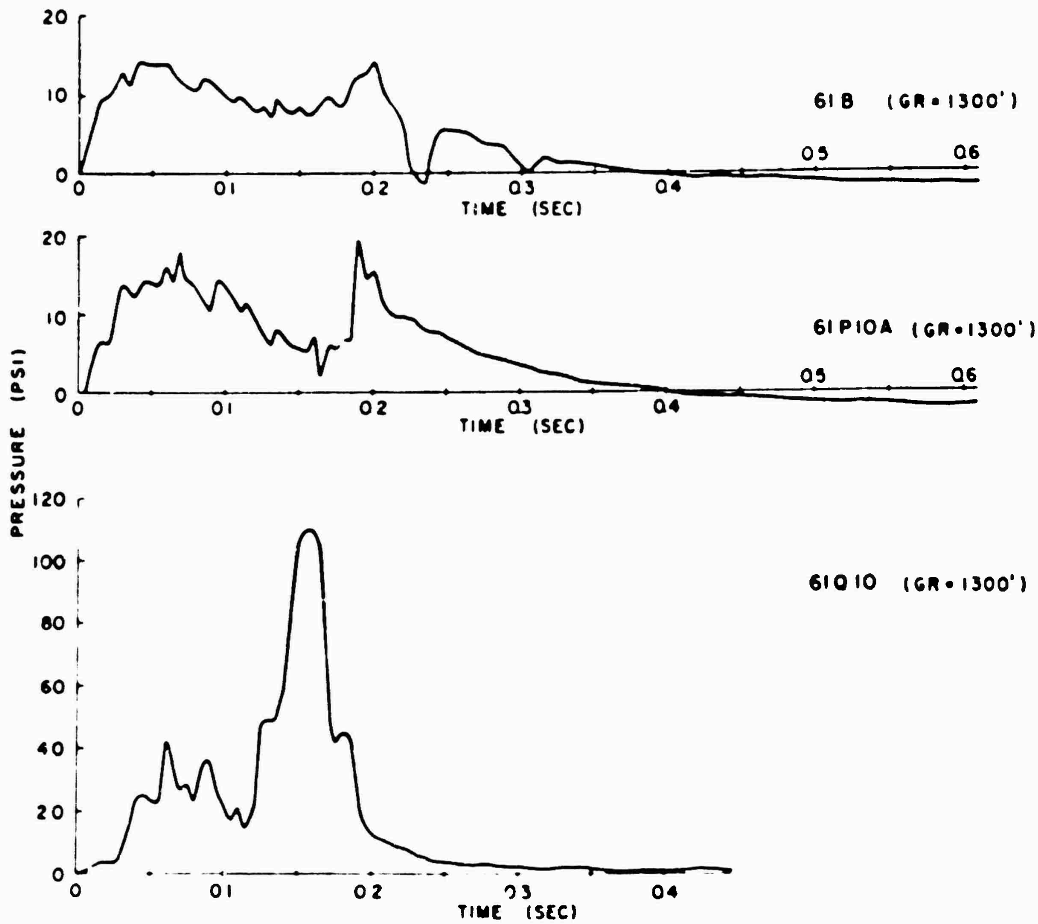

Figure 4.24 Pressure versus time, desert line, Shot 6 (ground range = 1,300 feet).

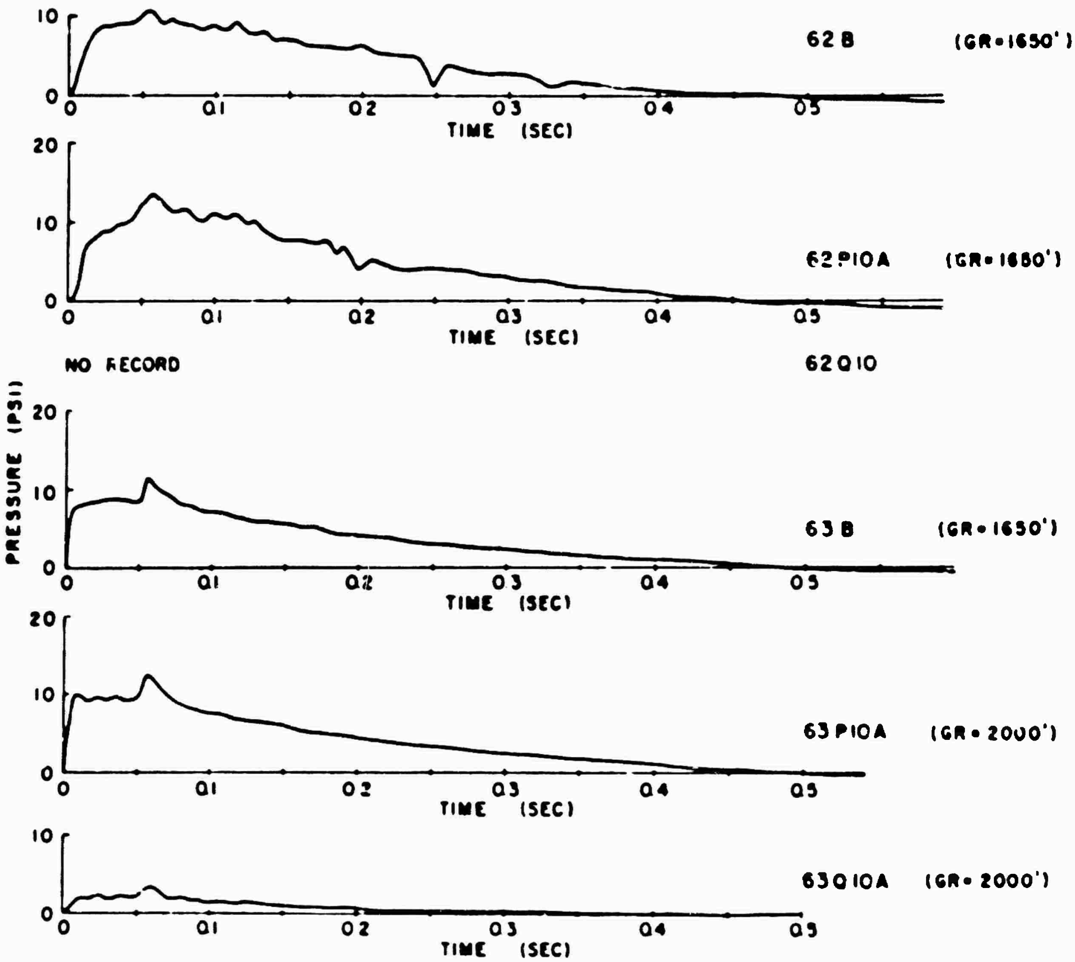

Figure 4.25 Pressure versus time, desert line, Shot 6 (ground range = 1,650 feet–2,000 feet).

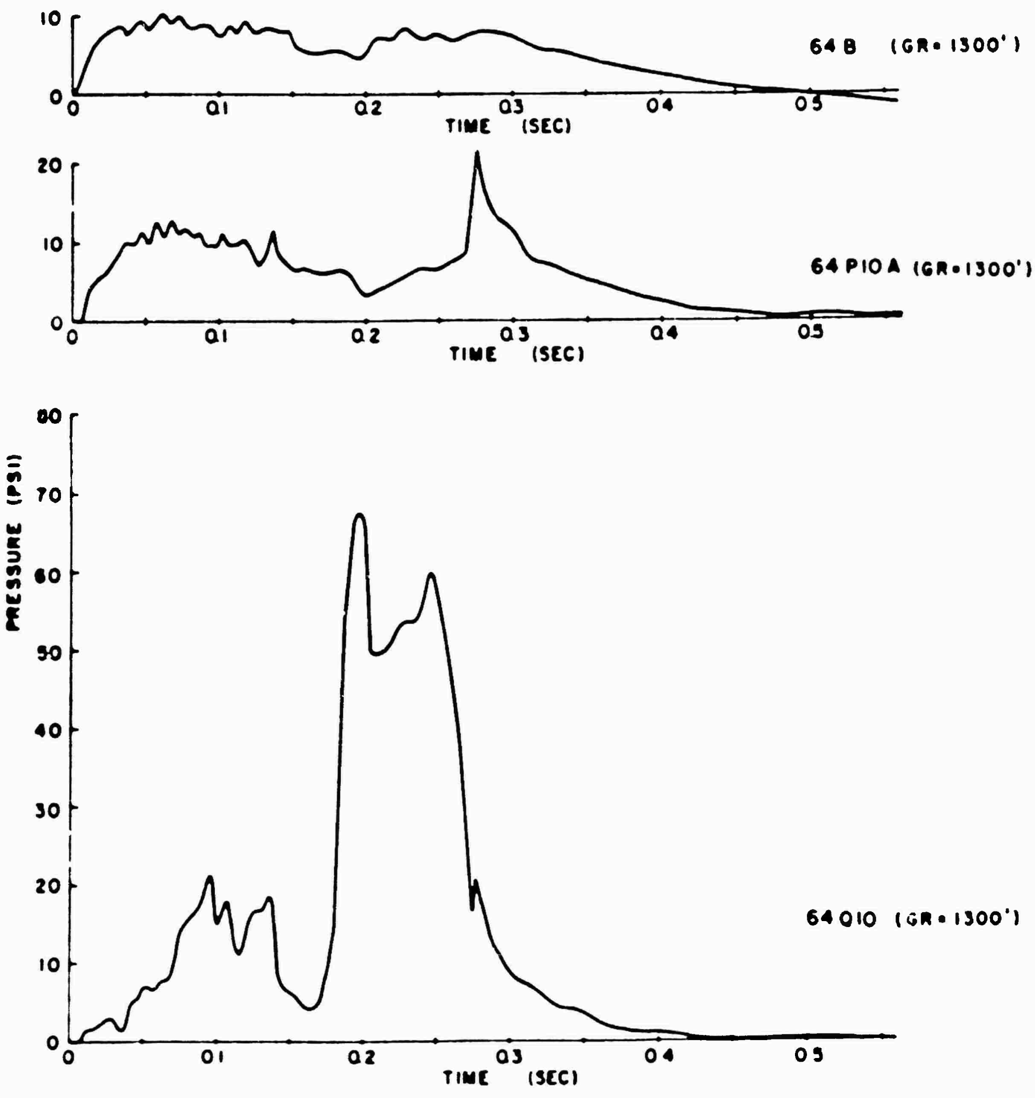

Figure 4.26 Pressure versus time, asphalt line, Shot 6 (ground range = 1,300 feet)

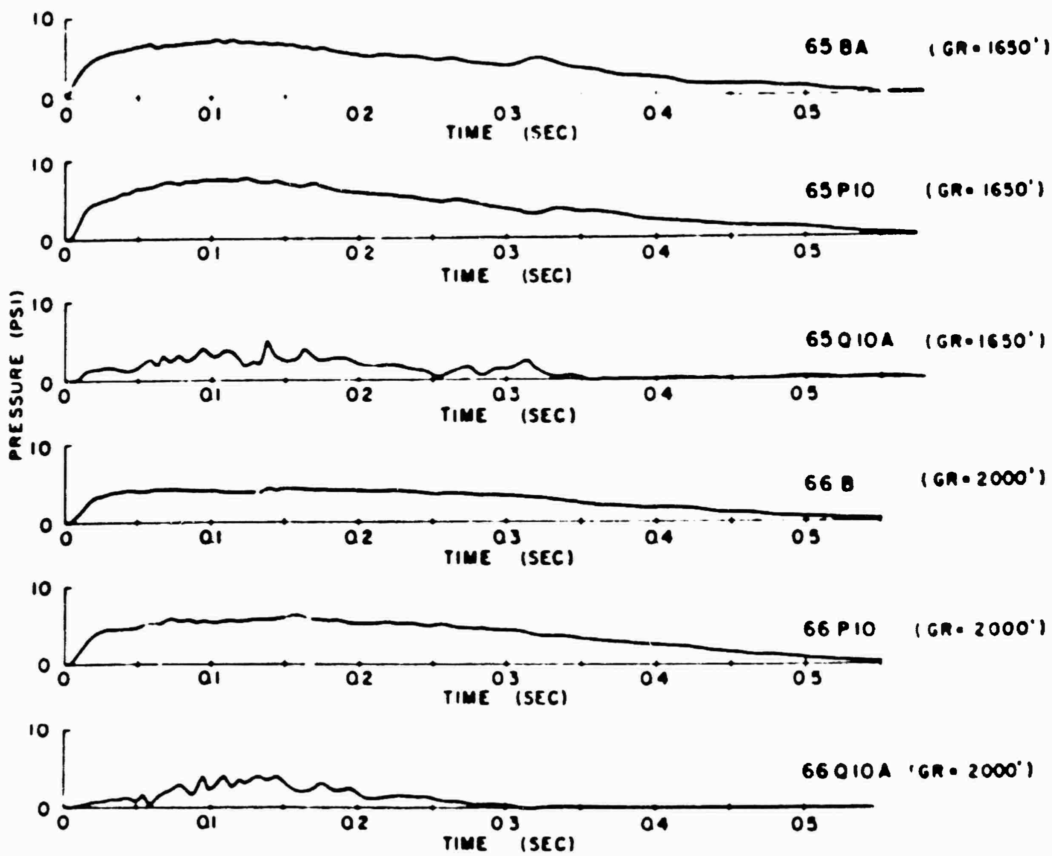

Figure 4.27 Pressure versus time, asphalt line, Shot 6 (ground range = 1,650 feet – 2,000 feet).

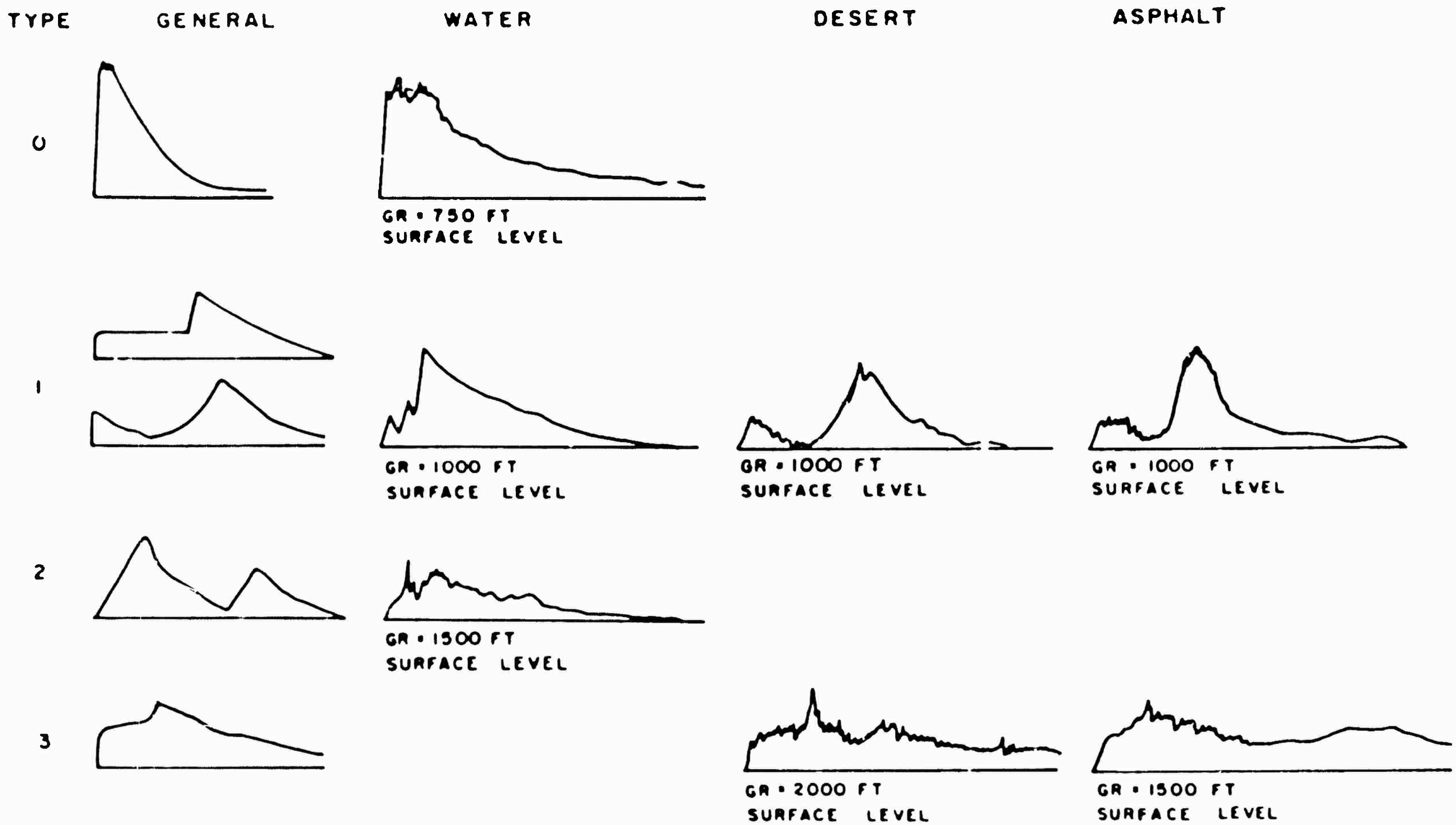

Figure 4.28 Wave forms of overpressure records, Shot 12, Types 0–3.

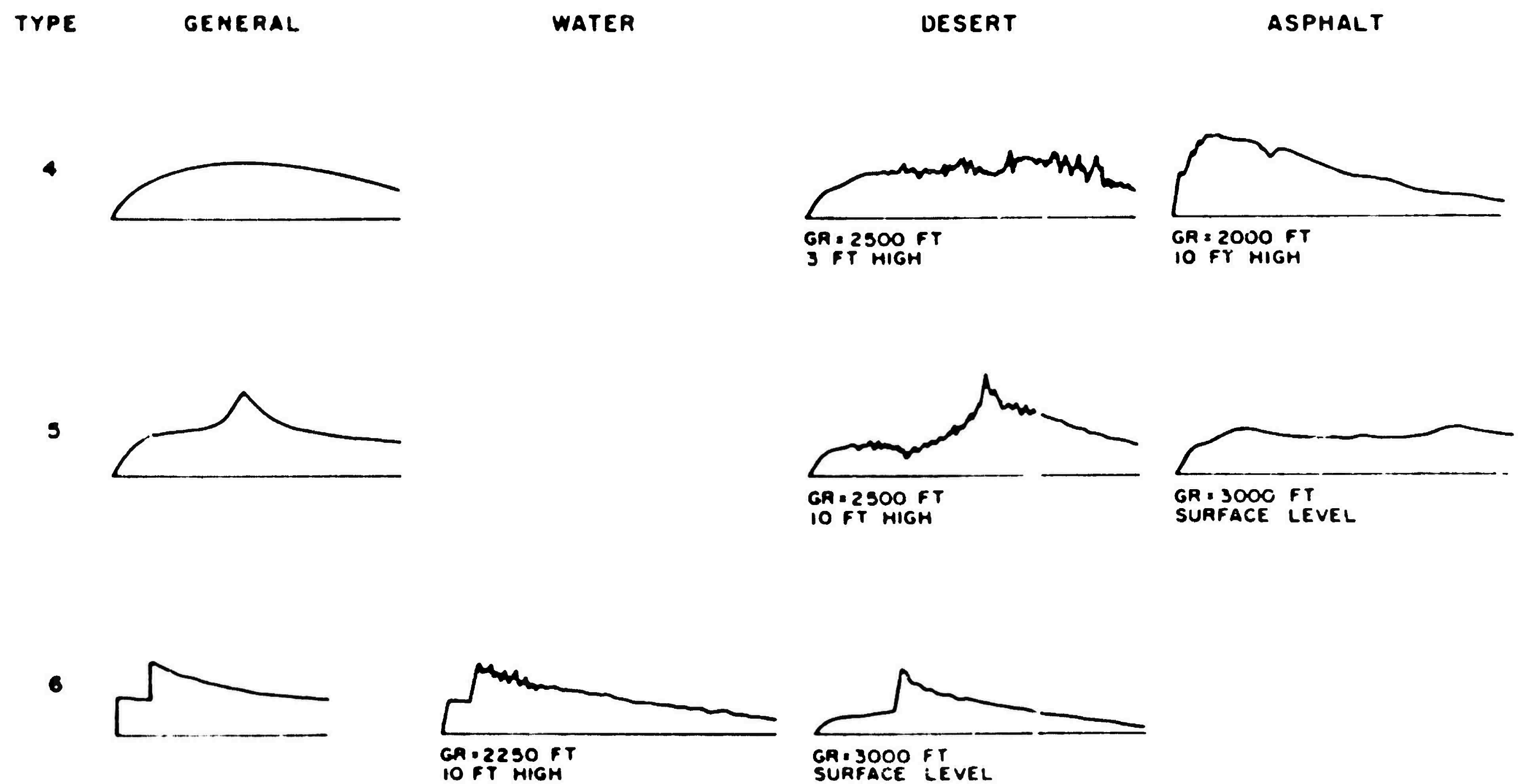

Figure 4.29 Wave forms of overpressure records, Shot 12, Types 4–6.

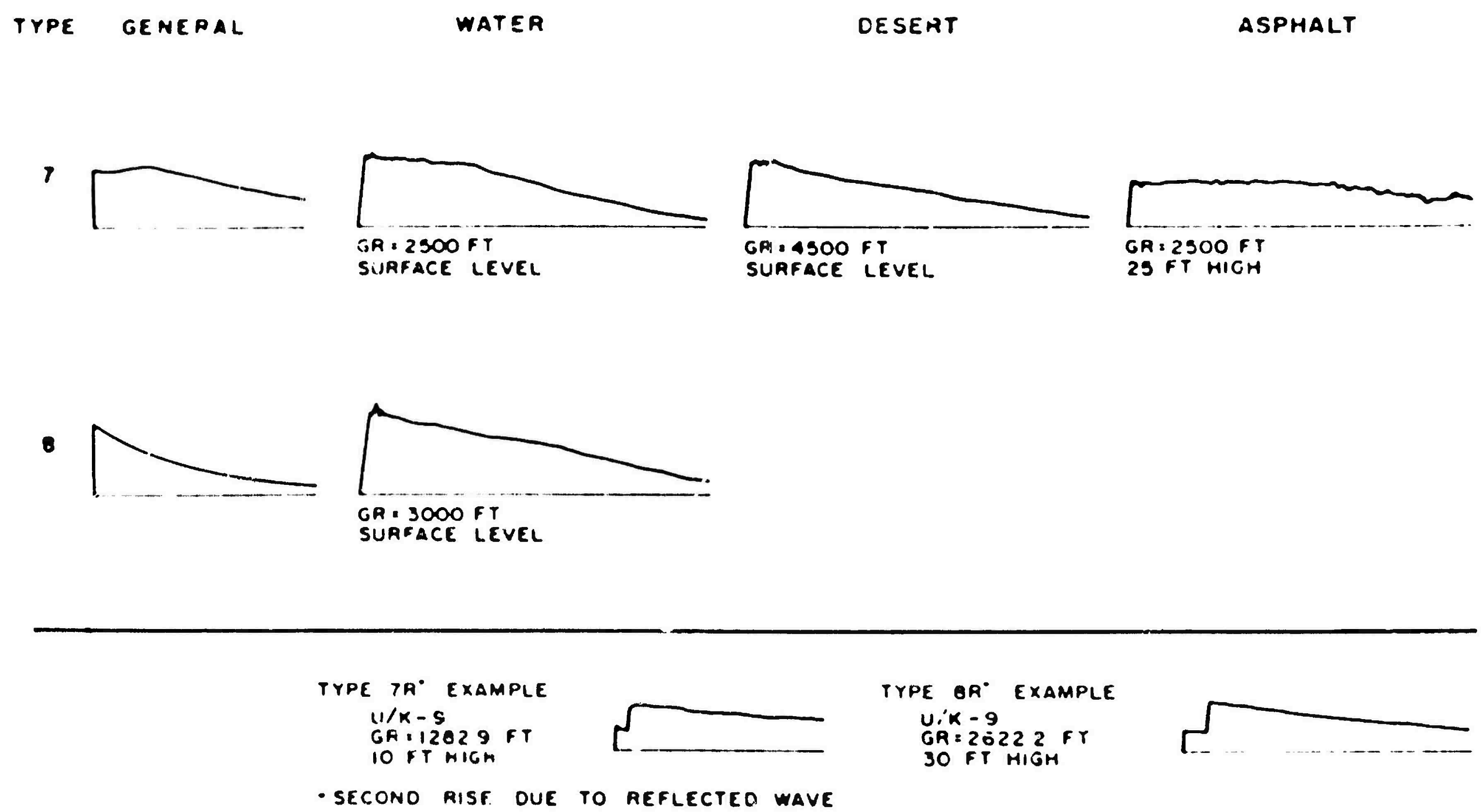

Figure 4.30 Wave forms of overpressure records, Shot 12, Types 7, 8, 7R, and 8R.

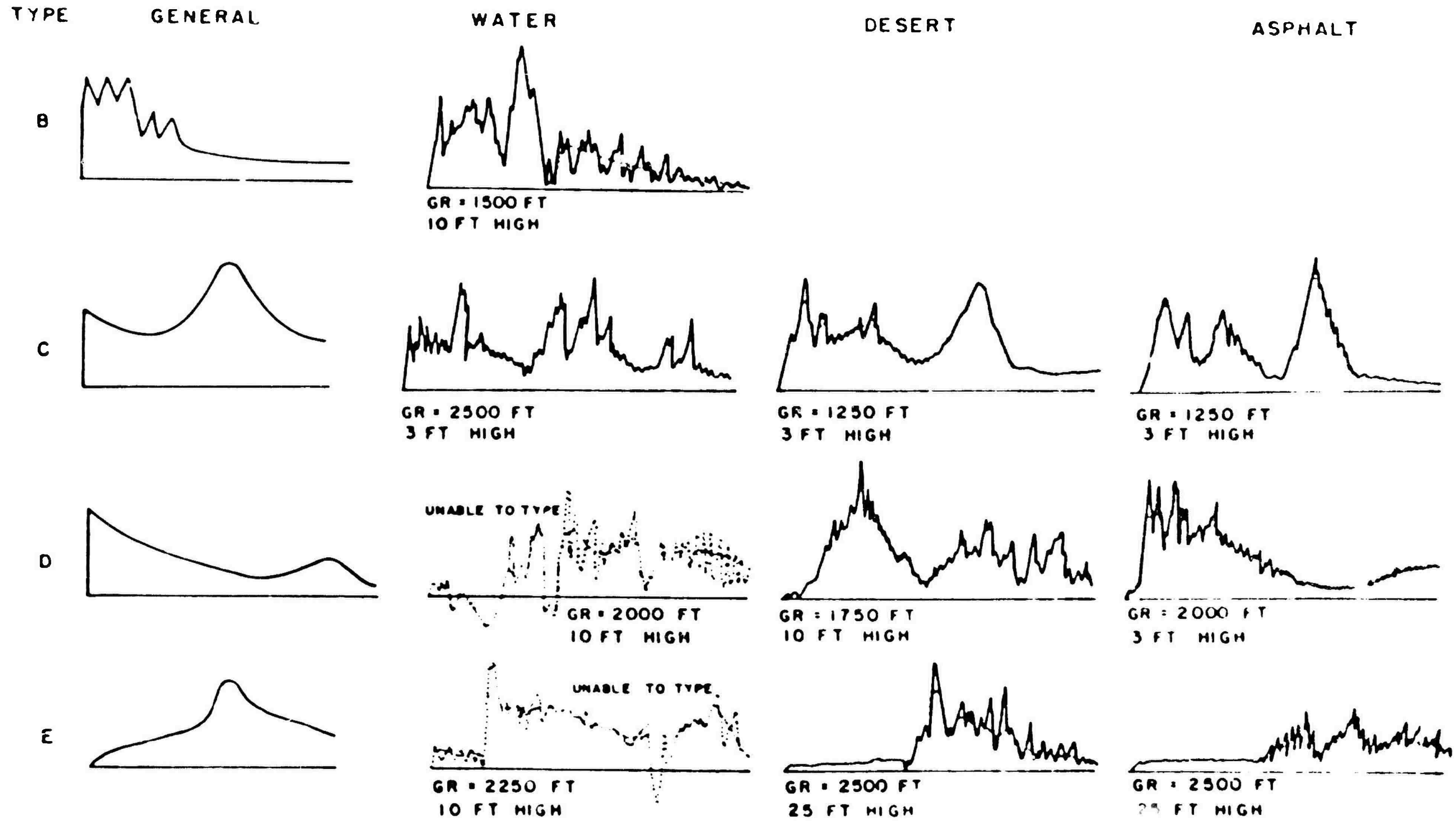

Figure 4.31 Wave forms of dynamic pressure records, Shot 12, Types B–E

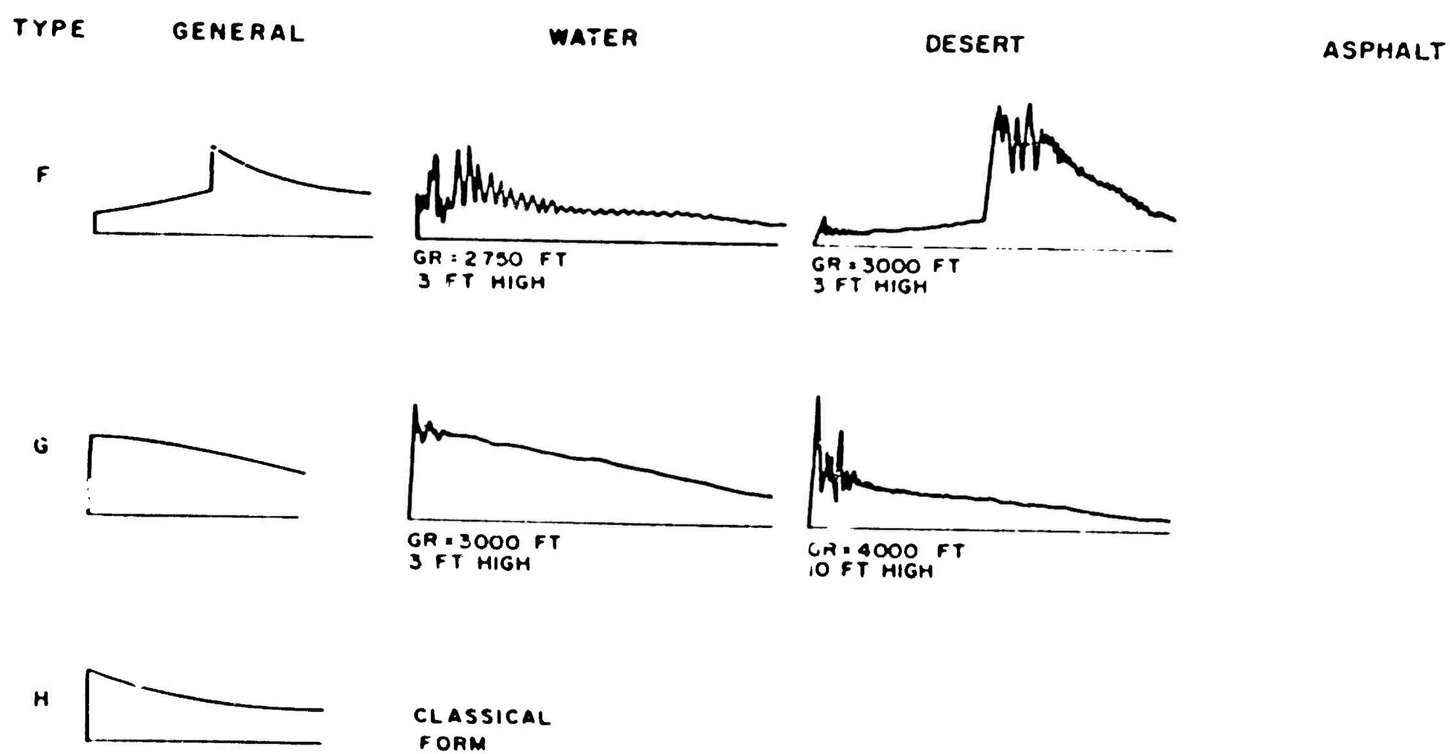

Figure 4.32 Wave forms of dynamic pressure records, Shot 12, Types F–H.

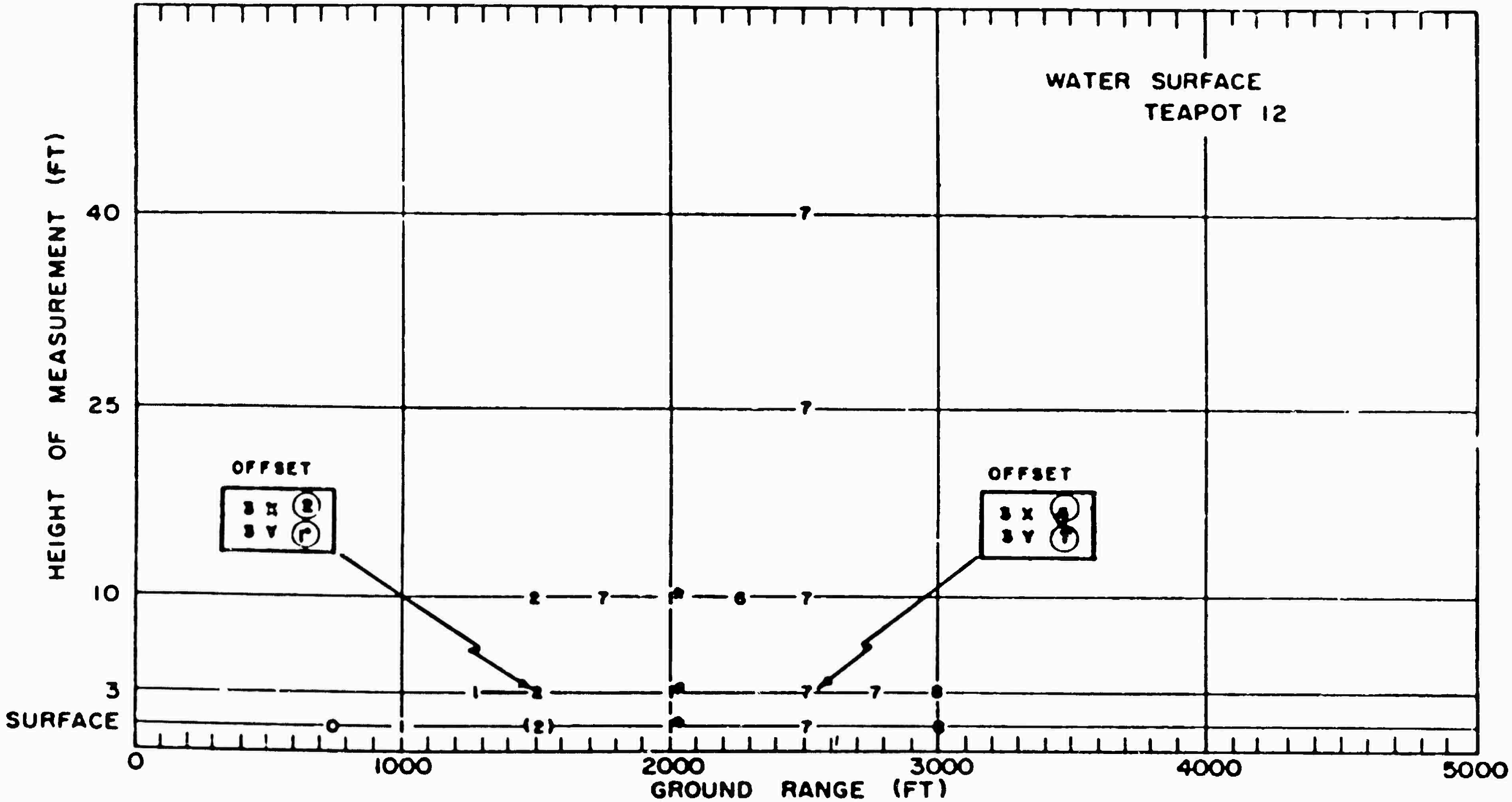

* See discussion in Section 4.5.2.

Figure 4.33 Overpressure wave form type versus ground range and gage height, water line, Shot 12.

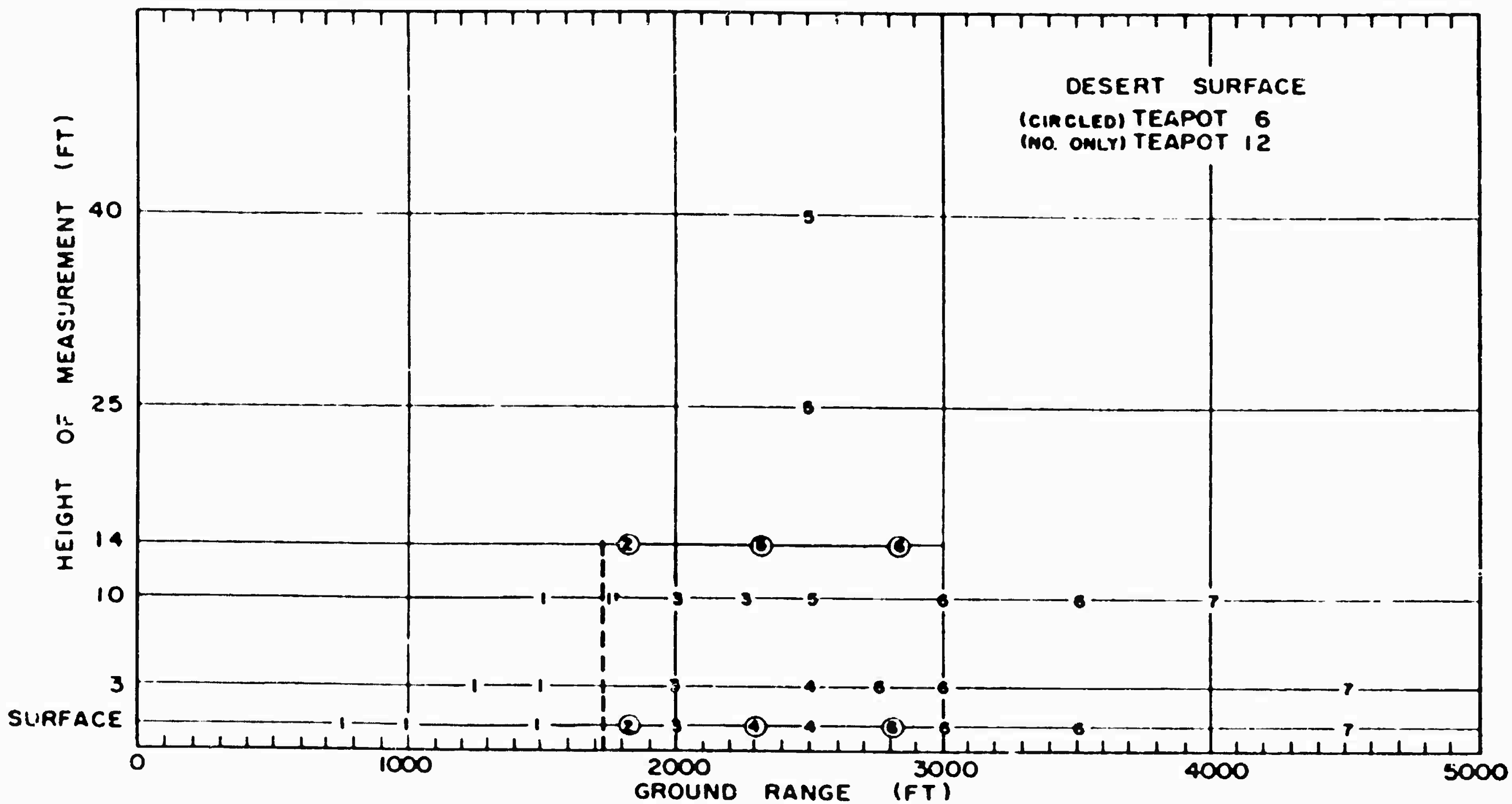

Figure 4.34 Overpressure wave form type versus ground range and gage height, desert line, Shots 6 and 12.

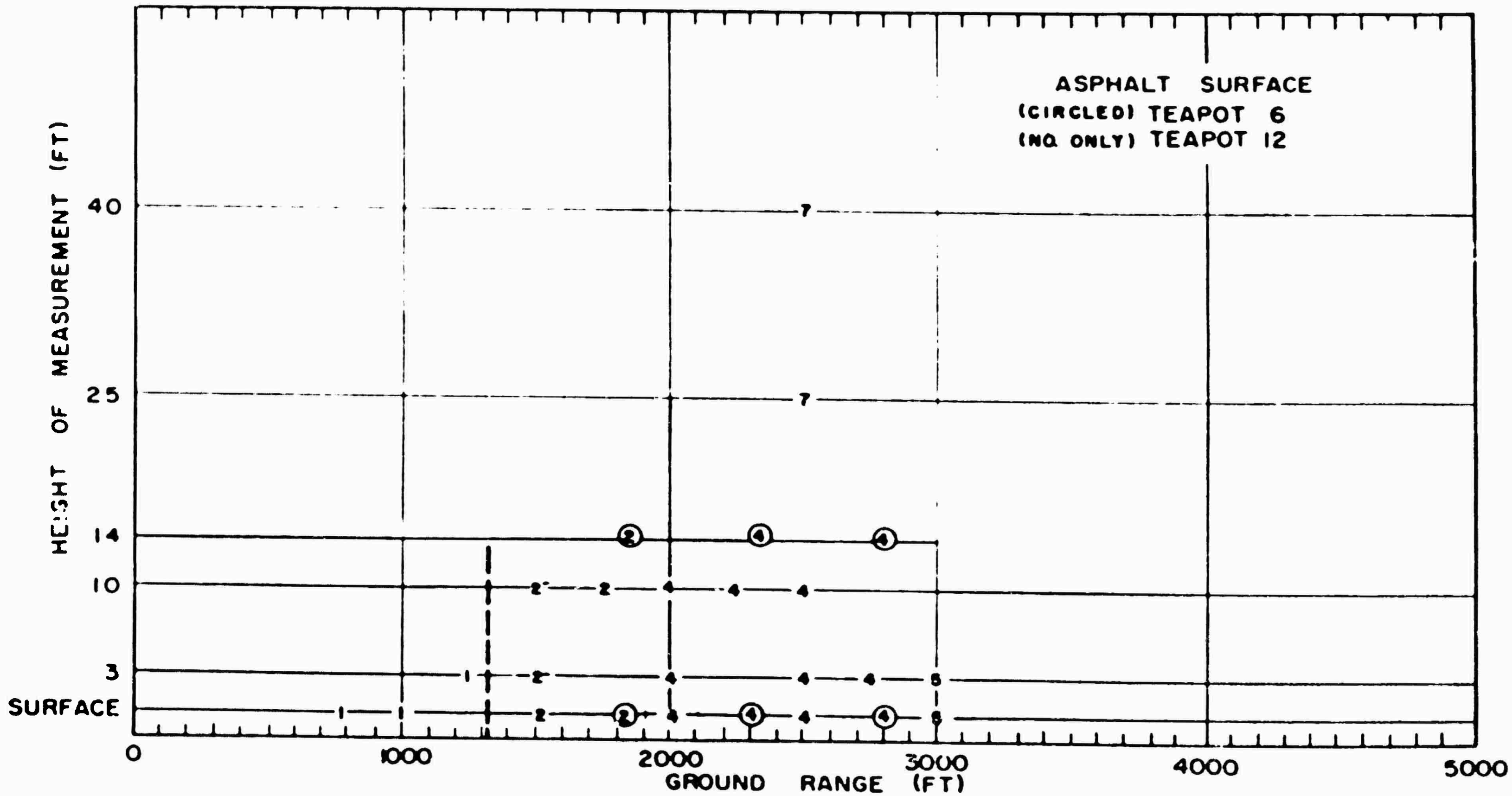

Figure 4.35 Overpressure wave form type versus ground range and gage height, asphalt line, Shots 6 and 12.

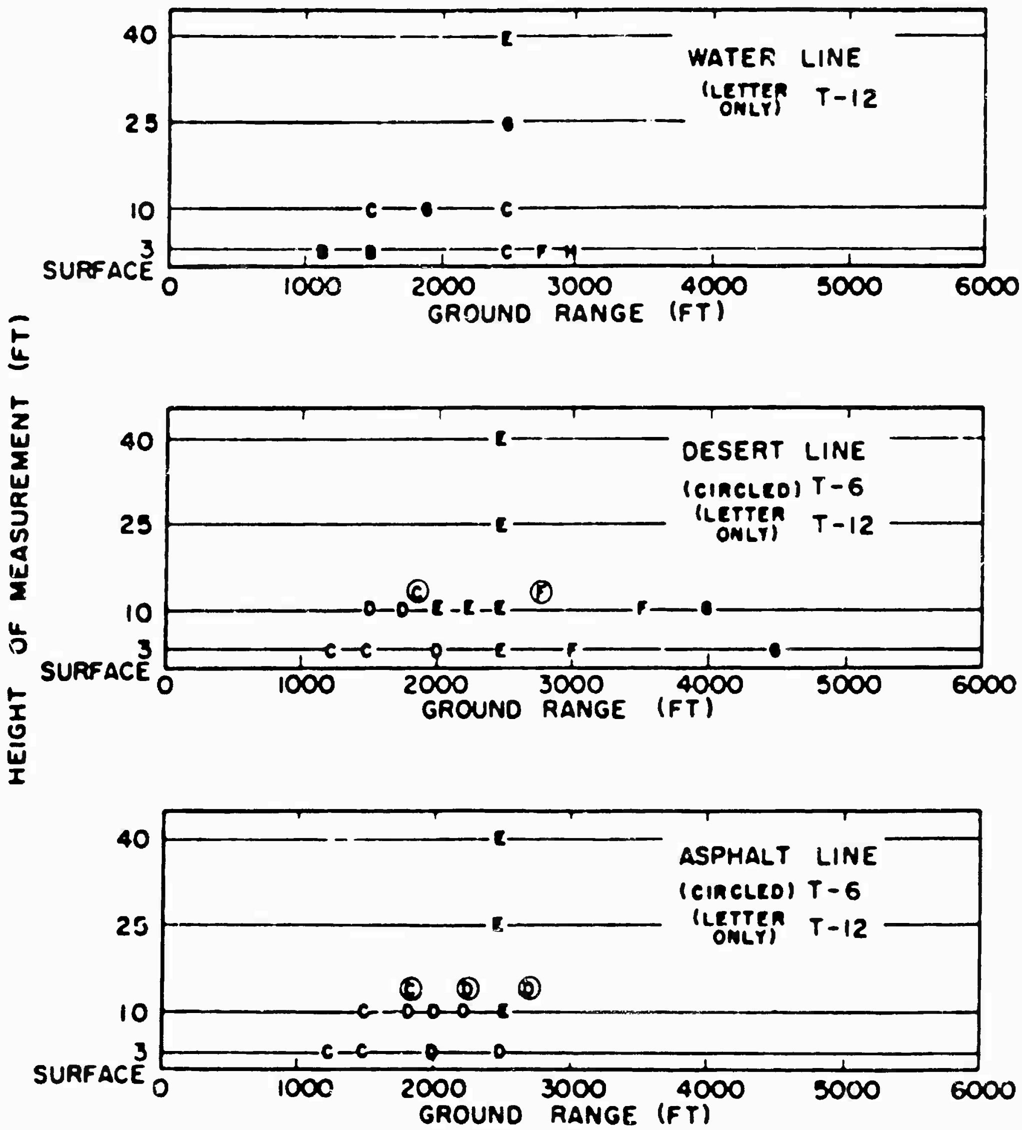

Figure 4.36 Dynamic pressure wave form type versus ground range and gage height, Shots 6 and 12.

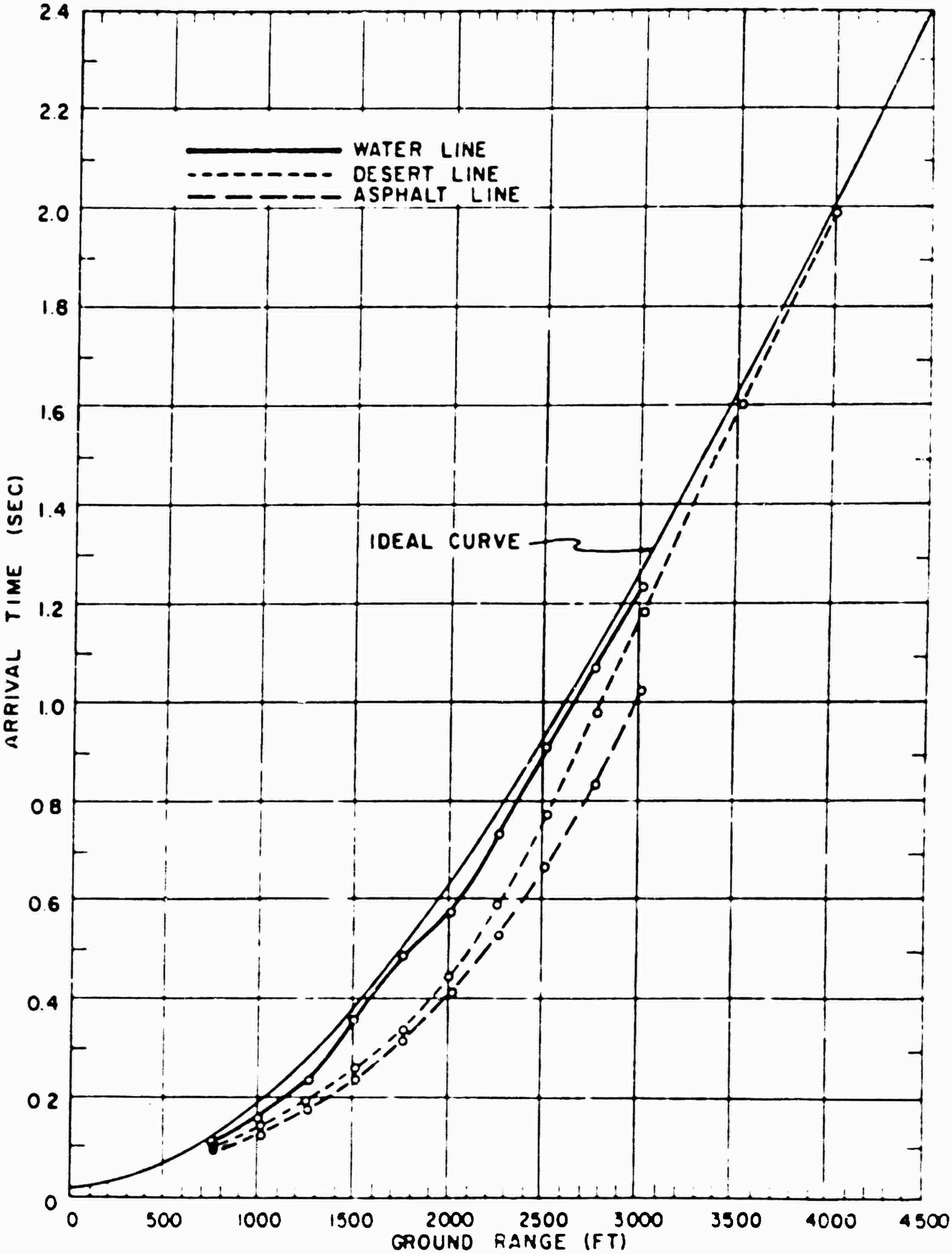

Figure 5.1 Arrival time versus ground range, Shot 12.

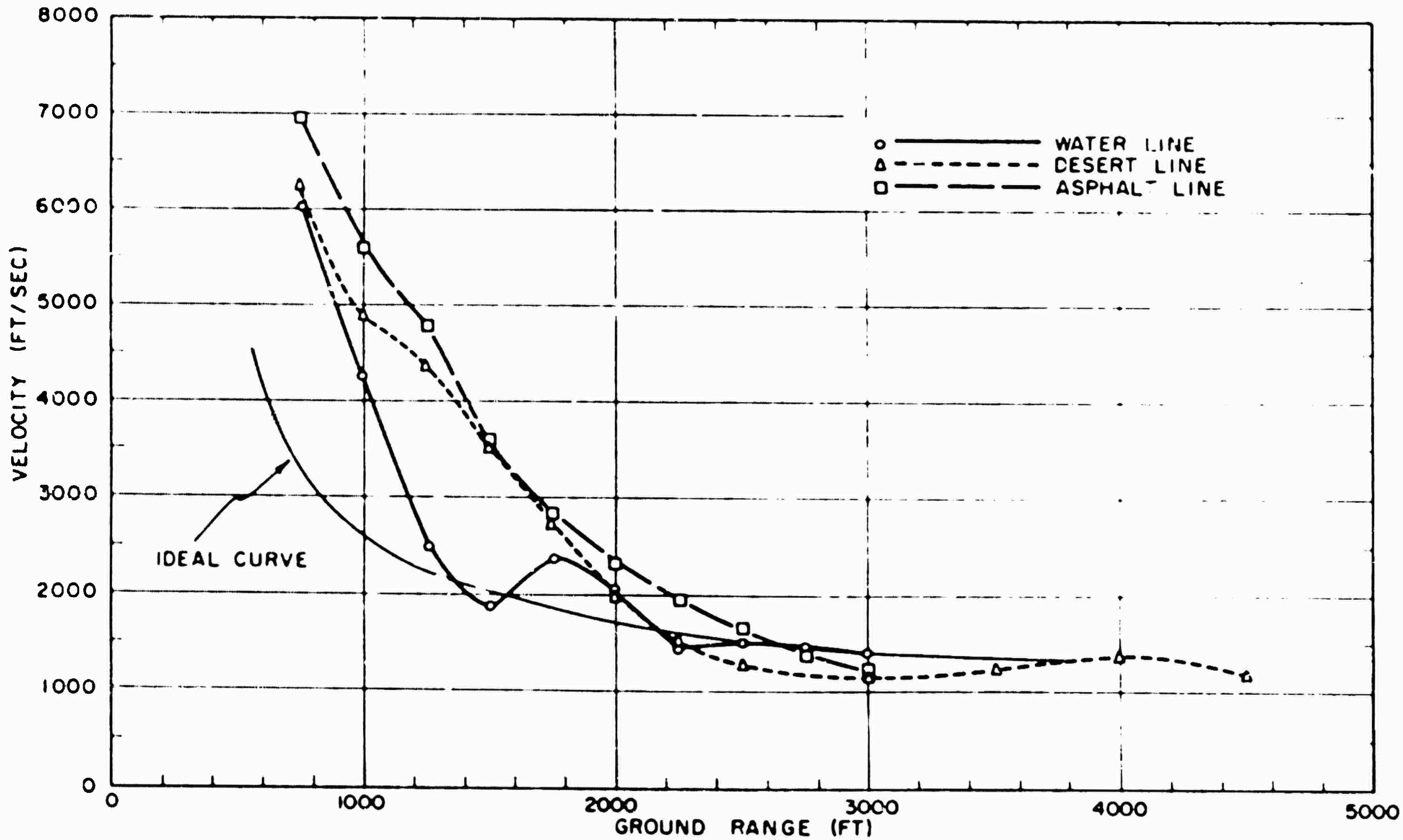

Figure 5.2 Shock velocity versus ground range, Shot 12.

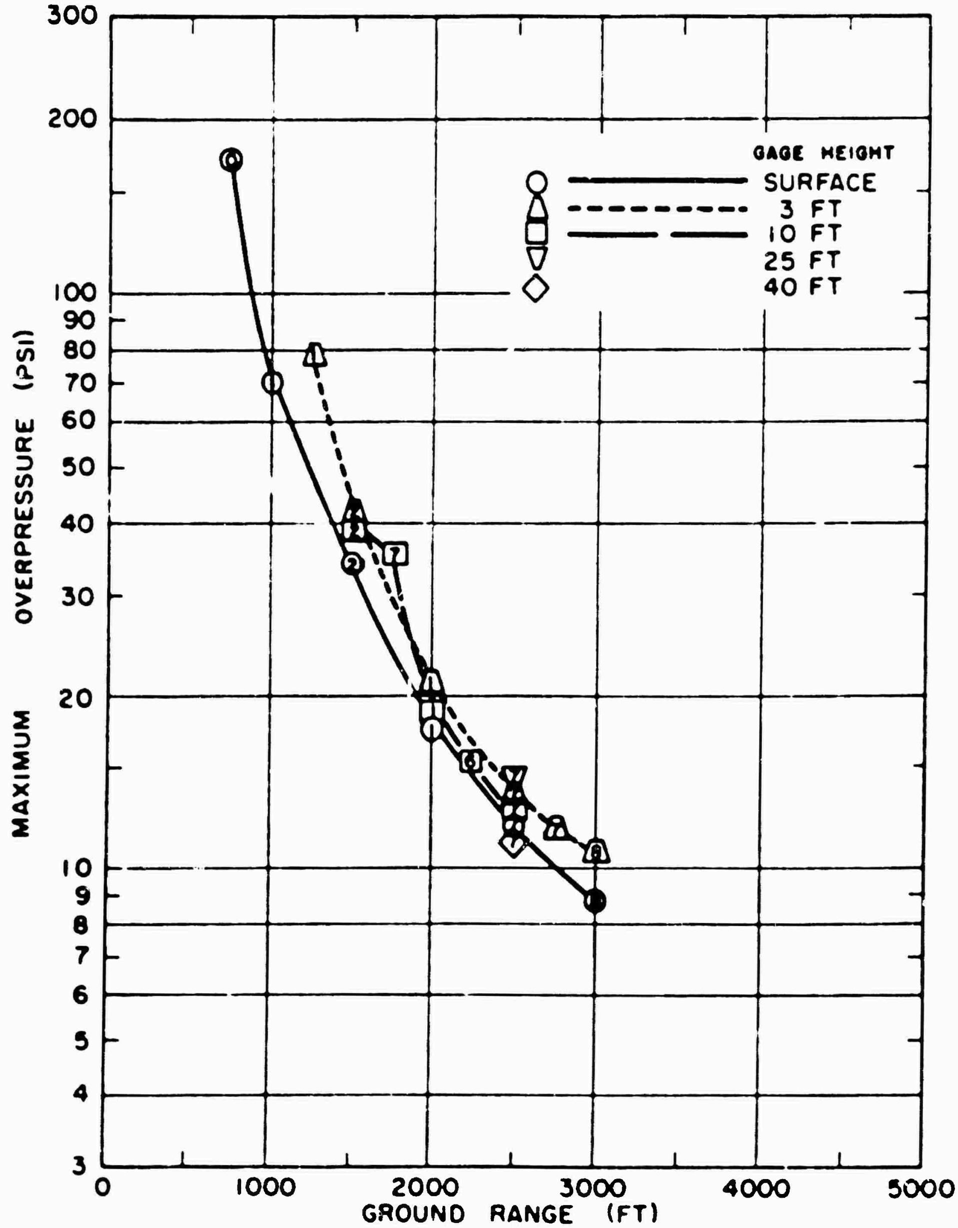

Figure 5.6 Maximum overpressure versus ground range, water line, Shot 12.

fact, peak pressures measured here are not unlike those measured near the center of the asphalt surface. At gage Stations 17 through 12 (BRL), although the results are irregular, there is evidence that maximum pressures were significantly higher in this desert sector. Proceeding around toward the water surface, both BRL and Project 1.10 overpressure data show large variations in magnitude, even from pressure gages located near the water blast line. Referring to wave-form classifications included in Figure 5.14, it is apparent that there is some correlation between the higher peak pressures and the gage records which exhibit more advanced wave forms, i.e., Types 6 and 7. This is thought to be characteristic of the so-called cleaning-up region of the disturbed-blast-wave evolution.

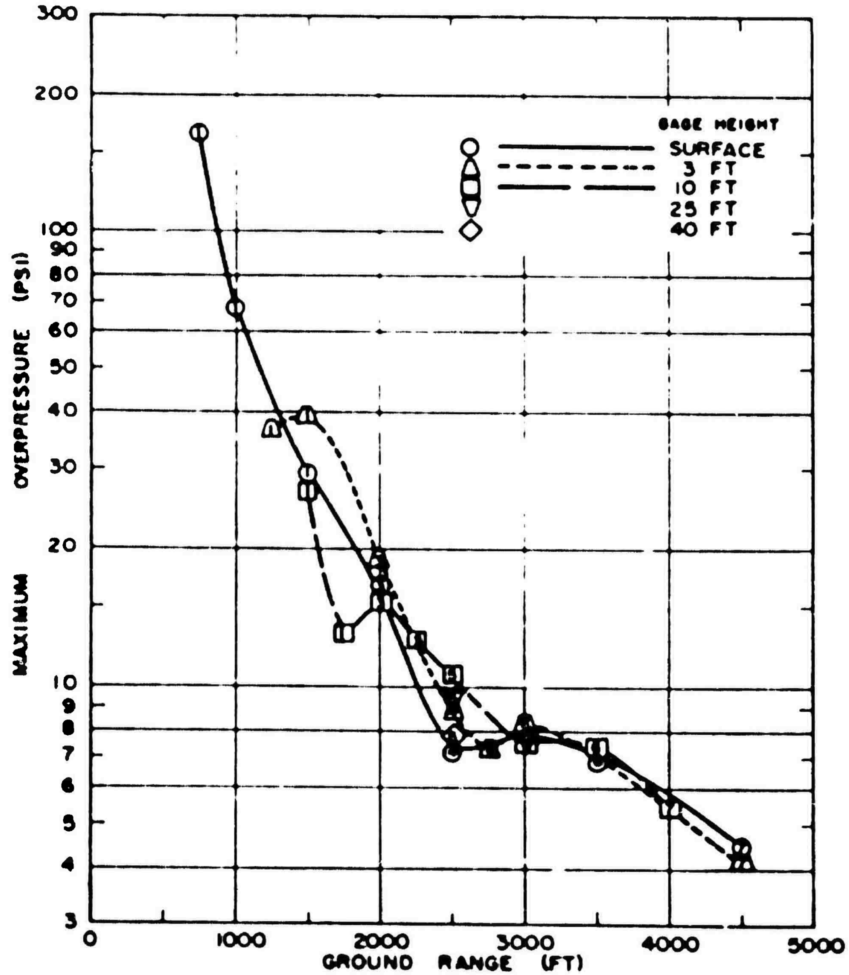

Figure 5.7 Maximum overpressure versus ground range, desert line, Shot 12.

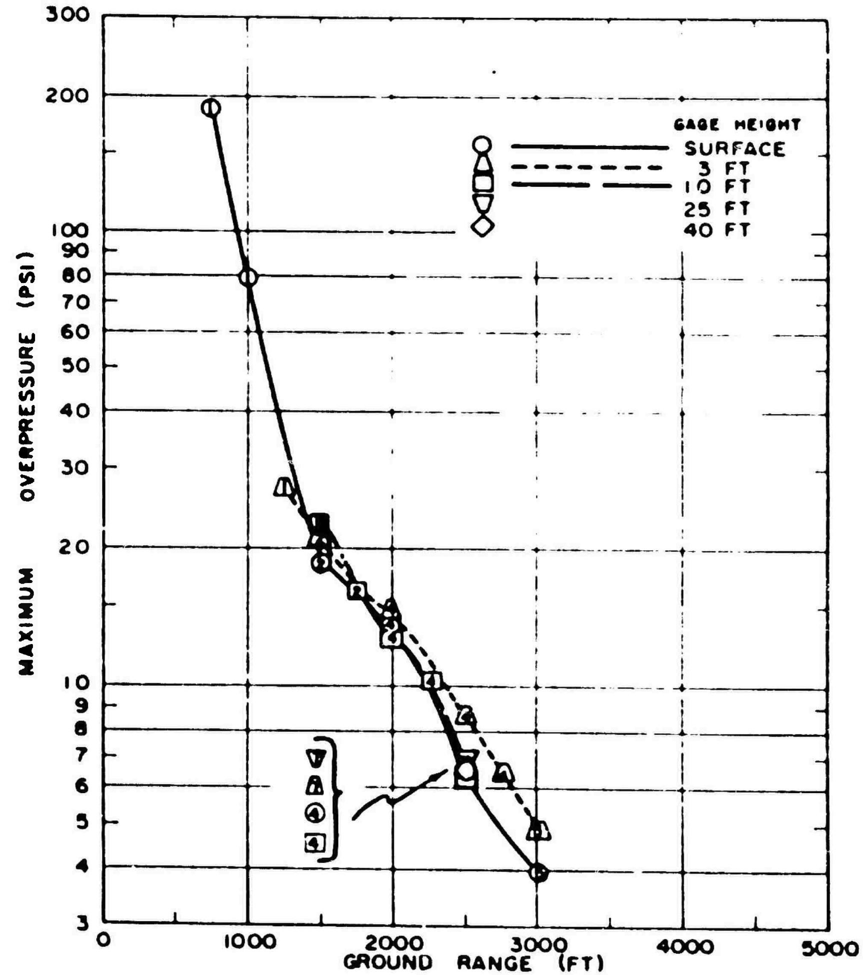

Figure 5.8 Maximum overpressure versus ground range, asphalt line, Shot 12.

DECLASSIFIED

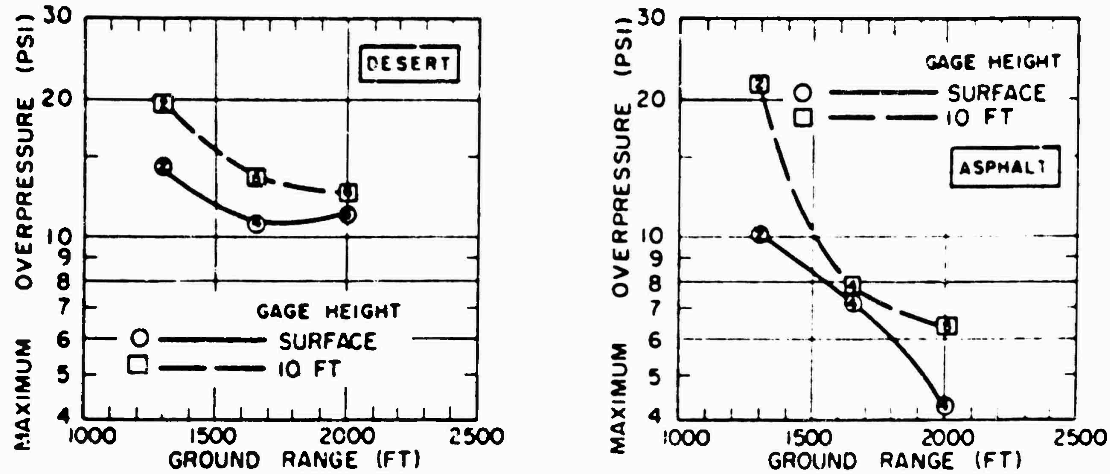

Figure 5.9 Maximum overpressure versus ground range, surface and 10-foot level, Shot 6.

The Shot 12 area map (Figure 5.15) might help to explain the phenomena observed by the BRL instrumentation This area map shows portions of the Frenchman Flat test area which have undergone stabilization for Teapot and previous operations; also shown on the map, for easy comparison, are the BRL gage-station locations around the instrumented arc. Figures 5.16 and 5.17 are postshot area photographs showing the character and extent of the stabilized areas. It may be more than mere coincidence that most of the BRL gages which recorded the higher peak overpressures were those located near or on a stabilized pad. The obvious conclusion is that abrupt localized changes in the characteristics of the surface over which a blast wave is traveling may have significant effects upon the peak overpressure and time history of a measurement taken in the near vicinity of the altered surface. Nonetheless, it should be emphasized that the symmetry measurements

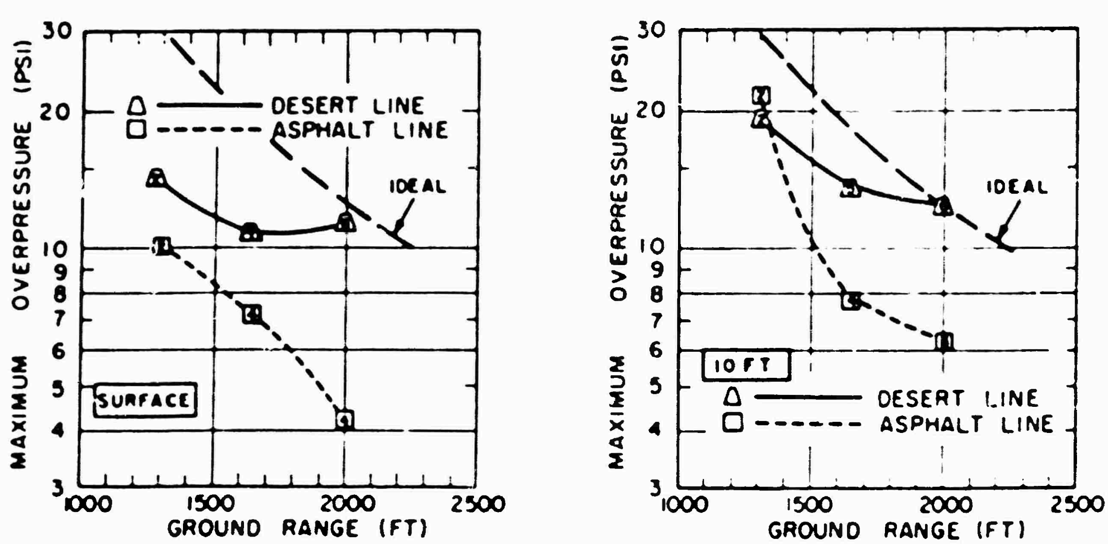

Figure 5.10 Maximum overpressure versus ground range, desert and asphalt, Shot 12.

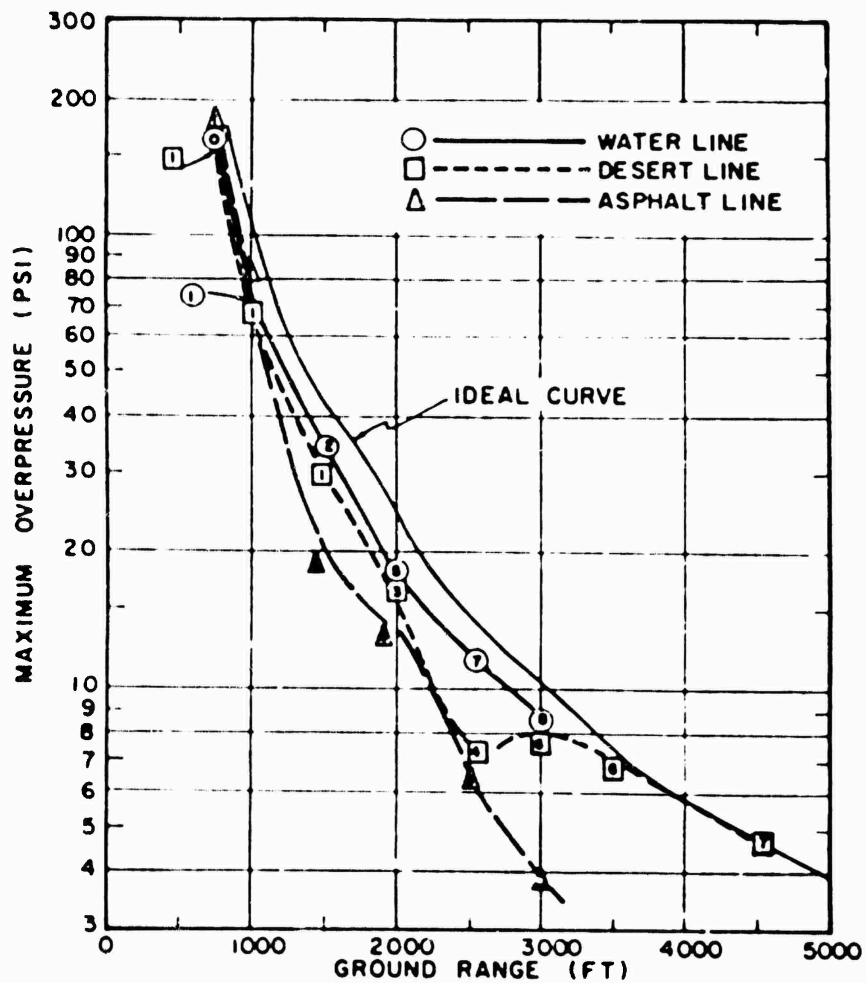

Figure 5.11 Maximum overpressure versus ground range, surface level, Shot 12.

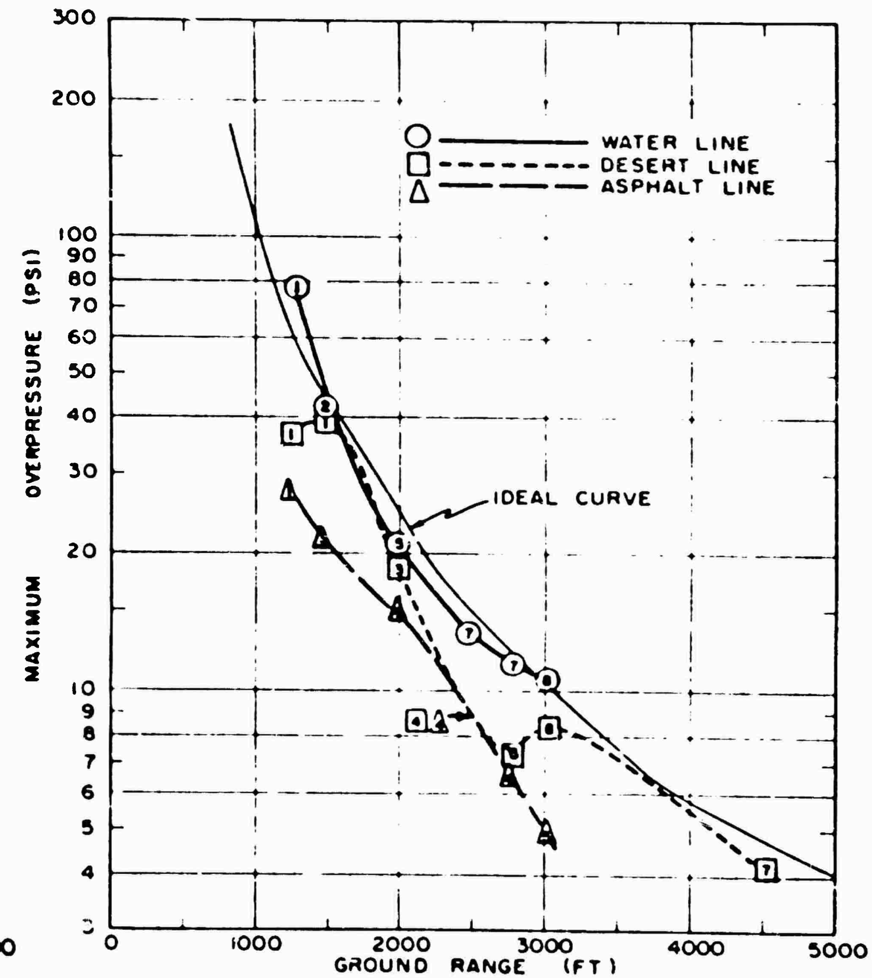

Figure 5.12 Maximum overpressure versus ground range, 3-foot level, Shot 12.

taken on only one shot in the test series were available and at a ground range (2,500 feet) where the blast wave disturbances were somewhat spent. Therefore, it is recommended that similar instrumentation be included on future tests, both within and beyond the regions of disturbed blast waves.

The above discussion logically leads to a consideration of the results obtained from the Shot 12 offset gages at 1,500 and 2,500 feet on the water blast line (see Figure 2.4). These gages were installed for the purpose of detecting the possible cross-feed of blast disturbances from the desert area to the water area. One method for analysis of cross-feed effects makes use of the arrival time and position data to compute interval velocities between the desert-water interface and the various gage stations. A summary of these velocities is listed in Table 5.2. The velocities have been determined assuming blast-

TABLE 5.2 CROSS-FEED DATA, SHOT 12

Gage	Surface	Ground Range	Arrival Time	Position	Distance from Edge	Velocity from Edge	Wave-From Type
		feet	sec		feet	fps	
21B	Water	750	0.1185	Blast line	400	27,000	0
1B	Desert	750	0.104	Blast line	0*		1
22B	Water	1000	0.1696	Blast line	400	19,500	1
2B	Desert	1000	0.149	Blast line	0*		1
23P3	Water	1250	0.255	Blast line	400	7,850	1
2P3	Desert	1250	0.202	Blast line	0*		1
25P3Y	Water	1500	0.3575	Offset	125	1,350	1
25P3X	Water	1500	0.3715	Offset	225	2,110	2
25P3	Water	1500	0.373	Blast line	400	3,700	2
5P3	Desert	1500	0.265	Blast line	0*		1
27B	Water	2000	0.589	Blast line	400	2,030	1†
7B	Desert	2000	0.4525	Blast line	0*		3
29P3Y	Water	2500	0.914	Offset	150	1,120	7
29P3X	Water	2500	0.903	Offset	270	2,200	4
29P3	Water	2500	0.913	Blast line	400	3,010	7
9P3	Desert	2500	0.700	Blast line	0*		4

* Blast-wave symmetry assumed

† A hybrid form of Type 1

wave symmetry, so that desert blast-line arrival times are the assumed arrival times at equal radii near the desert–water interface.

If a disturbance traveling over the desert surface is to feed-in energy across the desert–water interface, this energy would be propagated over the water with the local sound velocity. Table 5.2 indicates that Shot 12 times of arrival observed at the first three water-line stations (750- and 1,250-foot ranges) yield propagation velocities too high to be identified with sonic velocity. Therefore, the first disturbances as well as a major portion of the pressure–time history observed at these stations are free of cross-feed effects. However, Table 5.2 shows that at 1,500-foot ground range the offset gage nearest the interface (25P3Y) yields an arrival time which suggests cross-feed of energy at this gage. The other offset gage (25P3X) at this range and the blast-line gage (25P3) show later arrivals; however, it is probable that the cross-feed is manifest at some time following blast arrival on the gage records obtained at these stations.

The foregoing is supported by wave-form observations on the water line (Section 4.5.2); that is, at 1,500 feet the water-line offset gage closest to the desert is a Type 1, similar to the desert blast-line record, whereas the other offset gage trace (25P3X) resembles the measurement obtained on the water line.

Analysis of wave forms at 2,000 feet produces evidence of effect of cross-feed upon

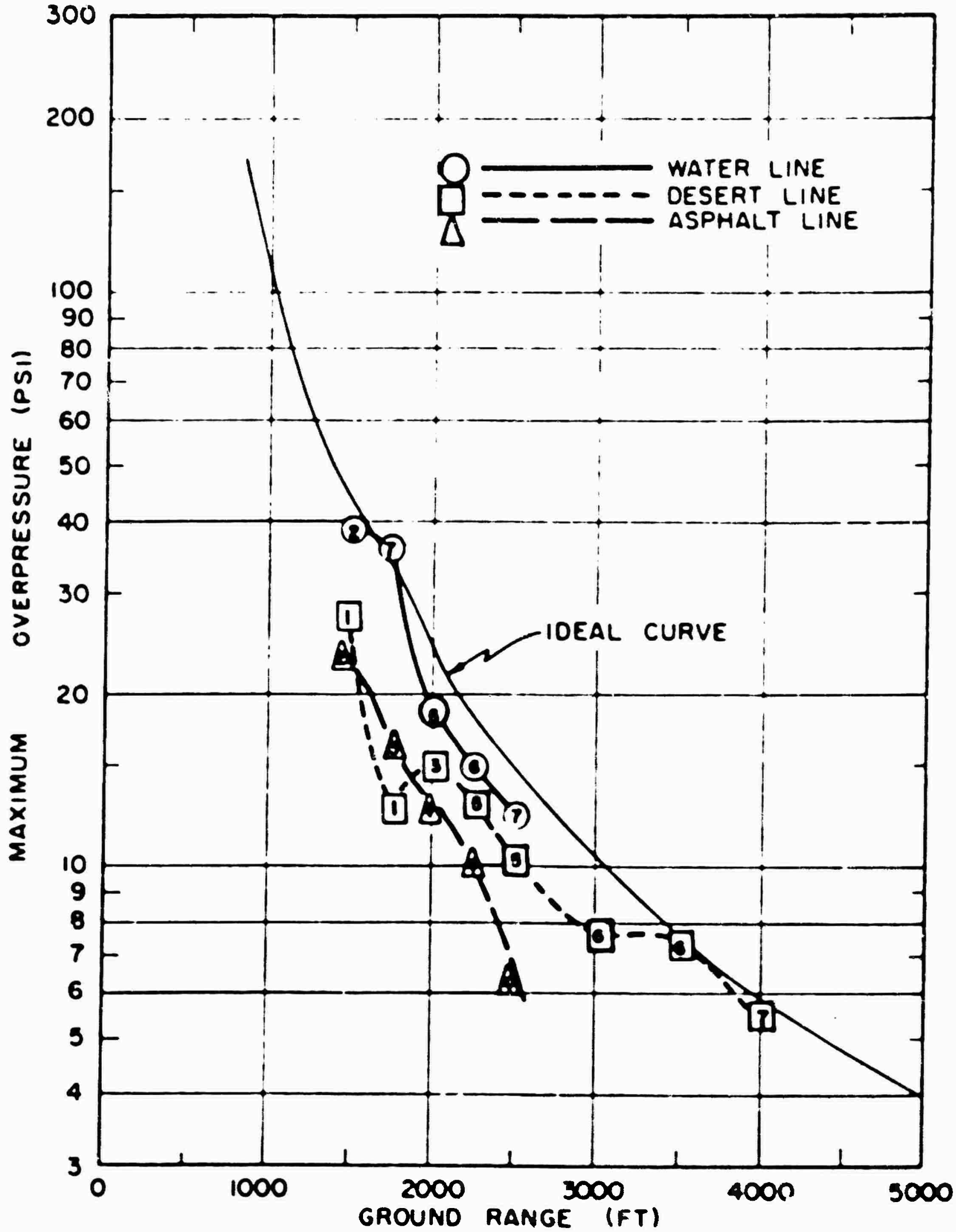

Figure 5.13 Maximum overpressure versus ground range, 10-foot level, Shot 12.

a blast-line gage record obtained over the water on Shot 12. The unsmoothed records (Appendix B) show that the 27B gage record (2,000 feet) is not a true Type 1 form because approximately 100 msec after arrival the pressure-time trace takes on the appearance of the 7B gage record (Type 3) which was recorded at the same ground range over the desert. At 2,500-foot ground range, the interval velocities (Table 5.2) are less than those for comparable gages at 1,500 feet. However, the trend is the same, and although the wave forms do not appear to be completely consistent, the BRL gage arc at this same ground range produced similar wave-form variations over similar gage-station separations.

In conclusion, it can be established with some assurance that the observation over the water line of earlier-than-ideal arrival times and Type 1 wave forms was not due to cross-feed from the desert surface. Since these observations are identified with the propagation of a precursor wave, it can be stated that a precursor formed over the water on Shot 12 and was observed at the close-in ground ranges.

A postshot view of the water line, looking toward ground zero, is shown in Figure 5.17, while Figure 5.18 is a postshot view of the Shot 12 asphalt line looking south toward ground zero. The highest gage tower, visible just left of center in the photograph, is the Project 1.10 2,500-foot gage station. It appears that the blast wave lifted off chunks of the surface, leaving deep pocks in the asphalt. However, the pocks are not distributed in a random fashion over the line; instead, there is a rather high density out to about 2,000 feet, then a relatively unmarked region out to about 2,800 feet, where a good deal of the asphalt surface is missing.

5.2.3 Overpressure Decay Behind Shock Front. An analytical representation of the overpressure profile of the classical shock wave at a given distance from an explosion is provided by:

$$p = p_m (1 - t/\Delta t)\, e^{-t/\Delta t} \qquad (5.2)$$

Where: p = overpressure at time t
p_m = peak value of the overpressure at t = o
t = time measured from shock arrival
Δt = positive phase duration of the blast wave (Reference 16)

Equation 5.2 is approximately valid for overpressures not exceeding 25 psi. In a theoretical paper on strong-shock spherical blast waves (Reference 17), some relations are derived for the pressure decay behind a spherical shock moving through an ideal gas medium. It shows that for peak pressures above one atmosphere the decay is not a simple exponential, since the early portion of the pressure–time function decays more rapidly than do the later parts. The results of Reference 17 and Equation 5.2 become identical when:

$$\frac{p_m}{p_1} = 0.5 \qquad (5.3)$$

Where: p_1 = ambient pressure in front of the shock front

Both of these methods of computation are strictly limited to the case of free-air wave propagation. Thus, any application of the methods to shock phenomena which are influenced by a ground plane (i.e., in regular or Mach reflection regions) necessarily involves an approximation of unknown magnitude. Nevertheless, it seems worthwhile to make some comparisons between theory and experiment using some of the Shot 12 data.

Comparisons of the calculated and measured decay of overpressure versus time on Shot 12 are shown in Figures 5.19 and 5.20. Only those records which appeared reasonably undisturbed were selected for analysis. Figure 5.19 includes all of the Shot 12 water-line records which were analyzed for pressure decay. For the records at 750 (21BA) and 1,750 feet (28P10A), as would be expected on the basis of their high peak pressures, the method of Reference 17 agrees better with the experimental results than does the method

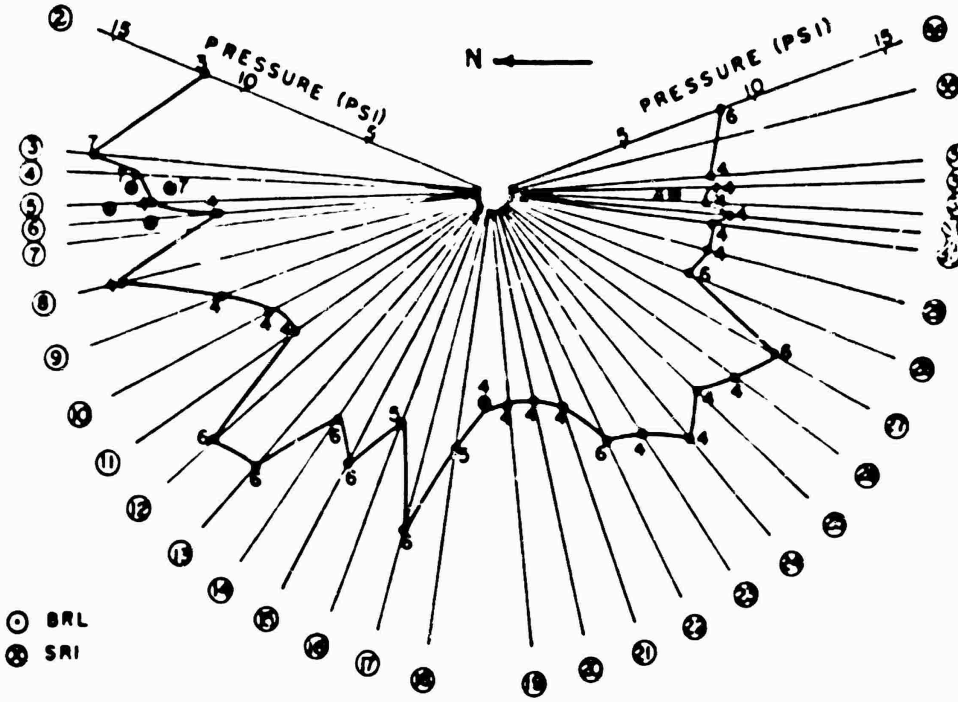

Figure 5.14 Results from BRL measurements on gage-arc. Shot 12.

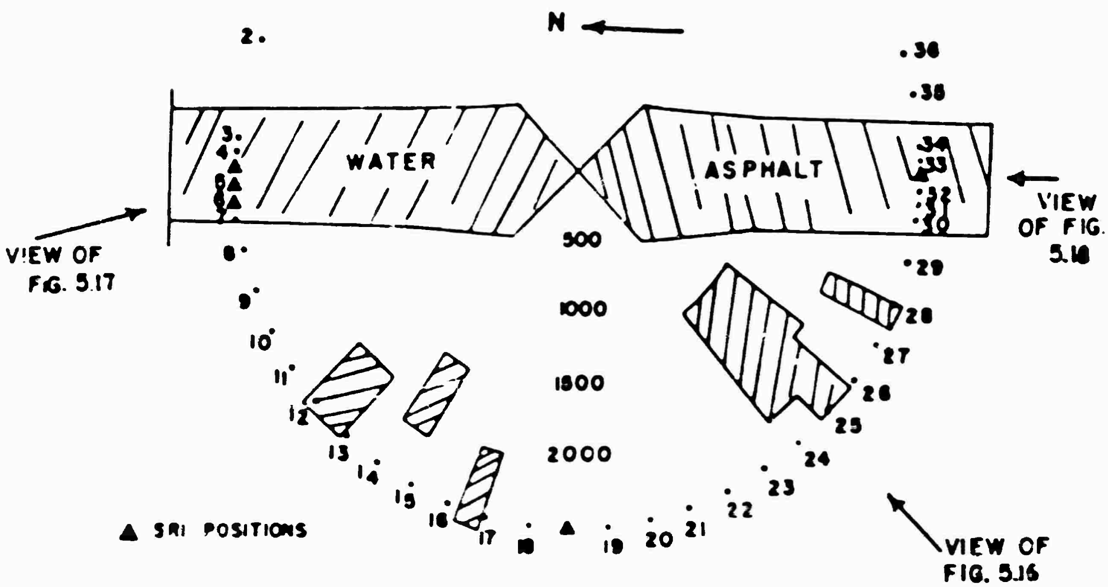

Figure 5.15 Area layout of Shot 12 test area, showing stabilized areas.

of Equation 5.2. At subsequent ground ranges on the water line (2,500 feet and beyond), the differences between the two computation methods appear small; however, if a choice must be made, it seems that the method of Equation 5.2 corresponds best with the experimental data. The gage records at 2,500 (29P3Y and 29P40A) and 2,750 feet (31P3) exhibit a definite nonclassic behavior in the first 100 msec after shock arrival. That is, if the measured peak pressure is taken as the basis for subsequent calculation, there appears to be a pressure hump when comparison is made with computed decay. However, it could equally well be assumed that these records (i.e., 29P3Y, 29P40A, and 31P3) are the result of a rounding-off of the more classical sharp-peaked wave form. If this latter con-

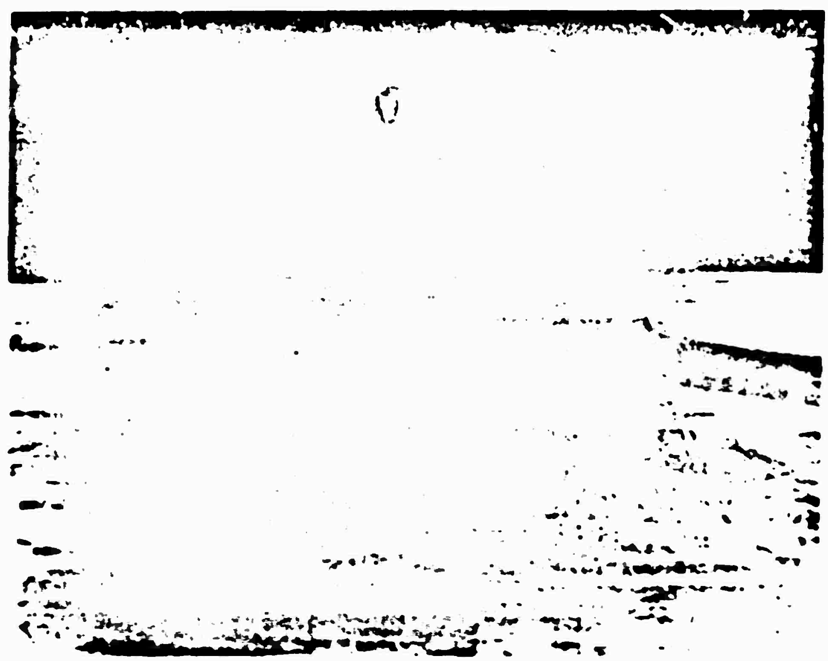

Figure 5.16 Post-Shot 12, desert line, looking northeast toward ground zero.

dition is considered, the decay calculation must be based upon an extrapolated (see Figure 5.19) peak pressure. It is evident from the figure that the decay computed from the extrapolated maximum pressure agrees well with the experimental record beyond about 150 msec.

The Shot 12 desert-line records (Figure 5.20) agree well with both methods of computation of overpressure decay. Since the peak pressures of the records approximately satisfy Equation 5.3 (p_m = 6.5 psi for Shot 12), it is to be expected that the two methods would be equivalent. Figure 5.20 also includes one gage record (49P40) obtained on the asphalt line. Because of the base-line corrections which were necessary for this record, the positive-phase duration is in doubt. For this reason, the Equation 5.2 decay calculation was performed using three possible positive durations; it is obvious from the figure that the gage record does not agree with any of the computed decay curves, indicating that deviations from the classical pressure-time wave form were most complete over the asphalt surface.

The fact that the Reference 17 method of calculating overpressure decay behind the shock front appears to agree best with experiment at high pressures leads to the conclusion

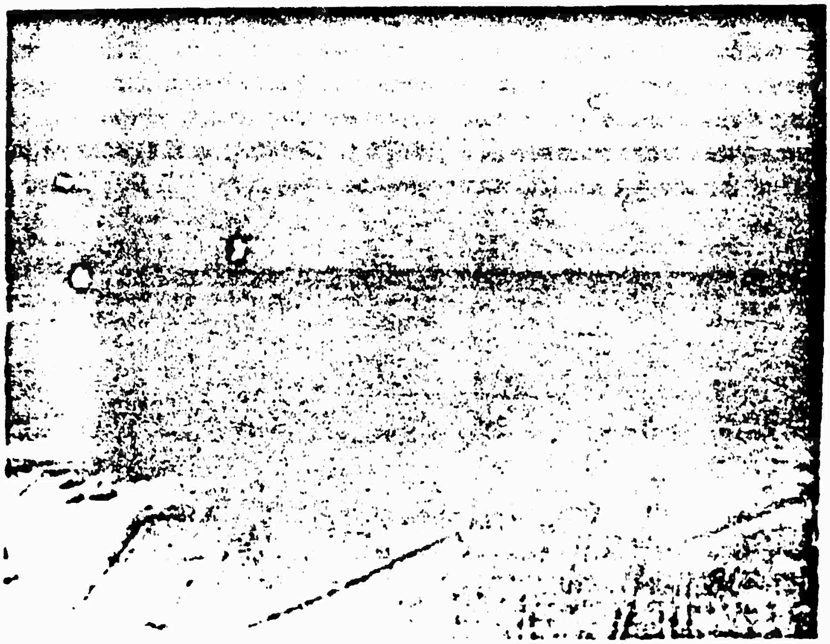

Figure 5.17 Post-Shot 12, water line, looking south toward ground zero.

Figure 5.18 Post-Shot 12, asphalt line, looking north toward ground zero.

that pressure–time records at close-in ground ranges (less than 750 feet) would probably exhibit the peaking effect shown on the 21BA record (Figure 5.19).

5.2.4 Comparisons with Previous Data. These comparisons can be made by considering such properties as pressure–time wave form, maximum overpressure versus ground range, impulse, and positive duration. The comparisons are made using, in all cases, the A-scaled data. Of course, only desert-line Teapot data are used.

For A-scaled comparisons, the pertinent shots may be divided into two main A-scaled classifications: (1) shots which have similar A-scaled burst heights, but different yields and (2) shots which have similar yields, but different A-scaled burst heights. The descriptions of these pertinent shots are summarized in Table 5.3. The wave-form comparisons

TABLE 5.3 SHOT DESCRIPTIONS FOR DATA COMPARISONS

Shot	Yield	Height of Burst	A-Scaled Height of Burst	Classification
	kt	feet	feet	
Teapot Shot 6	8.1	500	237	Variable Yield
Upshot-Knothole Shot 10	14.9	524	204	Similar A-scaled Height of Burst
Tumbler Shot 4	19.6	1,040	363	Variable Yield
Upshot-Knothole Shot 11	60.0	1,334	317	Similar A-scaled Height of Burst
Teapot Shot 12	23	400	135	Variable Yield
Upshot-Knothole Shot 1	16.2	300	113	Similar A-scaled Height of Burst
Upshot-Knothole Shot 1	16.2	300	113	Similar Yield
Upshot-Knothole Shot 10	14.9	524	204	Variable A-scaled Height of Burst
Upshot-Knothole Shot 9	26	2,423	764	Similar Yield
Teapot Shot 12	23	400	138	Variable A-scaled Height of Burst

for each pair of shots listed in the table are included in Figures 5.21 through 5.24. Both coordinates of these pressure–time plots have been normalized to 1-kt, sea-level conditions; an attempt is made to compare wave forms from gages at comparable A-scaled ground ranges. Figure 5.21, showing examples of Teapot Shot 6 and Upshot-Knothole Shot 10 wave-form comparisons, indicates that although the maximum pressure measured on the Teapot shot is significantly higher, the wave forms are very similar. The same is true for the Tumbler Shot 4 and Upshot-Knothole Shot 11 results shown in Figure [illegible]; it is noteworthy that these latter two shots had widely different yields (3:1). Proceeding to the next set of wave-form comparisons (Teapot Shot 12 and Upshot-Knothole Shot 1) shown in Figure 5.22, it is evident that at the close-in ranges (about 260 and 340 feet, A-scaled) the normalized wave forms from the two shots are similar. However, at about 500 feet (A-scaled) the Teapot record displays a prominent second peak which is absent on the Upshot-Knothole pressure–time result; these results indicate that greater differences in wave form are to be expected for a given change of burst height for heights of burst of the order of 100 feet (A-scaled) than would occur at heights of between 200 and 400 feet. It should also be noted that the Teapot normalized peak pressures are consistently higher, indicating that for detonations that have low A-scaled burst heights, A-scaled peak pressures may depend upon weapon yield.

The Upshot-Knothole Shot 1 and Shot 10 wave-form comparisons are included in Figure 5.23. As summarized in Table 5.3, these shots had similar yields but different A-scaled burst heights. The figures show little similarity in wave forms; specifically,

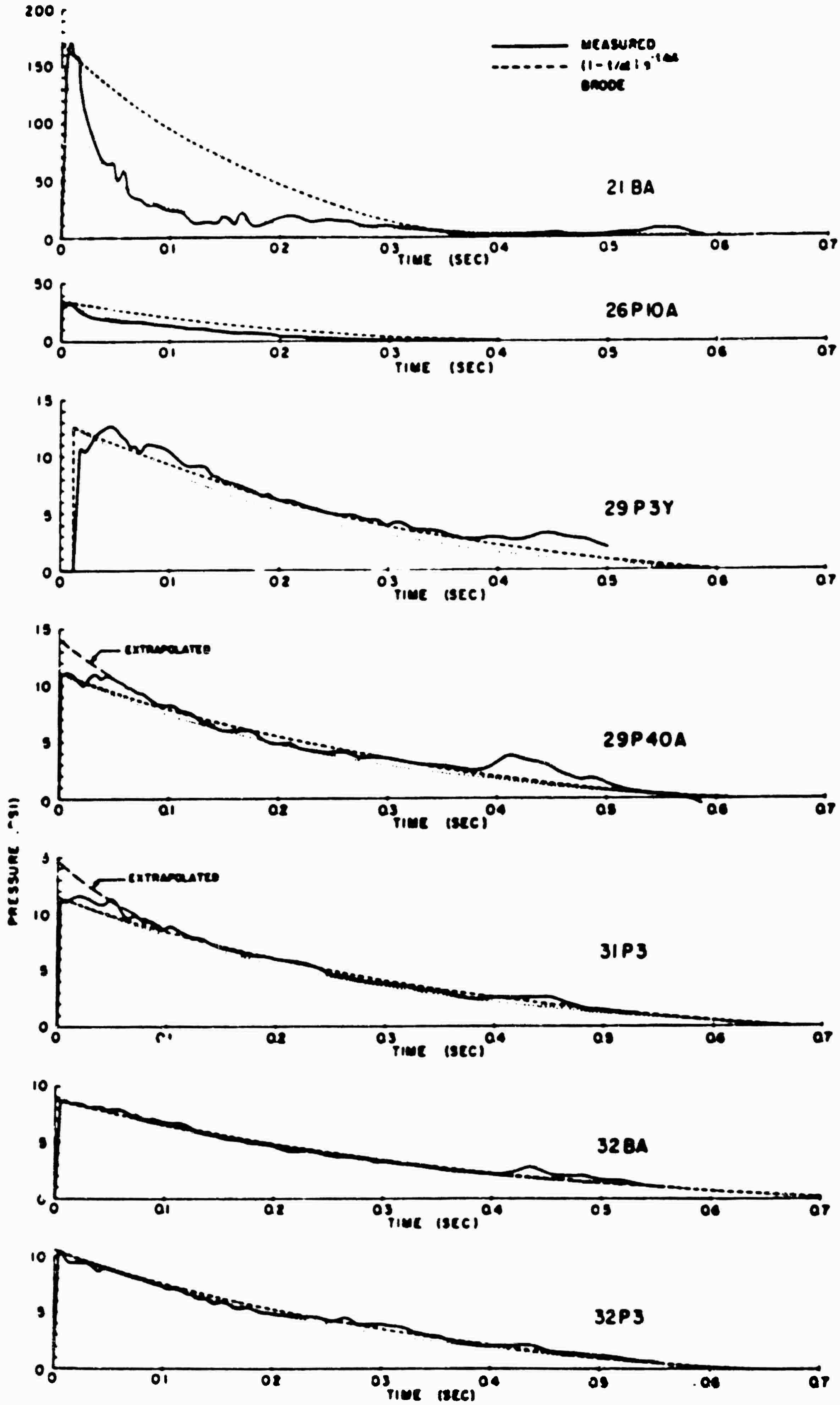

Figure 5.19 Decay of overpressure behind shock front, water line, Shot 12.

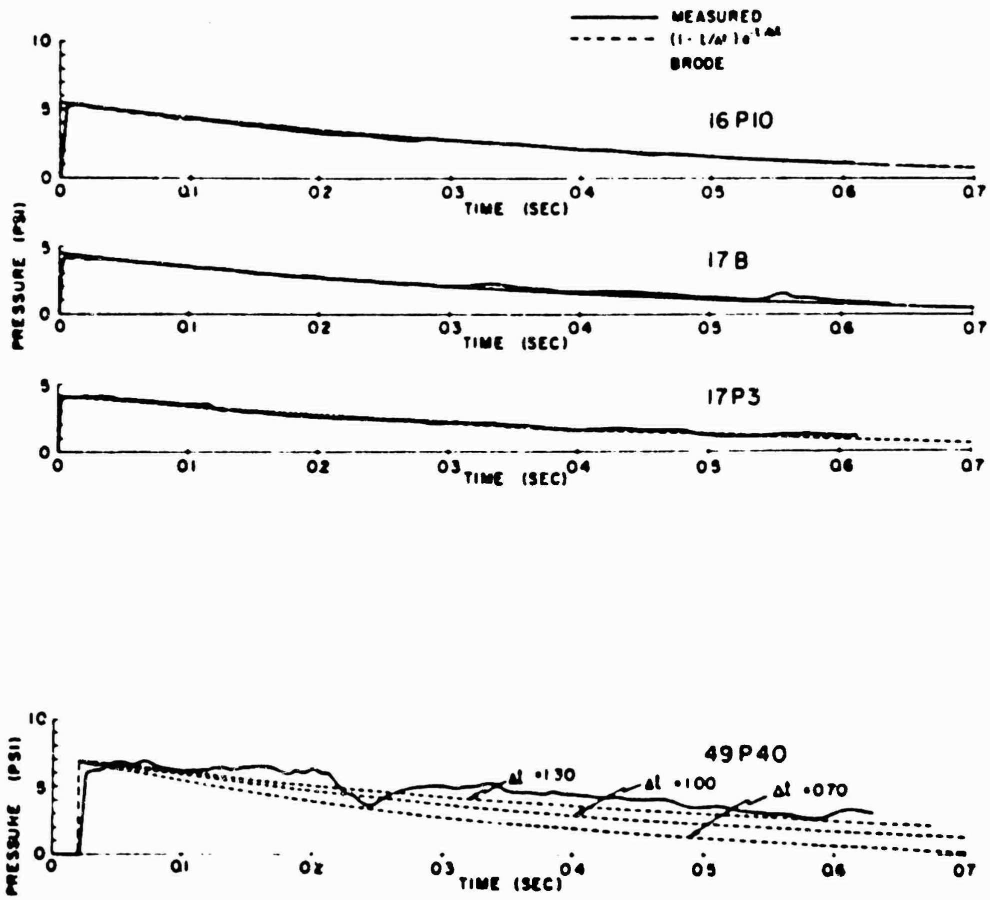

Figure 5 20 Decay of overpressure behind shock front, desert and asphalt lines, Shot 12.

the Shot 1 pressure–time records exhibit shock-like pressure rises, whereas the Shot 10 results show slow-rise, compression-like wave fronts, particularly at the close-in ranges. The last set of wave-form comparisons, shown in Figure 5.24, include Upshot-Knothole Shot 9 and Teapot Shot 12. The A-scaled burst heights for the former were too high for precursor formation (see Table 5.3), which explains the disturbed wave forms observed on the Teapot Shot only. The figures show the extremely poor correspondence between pressure–time wave forms obtained on these shots: the Upshot-Knothole records are consistently classical, while the Teapot results show the influence of disturbing effects out to about 1,100 feet (A-scaled range).

In addition to wave-form comparisons, the Project 1.10 data may be compared with previous results on the basis of peak overpressure versus ground range. This comparison is documented in Figure 5.25, where the A-scaled surface-level peak pressures are plotted against A-scaled ground range. Included on this figure are wave-form classifications, ideal overpressure curve (solid line), and the Teapot Shot 12 curve (dashed line). At A-scaled ranges less than 1,000 feet, peak pressure data are significantly depressed below ideal values; the experimental points appear first to merge with the ideal at about 1,200 feet (A-scaled), which corresponds to 7 or 8 psi (A-scaled). There is a tendency for Tumbler Shot 4 maximum pressures to be notably low at the close-in ranges, a result

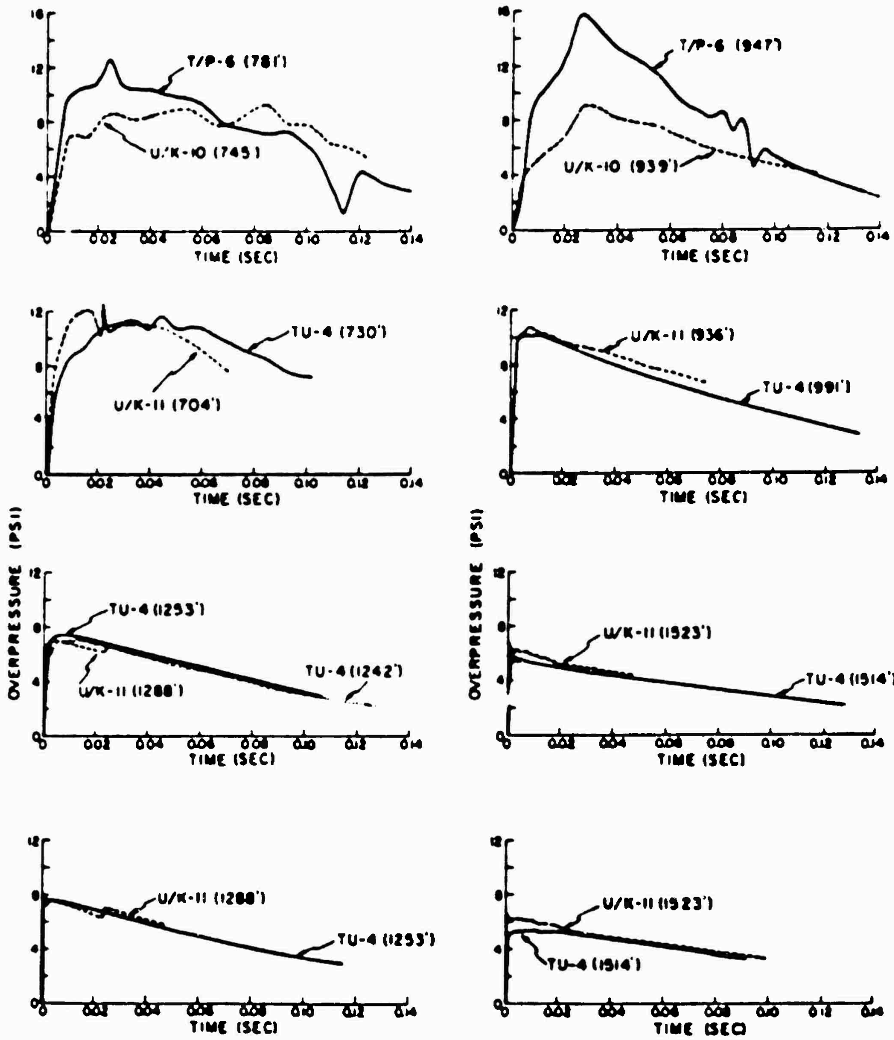

Figure 5.21 Wave form comparisons (A-scaled), Teapot Shot 6, Upshot–Knothole Shot 10, Tumbler Shot 4, Upshot–Knothole Shot 11.

which may be explained by the relatively high A-scaled burst height for this shot.

For Upshot-Knothole, Reference 9 presents a treatment of overpressure positive-phase duration and positive impulse as a function of peak pressure. This report includes composite plots of these quantities using A-scaled results from all nuclear air bursts detonated prior to the fall of 1953; it was possible to draw average smooth curves through the array of data points. These curves are presented in Figures 5.26 and 5.27, where the dashed lines define the ± 15-percent deviation from the average curve. Although the data from previous shots scattered a good deal, it was found that about 90 percent of the data points fell within the ± 15-percent limits. In addition, it was found that the smoothed curve did not fit data corresponding to pressures higher than about 30 psi (A-scaled). For completeness, Figures 5.26 and 5.27 include all data from Teapot Project 1.10 and only those data from previous shots which correspond to maximum pressures in excess of 30 psi.

The positive-duration-versus-maximum-pressure plot (Figure 5.26) shows that data from Teapot Shots 6 and 12 over all three types of surface agree well with the composite curve; however, at overpressures in excess of 30 psi there is a tendency for the Teapot and previous data to diverge. Data from other shots show a definite trend toward de-

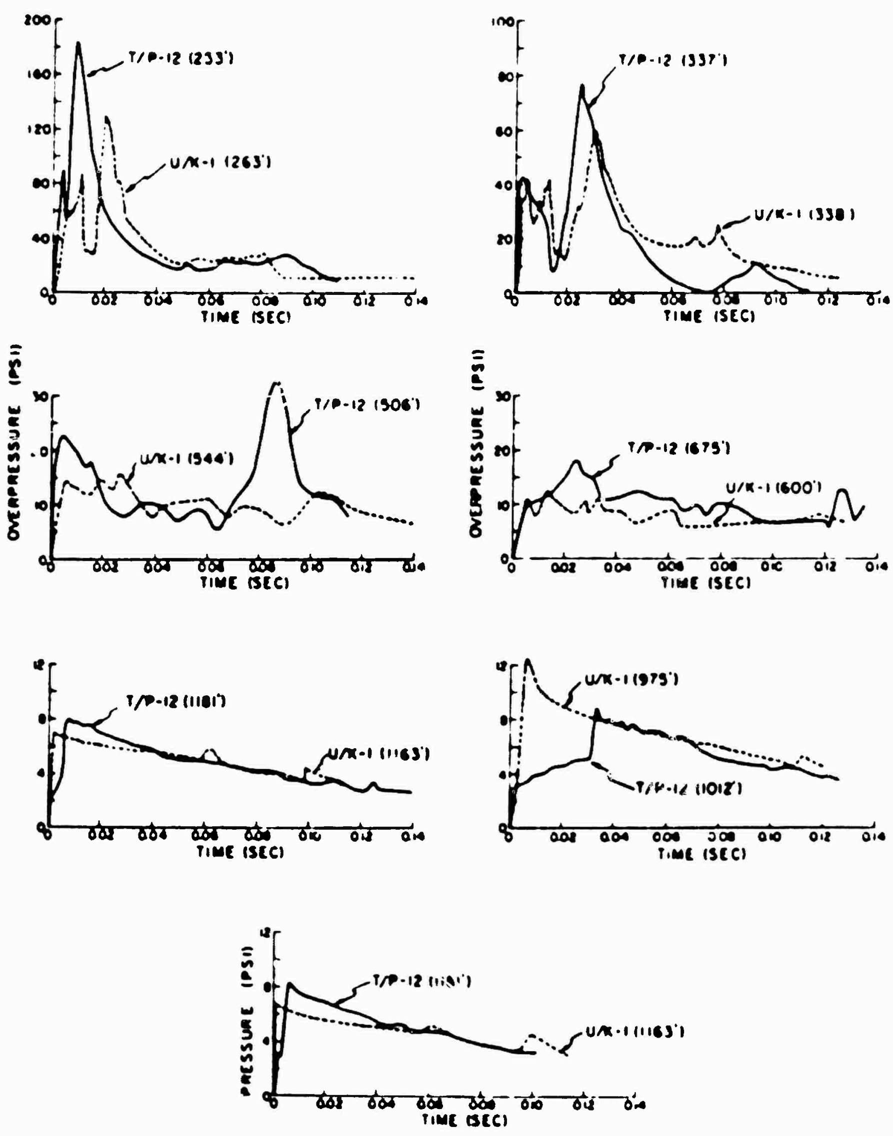

Figure 5.22 Wave form comparisons (A-scaled), Teapot Shot 12, and Upshot–Knothole Shot 1.

creasing duration with increased maximum overpressures in the high-pressure region; on the contrary, the Shot 12 positive durations corresponding to pressures near and above 100 psi (A-scaled) are significantly higher than previous data would predict. It is possible that the very long durations at close-in gage stations are due to some uncompensated instrumental error, e. g., a short time-shift in the zero-signal response characteristics of the gage immediately following shock arrival at the gage. However, it should be noted that the analysis of the free-air case in Reference 17 predicts the observed increase in positive-phase durations at the higher shock strengths.

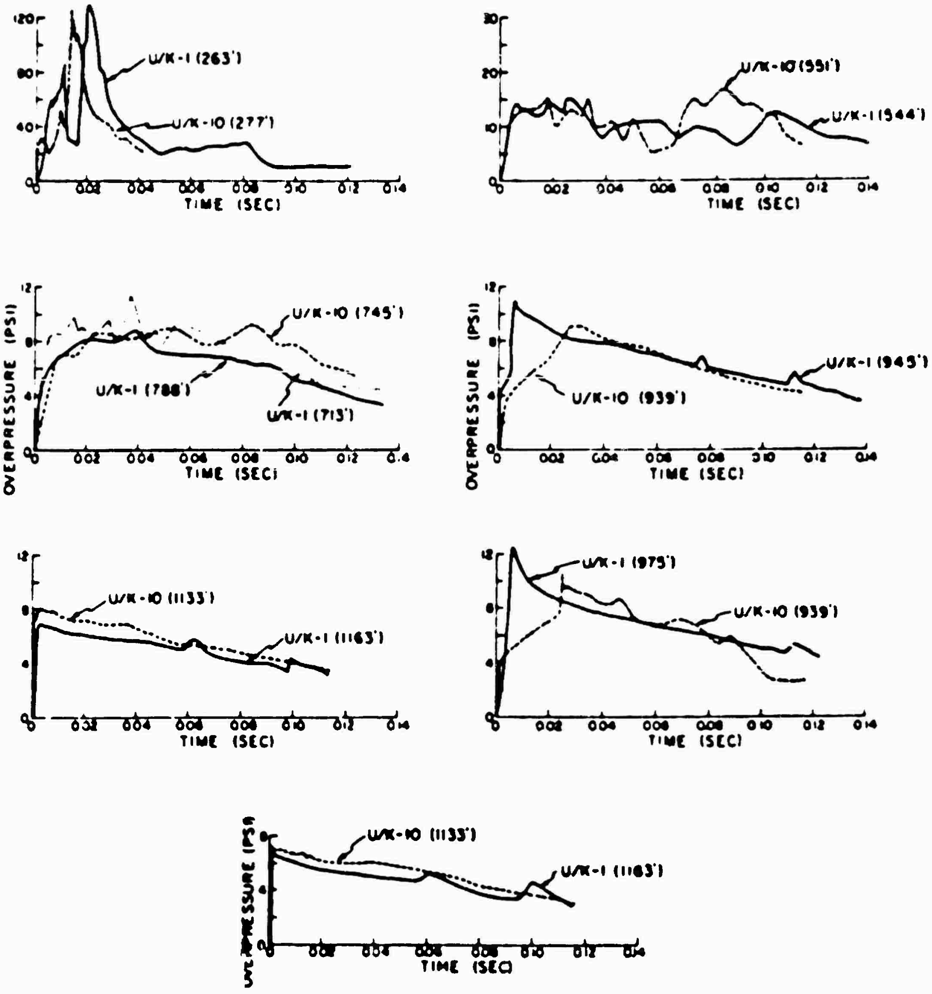

Figure 5.23 Wave form comparisons (A-scaled), Upshot–Knothole Shots 1 and 10.

The positive-impulse data shown in Figure 5.27 are presented in the same manner as were the positive-duration data. Although the Shot 6 asphalt-line impulse data are consistently too high and outside the ± 15-percent limits, the Shot 12 data show no definitive effects of surface properties. There appears to be some tendency for the Teapot Project 1.10 impulse data (below 30 psi) to be higher than the composite curve. For A-scaled maximum pressures above 30 psi, the Teapot impulse results do not disagree significantly with previous results; however, at these higher pressures, it appears that the positive impulse is always lower than would be indicated by the extension of the composite curve to pressures above 30 psi. In addition, since positive impulse is obtained by integration of the pressure–time record, it will be less critically influenced by possible short-time instrumental disturbances than will the positive-phase-duration variable.

5.3 DYNAMIC PRESSURE MEASUREMENTS q*(pitot)

The general method of presentation of the Project 1.10 overpressure data included in the previous section will be applied to the discussion of the q*(pitot) measurements. First, the effect of surface properties upon the data will be considered, after which com-

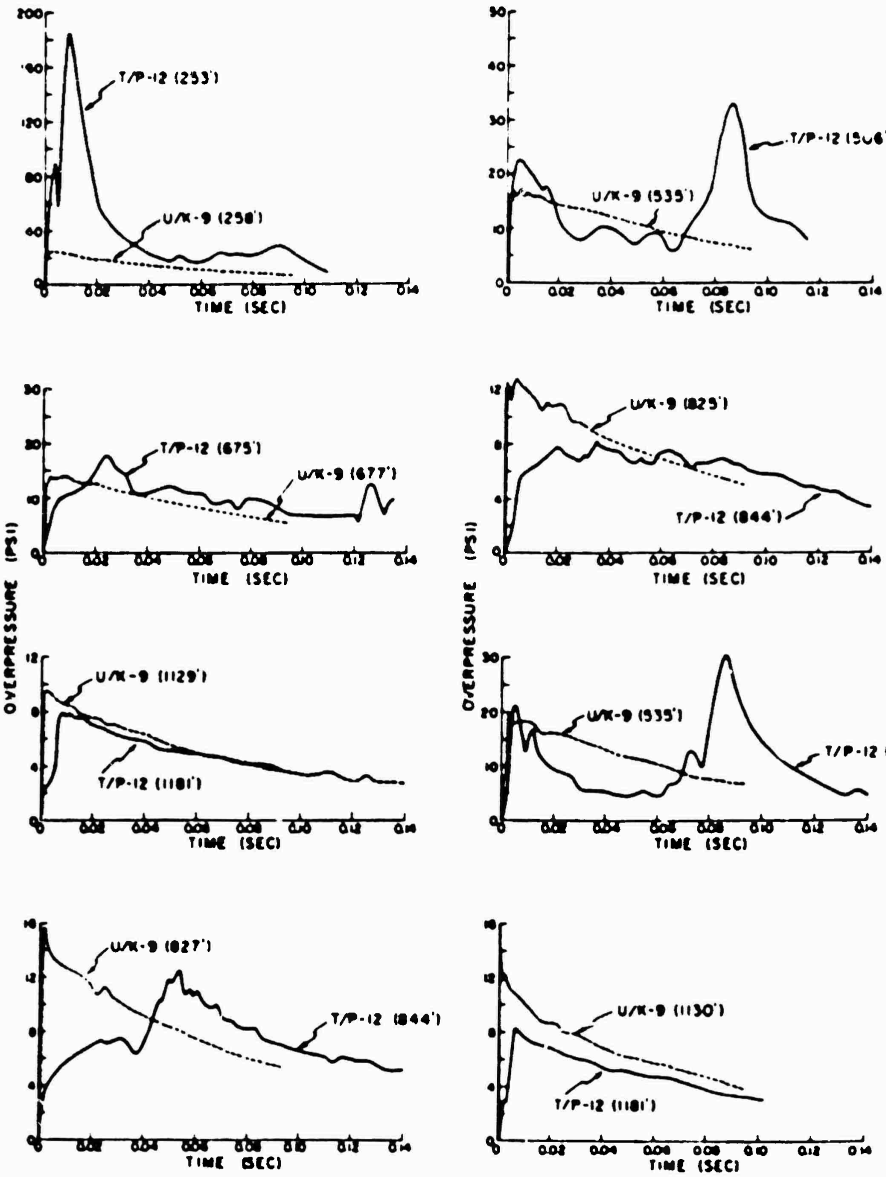

Figure 5.24 Wave form comparisons (A-scaled), Teapot Shot 12 and Upshot-Knothole Shot 9.

parisons will be made with available results from previous shots.

5.3.1 Effects of Surface Characteristics q*(pitot). The plots of maximum q*(pitot) pressure versus ground range for Shot 12 are shown in Figures 5.28, 5.29, and 5.30. The various symbols on these plots indicate the maximum q*(pitot) pressure recorded at each ground range, and the letters inside the symbols designate the wave-form type associated with each record; no letter inside a symbol indicates that the wave form does not correspond to any specific classification. Again, the data have been corrected for pitch angle and Mach number.

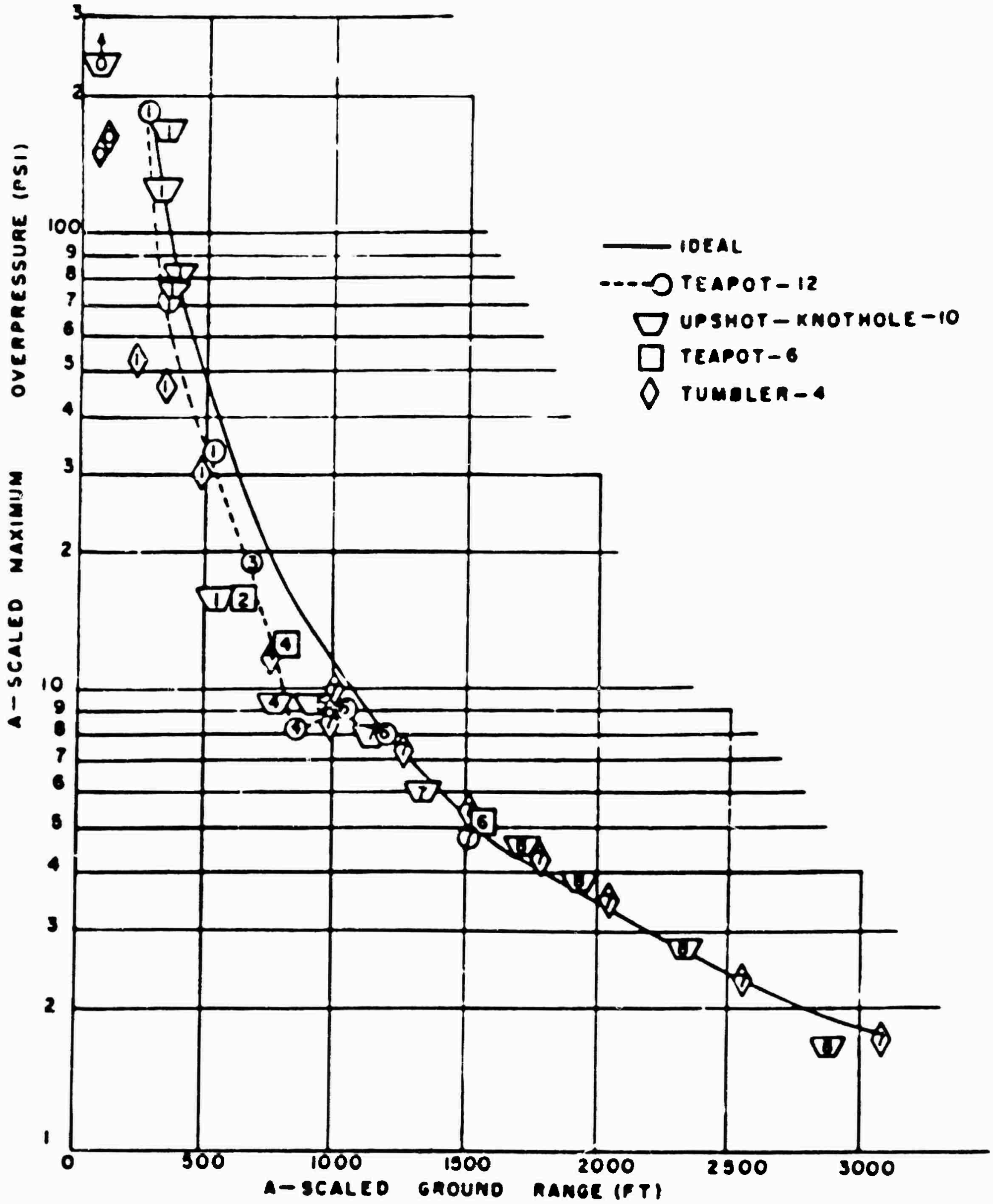

Figure 5.25 A-scaled maximum overpressure, surface level, Teapot Shots 6 and 12, previous shots, desert line.

The Shot 12 data for the water-line maximum q*(pitot) pressure shown in Figure 5.28 indicate that 3-foot pressures are significantly higher than those measured at 10 feet; however, because of the steep slope the position of the 3-foot data point at 2,000 feet ground range has a profound influence upon the shape of the curve. The attenuation of peak q*(pitot) pressure with distance is quite severe. The curve of Figure 5.28 indicates a drop in pressure from about 300 to 3 psi in a ground range interval of less than 2,000 feet. As stated previously, the water-line q*(pitot) records do not lend themselves well to wave-form classification, which accounts for the many blank symbols on Figure 5.28.

The desert-line q*(pitot) data of Figure 5.29 show an attenuation of pressure with distance which is similar to that observed over the water line; however, unlike the water line data, the 3-foot maximum pressures over the desert appear to be depressed relative to 10-foot values.

Figure 5.30, showing the q*(pitot) results over the asphalt line, is not significantly different in appearance from the plots corresponding to the water and desert lines. There is apparently little difference in the maximum pressures at 3- and 10-foot levels; moreover, the decrease in q*(pitot) peak pressure between 2,500-foot ground range (13.1 psi) and 3,000-foot ground range (0.85 psi) is most severe on the asphalt line. It is noted that the single data point at 3,000 feet produces the aforementioned appearance of serious attenuation; however, the fact that the 40-foot-level gage at 2,500 feet recorded a depressed q*(pitot) maximum lends some validity to the curves drawn in Figure 5.30. In fact, the obvious consequence of the marked attenuation characteristics (evident in Figures 5.28 through 5.30) is that one or two data points may influence profoundly the character of the best-fit curve drawn through the data. If this danger is kept in mind, the discussion of the composite Shot 12 q*(pitot) curves can proceed more profitably.

Figure 5.31 is the composite graph of Shot 12, 3-foot q* (pitot) maximum pressures over the three blast lines; the figure also includes the ideal-dynamic-pressure-versus-ground-range curve (Reference 12). Primarily, it is obvious that the q*(pitot) maxima over the three surfaces agree closely at the first gage station (1,250-foot ground range); also, the pressures recorded are larger than ideal at the same range by about a factor of five. Maximum q*(pitot) pressures approach ideal at 2,500-foot ground range on the water line, but on the desert the earliest indication of agreement is at 3,000 feet. The value over the asphalt at 3,000 feet falls appreciably below the ideal; it will be recalled (Figure 5.12) that a severely depressed peak overpressure was also recorded at this range.

The 10-foot level q*(pitot) composite for Shot 12, presented in Figure 5.32, indicates that at this gage height the effect of surface properties is more systematic than is the case for the 3-foot measurements. The pressures measured over the desert are highest; at the close-in 10-foot gage station (1,500 feet) the peak pressure is again larger than ideal by a factor of five. Desert-line q*(pitot) maxima are close to ideal at ground ranges of 3,500 and 4,000 feet; the same is true for water-line measurements at 2,250 and 2,500 feet. However, in the latter case, the wave forms of the q*(pitot)-time records are far from ideal in appearance (see Figure B.3). This suggests, as pointed out in Section 5.2.1 in connection with overpressure data, that it is misleading to label a blast wave ideal on the basis of its maximum pressure only.

The Shot 6 maximum q*(pitot) data are presented in Figure 5.33, all obtained from 10-foot-high gages. Because so few measurements were taken on this shot, the usefulness of the data is restricted to supplementing the Shot 12 results. Figure 5.33 shows that at the closest gage station (1,300-foot ground range) the peak q*(pitot) pressure was higher over the desert surface; also, the pressure exceeded the ideal value at the same ground range by factors of about four (over asphalt) and six (over desert). The Shot 6 q*(pitot) data, like those of Shot 12, exhibit severe attenuation of maximum pressure as a function of ground range.

It is possible, with reference to the Shot 12 photographic data reported by NOL (Reference 15), to determine the approximate arrival times at various ranges of what appears to be a dust front. Upon checking some of these dust arrivals against the pressure-time records obtained on Project 1.10, it appears that some measured effects may be attributed to the dust. An example is the 3-foot-level pitot-tube results at 3,000 feet (9P3 and 9Q3 of Figure B.7). The q*(pitot) record (9Q3) shows a slow pressure rise fol-

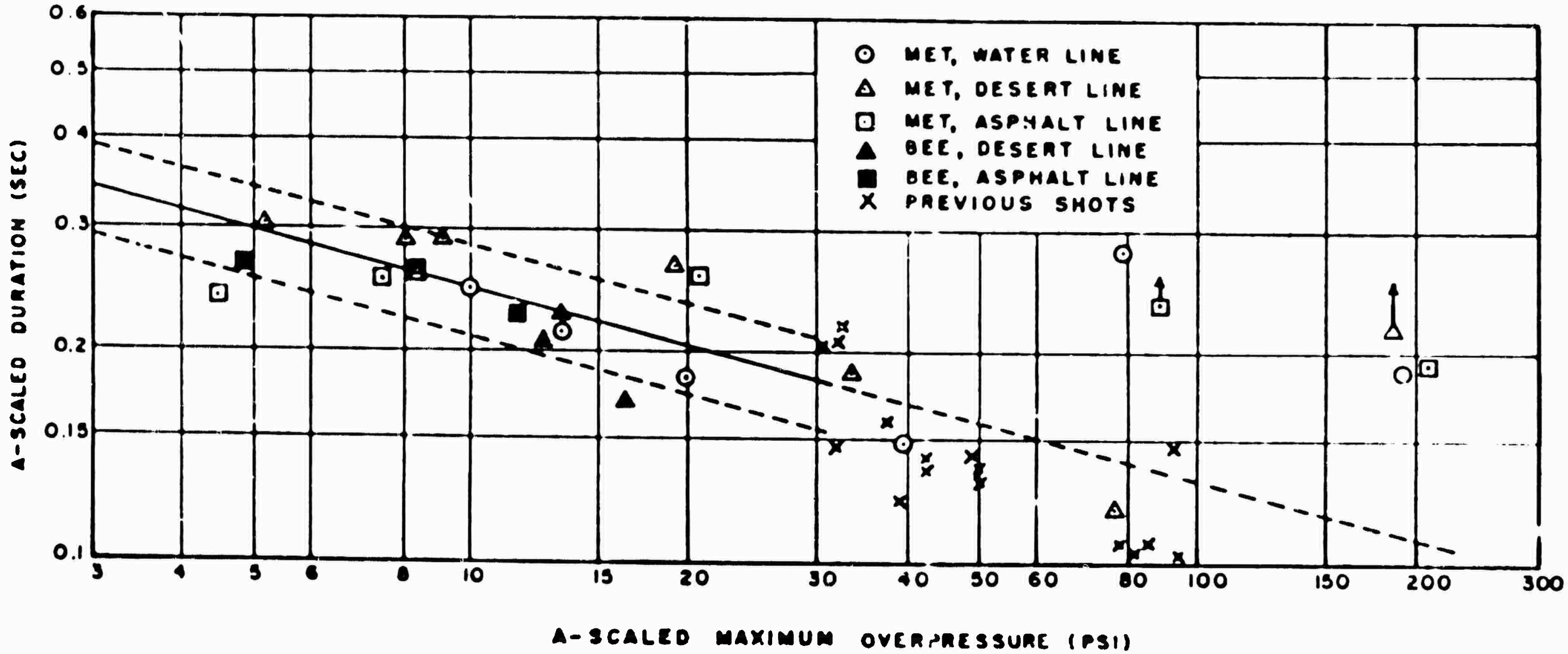

Figure 5.26 A-scaled positive phase duration versus A-scaled maximum overpressure, Teapot Shots 6 and 12, previous shots.

DECLASSIFIED

lowed (about 30 msec after the initial arrival) by a sharp, high amplitude disturbance. The delay between initial arrival and the high amplitude portion corresponds well to the NOL photographic data for time delay of dust-front arrival at this station. The side-on record (9P3) shows only a rather minor indication of dust arrival at a somewhat later time than observed for the head-on gage. This same behavior is characteristic of several pitot-tube gage stations on the Shot 12 desert line.

5.3.2 q*(pitot) Positive Impulse. It was realized from previous nuclear test series that the drag forces and the damage to certain classes of drag-sensitive targets in the regions of disturbed blast waves did not correlate with the results anticipated from utilization of measured overpressures. The limited pitot-tube dynamic-pressure measurements available indicated, in general, that in the disturbed region, q*(pitot) pressure is substantially higher than would be calculated using classical relationships and the measured overpressures. It is well-known that one of the most prominent characteristics of precursor blast waves, manifest in both dynamic pressure and overpressure measurements, is the marked increase in positive duration and impulse in the region of severe disturbance. Since damage to drag targets is of great interest, it was thought expedient to investigate the impulse associated with the q*(pitot) measurement of Project 1.10.

For this investigation, rather than attempt to obtain the total positive impulse, it was decided that a more useful purpose would be served if the impulse-versus-time function were determined for each q*(pitot) measurement. The results of these successive integrations are summarized in Figures 5.34 through 5.38. Some general statements can be made on the basis of these figures:

1. On Shot 12, out to 2,500-foot ground range, the 3-foot-level results show that the effects of the asphalt and water lines are comparable, while the desert q*(pitot) impulse reaches values as much as ten times larger than those indicated on the other blast lines (Figures 5.34 and 5.35).

2. At the 10-foot height, the impulse in order of decreasing value is desert—asphalt—water; the impulse magnitudes over the desert surface are usually three or four times larger than those measured over the asphalt or water surfaces.

3. Only at 3,000-foot ground range (see Figure 5.37), where the q*(pitot) impulse maximum is about one percent of the largest value measured, do the water-line data exceed those over the desert and asphalt.

4. The one Shot 6 comparison (see Figure 5.38) indicates that the impulse—time curves for the two blast lines are of the same form, with the desert-line values consistently higher.

It is believed that the very high q*(pitot) impulse values measured over the desert surface are caused by the presence of an excessive amount of particulate matter carried along by the pressure wave. It is further believed that this particulate matter affects the pitot-tube gage as would an additional pressure. In regard to using q*(pitot) impulse for damage correlation, some information is supplied by reference to the Teapot report on drag-target investigations (Reference 18). To summarize, those results indicated similar damage to drag targets on both the water and desert lines of Shot 12, but a slightly more severe damage level on the asphalt line. The fact that the q*(pitot) impulse curves of Figures 5.34 and 5.35 would not have predicted this general result suggests the possibility that the factors affecting the q-impulse measurements are not the same as those which significantly influence damage to drag-sensitive targets.

5.3.3 Comparisons with Previous Data. Unlike the situation with regard to overpressure measurements, there are only a few q*(pitot) results from previous shots which

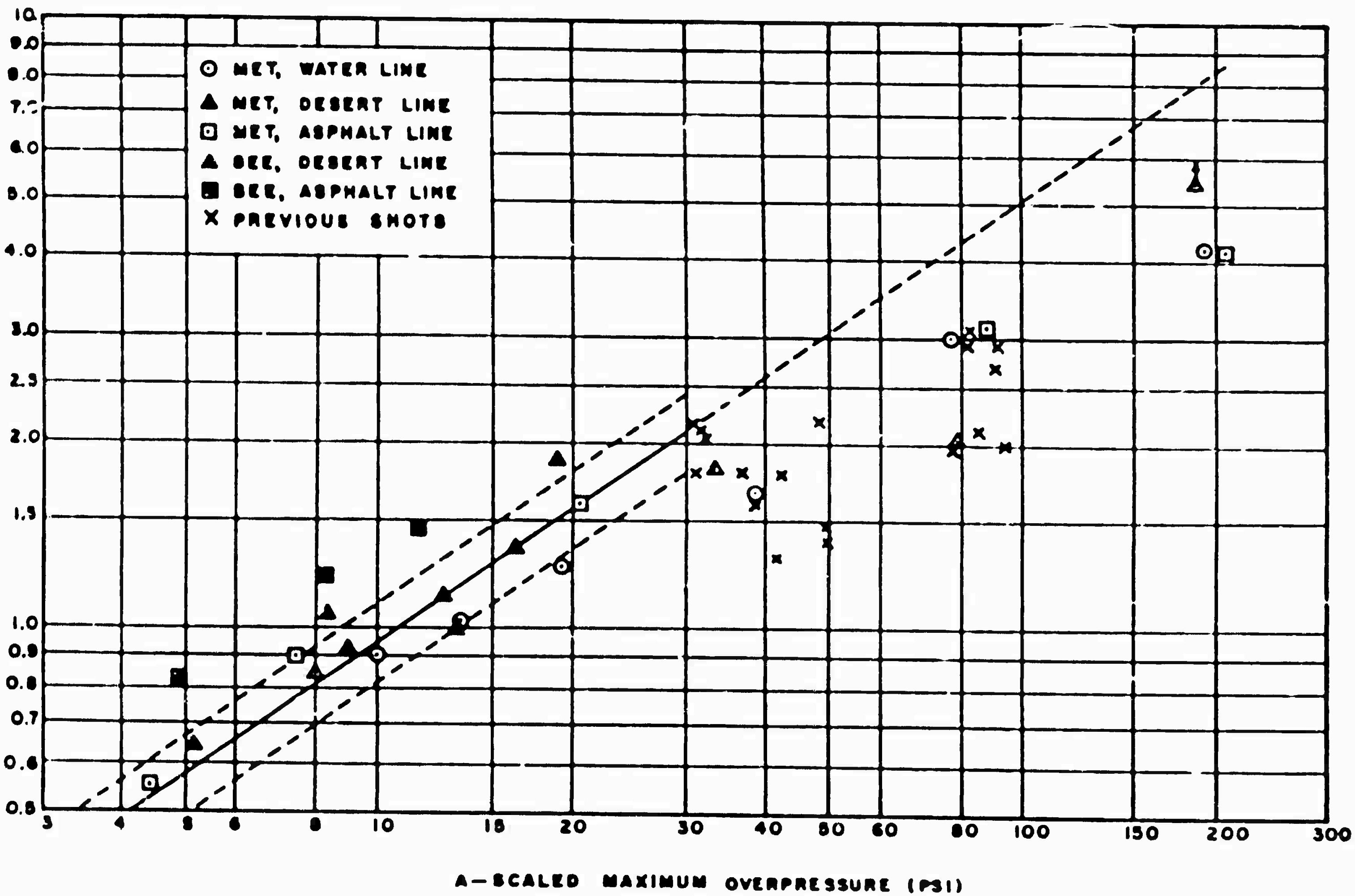

Figure 3.27 A-scaled positive impulse versus A-scaled maximum overpressure, Teapot Shots 6 and 12, previous shots.

DECLASSIFIED

CONFIDENTIAL

can be compared with Project 1.10 desert-line data. The plot of maximum q*(pitot) pressure versus ground range (A-scaled) is shown in Figure 5.39. Included are wave-form classifications (where possible), the ideal q*(pitot) curve (solid line), and (for Shot 12) the 10-foot-level desert-line data and curve (dashed line). Also shown in Figure 5.39 are the available q*(pitot) pressure data (corrected for Mach number) from previous shots: namely, Upshot-Knothole Shots 10 and 11. The Upshot-Knothole Shot 10 data at A-scaled ground ranges less than 1,000 feet are probably low (note arrows on symbols) due to suspected gage overload (Reference 6). The remaining Upshot-Knothole data, the Shot 11 result near 800-foot range and the Shot 10 result near 1,500 feet, are in agreement with the ideal values at these A-scaled ranges. Finally, it is apparent that, at A-scaled ground ranges less than 1,000 feet, the Teapot Shot 12 q*(pitot) maximum pressures over the desert are much greater than have been measured on any previous shots.

5.4 PRECURSOR PHENOMENA

The most significant airblast results of Operation Teapot, and more specifically, Project 1.10, were obtained where airblast behavior departed from ideal. Such departures have been attributed to surface and/or thermal effects on blast and may be classified as precursor phenomena.

5.4.1 Background. Since it was not possible to study the blast characteristics of nuclear explosions without the effects of accompanying thermal radiation on the surface, there were no means before Teapot of experimentally separating the mechanical and thermal effects on blast. High-explosive tests, which have negligible accompanying thermal radiation, showed minor blast effects due to differences in surface mechanical reflection properties and surface dust. Surface nuclear explosions, where geometry limits the thermal radiation incident on the blast surface, gave results similar to TNT tests. In any case, the extreme deviations from ideal blast phenomena which were observed on several low-burst-height nuclear detonations are far greater than the perturbations observed for scaled TNT tests or for surface nuclear tests over the same kinds of surfaces. It therefore appears safe to assume that thermal radiation is the principal cause of blast wave departures from ideal. Of course, the properties of the surface, including dust, can have a profound influence upon the degree to which the thermal radiation affects blast.

It has been customary to use the term precursor to describe the blast conditions representative of low bursts where the thermal effects on blast are of major importance. It must be noted that the disturbing effects on blast can be significant without the actual generation of a precursor wave, or outside the range of the precursor region. The term precursor is used frequently in a general sense to describe the whole region where the thermal effects on blast cause significant departures from the ideal case. In some circumstances the term nonideal is used to describe this behavior.

Anomalous blast behavior was observed on most nuclear test series prior to Teapot. The role of thermal effects on blast was first clearly delineated on Tumbler-Snapper, where the precursor phenomenon was identified. Subsequent re-examination of Buster and Greenhouse blast measurements confirmed precursor existence and showed similar thermal perturbations on blast. It remained for the Upshot-Knothole test series to investigate the effects of such nonideal blast waves on targets and to study further the associated basic-blast phenomena. Much additional valuable information was obtained during Upshot-Knothole which led to qualitative explanations of the thermal effects on blast waves; however, it was the objective of the Teapot series to put this thermal phenomenon

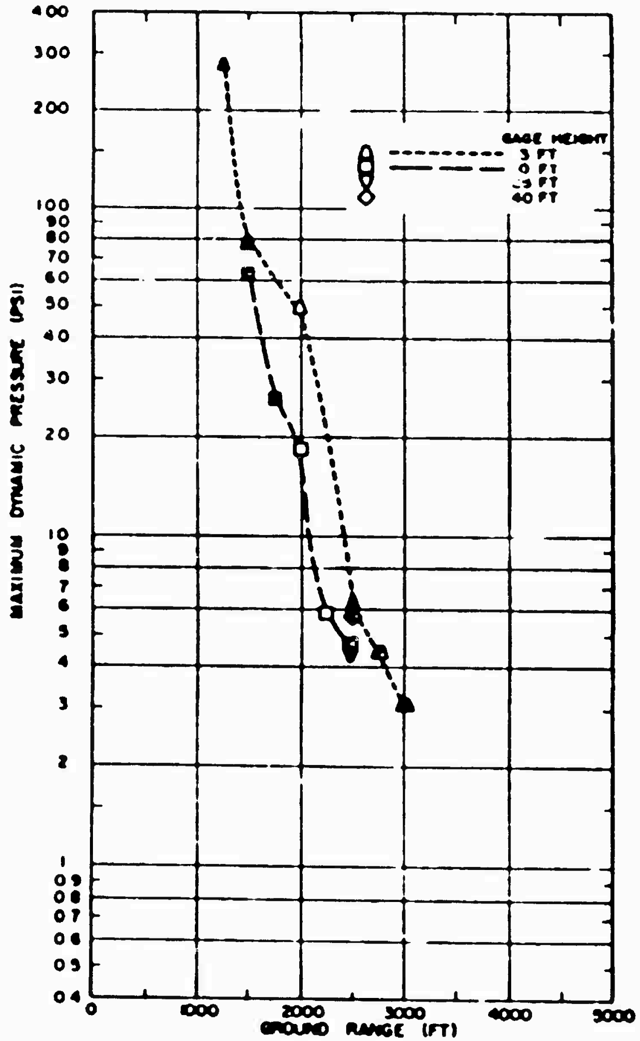

Figure 5.28 Maximum q* pitot) pressure versus ground range, water line, Shot 12.

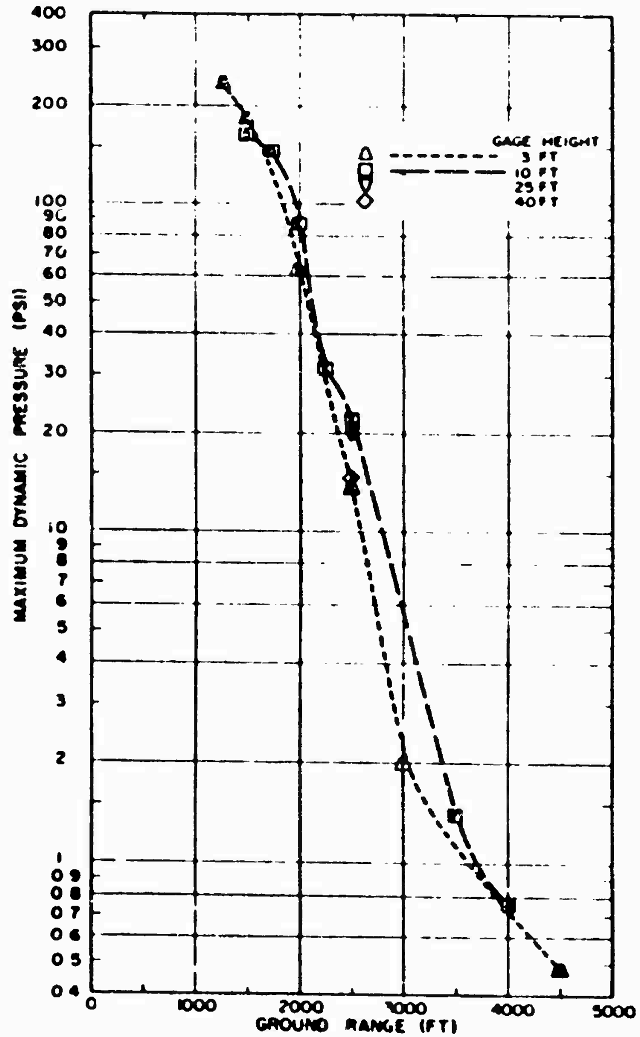

Figure 5.29 Maximum q* (pitot) pressure versus ground range, desert line, Shot 12.

on a firmer quantitative basis and to aid in the prediction of the blast behavior of nuclear weapons (at low burst heights) over surfaces other than those characteristic of desert areas.

The blast disturbances observed on previous test series have been explained in part, qualitatively, by the hypothesis that the thermal radiation creates a heated layer of air adjacent to the ground surface prior to shock arrival at the point of observation. Analytical considerations and some supporting shock-tube experiments indicate that a conventional shock wave is markedly influenced by passage into a region having a nonuniform temperatur. or, more particularly, a nonuniform sonic velocity.

To date there has been no adequate description of the effective mechanism of heat transfer responsible for the generation of the assumed thermal layer. Experimental measurements on previous nuclear tests and additional measurements on Teapot were designed for the purpose of investigating the properties of the thermal layer prior to shock arrival. Such measurements were only moderately successful; general instrumentation problems, plus turbulence and atmospheric instability effects characteristic of the heated region being investigated, have reduced the value of these measurements in a quantitative sense. Therefore, although measurements have proven the existence of a preshock thermal distrubance near the ground, details concerning temepratures, temperature gradients, and height of effective layer at shock arrival have been inconclusive.

5.4.2 Measured and Computed Preshock Temperature. A sizable fraction of the total energy released from a nuclear detonation is emitted in the form of thermal radiation. Large amounts of thermal radiation are incident upon the ground before shock arrival, and thus, the existence of a near-surface thermal layer appears to be a sound assumption. Actual measurements of preshock air temperatures (Project 8.4) and preshock sonic velocities (Project 1.5) on Teapot Shot 12 appear to be incompatible; in addition, neither set of these data appears to describe adequately the preshock thermal picture in an understandable manner.

If a near-surface thermal layer is assumed prior to shock arrival, it is possible to set up analytical relationships which can be used to deduce the general characteristic of the thermal layer from the observed blast behavior. Temperatures computed in this manner are, at best, gross averages and apply only to conditions which exist just prior to shock arrival at the range in question. The relationships based upon blast parameters can be divided into three main classifications: (1) those using shock wave equations, measured initial overpressures, and some average wave-front orientation angle (called pressure calculation); (2) those using the assumption that wave propagation velocity equals the sonic velocity characteristic of the medium (called sonic calculation); and (3) those using only angles of shock-wave-front orientation (called angle-of-front calculation). These three methods of approach will be discussed in order.

Pressure Calculation. With a shock front moving through a medium of constant γ (ratio of specific heats), analysis yields:

$$\frac{p_2}{p_1} = \frac{2\gamma}{\gamma + 1}\left[\left(\frac{v \sin \theta}{C_1}\right)^2 - 1\right] \qquad (5.4)$$

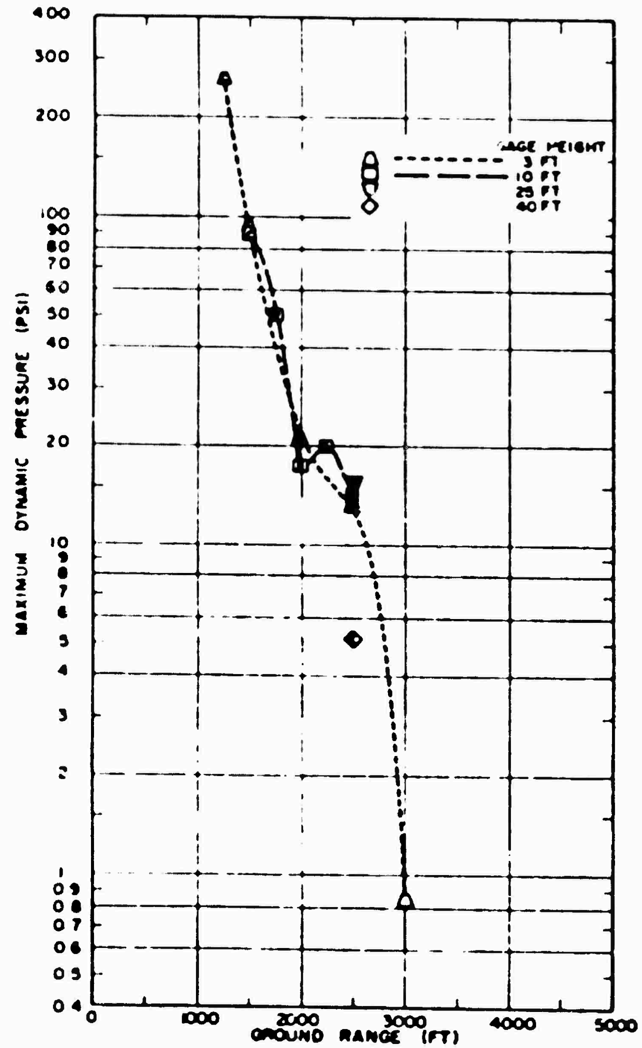

Figure 5.30 Maximum q* (pitot) pressure versus ground range, asphalt line, Shot 12.

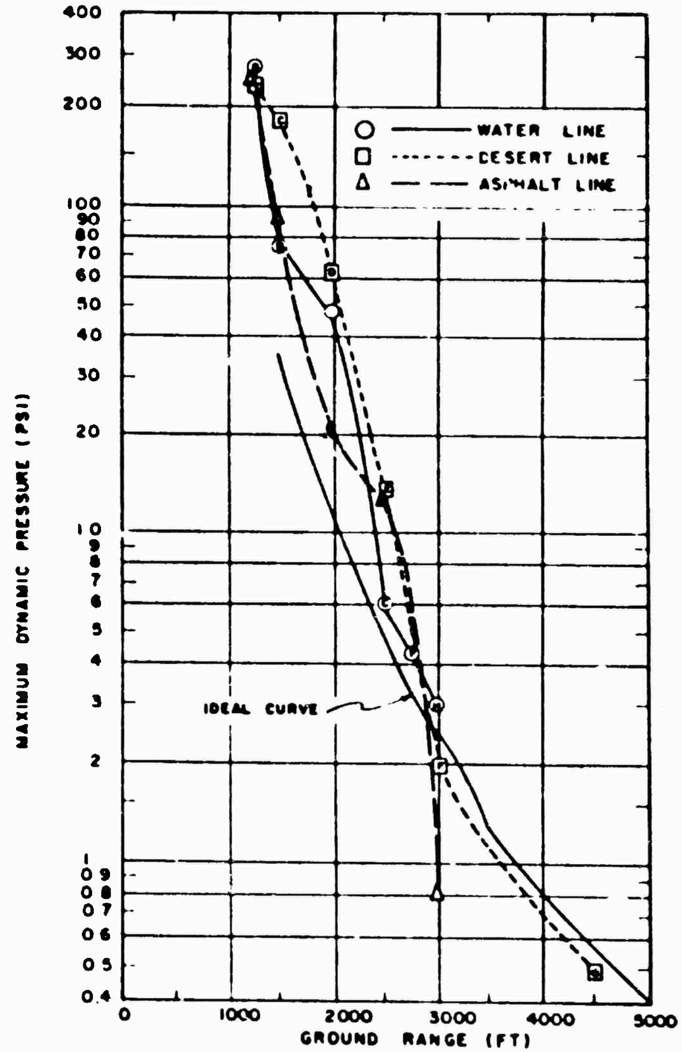

Figure 5.31 Maximum q* (pitot) pressure versus ground range, 3-foot level, Shot 12.

Where: p_2 = initial overpressure behind the shock front
v = horizontal trace velocity of the front
θ = acute angle which the shock front makes with the ground surface
C_1 = sonic velocity and pressure of the medium just ahead of the shock front (see Figure 5.40)
p_1 = sonic velocity and pressure of the medium just ahead of the shock front (see Figure 5.40)

From the measured overpressures and the photographic data (Reference 15) showing the orientations of the shock fronts, Equation 5.4 may be used to compute C_1. Then the preshock temperature T_1 is related to C_1 by:

$$\left(\frac{C_1}{C}\right)^2 = \frac{T_1}{T} \tag{5.5}$$

Where: C = sonic velocity corresponding to ambient atmospheric conditions
T = absolute temperature corresponding to ambient atmospheric conditions

This method may be extended somewhat to incorporate the assumption that at the ground plane the flow must be parallel to the surface, i. e. $\theta = 90°$. Then, for surface-level temperature calculations, Equation 5.4 reduces to:

$$\frac{p_2}{p_1} = \frac{2\gamma}{\gamma + 1}\left[\left(\frac{v}{C_1}\right)^2 - 1\right] \tag{5.6}$$

If an error analysis is made on Equation 5.4, it is concluded that for overpressures up to about 30 psi, errors in the computed C_1 are not very sensitive to errors in p_2; however, errors in the computed p_2 are quite sensitive to errors in C, v, and θ, if θ is small.

Sonic Calculation. This method is based upon the existence of a compression-type acoustic wave. If this condition is fulfilled, the propagation velocity of the initial disturbance (pressure) equals the sonic velocity of the medium, and Equation 5.5 is immediately applicable for the temperature calculation. Hence:

$$\left(\frac{v \sin \theta}{C}\right)^2 = \frac{T_1}{T} \tag{5.7}$$

$$\left(\frac{v}{C}\right)^2 = \frac{T_1}{T} \tag{5.8}$$

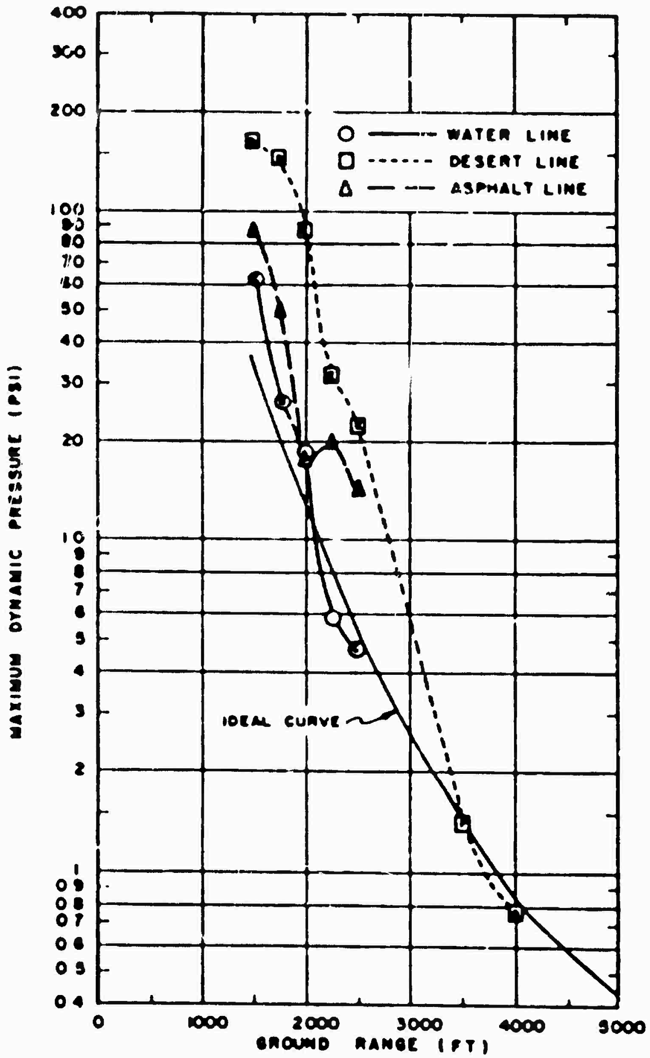

Figure 5.32 Maximum q* (pitot) pressure versus ground range, 10-foot level, Shot 12.

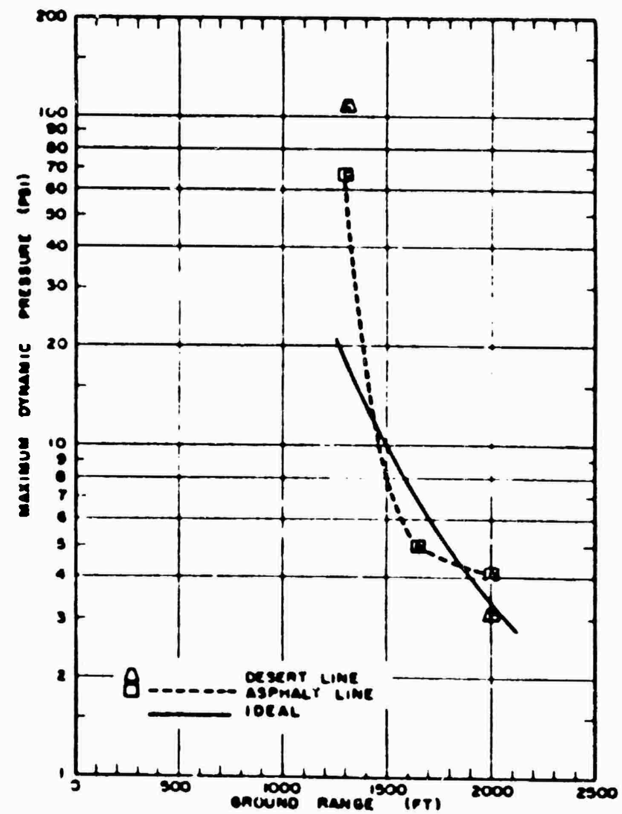

Figure 5.33 Maximum q* (pitot) pressure versus ground range, Shot 6.

This calculation (which assumes the wave propagation velocity to be the same as the sonic velocity) if applied erroneously to a shock wave would yield temperatures much larger than those computed from the pressure-calculation or angle-of-front methods.

Angle of Front. The assumptions inherent in this method of temperature computations are, in the shock wave region: (1) γ is constant; (2) the precursor front is a shock front which obeys Rankine-Hugoniot relations; (3) the peak pressure is everywhere constant along the shock front; and (4) the precursor front moves along with constant shape; i. e., every part of the front moves at the same horizontal velocity. On the basis of application of the method to a compressional wave front (the acoustic case), only assumptions (1) and (4) are necessary. Referring to Figure 5.41, Equation 5.4 can be written for conditions at the two points of interest in the shock region.

Region A:

$$\frac{p_A}{p_1} = \frac{2\gamma_A}{\gamma_A + 1}\left[\left(\frac{v_A}{C_A}\right)^2 - 1\right] \qquad (5.9)$$

Region B:

$$\frac{p_B}{p_1} = \frac{2\gamma_B}{\gamma_B + 1}\left[\left(\frac{v_B}{C_B}\right)^2 - 1\right] \qquad (5.10)$$

Where: C_A, C_B = sonic velocities ahead of the shock at points A and B.

If $\gamma_A = \gamma_B$ and $p_A = p_B$ (see assumptions above), then:

$$\frac{v_A}{C_A} = \frac{v_B}{C_B} \qquad (5.11)$$

And, if all points on the wave travel forward at the same horizontal velocity v then:

$$v = \frac{v_A}{\sin\theta_A} = \frac{v_B}{\sin\theta_B} \qquad (5.12)$$

Equations 5.9 and 5.10 reduce to:

$$\frac{C_A}{\sin\theta_A} = \frac{C_B}{\sin\theta_B}, \qquad C_B = \frac{\sin\theta_B}{\sin\theta_A}\,C_A \qquad (5.13)$$

If it is assumed that close to the ground surface and within the thermal layer the shock front is perpendicular to the ground plane (Figure 5.41), then (Reference 7):

$$\frac{v}{\sin\phi} = v_1, \qquad \frac{v}{v_1} = \frac{C}{C_1} = \sin\phi \qquad (5.14)$$

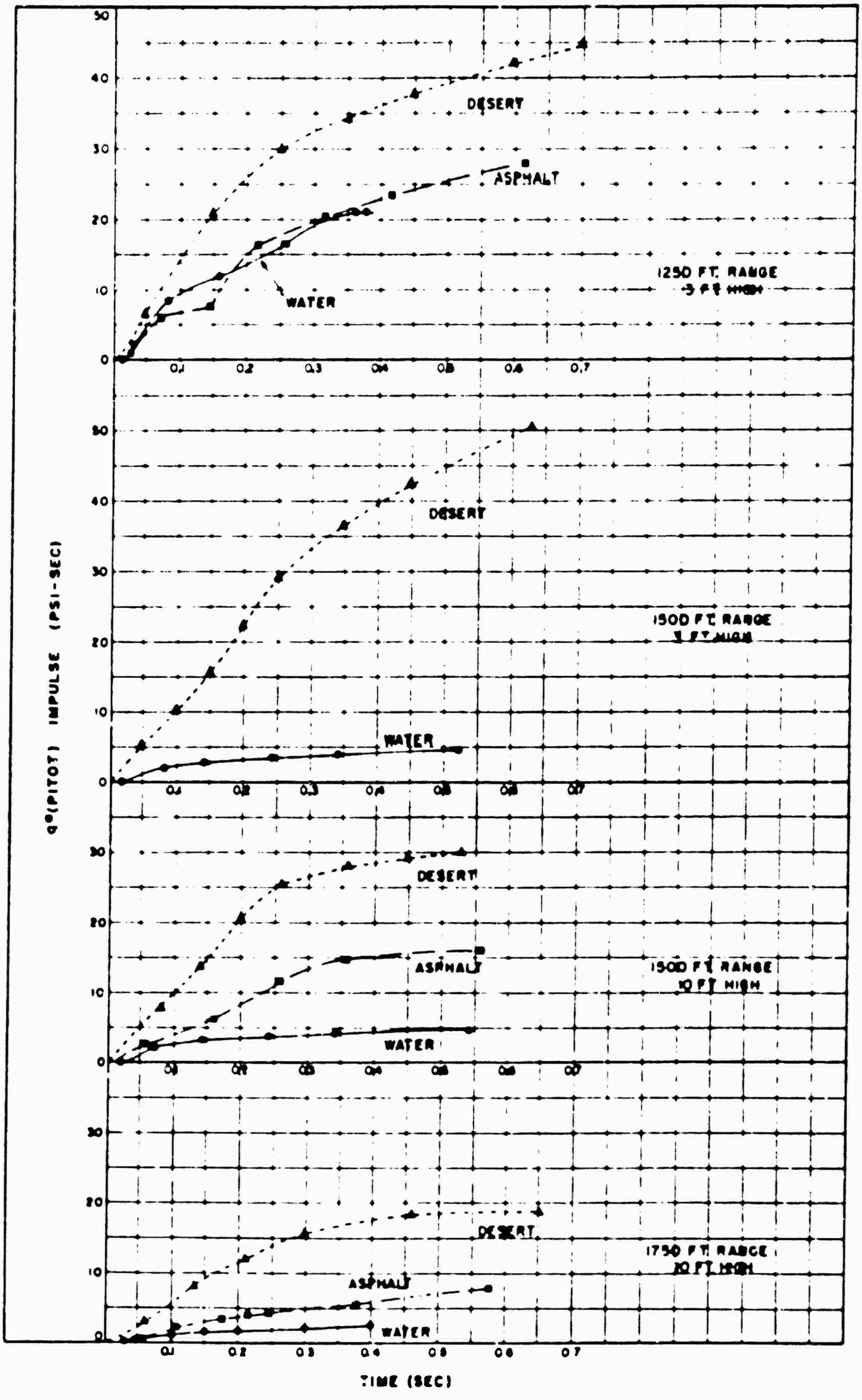

Figure 5.34 q*(pitot) impulse versus time, 1,250 feet–1,50^ feet–1,750 feet, Shot 12.

This last equation was used when, on the shock photographs, a portion of the precursor wave front was obscured by dust near the ground surface. It is obvious that Equation 5.14 will yield higher preshock sonic velocities (and temperatures) than will Equation 5.13. Equation 5.13 applies if the wave is continuously a shock front from A to B or (directly from Equation 5.7) a compression wave from A to B. If the wave front is a compression wave near the ground and a shock wave at higher elevations, as is sometimes the case, Equation 5.13 is in error. If the shock wave merges sharply with the compression wave at E, then the propagation velocity v_E^+ slightly above E (in the shock region) will be greater than the propagation velocity v_E^- slightly below E (in compression region) due to the overpressure; i.e.:

$$[v_E^- = C_E] < v_E^+ \qquad (5.15)$$

If the horizontal propagation velocity remains a constant on both sides of E (which it obviously must) then the wave front must contain a cusp, since:

$$v = \frac{v_E^-}{\sin\theta_E^-} = \frac{v_E^+}{\sin\theta_E^+} \qquad (5.16)$$

And hence, using Equation 5.15:

$$\theta_E^- < \theta_E^+ \qquad (5.17)$$

In the compression region of Figure 5.41:

$$v = \frac{v_D}{\sin\theta_D} = \frac{v_E^-}{\sin\theta_E^-} = \frac{C_D}{\sin\theta_D} = \frac{C_E}{\sin\theta_E^-} \qquad (5.18)$$

In the shock region from Equation 5.13:

$$\frac{C_A}{\sin\theta_A} = \frac{C_B}{\sin\theta_B} = \frac{C_E}{\sin\theta_E^+} \qquad (5.19)$$

And hence from Equation 5.17:

$$\left[\frac{C_A}{\sin\theta_A} = \frac{C_E}{\sin\theta_E^+}\right] < \left[\frac{C_E}{\sin\theta_E^-} = \frac{C_D}{\sin\theta_D}\right] \qquad (5.20)$$

Or:

$$\frac{C_A}{\sin\theta_A}\sin\theta_D < C_D \qquad (5.21)$$

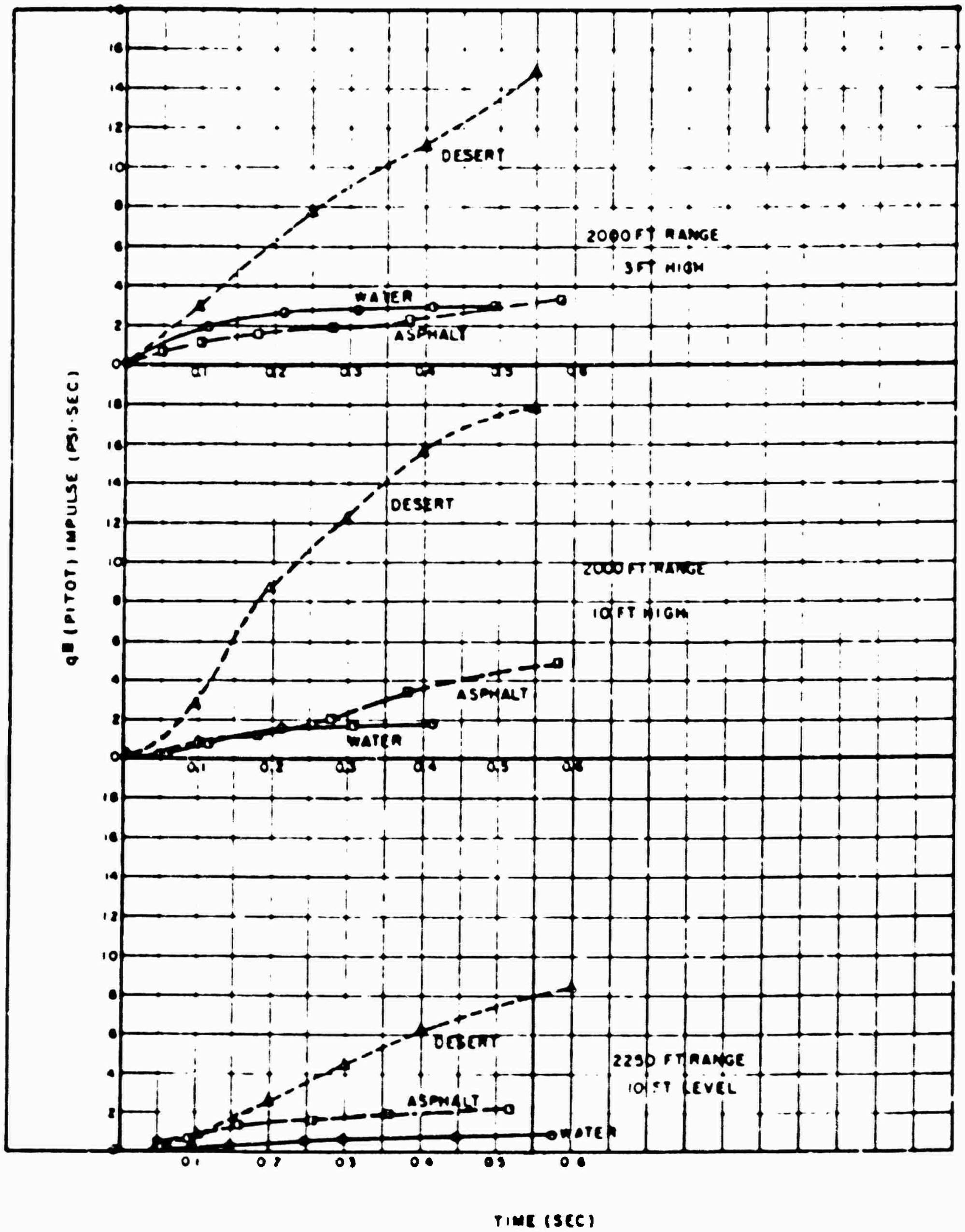

Figure 5.35 q*(pitot) impulse versus time, 2,000 feet – 2,250 feet – Shot 12.

Thus the computed sonic velocity using Equation 5.13 will be less than the actual sonic velocity whenever point A is in a shock region and point D is in a compression region. This error is proportional to the over-velocity caused by peak overpressure and hence the inequality of Equation 5.21 increases with overpressure.

Now that the main elements and limitations of the three methods have been established, the temperature calculations from Shot 12 data may be analyzed critically. Tables 5.3, 5.4, and 5.5 present the results of the computed temperatures along the three Shot 12 blast lines. In each table, the source of data for the temperature calculation is given in the appropriate column heading. In Tables 5.3 and 5.4, the column headed Equation 5.4 contains several temperature values in parentheses—it was sometimes difficult to choose a single unambiguous maximum pressure associated with the precursor wave. Occasionally, therefore, computations were carried out using the two most likely choices. The last column of each table lists what is considered as the best value of computed temperature; this choice is based upon the types of pressure-time record observed at each station; i.e., a shock-type pressure rise would suggest that the best temperature calculation is either the pressure method or the angle-of-front method, whereas a compression-type pressure-time history points to the sonic method. Naturally, the so-called transition form of record presents a problem; however, since it was stressed that the angle-of-front method was equally applicable to the shock or compression cases, it would seem that these angle-of-front temperature calculations, where available, should influence the best value choice in a transition region. In the tables, the best values in parentheses are based upon rather weak assumptions and are included only as approximate temperatures.

Figure 5.42 presents the best-value near-surface temperatures plotted against ground range for the three blast lines of Shot 12. Although the data are meager and of questionable accuracy, some general statements can be made:

1. Near-surface preshock temperatures at ground ranges between about 650 and 1,000 feet are comparable over the asphalt and desert lines.

2. The greatest discrepancy of computed preshock temperature over the desert and asphalt surfaces occurs at 1,500-foot ground range.

3. At 1,500-foot ground range, computed preshock temperature over the water surface is not significantly less than the desert-line surface temperature; however, at 2,500 feet, the value over water is severely depressed with relation to the desert data.

It may be significant that the surface preshock temperatures at close-in stations over the desert all bunch around values in the 1,500°C-region. Reference to the data handbooks (Reference 19) shows that many of the common desert-soil constituents (e.g., silicon oxide, alumina silicate, etc) possess melting temperatures in the range 1,500-2,000°C. This suggests that the chemical composition of the surface material might influence the maximum temperature rise prior to shock arrival.

One additional piece of evidence pertinent to the analysis may be obtained from a theoretical calculation of the preshock surface temperature on the desert line. The maximum temperature rise of the air at grade level during Tumbler has been shown to be correlated with the total thermal energy delivered normal to the surface divided by the square root of the time to the second thermal maximum i.e., $Q_n \div \sqrt{t_m}$ (Reference 20). Since shock arrival does not appear to correspond to the time at which the surface temperature is at maximum, the above temperatures must be corrected by the method outlined in Reference 21, Pages 16-18.

Since thermal-yield measurements were not a primary measurement on Shot 12, thermal yield and time of the second thermal maximum were determined from Reference 22. Thermal yield may be calculated as an air burst (8.5 kt) or, since the maximum

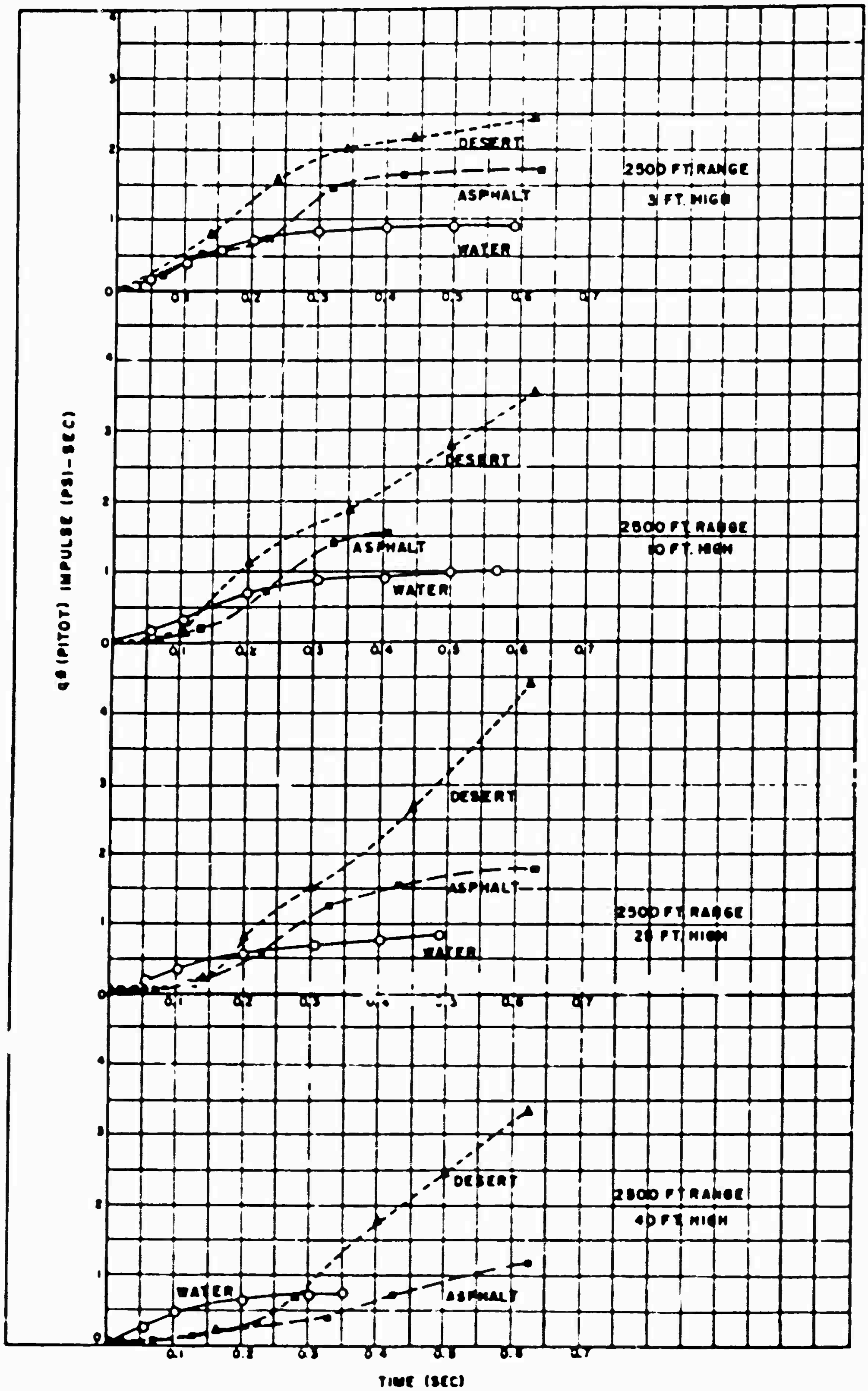

Figure 5.36 q*(pitot) impulse versus time, 2,500 feet, Shot 12.

fireball radius exceeded the height of burst, by the method of Reference 22, Page 47, (6.5 kt).

Temperatures corresponding to both these yields were computed as follows: $Q_n \div \sqrt{t_m}$ was found for each station, assuming the cosine law to hold. The maximum temperature rise was found from Figure 8 of Reference 20. From Figure 5 of Reference 21, the ratio of time of maximum temperature rise to time of thermal maximum was

TABLE 5.4 DESERT-LINE COMPUTED TEMPERATURES FOR SHOT 12

Ground Range	Arrival Time	Height	Computation Methods: Eqn. 5.4 SRI Data	Eqn 5.12 NOL Data	Eqn. 5.12 SRI Data	Eqn 5.8 SRI Data	Eqn. 5.7 SRI Data	Type of wave	Best Value
feet	sec	feet	°C	°C	°C	°C	°C		
650		0		1,180					1,180
750	0.104	0		1,365		8,700		Shock	1,365
850		0		1,811					1,811
1,000	0.140	0		1,441		6,200		Shock	1,441
1,200		0		1,084					
1,250		3	180*			4,100		Shock	(180)
1,500	0.265	0	540	971	590	2,600	1,580	Shock	540–890
		3	430				1,000	Shock	430
		10	17				315	Trans.	17–315
1,700		0		753					
1,750		10				1,430	(440)†	Trans.	(<440)
2,000	0.483	0	72	325	135	610	350	Trans.	135–350
		3	17				185	Trans.	17–185
		10	22				72	Trans.	22–72
2,250		10				260	(80)†	Trans.	(80)
2,500	0.780	0	-30(-60)		-10	96	27	Comp.	27–96
		3	0(-50)				25	Comp	25
		10	-10(-40)				30	Trans.	< 30
		25	-5(-40)				35	Trans.	< 35
		40	40(8)				98	Trans.	< 96
3,000	1.192	0	22		60	46	45	Comp	45
		3	17				40	Shock	17
		10	-30				-10	Shock	-30
3,500	1.012	0	30		90	66	78	Shock	30–90
		10	26					Shock	26
4,000		0				181		Shock	
4,500		0	-10		30	41	35	Shock	30
		3	-10					Shock	

* Used NOL wave front angle data.

† Used same wave front angle as observed at nearest gage station.

found to equal 2.4.[1] Using the observed time of arrival, the ratio of time of arrival to time of maximum temperature was computed. Then using Figure 3 of Reference 21, the temperature ratios may be found and the temperature at shock arrival computed. These results are shown in the table below. Temperatures at stations closer than 2,000 feet are not tabulated due to the tenuous nature of the calculation in these regions. Note that the values in the table are larger than those given by the shock-wave calculation.

[1] Operation Tumbler data yield $\alpha / \sqrt{KSC} \leq 33$. Estimated values are $\alpha = 0.7$, $\epsilon = 0.5$ so that $\epsilon\sqrt{t_m} / \sqrt{KSC} \leq 10$.

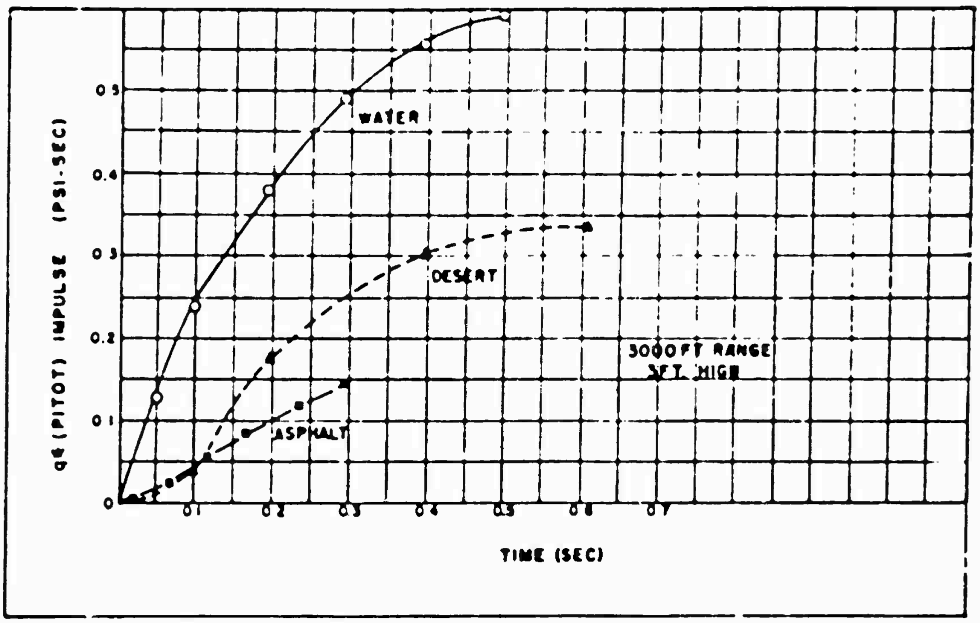

Figure 5.37 q*(pitot) impulse versus time, 3,000 feet, Shot 12.

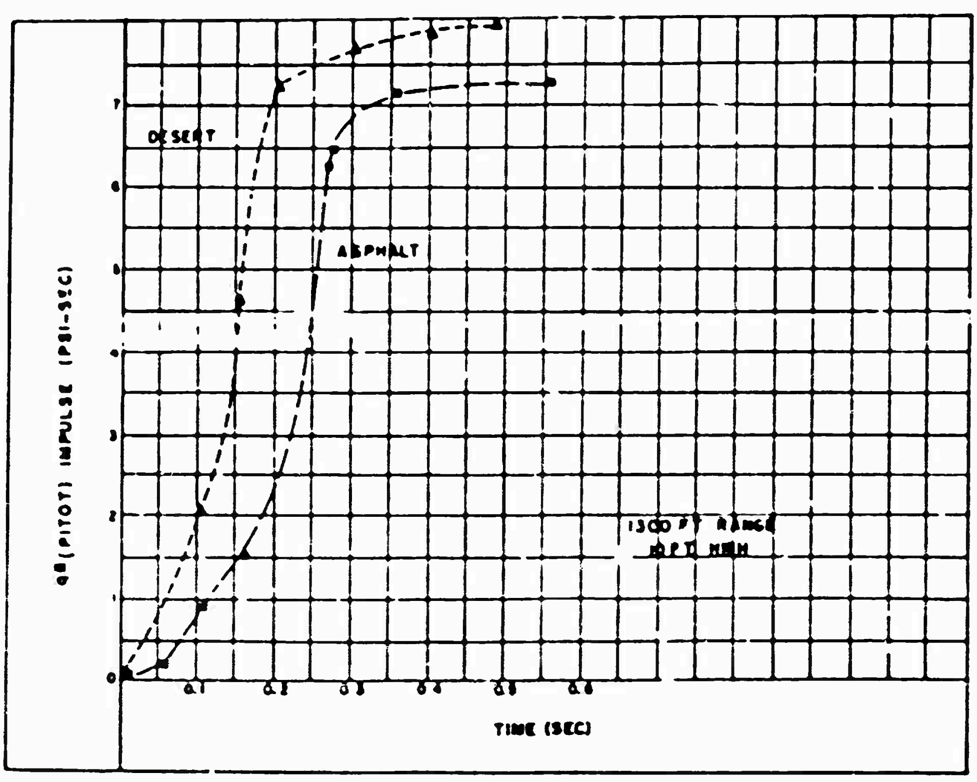

Figure 5.38 q*(pitot) impulse versus time, 1,300 feet, Shot 6.

Ground Range	Surface Temperature, Desert Line	
	Thermal Yield 8.5 kt	Thermal Yield 6.5 kt
feet	°C	°C
2,000	1,300	825
2,500	445	200
3,000	100	75
4,000	40	30

Since the computed temperature is determined on the basis of conditions obtaining at shock arrival, it is obvious that the computations over the different blast lines, although they refer to the same ground range, correspond to different absolute times. Therefore, a legitimate criticism of the Figure 5.42 presentation of temperatures is that at the same ground range, temperatures over asphalt are determined at times significantly earlier than those computed over the desert. So, to complete the analysis, Figure 5.43 presents the computed temperatures as a function of arrival time for Shot 12. This presentation indicates a rather consistent behavior over the three blast-line surfaces — it is possible to draw a single average curve which agrees well with the derived temperature data. The general form of this curve is a flat maximum out to about 0.2 second, followed by a sharp drop in temperature to about 0.5 second, and then a slower decline out to approximately ambient values at 1.6 second. It is noteworthy that on the time plot of Figure 5.43 the asphalt data near 2,000°C and the water temperature near 400°C appear quite compatible with the remaining results — only at later arrival times do the water line preshock temperatures fall well below the average curve.

To conclude, it can be stated that a careful analysis of airblast data will yield some useful information concerning preshock temperatures near the ground surface. It would be desirable in future operations to obtain more complete data from which to compute wave-front orientations, in addition to the more conventional pressure-time documentation.

5.4.3 Precursor Development. Although much attention has been directed toward the study of the precursor wave, its formation and development, the origin and mechanisms responsible for this phenomenon have not been clearly explained. Some questions which are as yet unanswered are: Can the heated-layer theory predict the formation and development of the precursor wave from a particular weapon detonated over a particular surface? Does the heated layer concept exclude the existence of a so-called thermal-shock wave? What is the origin of the precursor wave? How do precursor phenomena scale? Are there meaningful correlations in the detailed results obtained on precursor-producing nuclear weapon tests? These questions will be considered briefly in the discussion which follows.

Considering first the nuclear explosion as a source of thermal radiation, it is pertinent to investigate the dynamic effects produced in a medium as a result of heat release in the medium (Reference 23). (Reference 24 deals with the problem of pressure waves generated by addition of heat in a gaseous medium and obtains the exact solution of an idealized problem in which a finite amount of heat is released uniformly at a section of a tube with a given rate; from this solution, strength of the

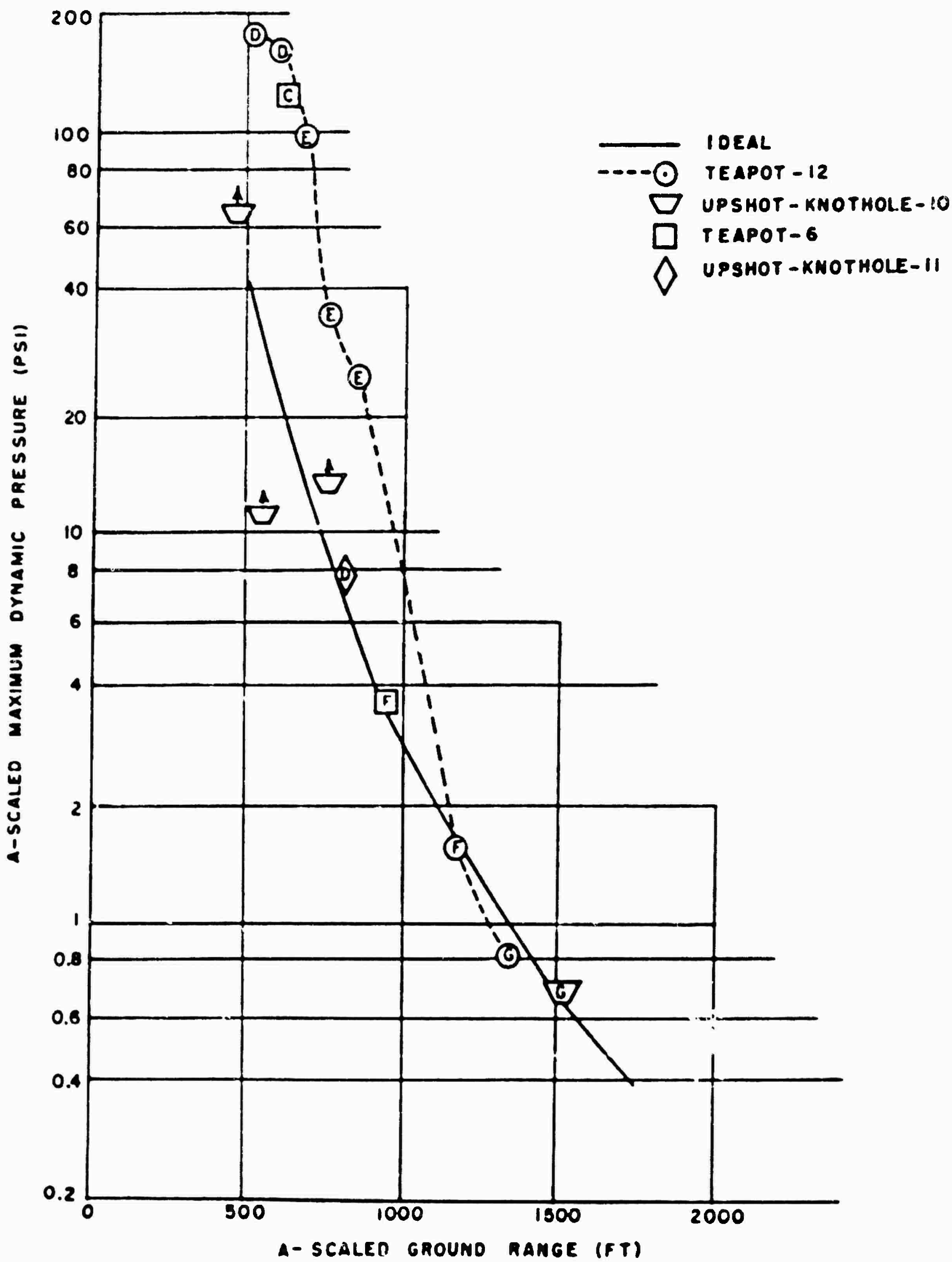

Figure 5.39 A-scaled maximum q*(pitot) pressure, 10-foot level, Teapot Shots 6 and 12, previous shots.

shock generated is computed. The basic mechanism by which pressure waves are produced by heat addition is that when heat is added to a volume of gas, the density of the gas is in general reduced. This causes an expansion of the volume occupied by the heated gas, which expansion produces the pressure waves.

In seeking the exact solution to the two-dimensional problem, Reference 24 characterizes the undisturbed medium by two thermodynamic parameters, the pressure p and temperature T. Since the velocity of sound a in the undisturbed medium is uniquely related to the temperature T, p and a may be used as the two parameters characterizing the undisturbed medium. The strength of the shock wave can be described in terms of the pressure ratio p_2/p_1 across the shock, where p_2 is the pressure immediately behind the shock. It is clear that, in general, the strength of the shock depends upon the rate of heat release per unit area S, the state of the undisturbed medium being characterized by p and a as well as by the time t. That is:

$$\frac{p_2}{p_1} = F(S, a, p, t) \qquad (5.22)$$

The viscous and heat-conductive effects have been neglected in Equation 5.22. Because of dimensional considerations it is necessary to write the above relation as:

$$\frac{p_2}{p_1} = F_1\left(\frac{S}{ap}\right) \qquad (5.23)$$

That is, the shock strength must be independent of the explicit time t, which is actually a direct consequence of the fact that there is neither a characteristic time nor a relevant characteristic length in the problem. The derivation yields:

$$\frac{S}{ap} = \frac{2}{\gamma - 1}\frac{p_2}{p_1}\left(\frac{p_2}{p_1} - 1\right)\left[\left(\frac{\gamma + 1}{2\gamma}\right)\frac{p_2}{p_1} + \frac{\gamma - 1}{2\gamma}\right]^{-1/2} \qquad (5.24)$$

The tabulation below lists values of S/ap computed for selected p_2/p_1 ratios. Also, shown in the tabulation are the corresponding overpressures $p = p_1 + p_2$ and S quantities; the latter are determined on the basis of a = 1,100 fps and p_1 = 14.7 psi. The heat delivery rate for substantial pressures is not extraordinarily large when compared with thermal energies delivered by nuclear explosions.

p_2/p_1	S/ap	p	S
		psi	cal/cm² sec
2	7.3	14.7	42
4	31.8	44	180
6	65.2	74	370
8	105.7	103	600
10	152.5	132	870

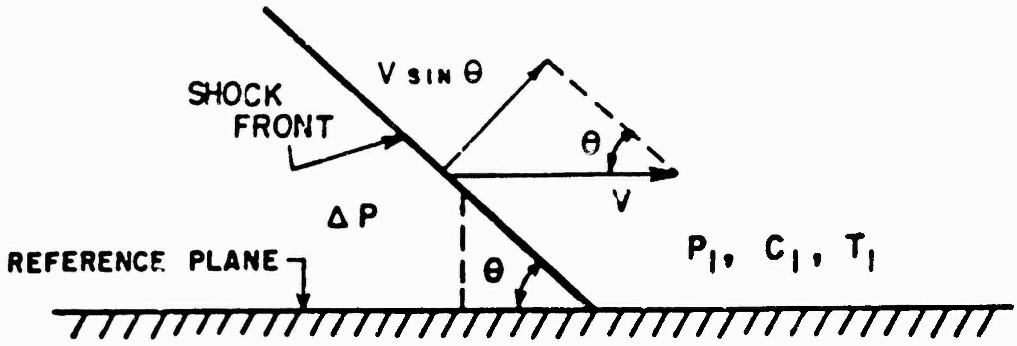

Figure 5.40 Shock front diagram for pressure calculation of preshock temperature.

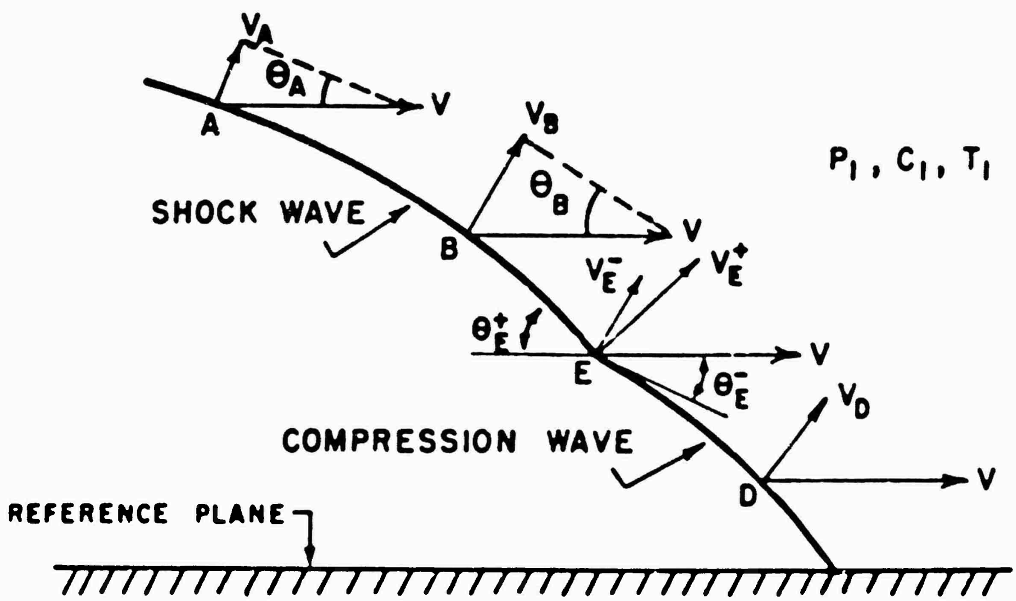

Figure 5.41 Wave front diagram for angle-of-front calculation of preshock temperature.

With this analysis in mind, it is possible to hypothesize concerning the observed propagation velocities of precursor-forming shots. Consider the four ground-range regions shown on Figure 5.44. In each region it is postulated that the velocity of the initial disturbance is governed by different conditions. Now suppose that a pressure wave may be created by addition of heat to the air near the ground (as described in Reference 24) and that there is a threshold criterion which is related to the delivery of thermal energy to the ground. Then, by virtue of the inverse square law for radiation and the time dependency of radiant flux, the threshold will be surpassed at different ground ranges at various times. That is, time of arrival and a velocity can be assigned to the threshold condition and hence to the generated pressure wave. The velocity of this thermal pressure wave, v_d, as a function of ground range will be markedly influenced by the choice of the threshold criterion. However, the mechanism by which the thermal flux is related to the pressure wave is of no matter; all that is necessary is to postulate the existence of such a phenomenon.

TABLE 5.8 ASPHALT-LINE COMPUTED TEMPERATURES FOR SHOT 12

			Computation Methods						
Ground Range	Arrival Time	Height	Eqn 5.4 SRI Data	Eqn. 5.13 NOL Data	Eqn. 5.12 SRI Data	Eqn. 5.8 SRI Data	Eqn. 5.7 SRI Data	Type of Wave	Best Value
feet	sec	feet	°C	°C	°C	°C	°C		
650		0		1,643					1,643
750	0.093	0		1,537		10,800		Shock	1,537
850		0		1,498					1,498
1,000	0.134	0		1,643		6,950		Shock	1,643
1,200		0		1,498					
1,250		3	220*			4,900		Shock	(220)
1,500	0.241	0	1,150	1,206	1,500	3,650	2,230	Trans.	1,150 – 2,230
		3	560				1,130	Shock	560
		10	-120				100	Shock	
1,700		0		933					
1,750	0.324	0				1,550	(640)†	Trans.	(< 640)
2,000	0.418	0	106		75	950	395	Trans.	106 – 395
		3	95				370	Trans.	95 – 370
		10	45				225	Trans.	45 – 225
2,250		10				600	(94)†	Trans.	(< 94)
2,500	0.674	0	-10(-30)		60	350	55	Comp.	55
		3	0(-28)				75	Comp.	75
		10	-50(-65)				5	Comp.	5
		25	(-28				25	Trans.	-28 – 25
		60	45				175	Shock	45
2,750		0				300	(35)†	Comp.	(35)
3,000	1.034	0	30		30	100	75	Comp.	30 – 70
		3	15					Comp.	

* Used NOL wave front angle data.

† Used same wave front angle as observed at nearest gage station.

Referring to Figure 5.44 and Region I, suppose the velocity of the incident wave along the ground (or that of a Mach shock), v_i, is initially greater than v_d. This condition will undoubtedly be satisfied at some weapon burst height, since $v_i \rightarrow \infty$ at ground zero (G = 0) and there is some time lag before an appreciable amount of thermal energy is delivered to the medium near ground zero. If $v_i > v_d$ at G = 0, then the incident wave will outrun the thermal disturbance until the arrival times are equal; hence in Region I,

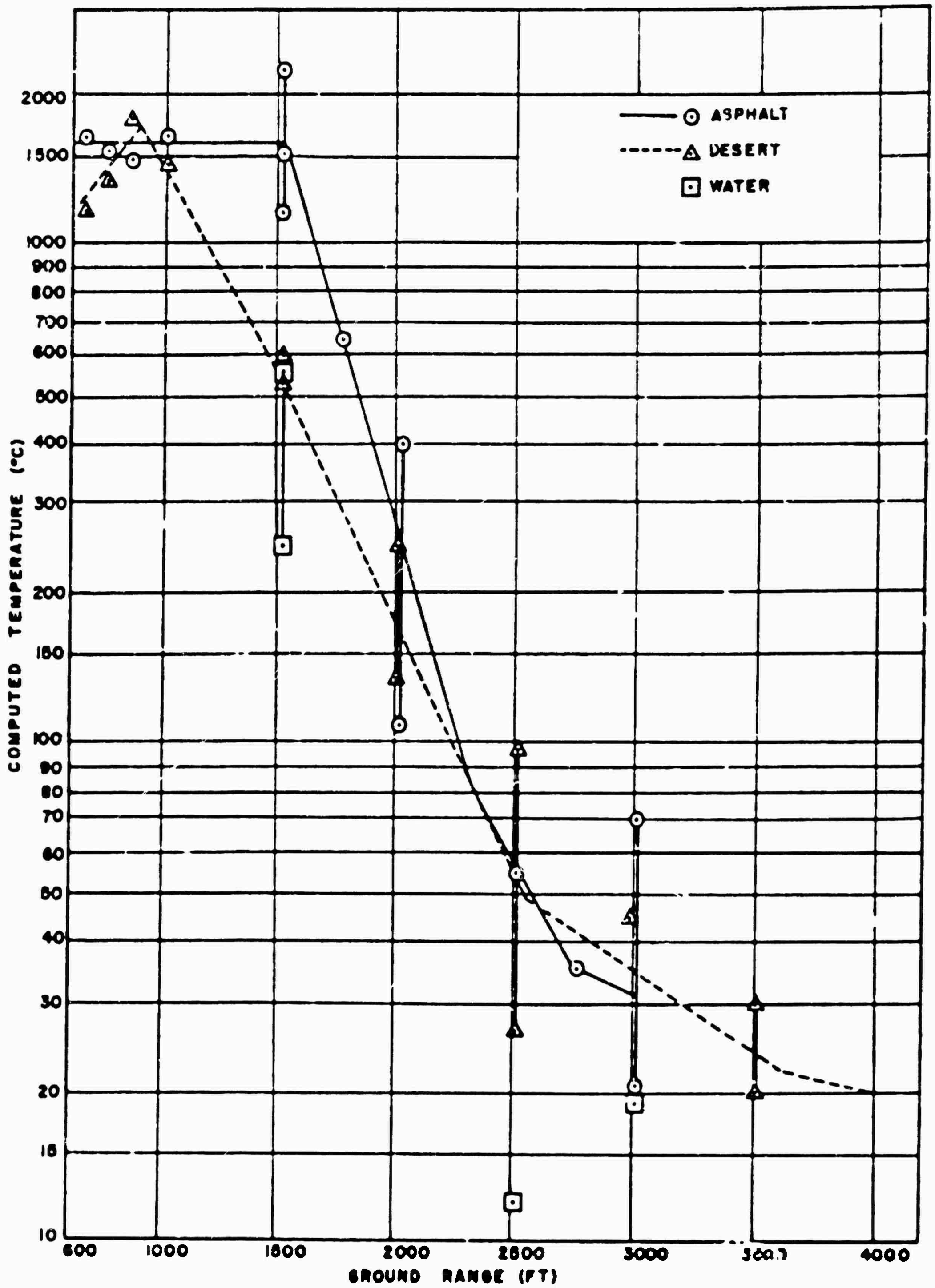

Figure 5.42 Computed preshock temperature versus ground range, Shot 12.

$v = v_i$. For the thermal disturbance to catch up, v_i must drop below v_d at some range. The existence of Region II depends on a subtle relationship between yield, height-of-burst, surface properties, and the mechanism of the generation of the thermal pressure wave. For instance, if the height-of-burst is too high, v_i may never become less than v_d and a thermal pressure wave would not be observed in Region II.

In Region II (Figure 5.44), $v_d > v_i$ (incident or Mach stem velocity, as the case may be) and $v = v_d$. Also, in this region the thermal pressure wave is a shock wave; however, the pressure–time records now show a precursor because the disturbance is traveling faster than the horizontal component of the incident wave velocity. The precursor wave-front angle or angles adjust themselves to maintain the proper geometrical relationships between local sonic and wave velocities. The apparent discontinuity in the velocity curve at the range separating Regions I and II may be resolved by showing a hypothetical arrival-time–distance plot over the same region. Figure 5.45 indicates how reasonable arrival-time data could result in very abrupt velocity variations.

Returning to Figure 5.44, it is apparent that in Region II the sonic velocity ahead of the wave is increasing steadily as more heat is added to the medium. When $v \rightarrow C$, the wave spills out in the usual manner under these conditions, and the shock front degenerates into a compression wave. The toe of the compression wave (near ground surface) now propagates with sonic velocity (Region III) until the compression wave inevitably shocks up and $v > C$ due to overpressure (Region IV). The tabulation below summarizes the four regions of interest:

Region	Wave Forms	Propagation Velocity	Precursor
I	shock-type	High ($v >> C_1$)	No
II	shock-type	High	Yes
III	compression-type	$v = C_1$	Yes
IV	shock-type	$v = f(p)$	No

Now that the hypothesis has explained some of the details of the precursor velocity picture, it would be profitable to attempt to determine how the phenomena may scale, i.e., to determine if the data from various tests fall into any consistent pattern or system.

5.4.4 <u>Precursor Arrival-Time and Velocity Characteristics</u>. If arrival-time data are plotted versus slant range on logarithmic coordinates, as in Figures 5.46 and 5.47, some details of behavior are revealed which are not apparent in Figure 5.1. The precursor arrival data were taken from Project 1.10 pressure–time results and the NOL photography near the ground surface. The incident wave and ideal arrival curves were constructed as previously explained. Evident in Figures 5.46 and 5.47 is the fact that the initial slope, corresponding to the incident wave arrivals, is only slightly less than 5/2 whereas the precursor data indicate a consistent 3/2 slope in the initial portions. Although Teapot Shot 12 data are not sufficient close to the point of precursor formation to justify extrapolation of arrival times in this direction, critical examination of other precursor-forming shots, particularly Tumbler Shot 4, Upshot–Knothole Shot 10 and Buster Shot Charlie, confirm the fact that initial 3/2 slope is indeed quite consistent.

The intersection of the precursor curves with the incident gives a good indication

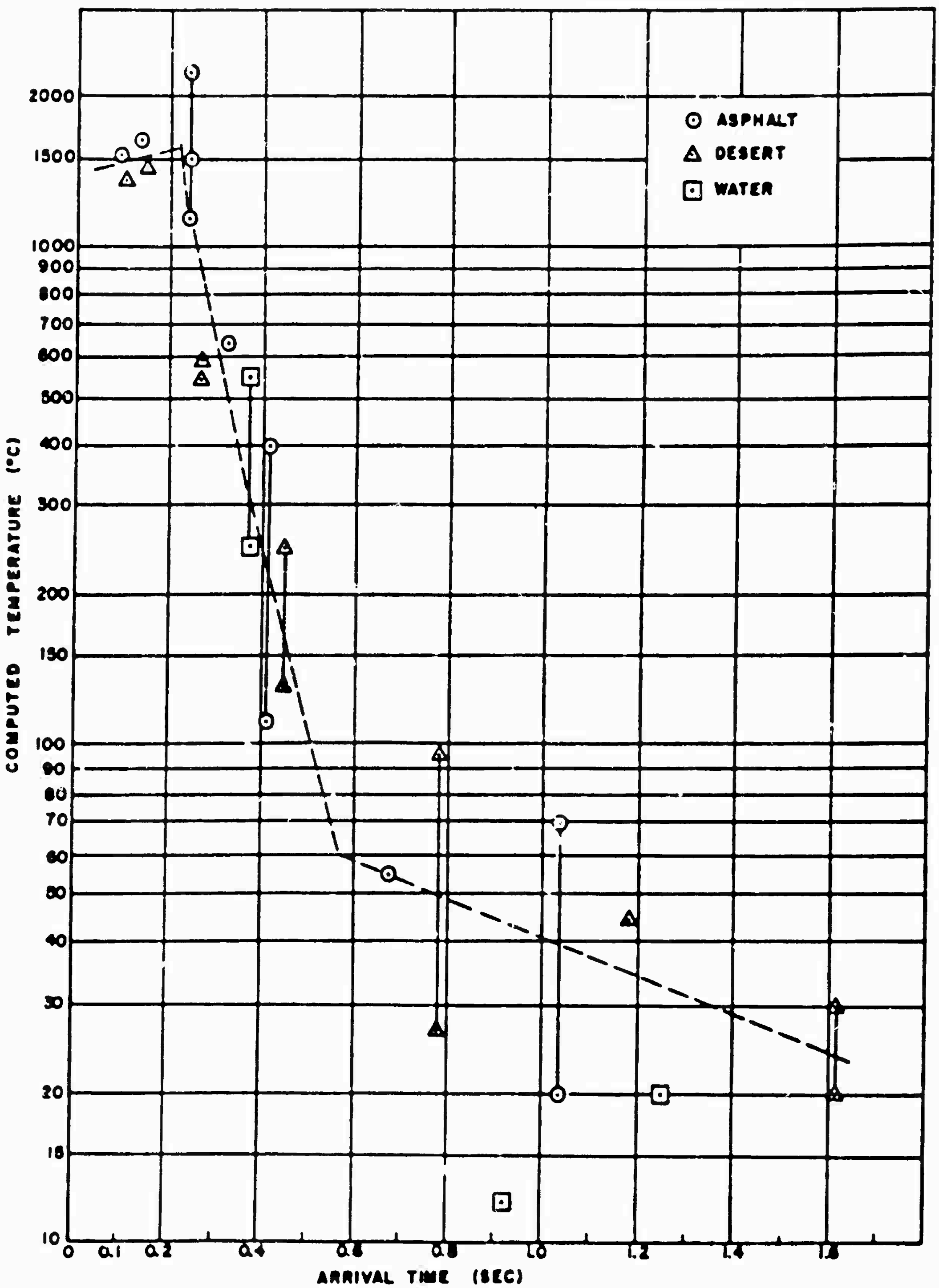

Figure 5.43 Computed preshock temperature versus arrival time, Shot 12.

of the time (or ground range) at which the precursor forms over each of the surfaces considered. In Figure 5.43, the curve corresponding to the water-line data exhibits the same 3/2 slope as observed for the desert and asphalt data; however, the water curve intersects the incident-wave curve latest (at about 710-foot ground range), and it seems to begin to deviate from the 3/2 slope near 1,000-foot range. This result would indicate that, although the effect was short-lived, a true precursor wave was formed over the water line on Teapot Shot 12. The desert and asphalt curves appear to persist along a 3/2 slope out to about 1,500-foot range.

Figure 5.47 shows only one Teapot Shot 6 curve (for asphalt) corresponding to the region of precursor formation. This is explained by reference to the Shot 6 area layout (Figure 2.1), which indicates that ground zero was located so that about 500 feet of asphalt surface was interposed between the shot tower and the desert line. Thus, the Shot 6 precursor formation picture may be considered only on the basis of an asphalt surface. It is further indicated in Figure 5.47 that the differences in surface characteristics (desert versus asphalt) become manifest over ground range distances of the order of 150 feet, e.g., the asphalt pad ends at 500 feet, and the first significant differences in times of arrival are observed at about 650 feet. The reverse situation existed on Teapot Shots 1 and 9 where about 520 feet of nonasphalted area was interposed between ground zero and the asphalt pad of the asphalt line. Initial precursor formation on these lines followed desert behavior until the asphalt pad was engulfed. Since Shot 1 arrival-time data indicate that a precursor did not form over the desert at this height of burst, the asphalt-line precursor over-velocity is more suppressed than on Shot 9, where a precursor did form over the interposed desert. These conclusions are consistent with the results described in Section 5.2.2 which dealt with the effects of localized changes in surface properties.

The similarity of the arrival-time–slant-range curves (Figures 5.46 and 5.47) suggests that a generalized relationship exists of the form:

$$t = BK\,R^{3/2}\,f(R) \qquad (5.25)$$

Where: t = the arrival time (A-scaled)

R = the slant range (A-scaled)

B = constant dependent on height of burst and/or yield,

K = a surface constant which depends on the surface characteristics, but should not change with distance over the surface

The velocity of propagation in the horizontal plane, i.e., the precursor velocity (A-scaled), is:

$$V_x = \frac{R}{G}\frac{dR}{dt} = \frac{2}{3}\frac{R^{1/2}}{G}\,\frac{1}{BK(f + Rf')} \qquad (5.26)$$

Where: G = ground range

' = differentiation with respect to R.

Multiplying each side of Equation 5.26 by t from Equation 5.25, the constants B and K are eliminated:

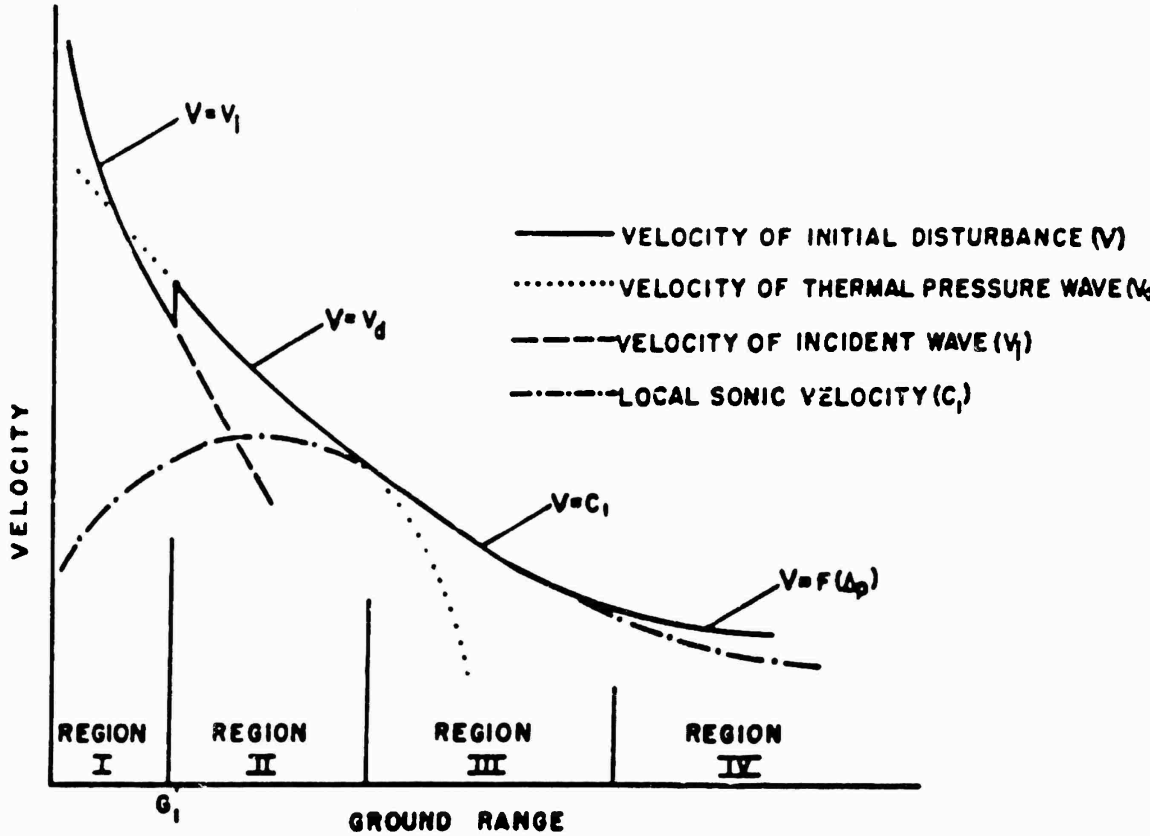

Figure 5.44 Schematic diagram of propagation velocity versus ground range.

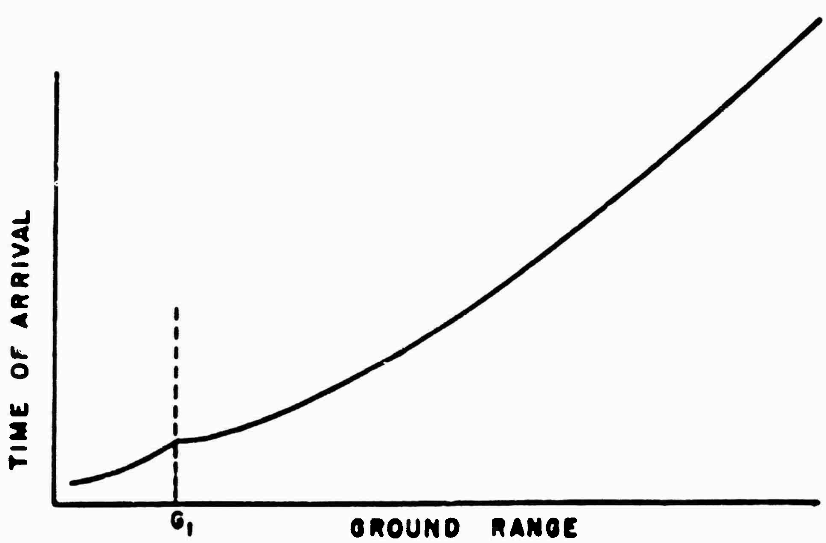

Figure 5.45 Schematic diagram of arrival time versus ground range in region of rapidly changing velocity.

$$\frac{V_x tG}{R^2} = \frac{2}{3}\,\frac{f}{(f + Rf')} - \frac{2J(R)}{3}$$

Where: J(R) = a new function of slant range.

Note the left side of Equation 5.27 is independent of scale factors.

Figure 5.48 is a plot of the quantity $V_x tG/R^2$ versus R for Teapot Shot 12; Figure 5.49 a plot for Upshot–Knothole Shots 1 and 10. For these shots, definitive time-of-arrival data are available from which accurate velocities could be determined. Reference to Figures 5.48 and 5.49 indicates that the points fall close to a single curve, as well predicted by the foregoing analysis. Decidedly different surface properties are represented in the data of Figure 5.49; Teapot Shot 12 asphalt and desert data are included, as well as data from a shot detonated over the Yucca Flat area (Upshot–Knothole Shot 1). The consistency of the velocity–distance pattern in these figures illustrates the validity of a surface-constant concept. In summary, it appears that although the surface constants of the surfaces considered here are different, the differences do not seem large.

Since Project 1.10 pressure–time data from Teapot Shot 6 are not sufficiently extensive for determination of the shock-velocity-versus-distance function, it is necessary to look elsewhere for time-of-arrival data. The NOL photographic data yield precursor arrival times over both the desert and asphalt surfaces of Shot 6. Using these data, a best-fit arrival-time curve is drawn through the points, and shock velocities are then determined employing the difference method (Reference 14) previously described (Section 5.1.1). Figure 5.50 shows Shot 6 data plotted on the same coordinates as Figure 5.48; also included on the Shot 6 plot is the curve from Figure 5.48. Even though large apparent variations in instantaneous velocity result from reduction of the photometric data, the general trends are consistent.

If the foregoing figures and analyses can be considered representative of what occurs on a precursor-forming shot, it can be concluded that pressure–time measurements on Teapot Shots 6 and 12 were not obtained at close enough range to detect the formation of the precursor wave. Based upon the formation hypothesis offered here, it is expected that if gages were installed in the region of regular reflection, the gage records would register Type 0 (classic) wave forms followed by Types 1, 2, etc., as the precursor forms and develops. It is believed that this behavior was observed on the Tumbler Shot 4 close-in pressure–time results. The NOL gage (Reference 25) closest to ground zero (Station 7-200 at 230-foot ground range) on this precursor-forming shot registered an arrival time and pressure–time history which indicated that the measurement was obtained just prior to the formation of the precursor wave. At the next gage stations (Station 7-201, about 35 feet from Station 7-200), the record was a definite Type 1 wave form with the characteristic double peak.

5.5 MEASUREMENTS ON BEAM DEVICE

The beam devices, described in Section 2.5.2 were used for another project on Upshot–Knothole and were included as part of the instrumentation of Teapot Shot 12 as a convenience in connection with Project 1.10. They were designed to yield preliminary information on the behavior of structural beams when subjected to the airblast loading. The two beams were placed at nominal ground ranges of 2,000 and 2,500 feet on the desert line, so as to be in the region of nonclassical blast waves. In the following sec-

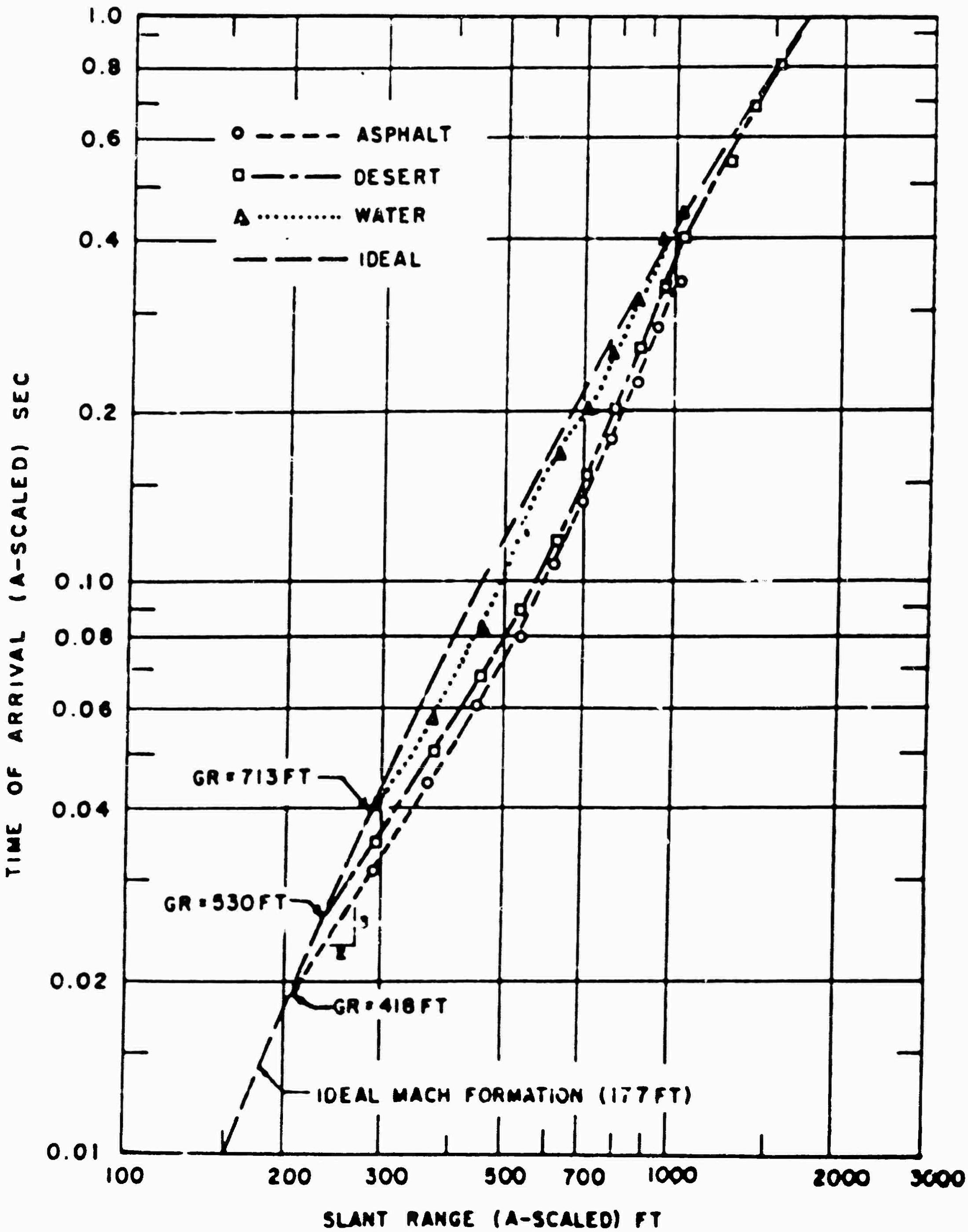

Figure 5.46 A-scaled time of arrival versus slant range, Teapot Shot 12.

tions, after a discussion of the background pertinent to these data, the beam results will be analyzed.

5.5.1 Background and Definitions. Fundamentally, so long as flow remains non-rotational, an incompressible fluid moving past a submerged body will impart no motion (i.e., force) to the body, for the resultant of the pressure distribution over the surface of any body in potential flow can never have a component in the direction of flow. Since the equations describing such motion involve only those forces caused by fluid pressure, the motion actually encountered in the case of immersed bodies is evidently due either directly or indirectly to the influence of fluid viscosity.

For flow velocities significantly less than sonic, the actual force imposed upon an immersed body will depend only upon the Reynolds number characterizing the flow and upon the geometrical form and orientation of the body. Dimensional analysis of the several variables involved will lead to the following expression for the resultant force:

$$F = \Phi\left(\frac{uL}{\eta}, \text{ form}\right) L^2 \rho u^2 \qquad (5.28)$$

Where: u = velocity
L = length
η = kinematic viscosity
ρ = density

The basic drag relationship is generally written in the more convenient form:

$$F = \Phi (R_e, \text{ form}) A \frac{\rho u^2}{2} \quad C_d \frac{A \rho u^2}{2} \qquad (5.29)$$

Where: A = the projected area of the body on a plane normal to the direction of motion

The term C_d is a variable coefficient of drag:

$$C_d = \Phi (R_e, \text{ form}) \quad \frac{2F}{A \rho u^2} \qquad (5.30)$$

Where $\frac{\rho u^2}{2}$ = the expression defining dynamic pressure.

The viscous action of flow may produce three essentially different types of drag force. At very low Reynolds numbers, inertial effects are secondary to those of viscous stress, the latter then extending a great distance into the surrounding flow; this is known as deformation drag. At much higher Reynolds numbers the region in which appreciable deformation occurs is limited to a thin fluid layer surrounding the body, the resulting shear then producing what is called surface drag. Finally, if the form of the body is such that separation occurs, the low intensity of pressure in the wake leads to a force on the immersed body; since the magnitude of this force varies with the shape of the body, it is customarily termed form drag. Under higher-velocity flow conditions

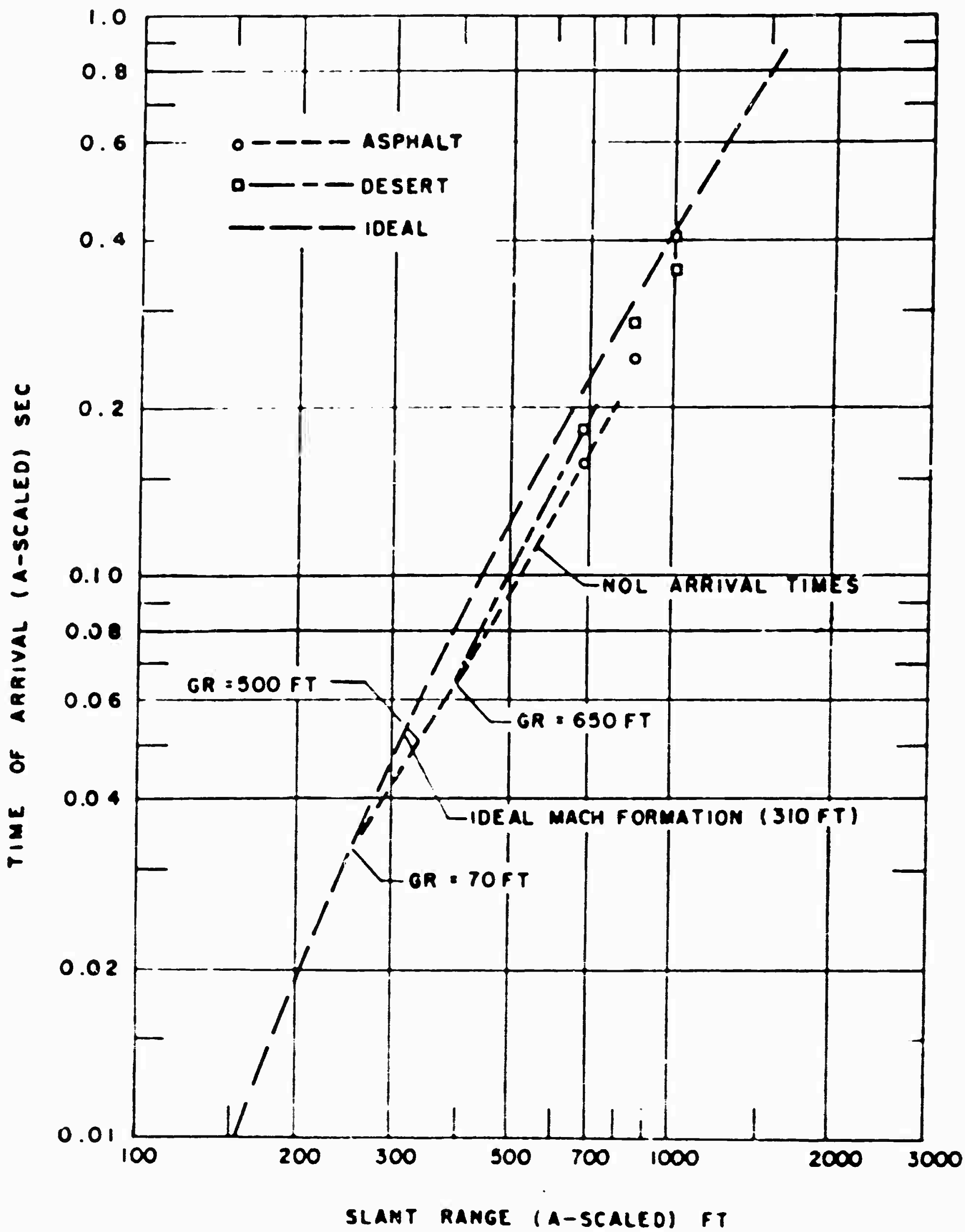

Figure 5.47 A-scaled time of arrival versus slant range, Teapot Shot 6.

(i.e., flow velocities approaching the velocity of sound in the medium), the incompressible flow approximations and use of Reynolds number for establishing dynamic similarity are no longer valid. The two significant dimensionless parameters for compressible flow are the ratio of specific heats and the Mach number M. At high velocities, the drag is primarily a function of Mach number, so that Equation 5.30 would read:

$$C_d = \psi(M, \gamma, \text{form}) = \frac{2F}{A\rho u^2} \qquad (5.31)$$

Only in the most elementary cases of deformation drag has it been possible to determine C_d analytically for certain basic body forms. Cases of motion involving separation have been attacked from various standpoints, but without much success. Quantitative study of drag has, therefore, remained largely experimental. The magnitude of the force on a given body form is usually determined experimentally as a function of Reynolds or Mach number, either in the wind tunnel or the towing tank.

As far as the Project 1.10 beam device field experiment is concerned, there is practically no known previous experimental evidence with which to compare the data. The only wind-tunnel work done on H-beams has been in connection with bridge-design studies. For these purposes, the measurements of drag force are confined to maximum wind pressure of about 50 psf and peak wind velocities of 100 miles per hour. For comparison, the Project 1.10 beam at 2,500-foot ground range (9F3) experienced a maximum pressure of about 1,500 psf (10 psi) and peak wind velocities probably in excess of 500 miles per hour. In addition, it is undoubtedly true that an unknown portion of the pressure on the beam was due primarily to the presence of particulate matter (e.g., water vapor, dust, etc.) suspended in the air stream. These considerations, therefore, lead to the rather convincing fact that the wind tunnel work on H-beams is not pertinent to the problem at hand.

Furthermore, in an analytical sense, the possible presence of particulate matter in the air stream introduces a fundamental anomaly, the significance of which has as yet not been adequately explained. That is, the reliability of Equations 5.30 and 5.31 may be questioned, because it is likely that the determination of drag coefficient as a function of Reynolds and/or Mach number is no longer valid when particulate matter is present. It is probable that it would be necessary to introduce new variables to account for particle size, particle density, and the aerodynamic properties of the suspended particles. Such an effort, although pertinent to all the drag measurements of Teapot, is beyond the scope of this report.

5.5.2 Beam-Device Results. The strain-gage records obtained from the two-beam devices are shown in Figure 5.52.

Due to the method of field calibration of these devices, the coordinates appearing on the figure require some explanation. The calibration of the beam was performed in the field as follows. First, the strain gage was mounted on the beam midway between the end supports. Then, using a calibrated hydraulic jack, known loads were applied near the center of the beam span. While these loads were being applied, the strain gage response was noted and the calibration of the beam-gage system completed.

However, it is at once apparent that the method of load application for calibration does not correspond to the loading expected from airblast. For the latter case, the load would necessarily be distributed more or less uniformly over the entire beam length. Simple analysis reveals the relation:

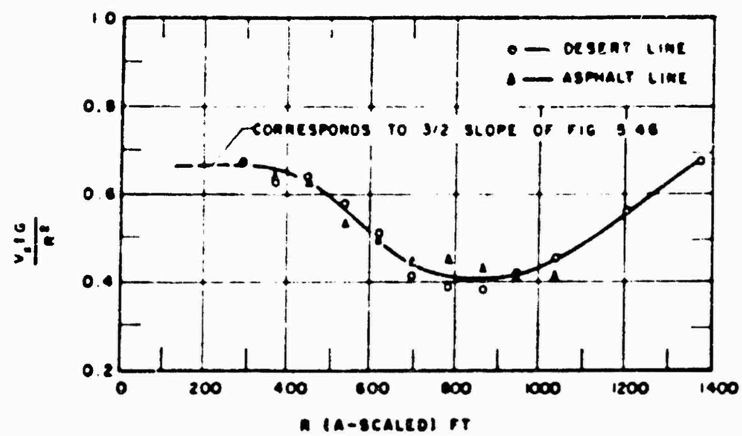

Figure 5.48 A-scaled ($V_x tG/R^2$) versus slant range, Teapot Shot 12.

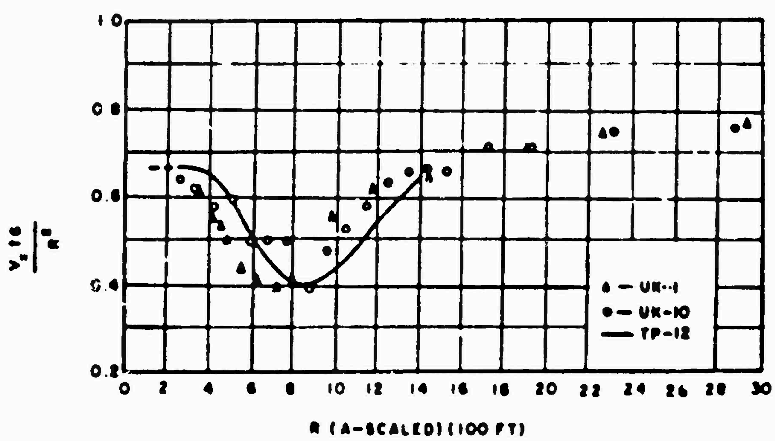

Figure 5.49 A-scaled ($V_x tG/R^2$) versus slant range, Upshot–Knothole Shots 1 and 10 compared with Teapot Shot 12.

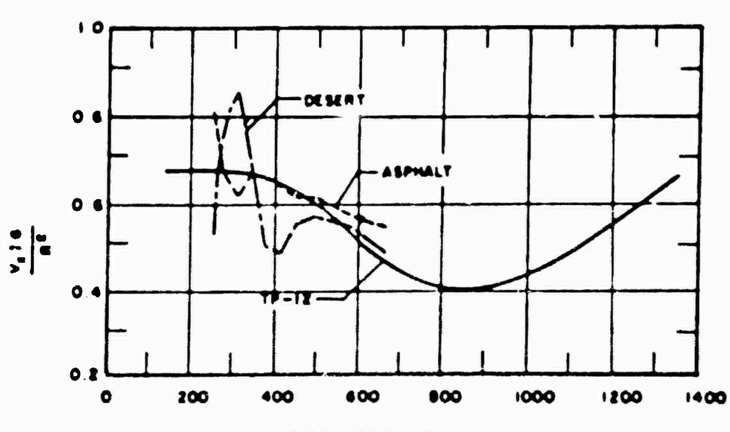

Figure 5.50 A-scaled ($V_x tG/R^2$) versus slant range, Teapot Shot 6 compared with Teapot Shot 12.

$$w = \frac{2P}{L}$$

Where w = distributed load per unit length
P = the calibrating load (applied near center of span)
L = the length of the beam span.

Applying the above relation to the results of Figure 5.51, it is possible to compute the drag force per unit area; the right hand coordinate shown in the figure presents this drag force calibration for the two-beam devices used. The necessity for presentation of two 7F3 records is caused by some confusion due to a base-line shift for this record. The two records represent the extremes of placement of the base line. Data reduction was terminated when the difference in reduced force exceeded 2 : 1.

TABLE 5.6 WATER LINE COMPUTED TEMPERATURES FOR SHOT 12

Ground Range	Arrival Time	Height	Computation Methods: Eqn. 5.4 SRI Data	Eqn. 5.13 NOL Data	Eqn. 5.12 SRI Data	Eqn. 5.8 SRI Data	Eqn. 5. SRI Data	Type of Wave	Best Value
feet	sec	feet	°C	°C	°C	°C	°C		
750	0.119	0				8,000		Shock	
1,000	0.176	0				3,850		Shock	
1,250		3				1,200		Trans	< 1,200
1,500	0.[illegible]	0	250		< -270†	550	< -270†	Trans	250 - 550
		3	-156				50	Shock	
		10	-75				330	Shock	
1,750		0				1,050		Shock	
2,000	0.589	0	—*		—*	700	—*	Shock	
		3	35				600	Shock	35
		10	35				700	Shock	35
2,250		10				250		Shock	
2,5[illegible]	0.[illegible]14	0	-10		12	250	150	Shock	12
		3	20				240	Shock	20
		10	25				250	Shock	25
		25	10				250	Shock	10
		40	35				250	Shock	35
2,750		0				250		Shock	
3,000	1.246	0	-15		20	200	110	Shock	20
		3	-25				110	Shock	

* Indeterminant computation — due to angle larger than 90° near ground surface

† This excessive negative temperature due to angle at surface being smaller than aboveground wave front angle, i.e., θ' = 38°

‡ No data available

Since the drag force per unit area (versus time) is known and measurements near the beams of q (pitot) dynamic pressure (versus time) are available, application of Equation 5.30 leads to determination of a drag coefficient C_d as a function of time. These results are presented in Figure 5.52; it should be emphasized that smoothed q* (pitot) records were used for the drag-coefficient calculations. Referring to the figure, several general characteristics are evident:

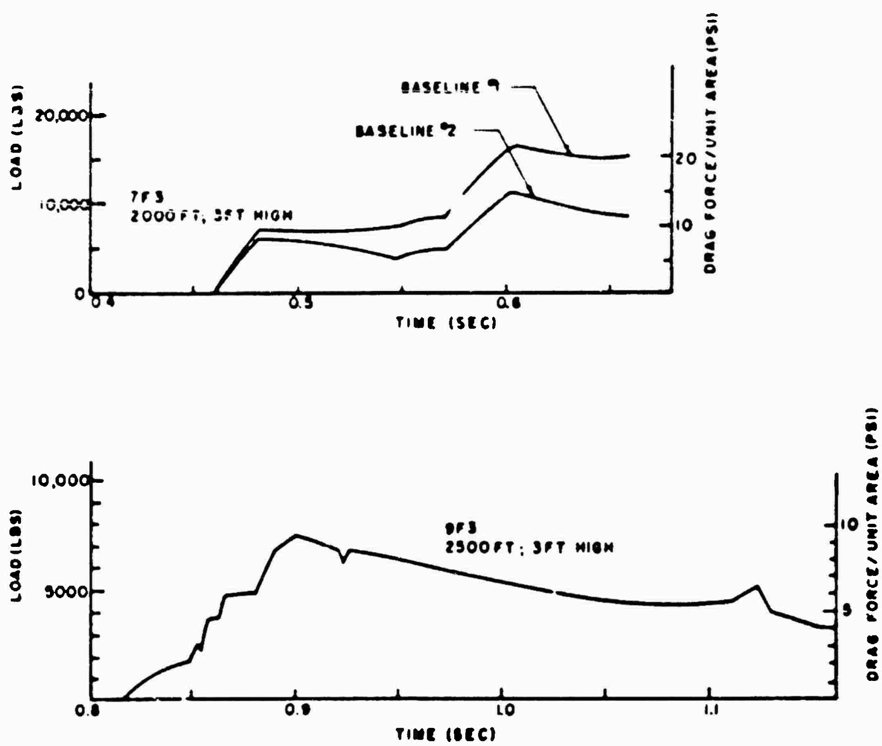

Figure 5.51 Records of force versus time from H-beam devices, Shot 12.

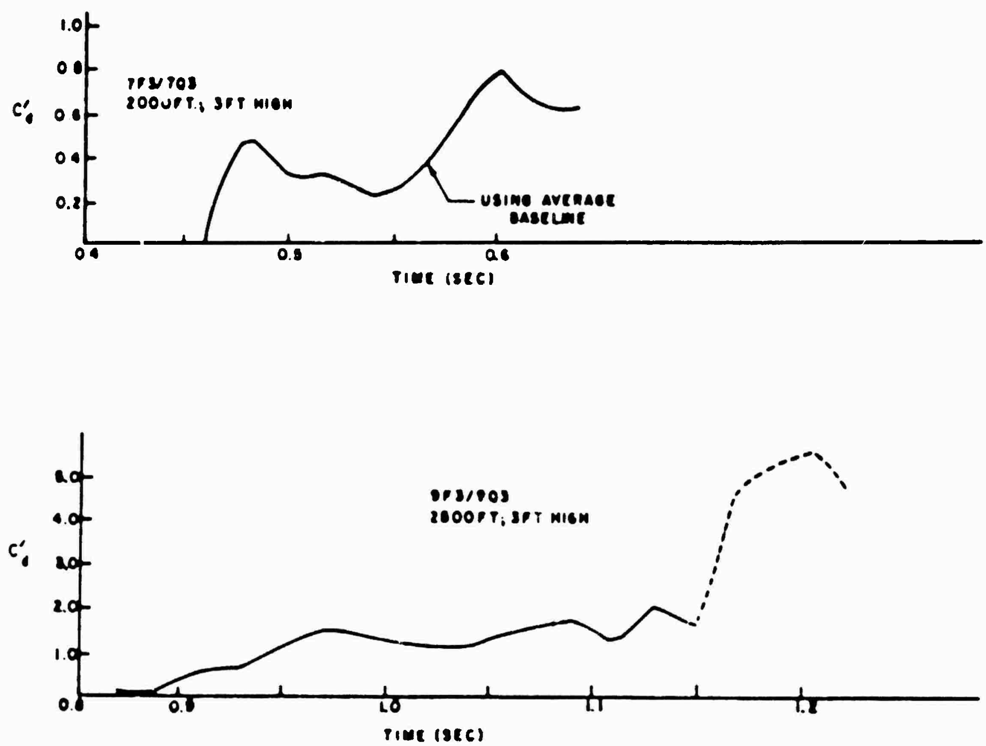

Figure 5.52 Computed drag coefficient versus time for H-beam devices, Shot 12.

1. The computed drag coefficient for a single beam may vary markedly with time (see 7F3/7Q3 trace, Figure 5.22).

2. The results at 2,000-foot ground range show a rather sharp initial rise of drag coefficient, as opposed to the long, slow increase associated with the 2,500-foot measurement.

3. Although it is not possible to compare the computed coefficients at the two stations, at comparable times the average (over the first 100 msec) drag coefficient appears to be significantly larger for the beam at 2,500 feet.

4. The very sudden increase in coefficient near 1.1 second on the 9F3/9Q3 record, Figure 5.52, is the result of a sharp decrease in the q* (pitot) pressure at this time; the strain-gage record (Figure 5.51) indicates no corresponding decrease in drag force near 1.1 second.

Since the drag coefficients referred to above have been determined from combining two separate measurements (i.e., drag force and q* (pitot) pressure and since no information is available concerning the effects of particulate matter upon each measurement, it is not possible to explain or evaluate the observations included in Figures 5.51 and 5.52. At present, these data represent an initial attempt to determine experimentally the drag force on an H-beam subjected to nonclassical airblast pressure loading. It is probable that when the effects of disturbed blast waves and particulate matter upon drag force and q(pitot) measurements become better known, the Project 1.10 beam data will be of more-significant value.

Chapter 6
CONCLUSIONS and RECOMMENDATIONS

6.1 CONCLUSIONS

6.1.1 Instrumentation Performance. For Teapot Project 1.10, full length records were obtained on 96 percent of the gage channels (this was not true of previous shots when measurements were made in the precursor region). This excellent performance was largely the result of well-designed instrument towers and mounts. The towers were entirely undamaged on both Shots 6 and 12, and damage to the mounts was limited to the tearing off of the gage baffles on three gages. Such failures as occurred (4 percent) were caused by electrical rather than mechanical damage.

The interpretation of the pitot-tube overpressure and dynamic pressure measurements is hampered by lack of calibration data under shock-wave flow conditions and also by inadequate knowledge of effect of particulate matter upon the measurement. Corrections for pitch, yaw, and Mach number should be available for transonic and supersonic flows.

From the available data obtained from the aboveground baffle-mounted overpressure gages and nearby pitot-tube static pressure gages, it is apparent that the two gage configurations are not equivalent in regions of high pressure and/or disturbed blast waves. In regions of supersonic flow, the above ground baffle-mounted gages are probably not desirable.

6.1.2 Wave-Form Classification. With a few exceptions (viz., the water line) it is possible to group the Project 1.10 pressure–time results into two sets of wave-form classification: one system for overpressure (Types 0 through 8) and another for q*(pitot) dynamic pressure measurements (Types B through H). As expected, wave-form behavior as a function of ground range is sensitive to the characteristics of the blast-line surface.

For Shot 12, the overpressure wave forms over the water line at least partially traverse two wave-form cycles, while the wave forms over the asphalt surface do not attain classical form (Type 8) even at the last gage station (3,000 feet) on the blast line. However, on the desert line the classical form is observed at 4,500 feet. Although the non-classical behavior persists to longer ranges over the asphalt, the precursor as a distinctly separate wave (Type 1) is observed at longer ranges over the desert. The same general remarks hold for the dynamic-pressure q(pitot) wave-form classifications.

When the wave-form classification is incorporated into the presentation of peak-pressure-versus-ground range, it becomes evident that it is possible for an ideal peak pressure measurement to be identified with a disturbed (non-ideal) wave form. Consequently, introducing both variables (wave form and peak pressure) into the analysis helps to reduce the ambiguities associated with comparing results from different nuclear tests.

6.1.3 Shock Velocity and Computed Preshock Temperature. Considering the horizontal-trace velocity of the shock front as determined from gage-arrival times over the various surfaces instrumented on Shots 6 and 12, the velocities over the asphalt and desert surfaces are well above ideal, particularly at close-in (less than 1,500 feet) ground ranges. Even over the water surface, shock velocities determined near 1,000-foot ground range are well above ideal values.

From a comprehensive review of the various methods of computing preshock temperature using shock parameters, it is evident that this computation is definitive only when sufficient wave-front orientation and pressure–time data are available. In any case, careful analysis is necessary in the calculation and naturally, the computed temperature yields only some average value at the time of shock arrival. This is a poor substitute for the more desirable direct-temperature-versus-time (i.e., from detonation time) measurement.

6.1.4 Surface Effects. The limited wave-front orientation data which could be derived from the Shot 12 results indicate that deviations of airblast phenomena from ideal over the asphalt surface persisted to greater ground range when compared with results over the desert and water surfaces. In general, the wave-front orientations determined from arrival-time data agree very well with the NOL shock photography data.

To summarize, the peak overpressures measured on Shots 6 and 12 were depressed most severely over the asphalt surface and least over the water; in addition, aboveground maximum pressures were generally higher than those measured at ground surface, a result also observed on Shot 10 of Upshot–Knothole.

The Project 1.10 dynamic-pressure q(pitot) results indicate a severe attenuation of peak pressure with distance for all surfaces. Also, the influence of surface characteristics appears least pronounced at the closest gage station (750 feet) on Shot 12.

From the Shot 12 results obtained on the BRL gage arc (2,500 feet), abrupt localized changes in the characteristics of a surface over which a disturbed blast wave is traveling may have significant effects upon peak pressure and/or wave form in the near vicinity of the surface discontinuity. Data from the offset gages on the water line reveal that precursor characteristics observed on the close-in water-line gage records are not due to cross-feed of energy from the desert surface.

6.1.5 Precursor Phenomena. When compared with the results from previous precursor-forming nuclear shots, Shots 6 and 12 display similar behavior: nonclassic wave forms, depressed peak overpressure above 7–8 psi, and close-in dynamic q(pitot) peak pressures which are several times ideal.

Consideration of the Shot 12 water-line wave-form development, shock velocities, measured pressure-time data, and offset-gage data shows that a precursor formed over the water evidently shortly before the pressure wave reached the first gage (750 feet) and continued to evolve normally out to about 1,500 foot ground range. Gage records at subsequent ground ranges indicate what appears to be a complex competition between normal precursor behavior on the one hand and energy feed-in from the adjacent desert areas on the other.

Basically, the precursor wave over the asphalt line was not much different from that over the desert—the only distinction being that the disturbance appeared more extended over the asphalt.

Analysis of the results of Shots 6 and 12, coupled with the related theoretical approach by Chu, has created renewed interest in the concept of a shock wave produced by high-flux thermal input. Some confidence in the concept is generated by the success of a semi-empirical analysis of data obtained from precursor-forming nuclear explosions.

Using the Project 1.10 data and some curve-fitting procedures, it is possible to compute the surface constants which apply to the desert and asphalt surfaces. The Shot 6 (T-7 area, Yucca Flat) and Shot 12 (Frenchman Flat) desert-surface constants deviate by only 3 percent, and the asphalt-surface constants differ, at most, by 12 percent from that of the desert.

6.1.6 Correlation with Damage. Analysis of the forces acting on the two H-beam devices instrumented on Shot 12 yields only very tentative conclusions. Although it was possible, using the q*(pitot)-time results, to determine the computed drag coefficient versus-time for the two beams, there is no pertinent theoretical or experimental data for such devices with which to compare the field results. Also, it is believed that the presence of particulate matter in the blast wave has a profound (but unknown) effect upon the drag (and drag coefficient) of such structural elements.

6.2 RECOMMENDATIONS

There appears to be a need for a change in the procedure used for measuring dynamic pressure, particularly in stream flows exceeding Mach 1.0. Impact pressure (total head) should be measured using a carefully designed supersonic tube, whereas the corresponding overpressure measurement should be obtained from a separate ground-level gage. In fact, there is need for a comprehensive investigation of instrumentation to determine what is most useful for measuring airblast parameters in regions of high pressure and high flow velocities. Also, future instrument design must consider effects of suspended particulate matter upon the measurement.

The scheme of wave-form classification and the idea of including considerations of wave-form information in the analysis of peak pressures should be retained and extended to other blast parameters. It is believed that more useful and understandable presentations would result from this method of analysis.

To confirm the conclusion about the influence of localized surface discontinuities upon blast parameters (Section 6.1.4), future nuclear tests should include careful and detailed measurements over areas which include such surface discontinuities.

Since there is some evidence that Shot 12 was not instrumented closely enough to ground zero to detect precursor formation, it would be wise in future tests to obtain at least time-of-arrival measurements at closer stations.

On future tests, in addition to the conventional pressure-time measurements some close-in measurements should be made which are specifically designed to detect and delineate the thermal shock wave, if it exists.

It is evident that more work, both in theory and laboratory testing, is needed in the field of airblast drag forces on structural elements before available (or future) field results can be made understandable.

REFERENCES

1. Porzel and Reines; "Height of Burst for Atomic Bombs"; LA-743R, Series B, August 3, 1949; Los Alamos Scientific Laboratory, Los Alamos, New Mexico; Circulation limited; Secret Restricted Data.

2. Gilbert, H. K., and Wilson, R. Q.; "Final Report, Operation Buster"; WT-412, July 1952; Armed Forces Special Weapons Project; Secret Restricted Data.

3. Salmon, V.; "Air Pressure versus Time"; Project 1 2, Operation Tumbler, WT-512, February 1952; Stanford Research Institute, Menlo Park, California. Secret Restricted Data.

4. Swift, L. M., and Sachs, D. C.; "Air Pressure versus Time"; Project 1.1b, Operation Upshot-Knothole, WT-711; Stanford Research Institute, Menlo Park, California; Secret Restricted Data.

5. Shreve, J. D. Jr.; "Air Shock Pressure versus Time for a Tower Shot"; Project 1.1c-1, Operation Upshot-Knothole, WT-712; Sandia Corporation, Albuquerque, New Mexico; Secret Restricted Data.

6. Broyles, Carter D.; "Dynamic Pressure versus Time and Supporting Air Blast Measurements"; Project 1.1d, Operation Upshot-Knothole, WT-714; Sandia Corporation, Albuquerque, New Mexico; Secret Restricted Data.

7. Morris, W. E., et al; "Air Blast Measurements"; Project 1.1a-1.2, Operation Upshot-Knothole, WT-710; Naval Ordnance Laboratory, Silver Spring, Maryland; Secret Restricted Data.

8. Cook, T. B. Jr., and Kammermeyer, K.; "Sandia Laboratory Shock-Gage Evaluation Tests"; Tumbler-Snapper Report WT-505, October 1952; Confidential.

9. "Summary Report of the Technical Director"; Operation Upshot-Knothole, WT-782; Armed Forces Special Weapons Project; Secret Restricted Data.

10. Pearson, A. O., and Brown, H. A.; "Calibration of a Combined Pitot-Static Tube and Vane-Type Flow Angularity Indicator at Transonic Speeds and at Large Angles of Attack or Yaw"; NACA RM L52F24, September 1952; Langley Aeronautical Laboratory; Unclassified.

11. Kelso, J., and Hesse; "Mach Shock Formation From a Nuclear Detonation"; AFSWP-510, March 10, 1955; Secret Restricted Data.

12. "Summary Report of the Technical Director"; Operation Teapot, WT-1153; Armed Forces Special Weapons Project; Secret Restricted Data.

13. Kauffman, W. F., and Shinbrot, M.; "A Method for Differentiation of Experimental Data"; J. Aero. Sci. 20, 428-430, June 1953; Unclassified.

14. Wang, Chi-Teh, and DeSanto, D. F.; "Differentiation of Experimental Data by Means of Higher Order Finite-Difference Formulae"; J. Aero. Sci. 20, 792-793, Sept. 1953; Unclassified.

15. Moulton, J. F.; "Shock Photography Measurements"; Project 1.2, Operation Teapot, WT-1102; Naval Ordnance Laboratory, Silver Spring, Maryland; Secret Restricted Data.

16. "Effects of Atomic Weapons"; Revised, September 1950; Los Alamos Scientific Laboratory, Los Alamos, New Mexico; Unclassified.

17. Brode, H. L.; "Numerical Solutions of Spherical Blast Waves"; J. App. Phys. 26, 766, June 1955; Unclassified.

18. Bryant, E. J.; "Response of Drag Type Equipment Targets in the Precursor Zone"; Operation Teapot, WT-1123; Secret Restricted Data.

19. "Handbook of Chemistry and Physics"; Chemical Rubber Publishing Company, 38th Edition, 1954; Unclassified.

20. Sauer, F. M.; "The Preshock Sound Velocity Field Over Inorganic and Organic Surfaces"; USDA, AFSWP-420, December 1954; Secret.

21. Sauer, F. M.; "Corrective Heating of Air Above an Inorganic Surface Heated by Radiation from a Nuclear Weapon"; USDA, AFSWP-862, November 1955; Confidential.

22. "Capabilities of Atomic Weapons"; Department of the Army Manual TM 23-200, July 1955, Revised Edition; Secret Restricted Data.

23. Porzel, F.; Armour Research Foundation, private communication.

24. Chu, Boa-Teh; "Pressure Waves Generated by Addition of Heat in a Gaseous Medium"; Johns Hopkins University, NACA TN 3411, June 1955; Unclassified.

25. Aronson, C. J., et al; "Free-Air and Ground Level Pressure Measurements"; Project 1.3 and 1.5, Operation Tumbler, WT-514; Naval Ordnance Laboratory, Silver Spring, Maryland; Secret Restricted Data.

Appendix A

ACCELERATION RESPONSE OF WIANCKO PRESSURE GAGES

It has been generally assumed that the Wiancko balanced-reluctance pressure gage has a negligible response to acceleration forces because of the two-coil, rocking-armature design. Figure A.1 shows that acceleration forces tend to move the armature similarly with respect to both coils, whereas pressure applied to the sensing element moves it in opposite direction from each coil. Thus, acceleration forces tend to maintain the balanced conditions, producing no electrical output. Measurements of this acceleration response show maximum responses of the order of 0.0005 psi/g for a 30-psi gage (0.0016 percent FS/G); Sandia Corporation tests show similar results (Reference 8).

The above measurements do not necessarily indicate the true performance. A change in the geometry of the transducer may produce no unbalance while the gage is balanced, but may seriously affect its response, in this case, to pressure. A force which moves the armature away from the coils, for instance, may drastically affect its sensitivity. Thus, if transient accelerations are applied while a steady pressure is simultaneously applied, a pronounced acceleration may result.

Tests were made on a small number of Wiancko pressure gages to determine their acceleration sensitivity under load. Each gage was provided with a check valve at its inlet, so that pressure could be applied and maintained after removal of the hose connection. The gages were mounted on a Schaevitz spin table in several orientations, with slip-ring connections to a normal demodulation circuit. The effect of spin-table speed (radial acceleration) up to 90 g was then observed. Figure A.2 shows the results on a typical 30-psi gage.

In this figure, the percentage error (of the reading, not of full scale) caused by various values of acceleration when the gage is deflected to one-third, two-thirds, and full range is shown for various orientations of the acceleration force. These results are typical of all gage ranges, but there is a considerable variation between gages. Higher-range gages (100 and 300 psi) show much smaller errors (25 to 30 percent as great), and 10-psi gages show slightly larger errors.

Note that transverse acceleration in the tangential direction tends to cause comparable errors to acceleration in the opening-closing direction — a somewhat unexpected result. It will be observed that proportional error is generally greater when the pressure is less than full scale, but is by no means constant in terms of full-scale reading. At zero pressure, no measurable deflection was observed up to 90 g except for longitudinal acceleration, where 90 g produced a deflection equivalent to about 0.04 psi.

The results of these tests intimate that some of the hash observed in pressure-time measurements after shock wave arrival may be caused by acceleration of the mounts.

In general, there is no way to check this possibility, but one approach appears profitable. In the pitot-tube gage, two Wiancko pressure transducers are mounted a few inches apart. These gages are mounted similarly with regard to transverse accelerations. Any response to transverse or vertical acceleration of the mount should be in the same direction on the two gages. A check of the records may then show relatively high-frequency disturbances which if due to acceleration should be in phase on the two records. No such results have been observed (see Section 2.5.5), which indicates that the high-frequency hash is probably not due to the acceleration of the gage mounts.

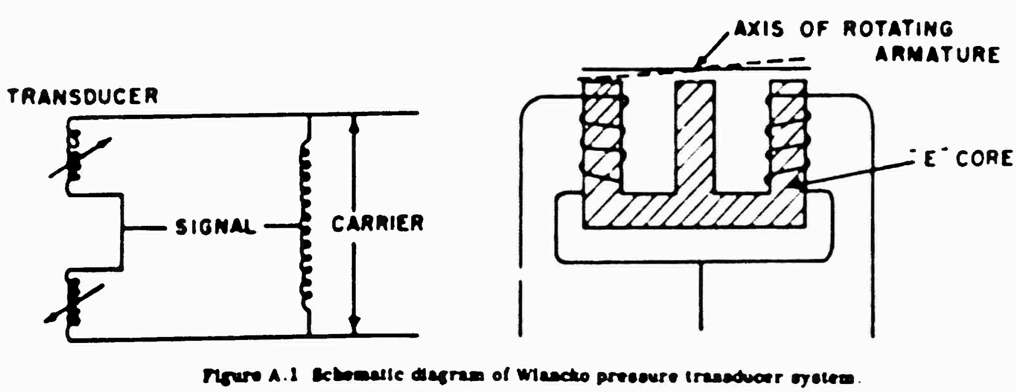

Figure A.1 Schematic diagram of Wiancko pressure transducer system.

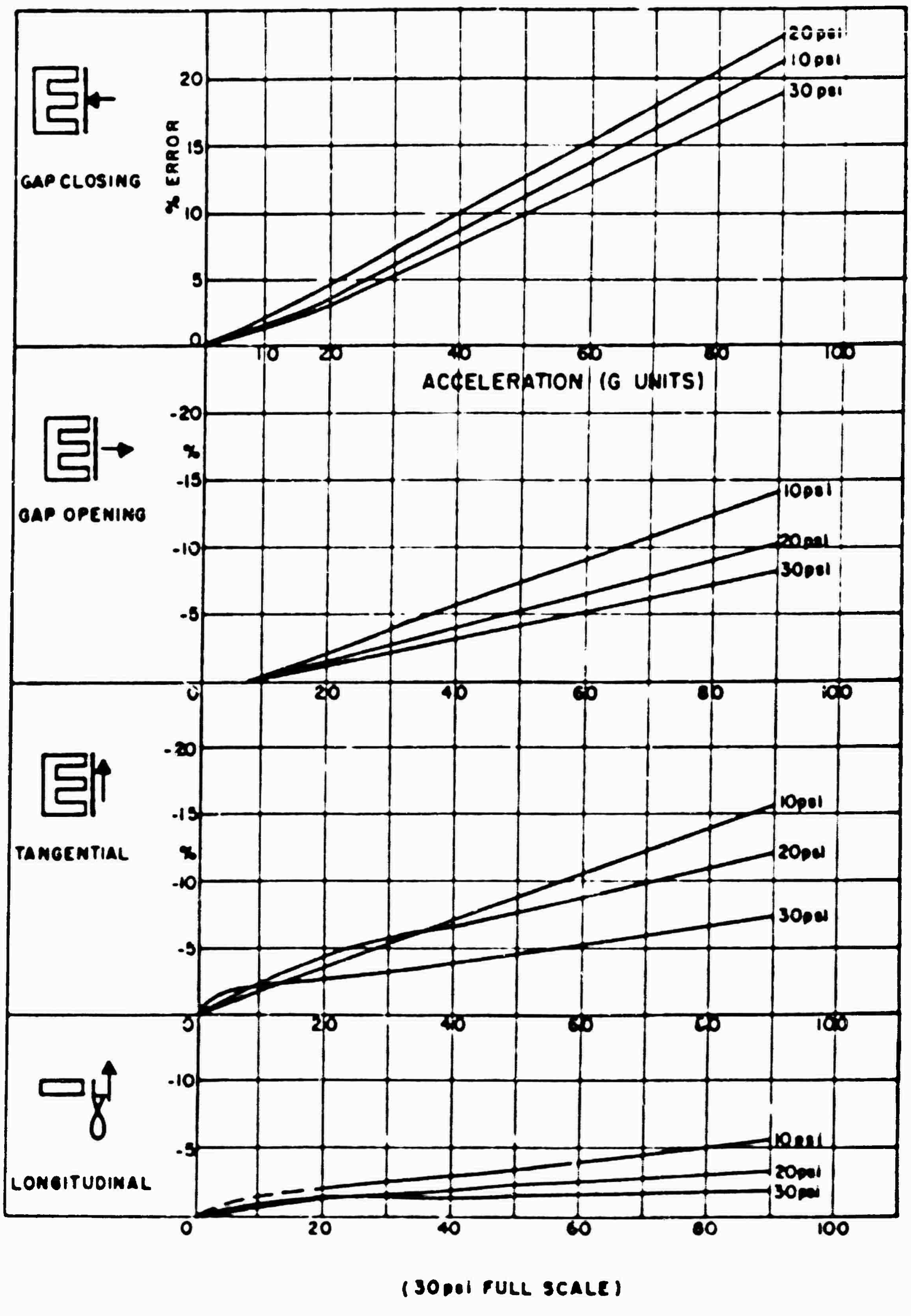

Figure A.2 Effects of acceleration; Wiancko gage.

Appendix B

GAGE RECORDS

Reductions of tracings of the significant portion of all usable gage records comprise this Appendix. Features such as lengths of positive phase and secondary shock do not appear in these reductions. These aspects of the pressure–time functions, where pertinent, are documented in the tables.

The records are arranged first by shot (Shot 12 precedes Shot 6), then by blast line (water, desert, asphalt), then by ground range for each vertical level (surface level first). Auxiliary records (offset gages, etc.) are introduced into the main sequence following the primary gage record.

Each record is provided with suitable time and pressure coordinates. The time indicated refers to zero time of the shot. The dotted curves document the manner in which the records were smoothed before corrections for pitch and/or Mach number were applied.

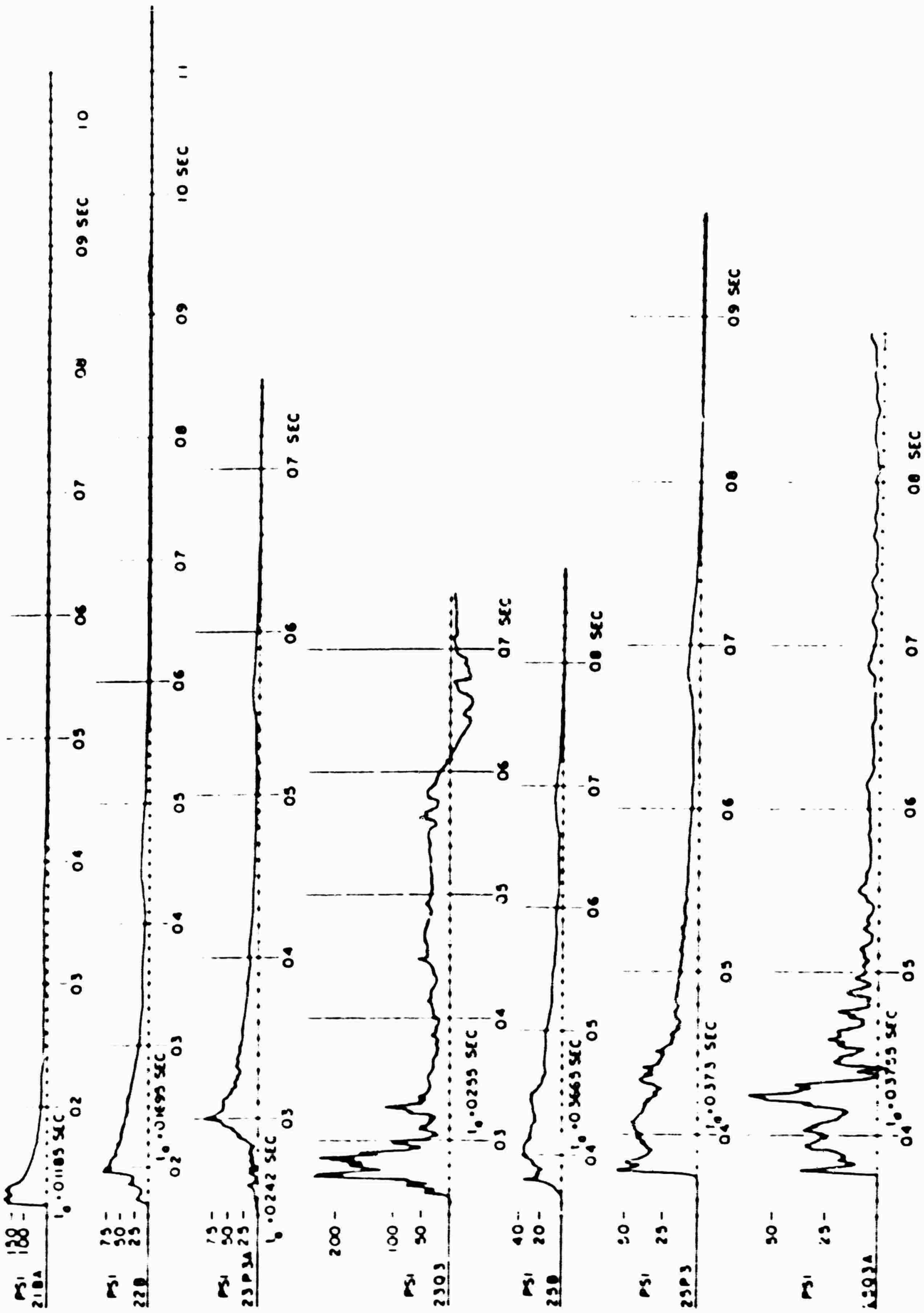

Figure B.1 Original records, Shot 12, water line, 750 feet—1,500 feet.

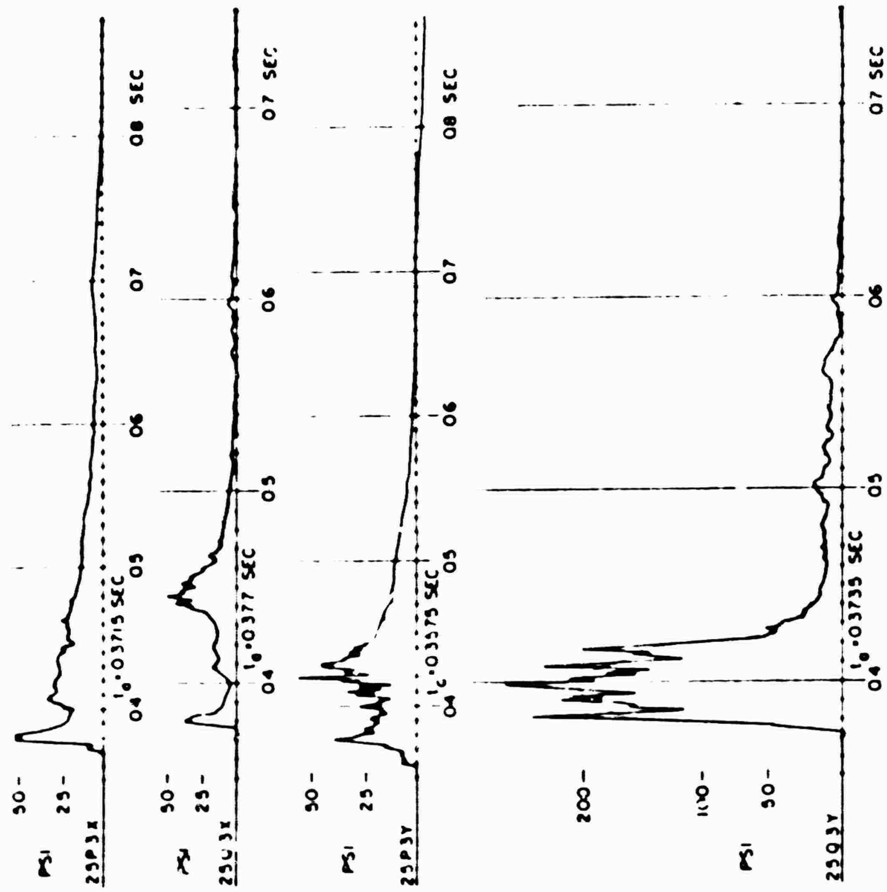

Figure B.1 Continued.

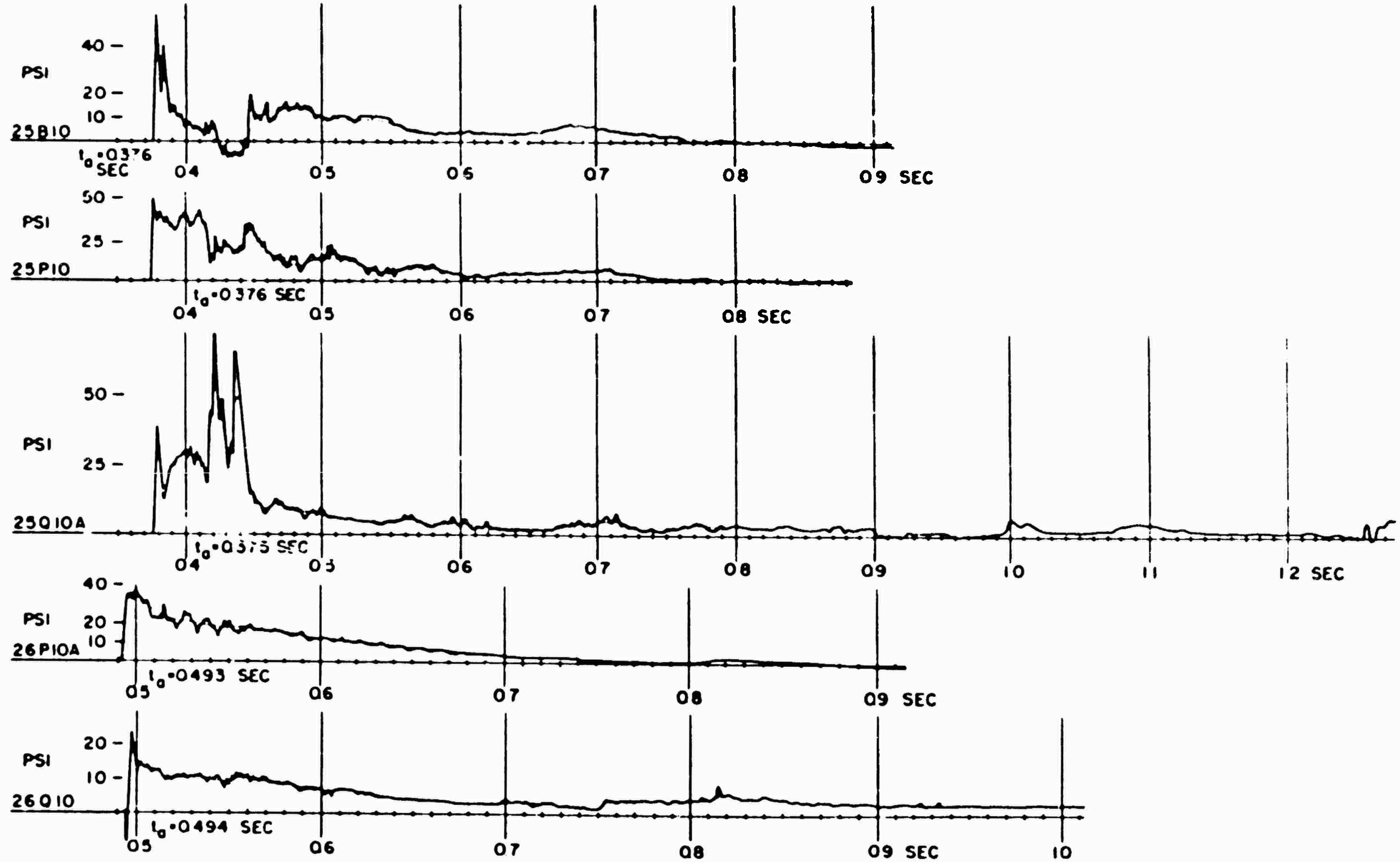

Figure B.2 Original records, Shot 12, water line, 1,500 feet–2,000 feet.

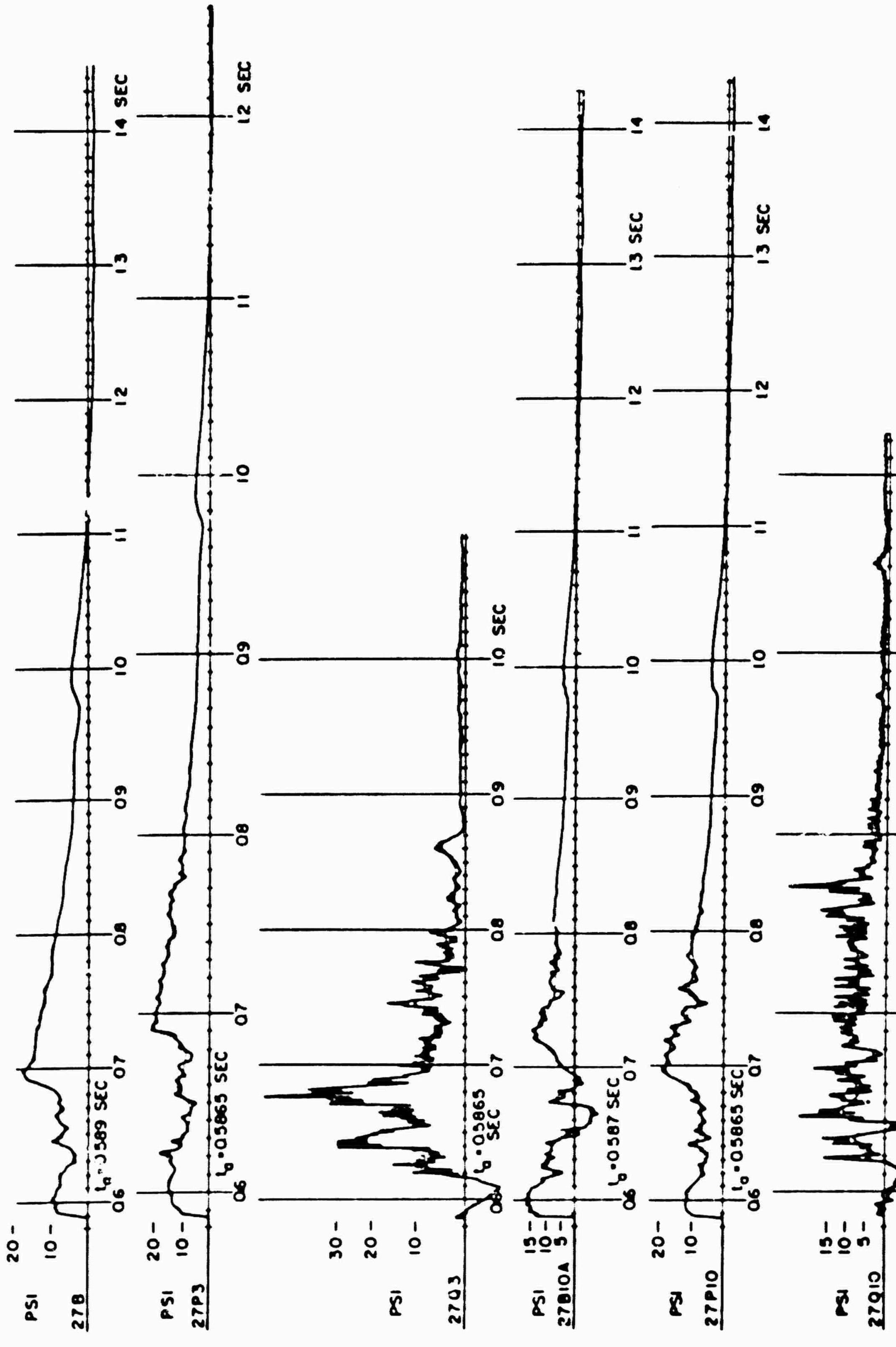

Figure B.2 Continued.

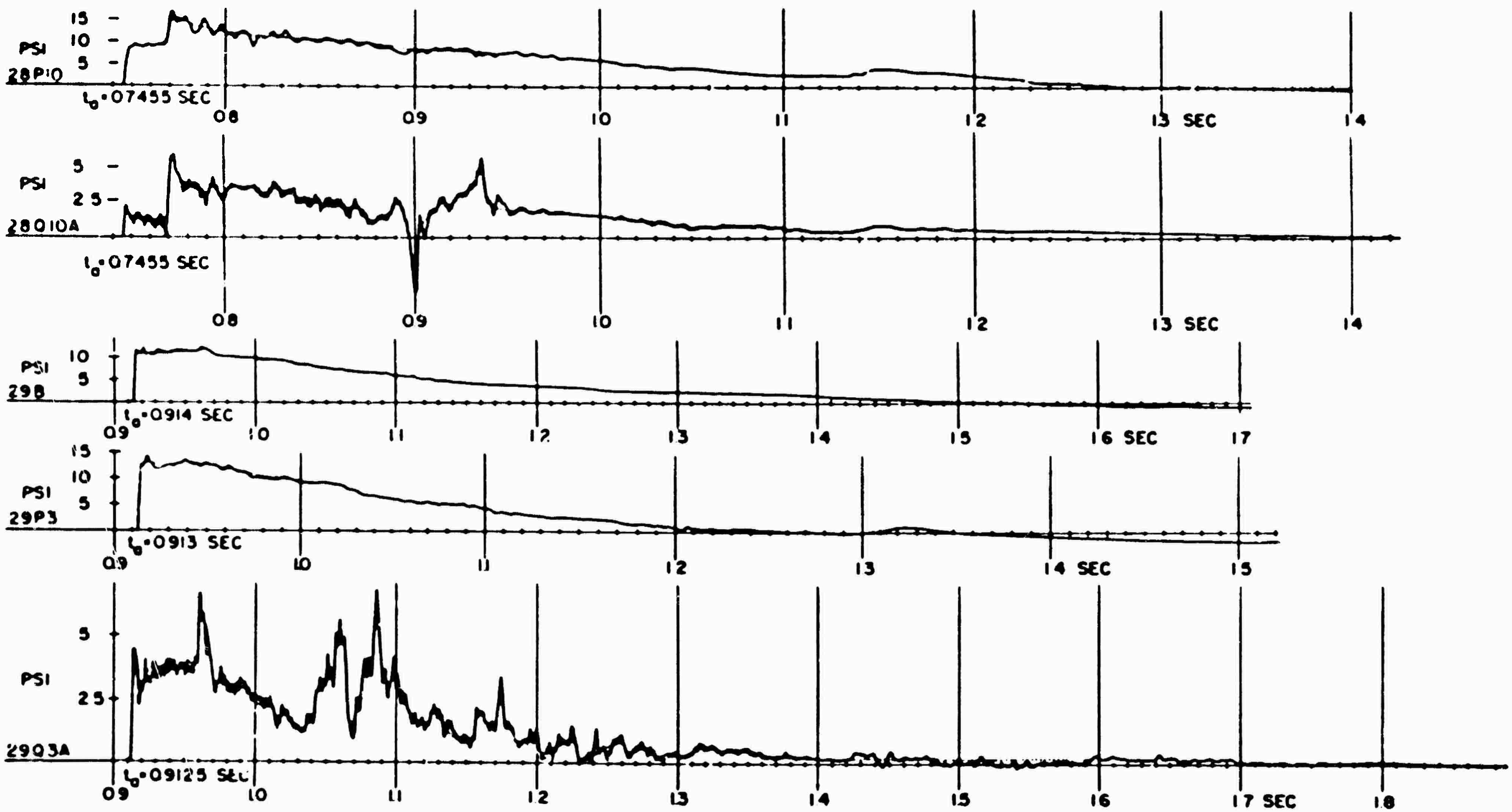

Figure B.3 Original records, Shot 12, water line, 2,000 feet—2,500 feet.

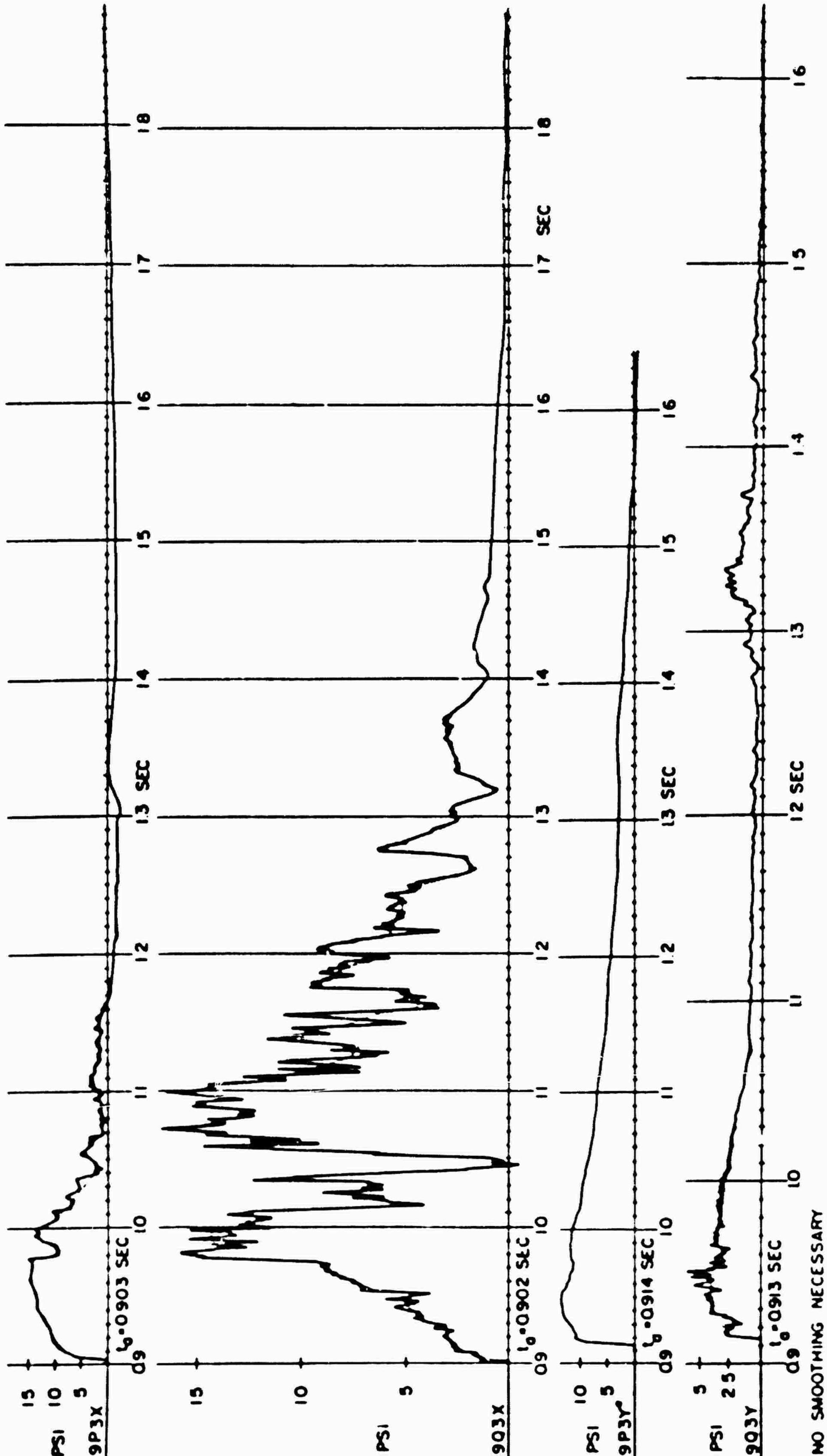

Figure B.3 Continued.

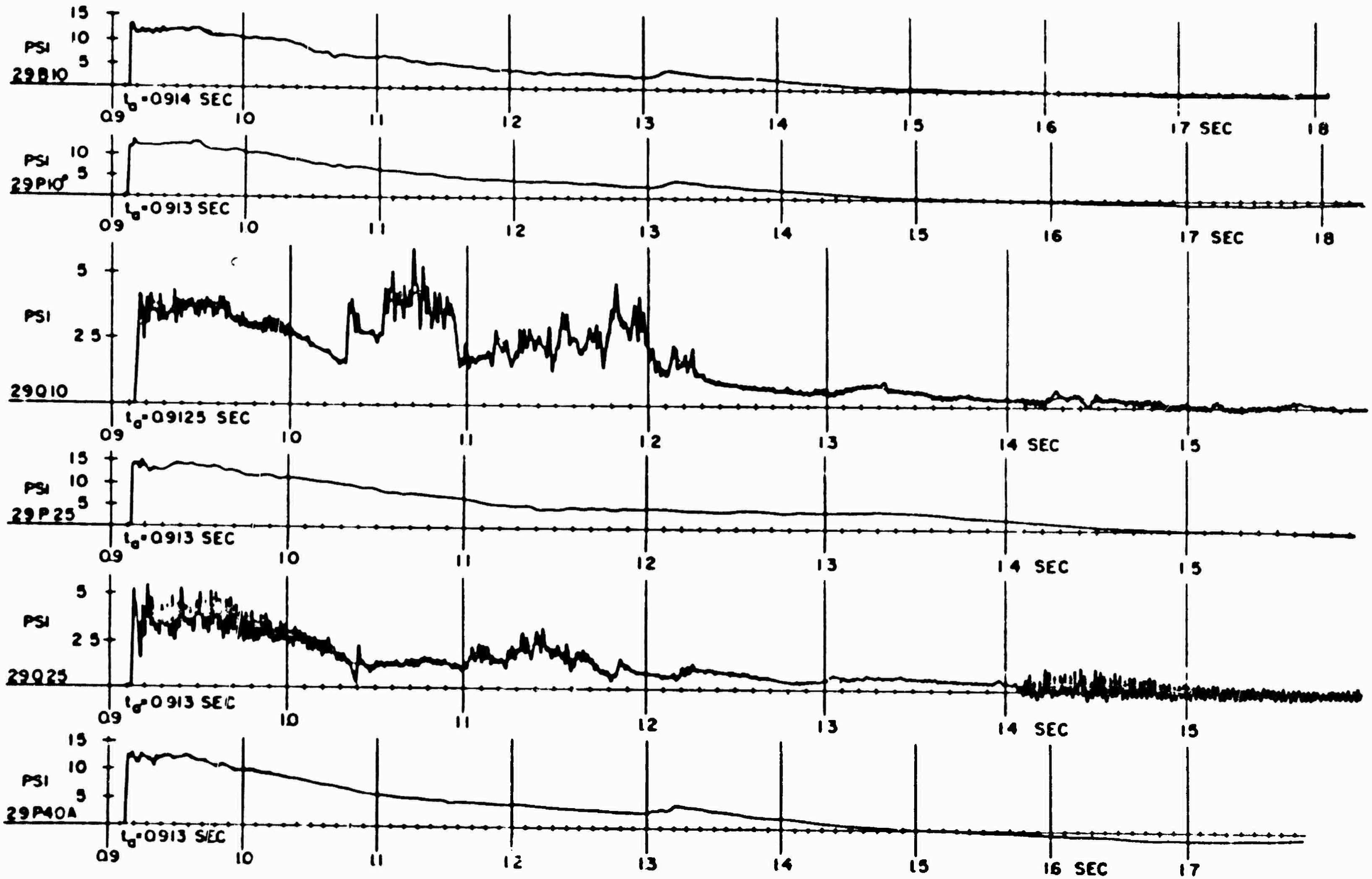

Figure B.4 Original records, Shot 12, water line, 2,500 feet–3,000 feet.

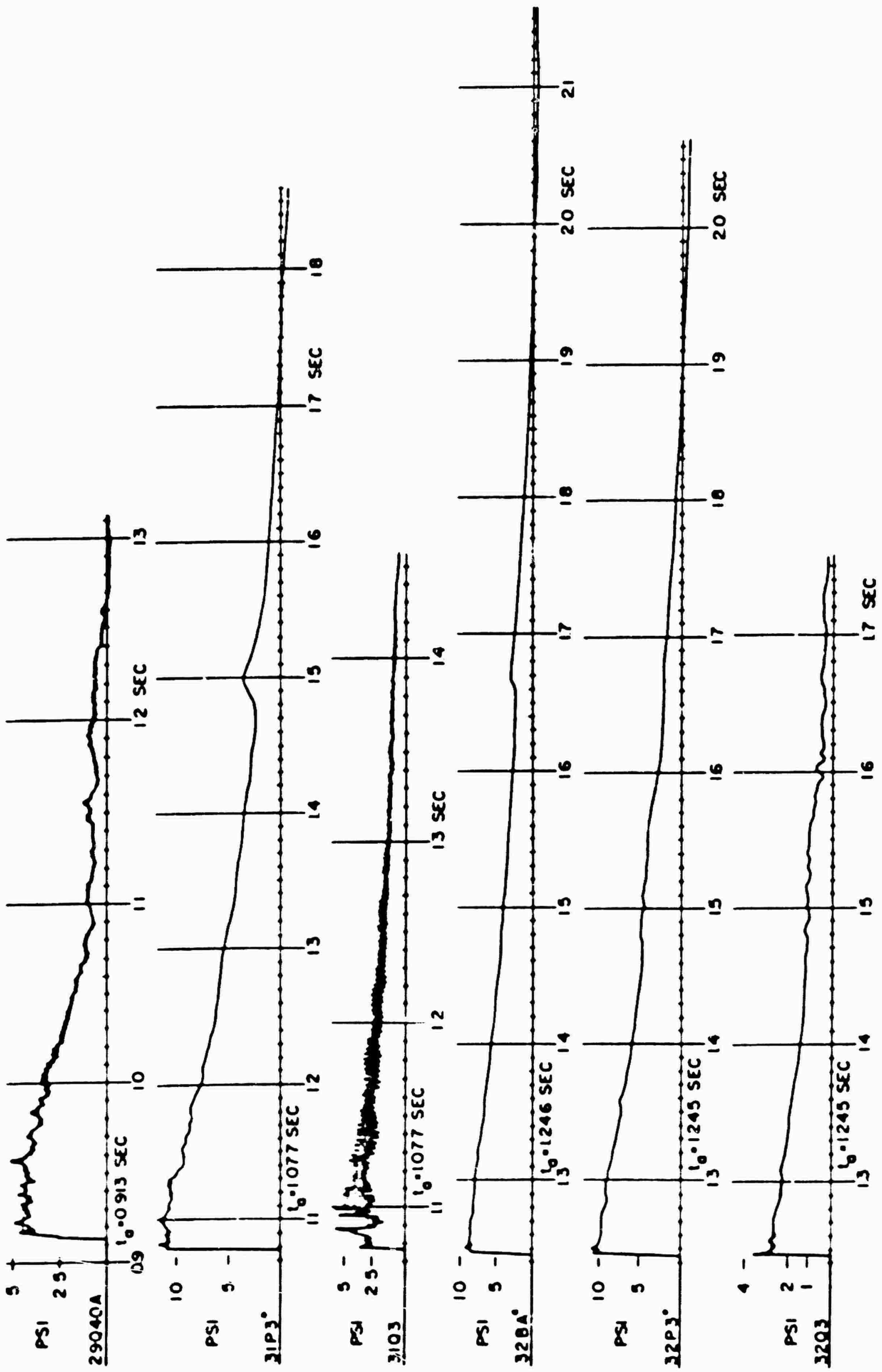

* NO SMOOTHING NECESSARY

Figure B.4 Continued.

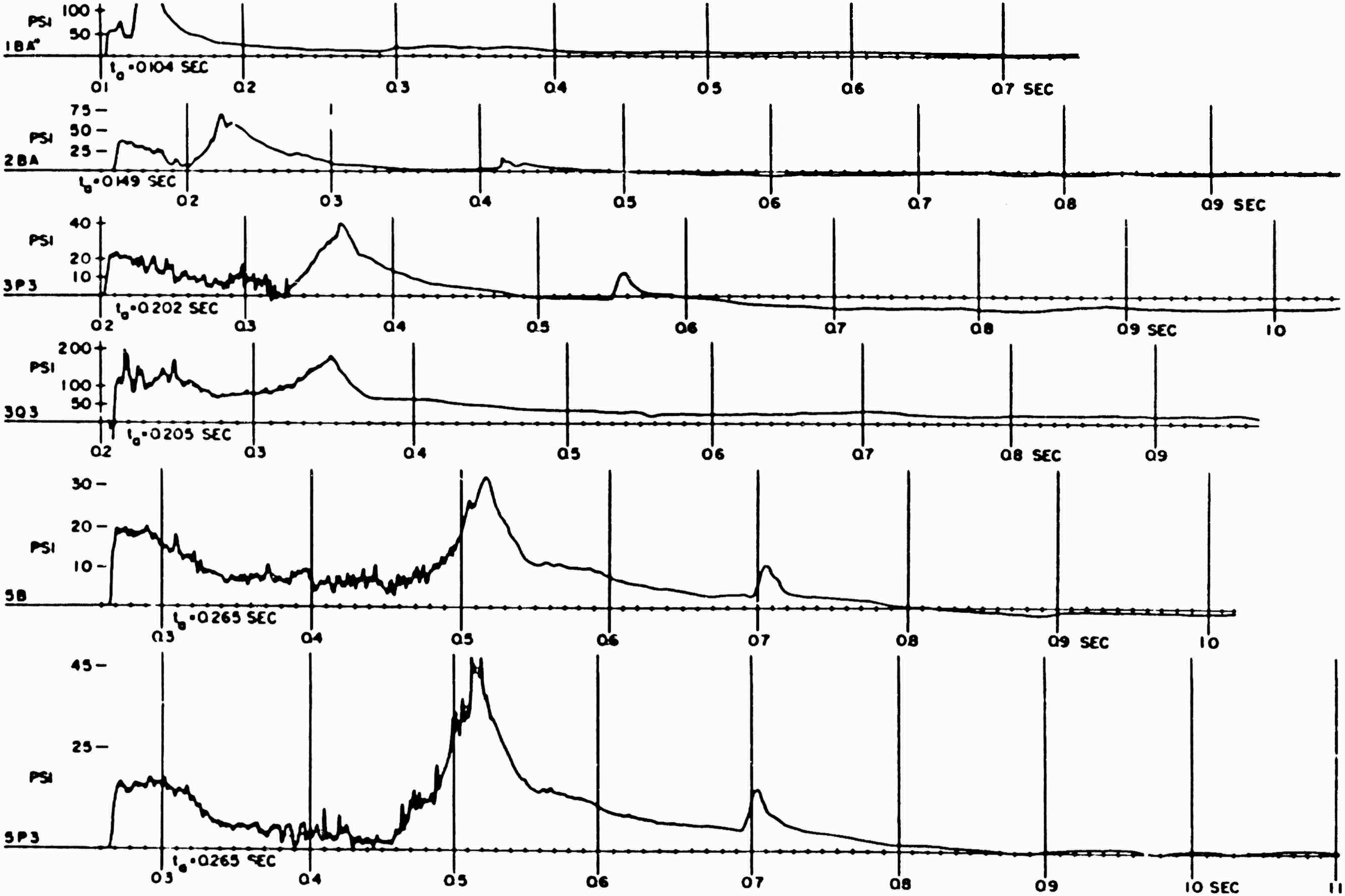

Figure B.3 Original records, Shot 12, desert line, 750 feet—1,500 feet.

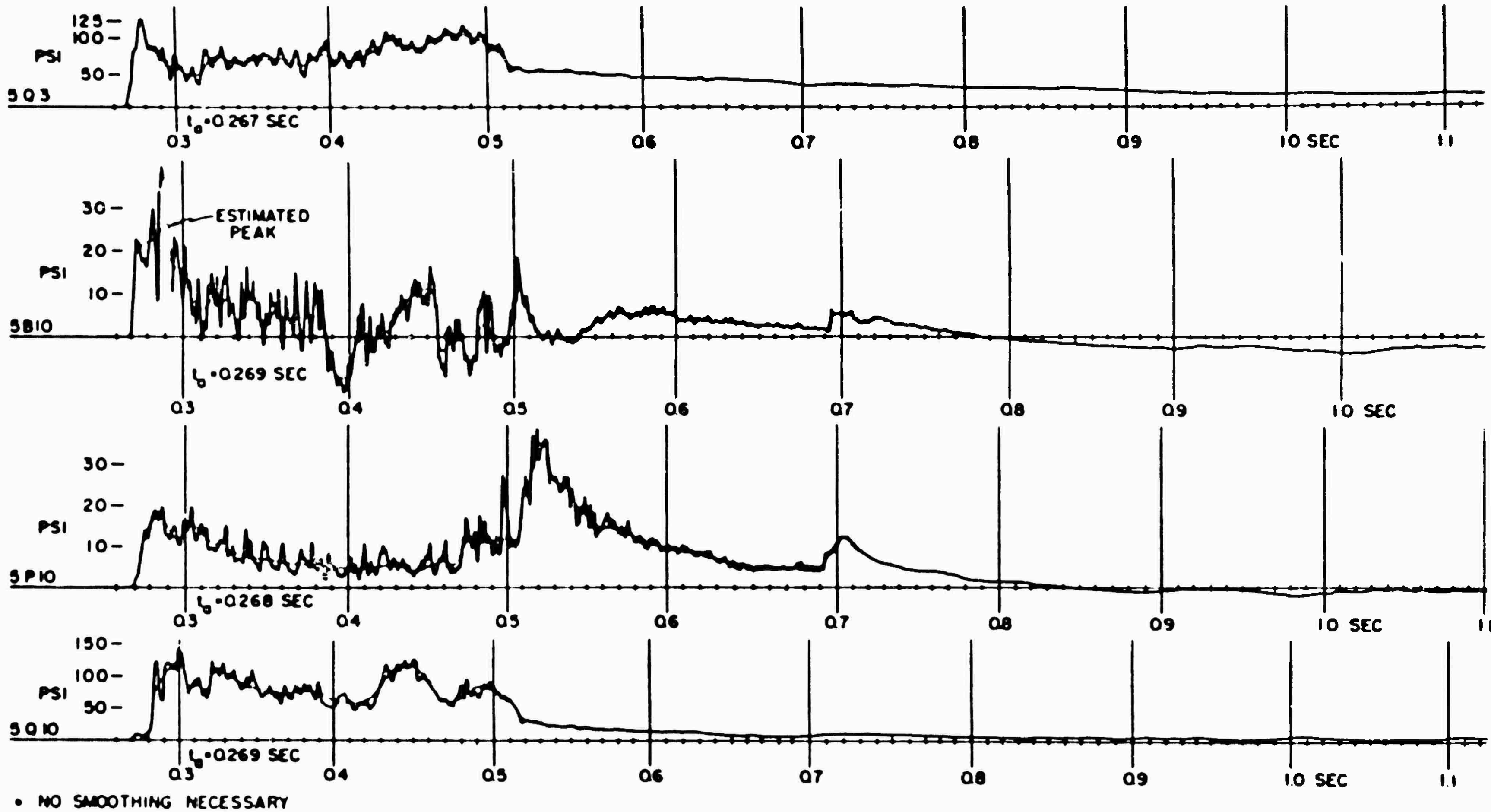

Figure B.5 Continued.

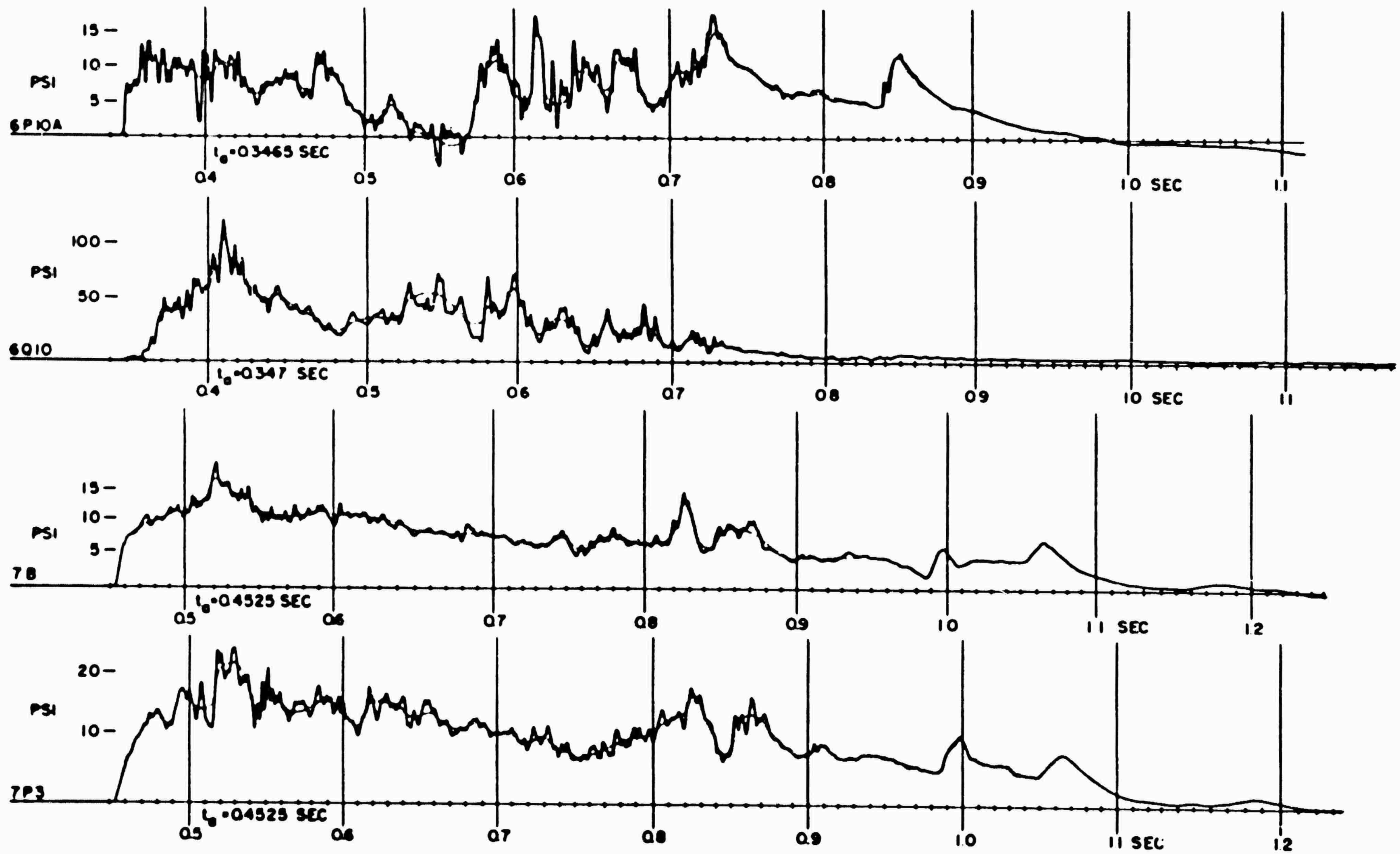

Figure B.6 Original records, desert line, 1,750 feet—2,000 feet.

DECLASSIFIED

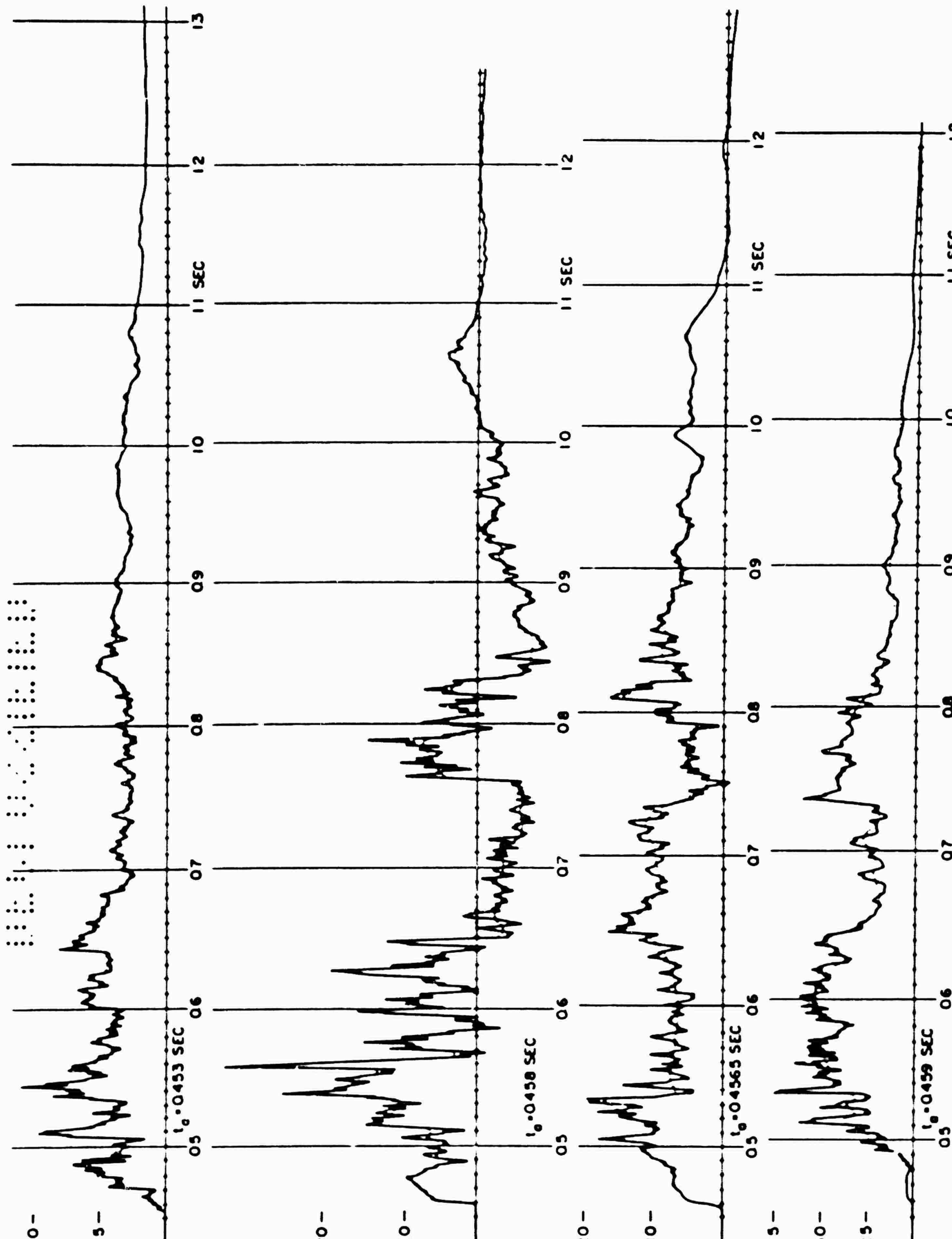

Figure B.6 Continued.

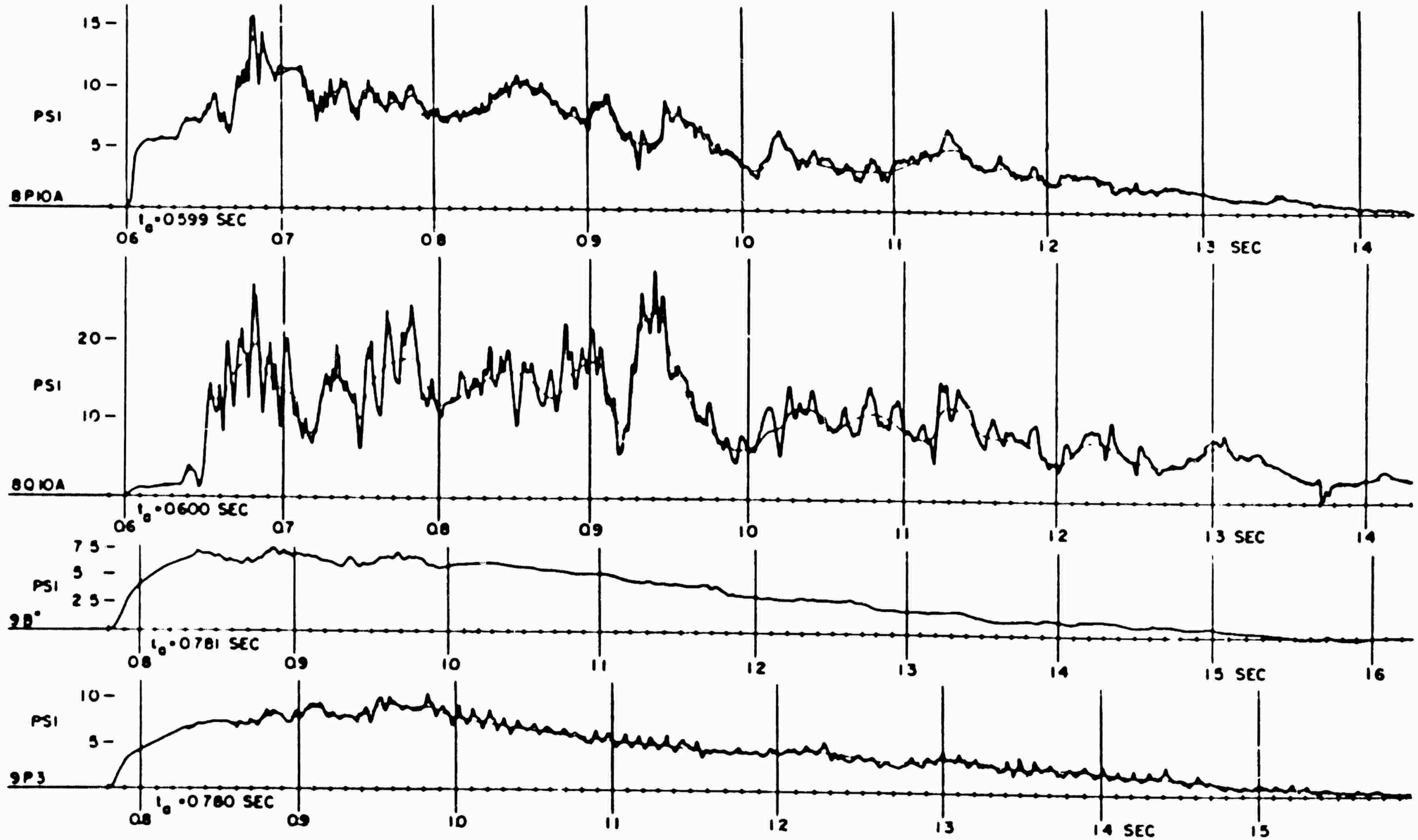

Figure B.7 Original records, Shot 12, desert line, 2,250 feet—2,750 feet.

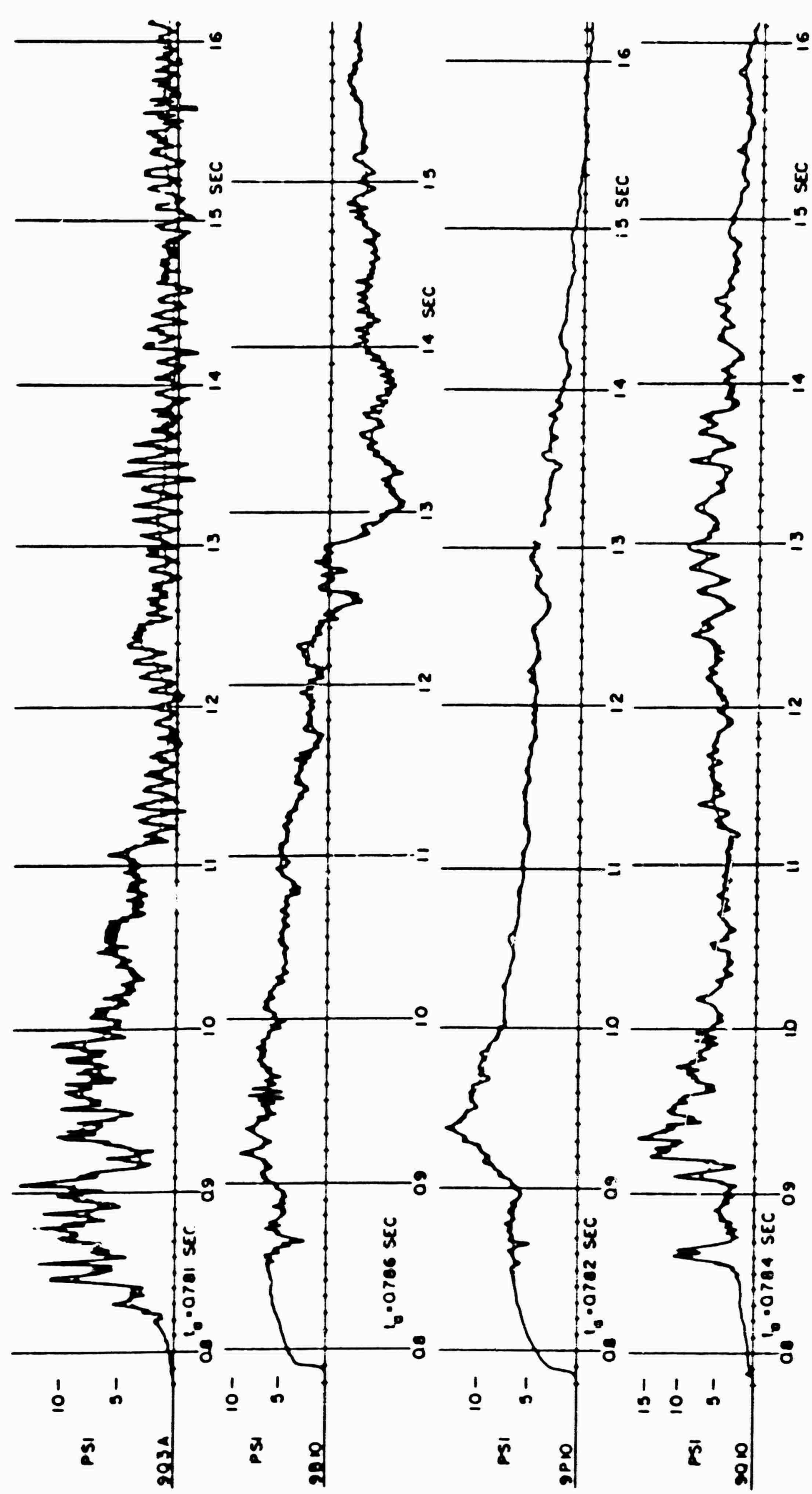

Figure B.7 Continued.

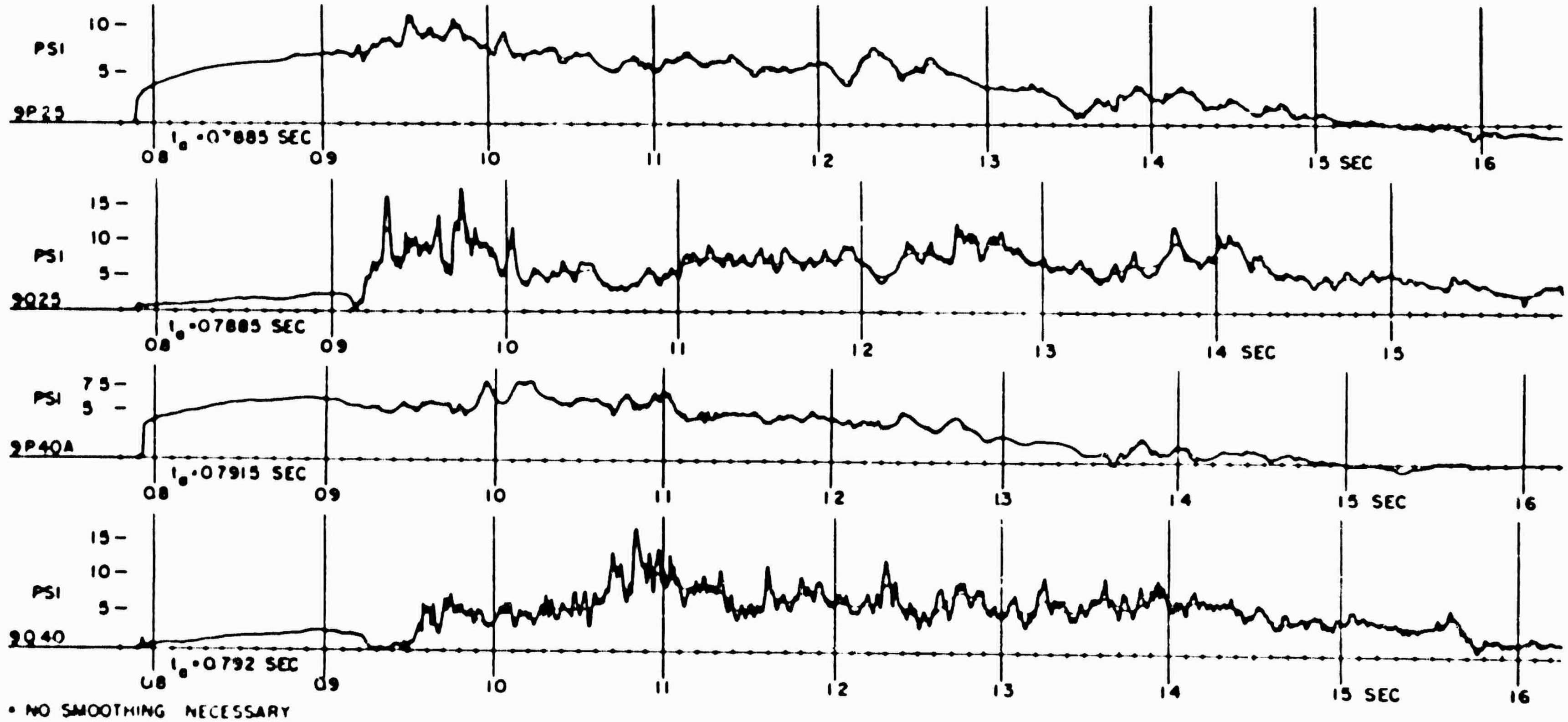

Figure B.7 Continued.

DECLASSIFIED

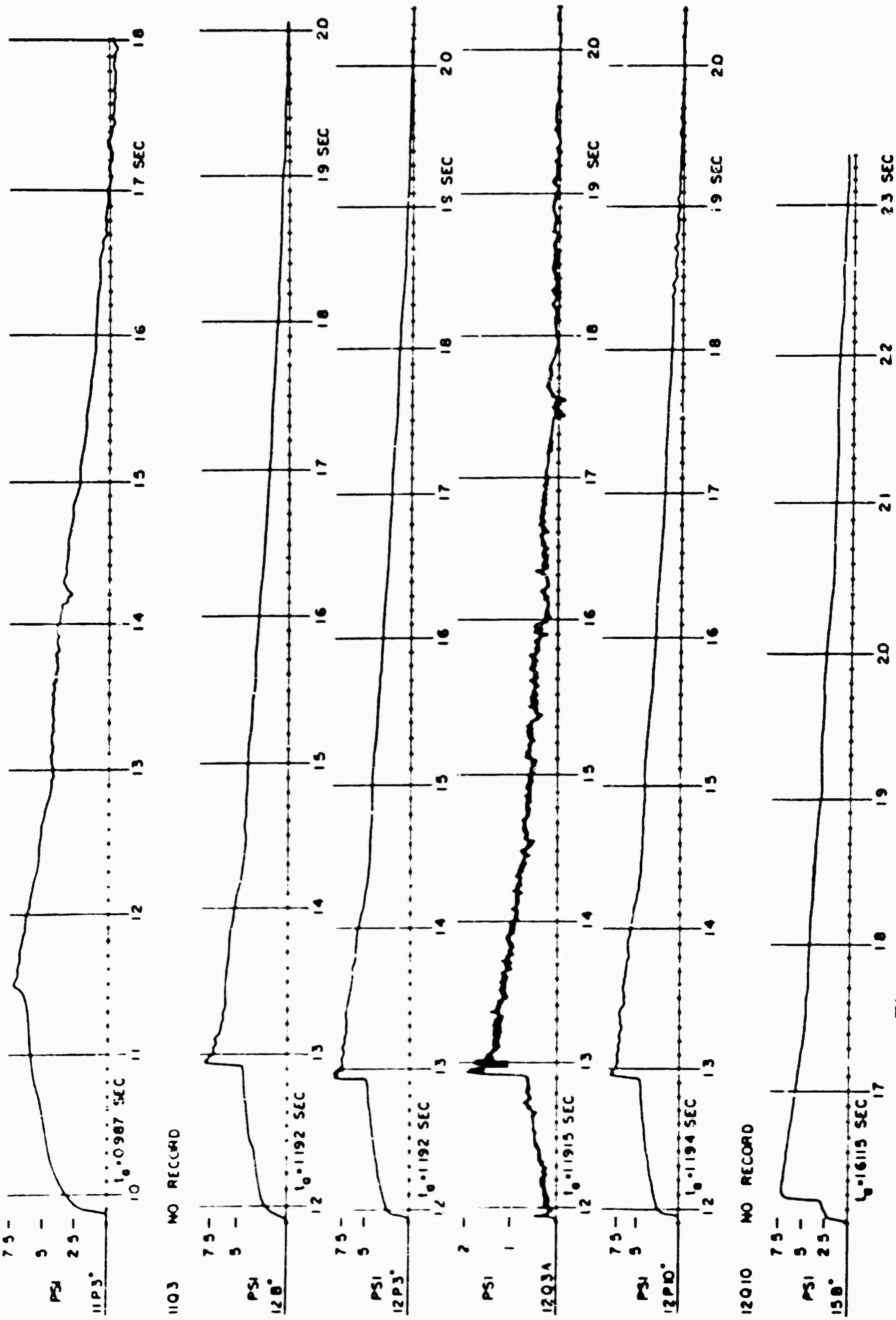

Figure B.8 Original records, Shot 12, desert line, 2,750 feet—4,500 feet.

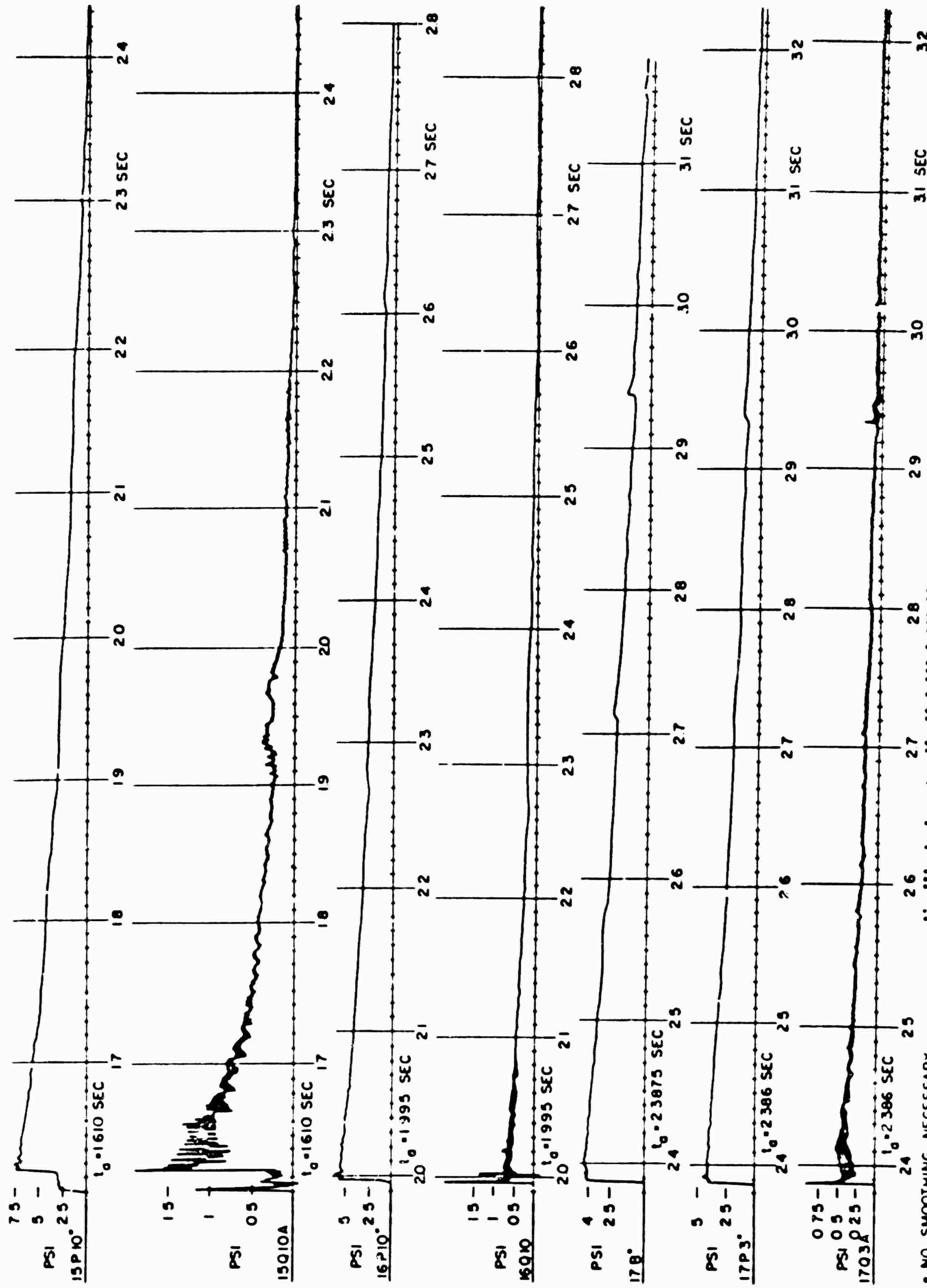

Figure B.8 Continued.

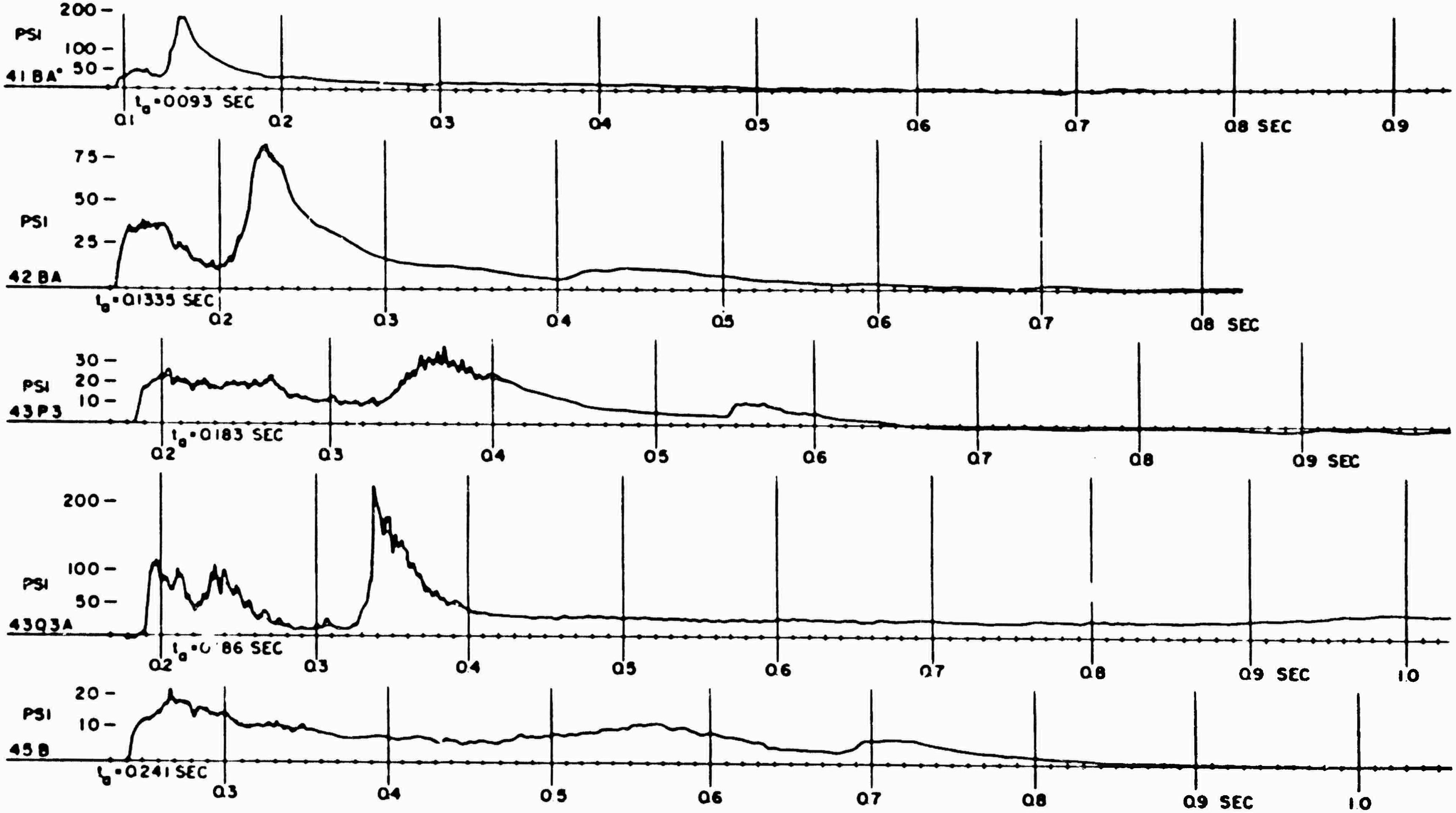

Figure B.9 Original records, Shot 12, asphalt line, 750 feet—1,500 feet.

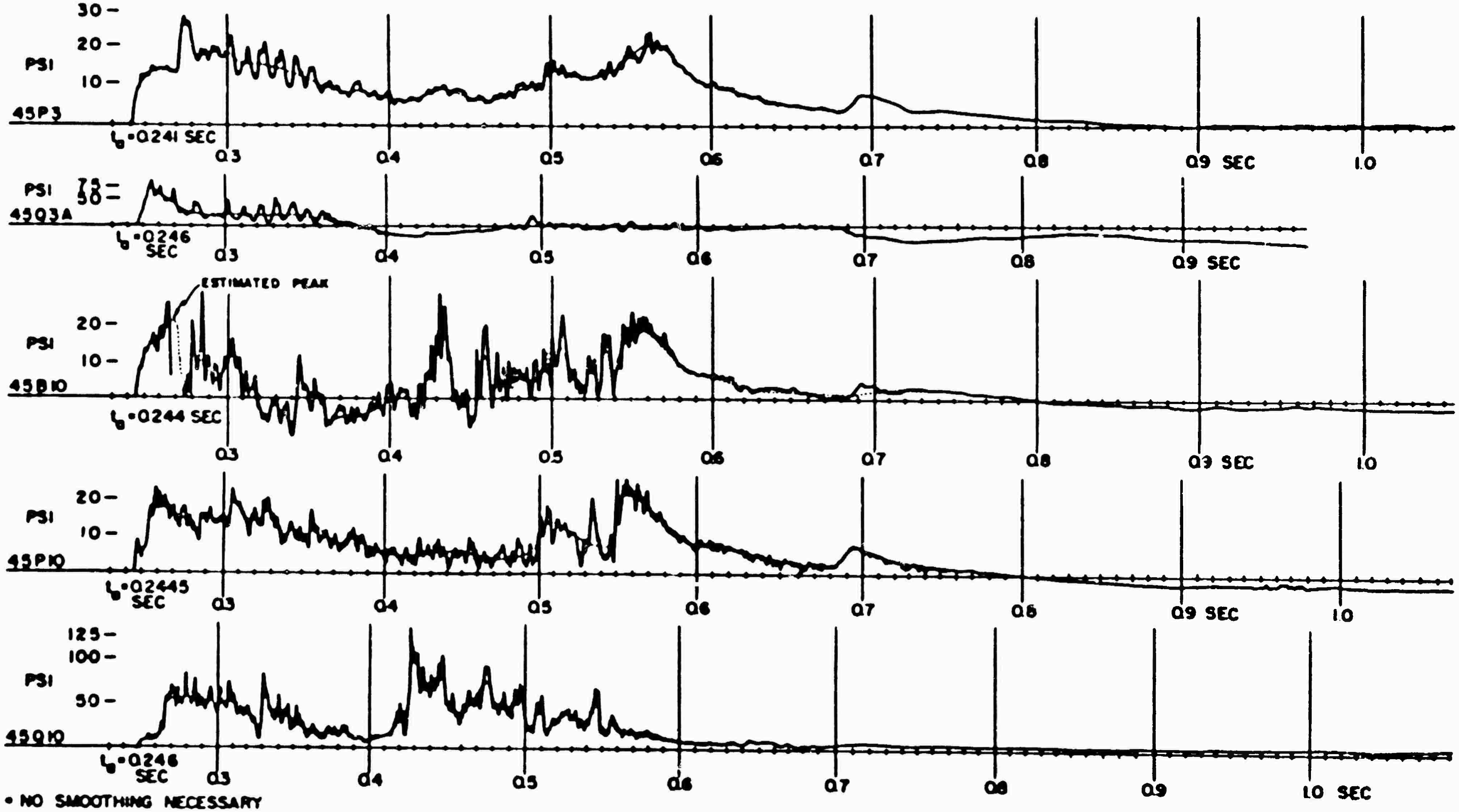

Figure B.9 Continued.

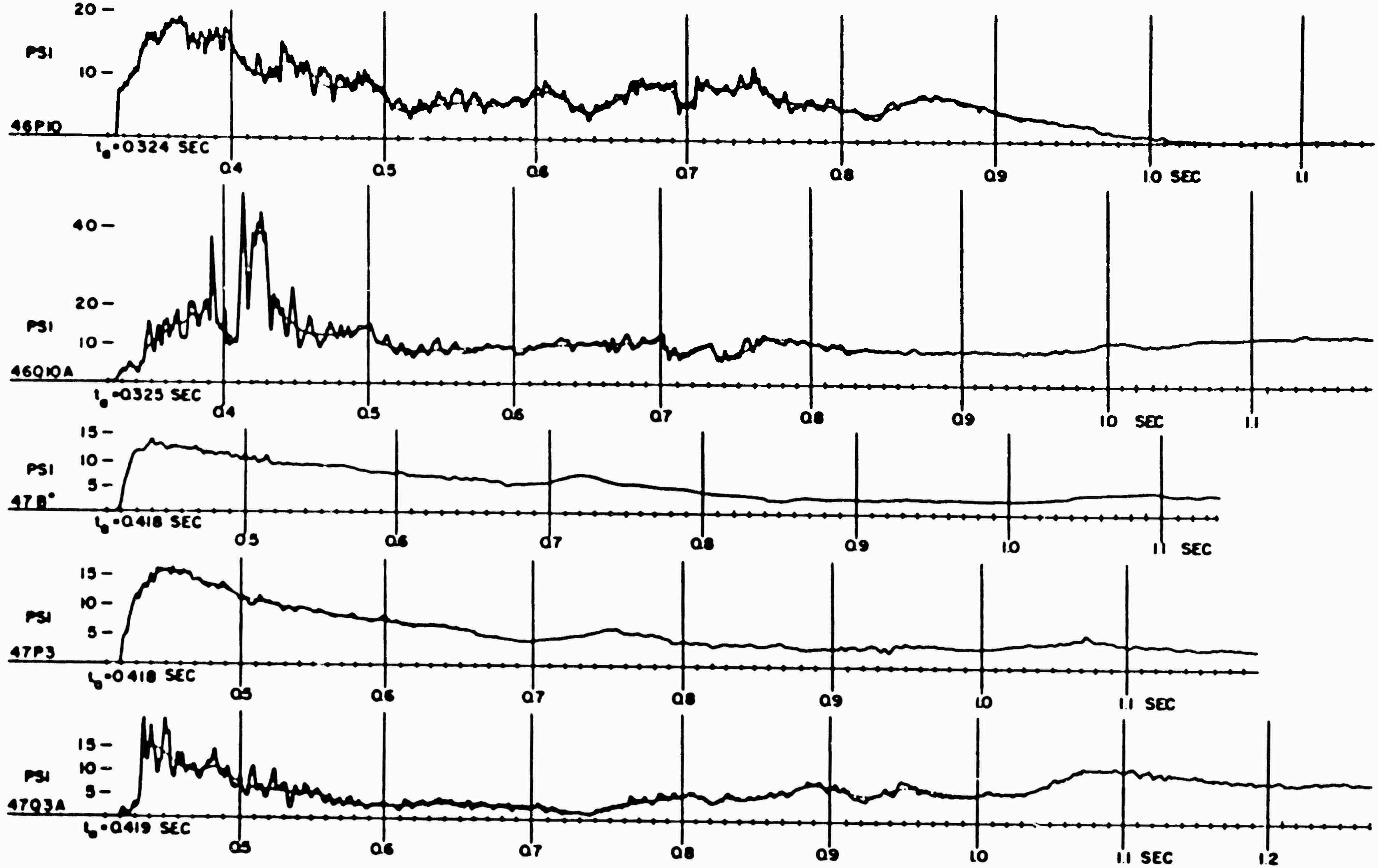

Figure B.10 Original records, Shot 12, asphalt line, 1,750 feet—2,250 feet.

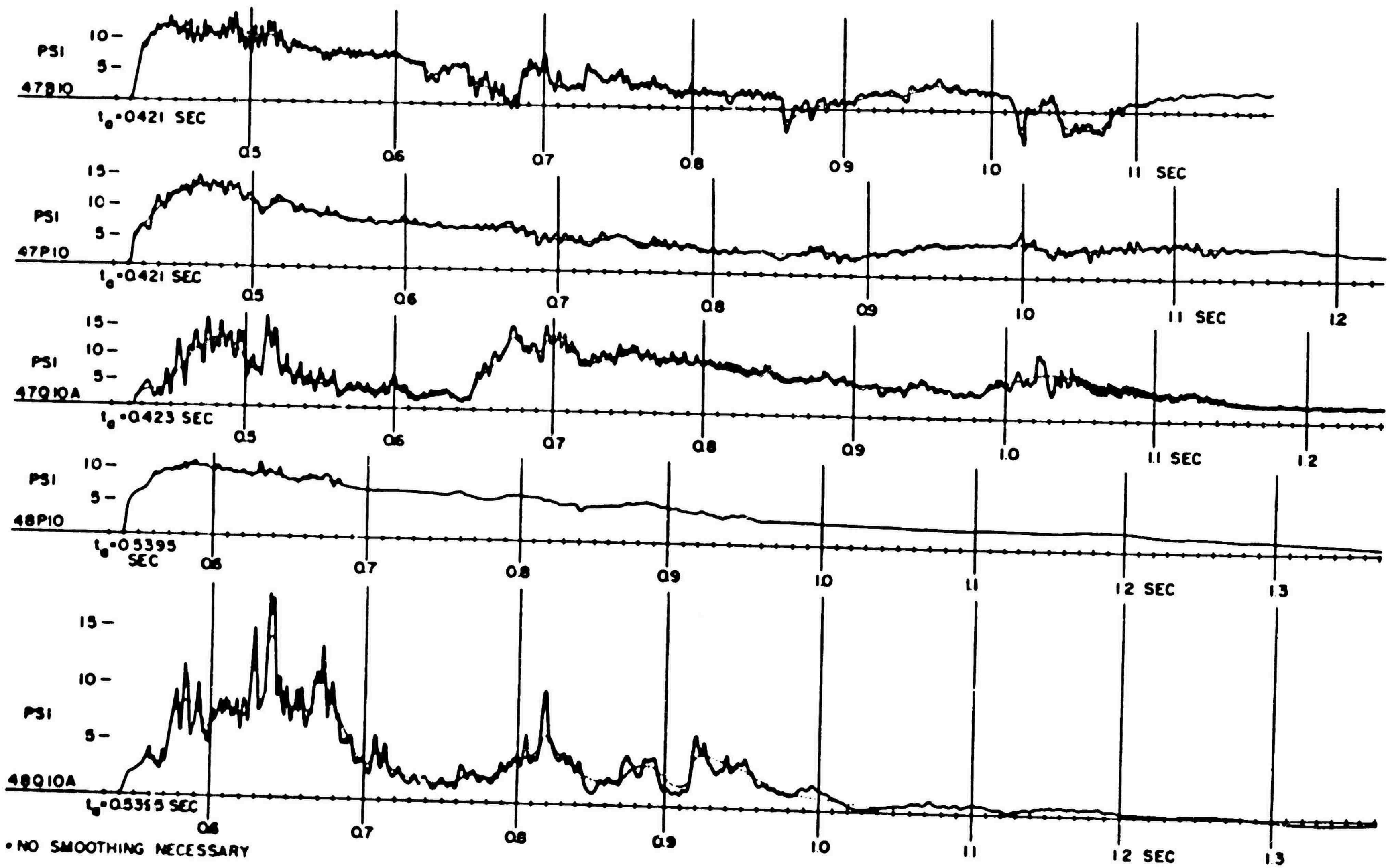

Figure B.10 Continued.

DECLASSIFIED

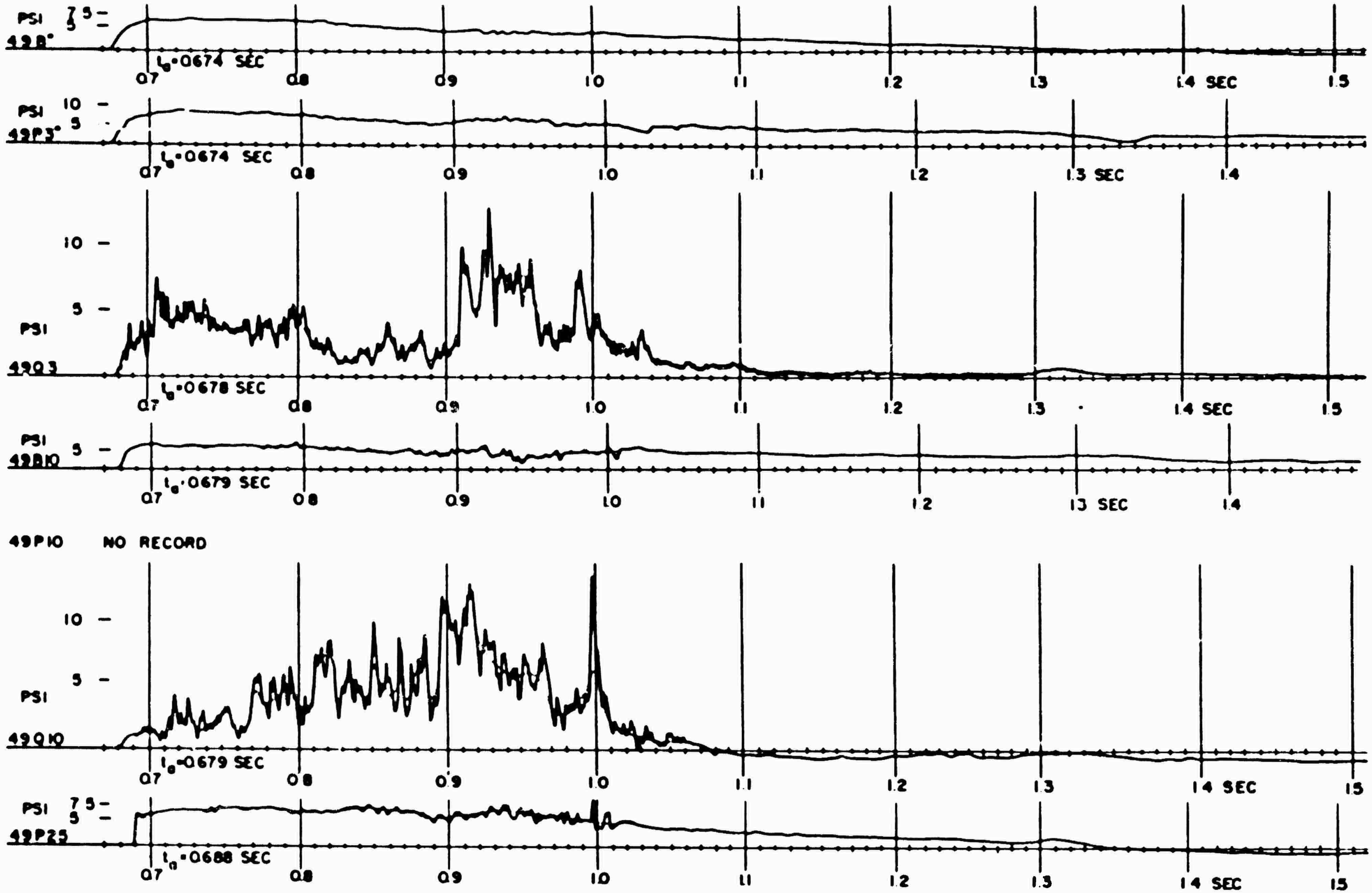

Figure B.11 Original records, Shot 12, asphalt line, 2,500 feet–3,000 feet.

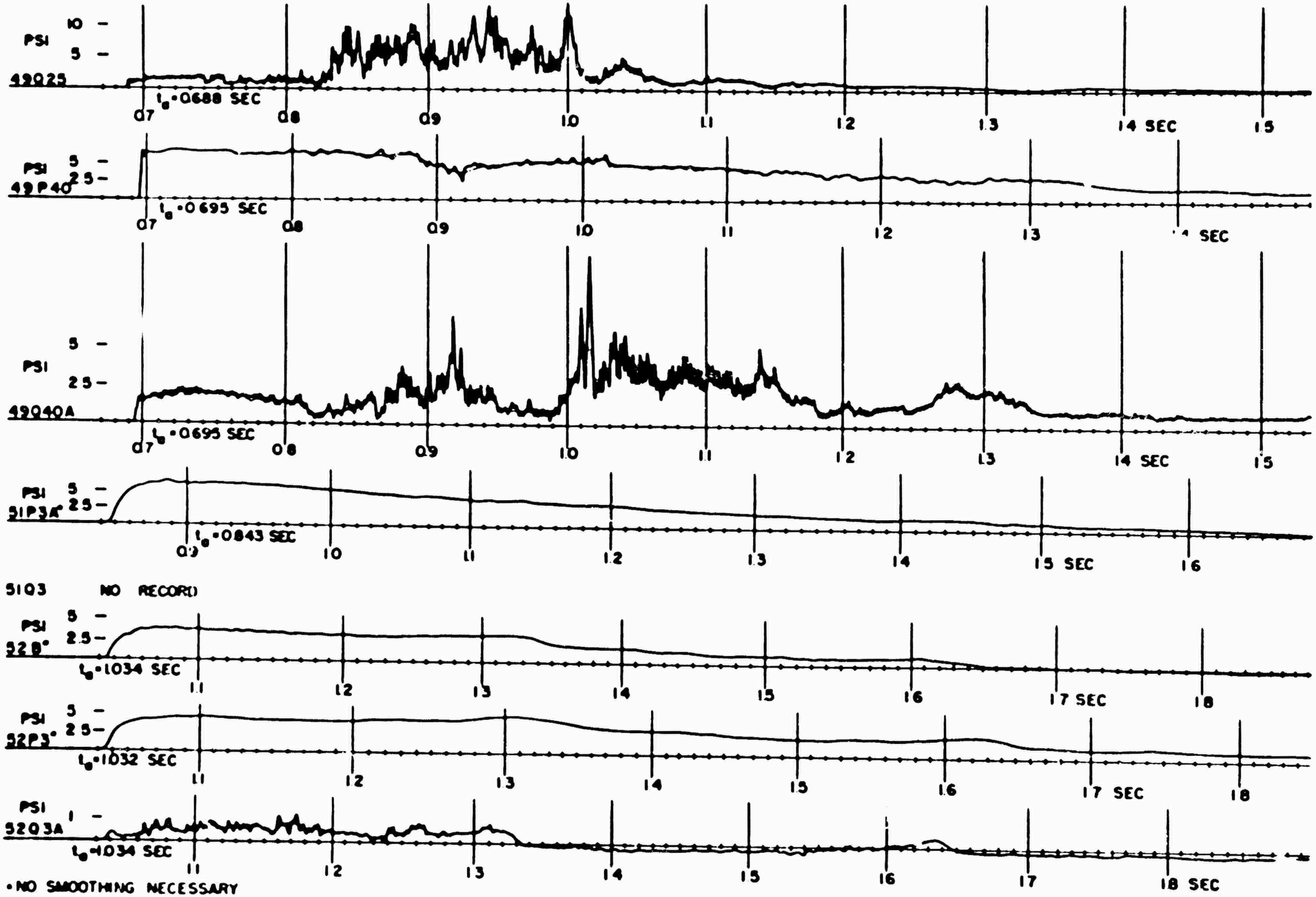

Figure B.11 Continued.

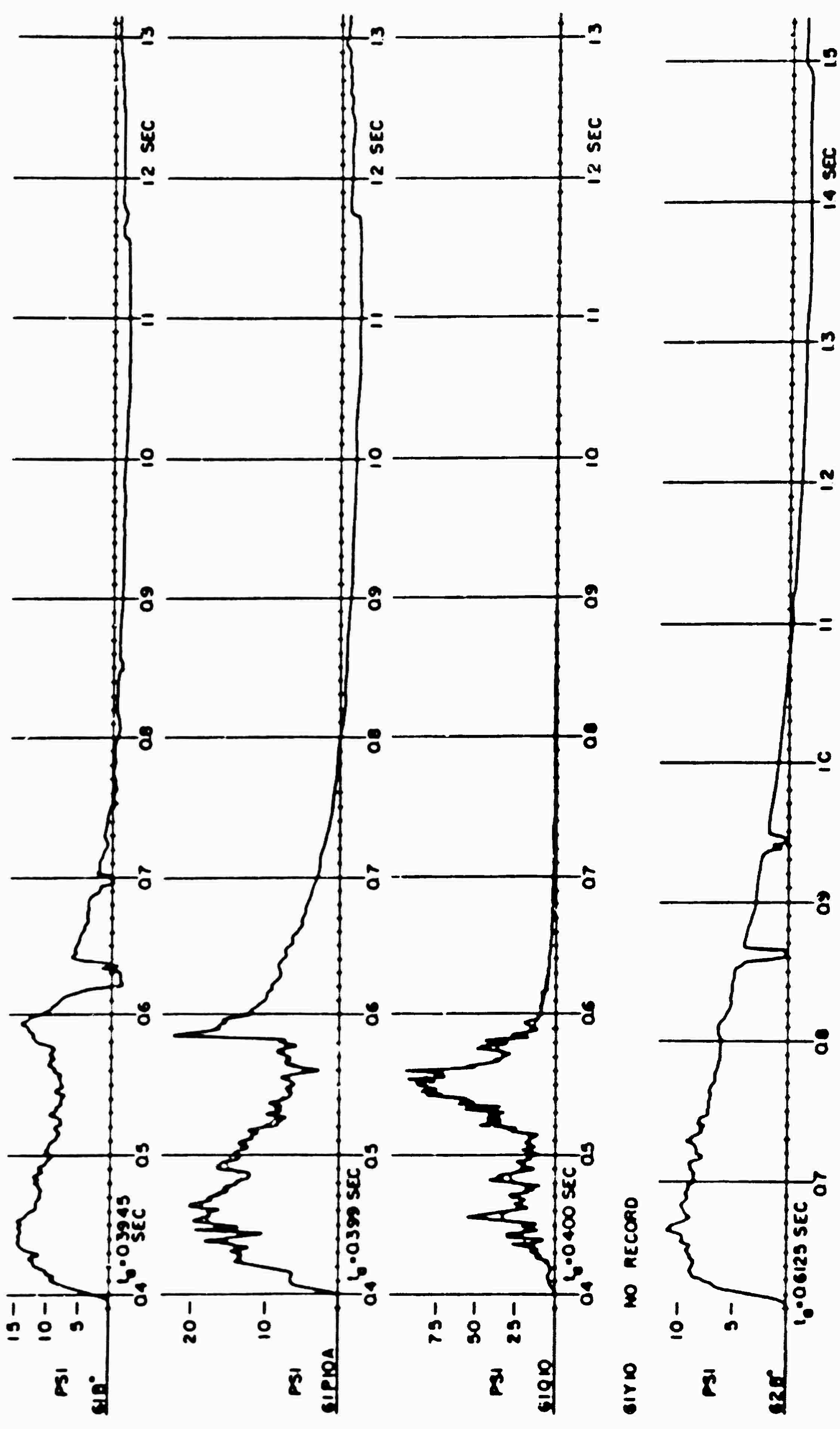

Figure B.12 Original records, Shot 6, desert line.

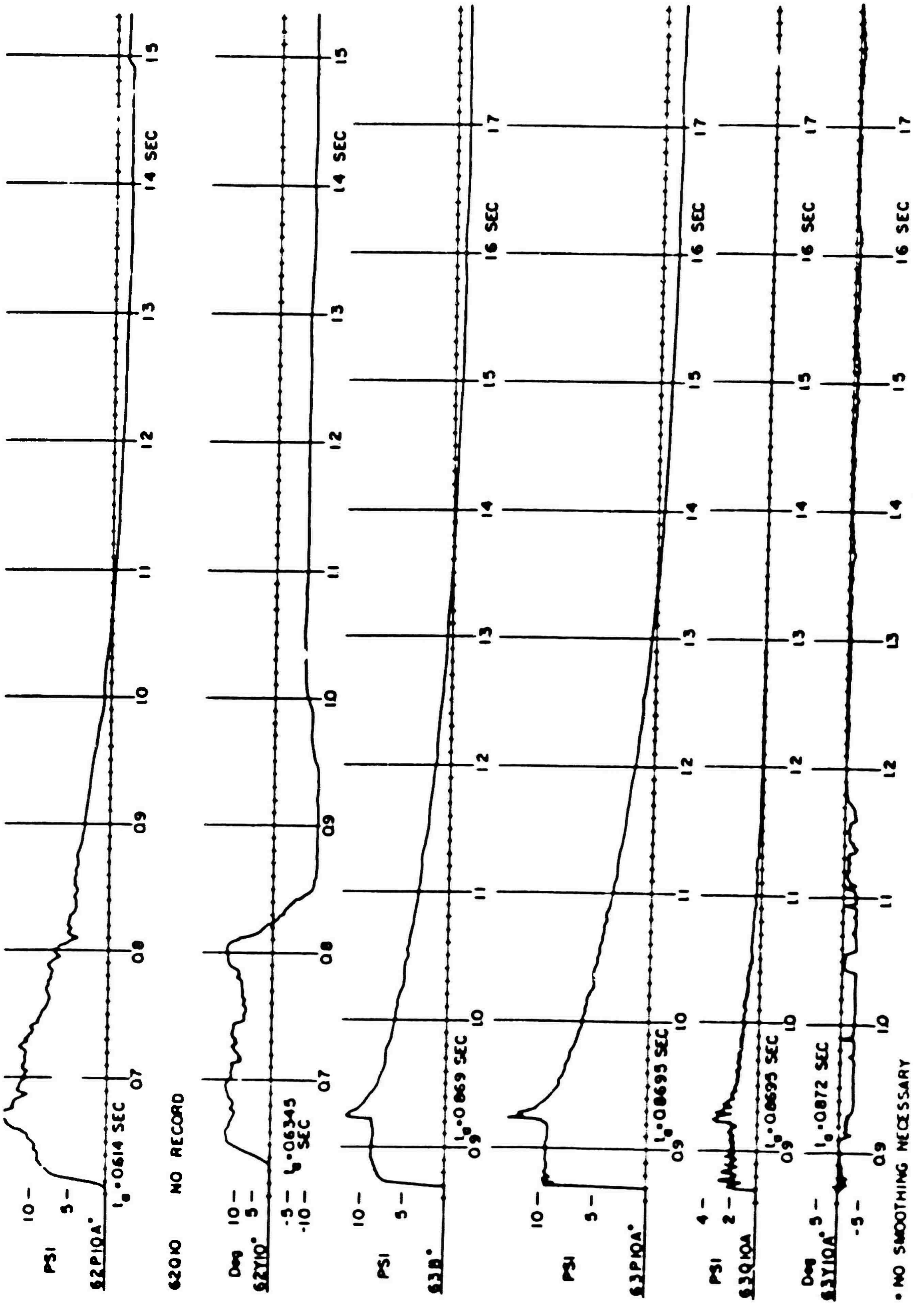

Figure B.12 Continued.

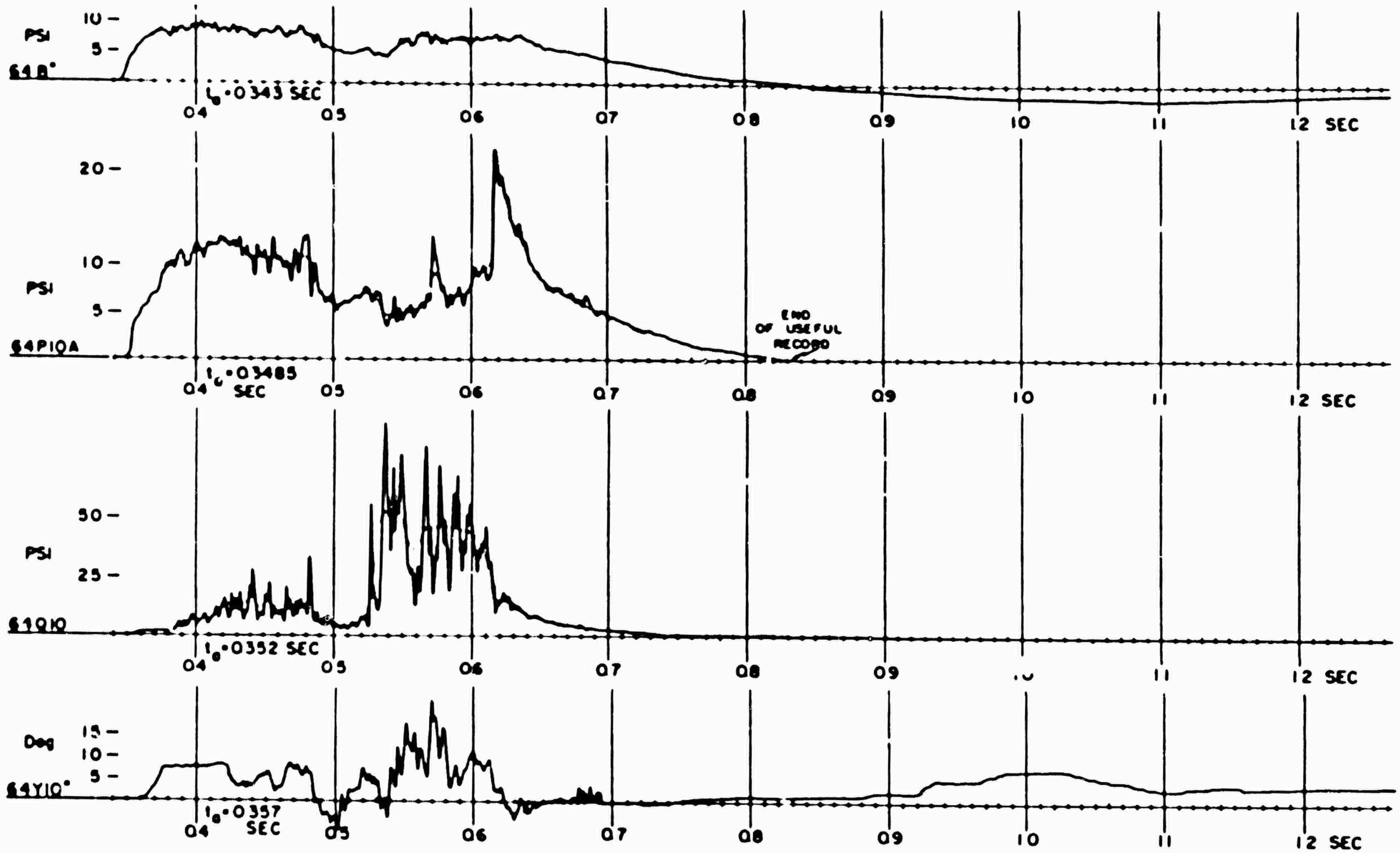

Figure B.13 Original records, Shot 6, asphalt line

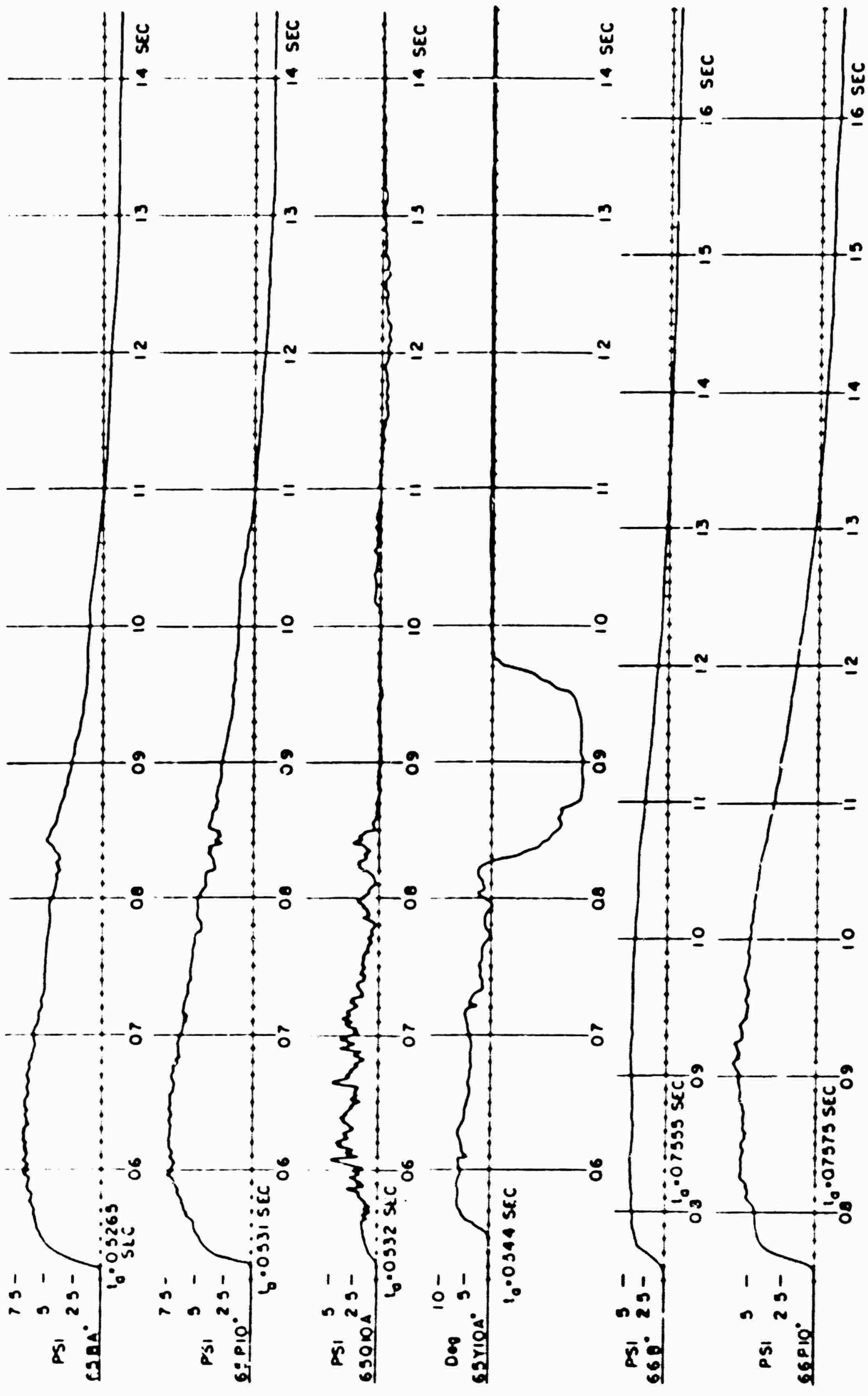

Figure B.13 Continued.

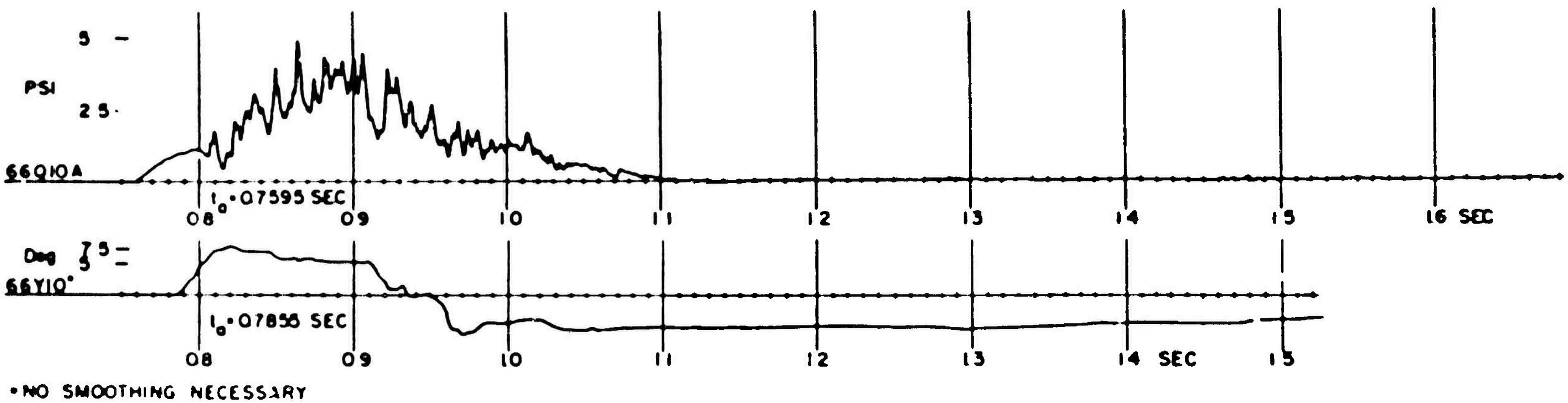

Figure B.13 Continued.

Appendix C

GAGE CALIBRATION DATA

TABLE C.1 SHOT 6 PRESSURE GAGES

Ground Range ft	Gage Number	Calibration (psi/in) $ax + bx^2$ A	L	Ground Range ft	Gage Number	Calibration (psi/in) $ax + bx^2$ A	B
			Desert				
1,300	61B	8.02	0	2,000	63B	5.51	0
	61BA	7.81	−0.13		63BA	5.18	−0.08
	61P10	9.48	0.11		63P10	5.27	0
	61P10A	6.90	0		63P10A	4.35	0
	61Q10	29.29	1.30		63Q10	3.43	0.30
	61Q10A	16.17	0.06		63Q10A	3.33	0.24
	61Y10	9.76	0.14		63Y10	+13.07	0
	61Y10A	18.41	−0.36		63Y10A	+11.46	0
1,650	62B	4.72	0				
	62BA	4.02	−0.07				
	62P10	2.63	0.06				
	62P10A	5.94	0				
	62Q10	14.72	−0.39				
	62Q10A	8.83	−0.11				
	62Y10	+12.27	0				
	62Y10A	+14.14	0				
			Asphalt				
1,300	64B	8.22	0	2,000	66B	6.30	0
	64BA	8.37	0		65BA	4.55	0
	64P10	8.42	0.07		66P10	2.77	0
	64P10A	5.21	0		66P10A	5.76	0.07
	64Q10	21.57	0.19		66Q10	4.09	0.09
	64Q10A	15.96	0.18		66Q10A	1.97	0
	64Y10	+11.27	0		66Y10	+9.00	0
	64Y10A	+11.33	0		66Y10A	+16.65	0
1,650	65B	5.34	0.08				
	65BA	4.40	0.07				
	65P10	4.30	0.07				
	65P10A	6.66	0.12				
	65Q10	6.42	0				
	65Q10A	5.23	0				
	65Y10	+13.23	0				
	65Y10A	+9.96	0				

[redacted]L

TABLE C.2 SHOT 12 PRESSURE GAGES

Ground Range ft	Gage Number	Calibration (psi/in) $ax + bx^2$ A	B	Ground Range ft	Gage Number	Calibration (psi/in) $ax + bx^2$ A	B
			Desert				
730	1B	138.1	2.4	2,500	9B	4.06	0.17
	1BA	98.7	1.7		9P3	5.24	0
1,000	2B	55.8	−0.8		9Q3	7.31	0
	2BA	56.4	−1.2		9Q3A	4.34	0
1,250	3P3	25.13	0.23		9B10	5.39	0
	3P3A	20.68	0		9P10	4.97	0.03
	3Q3	125.7	0		9Q10	5.96	0.48
	3Q3A	57.0	1.7		9Q10A	6.87	0.51
1,500	5B	12.33	−0.37		9P25	4.79	0.29
	5P3	11.31	0.18		9Q25	7.09	0.28
	5Q3	51.9	−6.5		9P40	4.64	0
	5Q3A	31.2	0		9P40A	5.37	0
	5B10	11.87	−0.10		9Q40	8.59	0.38
5	5P10	12.33	−0.16	2,750	11P3	3.42	0
	5Q10	78.0	0		11P3A	6.02	0
	5Q10A	35.7	0		11Q3	2.28	0.06
1,750	6P10	9.94	0		11Q3A	3.95	0.21
	6P10A	6.63	0	3,000	12B	4.77	−0.25
	6Q10	34.64	1.98		12P3	4.96	0
	6Q10A	18.04	0.28		12Q3	1.76	0.15
2,000	7B	8.19	0.58		12Q3A	0.921	0.034
	7P3	6.13	0.40		12P10	5.32	−0.10
	7Q3	16.65	−0.15		12Q10	2.08	0.01
	7Q3A	12.87	0	3,500	15B	4.75	0
	7B10	8.80	−0.28		15P10	4.28	0.11
	7P10	8.17	0.16		15Q10	1.08	0
	7Q10	24.61	0.37		15Q10A	0.519	−0.009
	7Q10A	12.32	0	4,000	16P10	4.93	−0.23
2,250	8P10	6.52	0.34		16Q10	1.09	0.02
	8P10A	3.91	0	4,500	17B	3.17	0.05
	8Q10	15.14	0.25		17P3	3.61	0
	8Q10A	6.10	0		17Q3	0.830	0
					17Q3A	0.887	0
				1,500	4BX	13.01	−0.11
					4BY	13.71	−0.36
			Water				
750	21B	183.7	−6.6	2,546	29B	11.13	0.21
	21BA	191.6	−7.6		29BA	9.22	−0.19
1,000	22B	77.9	−1.3		29P3	9.54	0
	22BA	68.8	−1.8		29Q3	3.99	0.04
1,250	23P3	74.7	1.2		29Q3A	2.01	0
	23P3A	74.6	−2.4		29B10	10.86	−0.31
	23Q3	78.6	4.9		29P10	11.65	−0.32
	23Q3A	59.0	0		29Q10	1.84	0.04
					29Q10A	4.02	0.21
					29P25	10.71	0.24
					29Q25	2.65	0.02
					29Q25A	3.01	−0.03
					29P40	9.30	0
					29P40A	8.89	0.06
					29Q40	3.89	0
					29Q40A	2.70	−0.04

TABLE C.2 CONTINUED

Ground Range ft	Gage Number	Calibration (psi/in) $ax + bx^2$ A	B
1,500	25B	41.06	0
	25BA	35.94	−0.68
	25P3	32.18	−1.05
	25Q3	43.90	−0.44
	25Q3A	21.26	−0.29
	25B10	20.81	0.07
	25B10A	33.49	0.67
	25P10	34.33	−2.44
	25Q10	29.94	−0.19
	25Q10A	18.06	−0.11
1,750	26P10	15.98	0
	26P10A	26.63	0
	26Q10	14.30	0.33
	26Q10A	18.1	−0.13
2,000	27B	13.04	0
	27BA	17.68	−0.37
	27P3	18.20	−0.45
	27Q3	5.76	0.89
	27Q3A	6.60	0.31
	27B10	19.70	−0.98
	27B10A	17.11	−0.74
	27P10	16.28	−0.80
	27Q10	11.01	1.12
	27Q10A	6.60	0.44
2,250	28P10	11.39	0
	28P10A	11.06	- 10
	28Q10	5.43	0.27
	28Q10A	3.29	0.09
2,750	31P3	4.52	0.17
	31P3A	7.98	0.31
	31Q3	3.09	0.71
	31Q3A	1.31	0.27
3,000	32B	7.85	0.39
	32BA	6.60	0.28
	32P3	5.72	0.14
	32Q3	2.04	0.16
	32Q3A	2.30	0.22
1,500	25P3X	33.82	−1.77
	25Q3X	37.71	0.55
	25Q3XA	24.41	0
	25P3Y	25.88	−0.60
	25Q3Y	33.19	1.63
	25Q3YA	20.65	−0.14
2,500	29P3X	9.64	−0.22
	29Q3X	2.42	0.05
	29Q3XA	3.17	0.07
	29P3Y	9.09	−0.15
	29Q3Y	3.74	0.32
	29Q3YA	2.80	0.22
Asphalt			
750	41B	109.3	0
	41BA	127.0	0
1,000	42B	48.8	4.1
	42BA	26.6	0.7
1,250	43P3	24.0	−0.4
	43P3A	42.3	−0.86
	43Q3	110.5	0
	43Q3A	74.2	0
1,500	45B	13.20	1.13
	45P3	10.79	1.00
	45Q3	255.2	−68.2
	45Q3A	89.1	7.73
	45B10	14.18	−0.45
	45P10	13.56	0.14
	45Q10	55.27	0.96
	45Q10A	25.98	−0.26
1,750	46P10	7.23	0
	46P10A	10.26	0
	46Q10	30.25	1.52
	46Q10A	11.96	0
2,000	47B	9.51	−0.34
	47P3	8.18	−0.22
	47Q3	21.70	−0.59
	47Q3A	10.05	−0.16
	47B10	7.48	0
	47P10	7.68	0
	47Q10	15.91	−0.20
	47Q10A	8.70	−0.18
2,250	48P10	6.82	0.21
	48P10A	8.26	0
	48Q10	7.32	0.41
	48Q10A	4.16	0.06
2,500	49B	9.99	−0.80
	49P3	11.98	0
	49Q3	3.50	0.06
	49Q3A	4.40	0.10
	49B10	13.24	−0.96
	49P10	5.97	0.28
	49Q10	3.23	0.14
	49Q10A	4.60	0.11
	49P25	8.96	−0.42
	49Q25	6.46	0.20
	49Q25A	2.90	0
	49P40	5.72	0.20
	49P40A	7.79	0.30
	49P140	8.91	0
	49P140A	2.93	0
2,750	51P3	4.99	0.15
	51P3A	6.31	0.20
	51Q3	3.17	0.32
	51Q3A	2.73	0.22
3,000	52B	5.80	0.51
	52P3	5.94	0
	52Q3	1.09	0.04
	52Q3A	1.91	0.12

TABLE C.3 SHOT 12 STRAIN GAGES (H-BEAM)

Ground Range	Gage Number	Calibration A	Calibration B
ft		lb-force/in^2/in	lb-force/in^2/in
2,000	7F3	38.40	−1.66
2,000	7F3A	17.08	−0.93
2,500	9F3	20.59	−2.25
2,500	9F3A	19.69	−1.80